ULTRASONIC FATIGUE OF E319 CAST ALUMINUM ALLOY IN THE LONG LIFETIME REGIME

by

Xiaoxia Zhu

A dissertation submitted in partial fulfillment
of the requirements for the degree of
Doctor of Philosophy
(Materials Science and Engineering)
in The University of Michigan
2007

Doctoral Committee:

Professor J. Wayne Jones, Co-Chair
John E. Allison, Co-Chair, Ford Motor Company
Professor Tresa M. Pollock
Professor Jwo Pan

Acknowledgements

I would like to extend my deepest gratitude to my thesis advisors, Prof. J. Wayne Jones and Dr. John E. Allison, for their mentoring, support, encouragement and patience throughout my graduate study. The guidance of these gentlemen has been outstanding. Further appreciation is due to the members of the dissertation committee, Prof. Pollock and Prof. Pan, for their guidance and suggestions.

The funding provided by National Science Foundation grant number DMR 0211067 and Ford Motor Company are gratefully acknowledged.

I would like to thank my fellow graduate students and research group members (past and present); Chris Torbet, Jianzhang Yi, Amit Shyam, Chris Szcepanski, Jiashi Miao and Liu Liu, who have assisted in this work and created an enjoyable atmosphere within which to work. I must acknowledge Chris Torbet, in particular, for his countless efforts in technical assistance and wisdom. His willingness to prioritize my work is deeply appreciated. Special thanks are also due to Dr. Jianzhang Yi for his great work in statistical analysis which allowed a deeper understanding of my research. I would also like to express my appreciation to Dr. Amit Shyam for his contributions to my learning process throughout my Ph. D study, which gave me a wonderful basis for the completion of my research project.

My colleagues at the Ford Scientific Research Laboratory were of invaluable assistance in the completion of this project. Larry Godlewski and Jake Zindel helped me in making all the castings with which I carried out the experiments. Carlos Engler-Pinto

and John Lasecki provided the conventional fatigue data that were used in this thesis to compare with the ultrasonic fatigue data. James Boileau shared good insight about fractographic analysis.

I also wish to thank my friends, who have been part of my life throughout graduate school, for their friendship and help whenever needed. Finally I express my deepest appreciation to my parents and my husband for their understanding, devotion and unconditional support. Special thank goes to my son, Michael, who made my graduate career more delightful and productive.

Table of Contents

List of Tables

List of Figures

Chapter 1

Introduction

1.1 Background and objectives

The use of cast aluminum alloys in automotive structural applications is growing rapidly due to the benefits of weight reductions in saving energy and reducing exhaust gas emissions. Cast aluminum alloys have been extensively used in the production of fatigue critical automotive components, including engine blocks and cylinder heads, which experience two distinct types of fatigue damage in service: low-cycle fatigue (LCF) or thermo-mechanical fatigue (TMF) resulting from engine start/stop cycles; and high-cycle fatigue (HCF) due to the variation of pressure within the combustion chamber [1]. For HCF, these components experience more than 10^8 alternating stress cycles during the expected service life and the high cycle fatigue properties are therefore of great interest. However, conventional fatigue testing techniques limit the acquisition of fatigue data to about 10^7 cycles. This leads to design approaches which must make conservative assumptions about fatigue behavior at lives greater than 10^7 cycles. To improve design approaches, new methods are needed to acquire very long life fatigue data and a more fundamental understanding of the role of microstructure on long life fatigue behavior is required.

Very long lifetimes can be achieved in a practical time frame by using ultrasonic fatigue in which cyclic loading is applied at frequencies of approximately 20 kHz [2]. With this technique, the S-N test can be greatly accelerated. For example, it takes less than 2 hours to accumulate 10^8 cycles by using ultrasonic fatigue. Had the test been performed using a servo hydraulic test frame operating at 75 Hz, a test time of over 15

days would have been required. Accelerated testing is especially important when fatigue properties of cast materials are studied because microstructural variability causes pronounced scatter in fatigue data, and characterization of these materials requires testing sufficiently high numbers of specimens to include statistical variation in the material characterization. Ultrasonic fatigue techniques may also be used for rapid generation of fatigue crack growth data and offers the possibility to study very low fatigue crack growth rates far below the conventional threshold (10^{-10} m/cycle). For example, it takes ten minutes to generate a crack of one millimeter at a growth rate of 10^{-10} m/cycle by using ultrasonic fatigue; while two days are required for completing this process with servo hydraulic fatigue instrumentation.

However, in actual applications of cast aluminum alloys, e.g. engine cylinder heads and blocks, the critical locations within these components are being subjected to a loading frequency of 20 -100 Hz for an engine running in the range of 2000-6000 RPM. The question of whether fatigue behavior determined by ultrasonic methods is comparable to that determined at conventional frequencies needs further examination. In this thesis, the fatigue behavior of a commercially important 319-type cast aluminum (referred to as E319) used in the production of automotive cylinder heads, was studied by using both an ultrasonic fatigue technique and a conventional fatigue technique to understand the potential effect of frequency on crack growth and therefore fatigue behavior of cast aluminum alloy. The potential use of ultrasonic fatigue techniques as a viable alternative or replacement for more conventional testing methods, especially in the very long life regime, is examined.

To increase engine efficiency, the maximum operating temperature of cylinder heads has increased from approximately 170°C in earlier engines to peak temperatures well above 200°C in recent engines [3]. The increase in the operational temperatures requires a material with optimized properties in terms of tensile, creep and fatigue strength. Although a number of studies have been performed on the fatigue properties of

319 cast aluminum alloys at room temperature [4-6], the description of the fatigue behavior of these alloys at elevated temperature is not well established. Therefore, it is important to examine the influence of temperature on fatigue performance of E319 cast aluminum alloy. In addition, the potential effects of frequency on fatigue behavior of E319 aluminum alloy at elevated temperature need to be investigated when extend the application of ultrasonic fatigue technique to elevated temperature condition.

Cast aluminum alloys contain porosity, which is a key microstructural feature controlling fatigue properties [4-13]. The porosity varies in size and distribution depending on the rate of solidification. Faster solidification generally results in a lower volume fraction of smaller pores than with slower solidification rate. In addition to reducing the amount of material that can carry the applied loads, porosity often acts as stress raisers and low-energy initiation sites for cracks. In almost all cases, fatigue cracks initiate at pores at the specimen surface or just beneath it. The initiation life is generally thought to be negligible, and the total fatigue life of the cast material is dominated by the crack propagation phase. In the very high cycle fatigue regime ($10^8 \sim 10^9$ cycles), the existence of an endurance limit has been observed in recent studies in cast aluminum alloys [6, 14]. The fundamental mechanisms responsible for the presence of endurance limits in E319 alloy needs to be explored. The effect of the casting porosity population on the endurance limit of this alloy also needs further study to aid in life prediction model development.

Therefore, the objectives of this research are:

1) To understand the potential frequency effects on fatigue crack growth and, therefore, fatigue behavior of cast aluminum alloy E319, at both room temperature and elevated temperature.

2) To identify the effect of temperature on fatigue behavior of E319 cast aluminum alloy, and to model temperature-fatigue life in temperature range of interest for automotive applications.

3) To understand the effect of porosity on very long life (10^7 to 10^9 cycles) fatigue of E319 cast aluminum alloy.

4) And finally, to assess the potential of ultrasonic fatigue techniques for rapid characterization of fatigue behavior.

1.2 Approach

In order to accomplish these objectives, S-N (stress amplitude vs. fatigue life) curves of E319 cast aluminum alloy were developed using an ultrasonic testing system operating at 20 kHz in the lifetime regime of 10^6 to 10^9 cycles, and at temperatures of 20, 150 and 250°C. Comparative studies were also conducted by using a servo-hydraulic testing system operating at 75 Hz for lifetimes as long as 10^7 cycles at each temperature. Thus, an extensive database of fatigue lifetime as a function of frequency and temperature was created. A statistical model, random fatigue limit (RFL) model, was then applied to the S-N results to quantitatively analyze and compare the fatigue performance of E319 cast aluminum alloy.

The fatigue life is generally divided into two phases: crack initiation and crack propagation. Once the specimens were fatigued to failure, the microstructural features associated with the fatigue crack initiation in this pore-containing material were determined by fractographic examination and their size and location were quantitatively measured. The effects of frequency and temperature on crack initiation behavior of E319 cast aluminum alloy were examined.

The fatigue crack propagation behavior was characterized in order to understand the influence of frequency and temperature on fatigue performance of E319 cast aluminum alloy. Fatigue crack propagation was studied by examining the small crack growth behavior in laser notched pore-free specimens at both 20 kHz and 30 Hz, and at temperatures of 20 and 250°C. Small crack growth tests were also conducted under controlled humidity in air at room temperature to investigate the effect of environment on

crack growth, which is coupled with the effect of frequency.

Through the analysis of the extensive experimental data acquired, the effects of frequency, temperature and porosity on fatigue behavior of E319 cast aluminum alloys, and associated mechanisms, were investigated.

This thesis is divided into six chapters. Background and objectives of this research is presented in Chapter 1. A review of the relevant literature is presented in Chapter 2. Chapter 3 describes the experimental method used in this study. In Chapter 4, the influences of frequency, environment and temperature on fatigue performance of E319 cast aluminum alloy, with the associated mechanisms, are investigated and characterized by a superposition model. In Chapter 5, the effect of porosity on fatigue strength at 10^8 cycles at room temperature is examined and a probabilistic model is developed to correlate the general casting porosity population with the fatigue strength of E319 cast aluminum alloy. Conclusions and recommendations for future studies are presented in Chapter 6.

Chapter 2

Literature review

This chapter reviews the literature most pertinent to the subject of this thesis and is presented in five sections. The first section describes the principles of operation and the instrumentation used for ultrasonic fatigue. The second section presents the fatigue behavior of aluminum alloys in the very high cycle regime. The third section presents the phenomenon of "small crack effect" and the associated mechanisms for the small crack growth behavior. Sections four through six review the effects of frequency, environment, temperature, and microstructure on fatigue in aluminum alloys, respectively.

2.1 Ultrasonic fatigue technique

Ultrasound in the frequency range of 15 to 22 kHz has been used to perform fatigue loading of solid materials under resonance conditions since 1950 [15]. Mason [16] first used ultrasonic (20 kHz) methods in 1950 with the adaptation of magnetostrictive and piezoelectric-type transducers to fatigue testing. This method translated 20 kHz electrical voltage signals into 20 kHz mechanical displacements. A displacement-amplifying acoustical horn and the test specimen were driven into resonance by the transducer. This approach has remained basically unchanged and is the foundation of the practices used in modern ultrasonic fatigue test technology. Ultrasonic fatigue testing is applicable to most engineering materials, including metals, ceramics, glasses, plastics and composites.

2.1.1 Principles of ultrasonic fatigue

Ultrasonic fatigue is a resonant test method, in which a large amplitude displacement wave must be established in a resonant system. Resonance is required to achieve the strain amplitude needed to produce fatigue in materials [2, 15].

As shown in Figure 2.1, a sound wave is emitted from an ultrasonic transducer into one end of the load train and travels along the load train at a velocity which is determined by the elastic constants (Young's modulus for axial waves and shear modulus for torsional waves), the density of the material, and the shape of the component. The sound waves enter the fatigue specimen and are reflected from the opposite end of the wave train, i.e. the lower end of the specimen or eventually the end of an additional mounting part. If the time required for traveling the length of the specimen and returning is equal to the period of the input sound waves, the reflected wave will be exactly in phase with the input wave, standing wave conditions will be established and the specimen will be in resonance. The length of the specimen is therefore required to be exactly half of the wavelength of the sound wave in the specimen.

The displacement amplitude distribution along the specimen length can be determined by solving the differential equation:

$$u(x)'' + \frac{A(x)'}{A(x)} u(x)' + \frac{4\pi^2 f^2 \rho}{E} u(x) = 0 \tag{2.1}$$

where *u(x)* is displacement amplitude in the longitudinal direction at distance *x* from one end of the specimen; *A* is cross sectional area; *f* is resonance frequency; ρ is density of the specimen; *E* is the dynamic Young's modulus of the material. It should be pointed out that dynamic modulus differs from the static modulus obtained from a tensile test. The static modulus is inadequate for converting the strain amplitude to stress amplitude, because it will include anelastic contributions to strain that are absent at ultrasonic frequency. Use of the static modulus gives stress estimates that are too low, because the static modulus is typically less than the dynamic modulus [15].

Consider a straight bar of material having a uniform diameter ($A' = 0$). Equation 2.1 is simplified as:

$$u(x)'' + \frac{4\pi^2 f^2 \rho}{E} u(x) = 0 \tag{2.2}$$

with boundary conditions of

$$\begin{aligned} u(0) &= u_0 \\ u'(0) &= 0 \end{aligned} \tag{2.3}$$

The variation of displacement amplitude at a point *x, u(x),* will be:

$$u(x) = u_0 \cos(2\pi f \sqrt{\frac{\rho}{E}} x) \tag{2.4}$$

The strain (ε) distribution along the bar will be the derivative of the displacement amplitude with respect to distance:

$$\varepsilon(x) = \frac{du(x)}{dx} = -2\pi f \sqrt{\frac{\rho}{E}} u_0 \sin(2\pi f \sqrt{\frac{\rho}{E}} x) \tag{2.5}$$

The resonance length (L) is determined by the first point of x, where $\varepsilon(x) = 0$, i.e.

$$\varepsilon(L) = -2\pi f \sqrt{\frac{\rho}{E}} u_0 \sin(2\pi f \sqrt{\frac{\rho}{E}} L) = 0 \tag{2.6}$$

$$L = \frac{1}{2f} \sqrt{\frac{E}{\rho}} \tag{2.7}$$

The stress (σ) distribution along the bar is obtained by an elastic conversion of the strain distribution:

$$\sigma(x) = E \cdot \varepsilon(x) \tag{2.8}$$

This example of the uniform resonant bar embodies the basic concepts of ultrasonic fatigue testing. With appropriate geometric modification, these concepts can be used to design the test specimen. Strain amplification is desirable at the center of the specimen. This is accomplished by reducing the cross-section area of the gage section to produce a dumbbell-shaped specimen. By reducing the cross-section, the total power

needed to drive the specimen into resonance is reduced. Consequently, the amount of heat produced in the specimen is reduced, which also reduces the cooling requirements. Figure 2.1 shows the distribution of displacement amplitude and strain amplitude along the length of a specimen. The minimum displacement amplitude and maximum strain amplitude occur at the center of the specimen. Similarly, the maximum displacement amplitude and minimum strain amplitude occur at the ends of the specimen.

Resonance lengths of typical fatigue specimens made of aluminum, steel, or titanium alloys are about 60–130 mm for axial and 30–80 mm for torsional vibrations, depending on the design of the specimens. Since the resonance length is inversely related to the resonance frequency, using significantly higher frequencies than 20 kHz would lead to relatively small specimens.

2.1.2. Instrumentation for ultrasonic fatigue

Figure 2.2 is a schematic of typical ultrasonic fatigue instrumentation. For fully reversed loading condition (R = −1), the mechanical system is composed at least of an ultrasonic transducer, an amplification horn, and a specimen [2, 6, 15, 17], as shown in Figure 2.2 (a).

The ultrasonic transducer [2, 6, 15, 17] generates an acoustic wave that produces a cyclic displacement at the end of the load train by transforming sinusoidal electric power into mechanical oscillations. The acoustic wave proceeds down the rest of the load train to the specimen. When the frequency of the electric power signal equal to the mechanical resonance frequency of the load train, a resonance condition is achieved and a large amplitude displacement wave is established, which is necessary to perform fatigue testing.

The amplification horn [2, 6, 15, 17] serves to magnify the vibration amplitude along the load train, which is realized by decreasing the cross-sectional area of the horn as distance from the input end varies. The length of the horn is adjusted in order to maintain resonance. The materials of the amplification horn are typically high strength

titanium alloys, for example Ti–6Al–4V, which shows good mechanical stability and low acoustic damping [2].

The specimen is mounted at one end of the horn. The displacement amplitude is measured with a gage at the ultrasonic horn close to the specimen's end. Strain can be measured by directly apply strain gages to the center of the specimen. It is assumed that the measured displacement amplitude is proportional to the strain amplitude in the specimen center as long as the specimen vibrates in the linear elastic regime. The fatigue experiment is controlled by the displacement amplitude and not by the strain amplitude[2, 6, 15], since strain gages frequently fail. Strain gages are used to calibrate the experiments, i.e. to determine the proportional factor between strain amplitudes and displacement amplitudes.

For fatigue experiments under fully reversed loading condition ($R = -1$), one end of the specimen may vibrate free (Figure 2.2 (a)). An addition load train can also be attached to the other end of the specimen, as shown in Figure 2.2 (b), to provide static mean loading [2, 6] or superposition of large-amplitude low-frequency cycling on top of the high-frequency cycling [18].

The operation frequency of ultrasonic fatigue tests is approximately 20 kHz. The cyclic resonance frequency is controlled with very high accuracy, within ±1 Hz. Decrease of resonance frequency and increase of the fatigue crack length are correlated, if the temperature of load train and specimen are constant. Thus, frequency limit can be used to automatically stop the experiments when fatigue cracks grow to a certain length. When the cyclic frequency is lower than the selected minimum frequency, the process stops due to frequency error [6].

The cyclic load is not applied continuously but in a pulse-pause sequence. Pauses of adequate length and additional forced-air cooling serve to keep specimen temperature within a close range [2, 6, 15].

2.1.3 Advantages and limitations of ultrasonic fatigue technique

The advantages and limitations of ultrasonic fatigue testing technique were reviewed by Mayer [2] as listed below:

Advantages:

1) Time saving

Ultrasonic fatigue experiments need an average test time 100–1000 times shorter than investigations with conventional equipment. Therefore, it is possible to apply very high numbers of cycles (10^8–10^9 cycles) in less than 1 day. This allows the investigation of fatigue properties in the very long lifetime regime or in the regime of very low crack growth rates ($10^{-13} \sim 10^{-14}$ m/cycle), which would be uneconomic with conventional fatigue testing equipment. A shorter testing time makes it possible to investigate a larger number of specimens within a certain time period. This is especially important for inhomogeneous materials where numerous experiments are necessary to obtain statistically reliable data.

2) Energy saving

As loading is in resonance, the power requirement necessary to perform fatigue experiments is relatively low. Fatigue tests may be performed within a short time period, thus demanding only a small amount of energy.

3) Possible testing procedures

Studies of lifetimes, fatigue crack initiation, and fatigue crack propagation may be performed under high frequency tension–compression cycling as well as under high frequency torsional loading. It is possible to superimpose external static or slowly varying axial or torsional loads on the ultrasonic vibration. The experiments may be performed at different temperatures [6] and in fluids, gases, or in a vacuum [19].

4) Specimen fixture

Mechanical stress of the specimen ends is low. Brittle materials, such as ceramics, can be tested without the problem of fracture near the specimen fixture. If fatigue

experiments under fully reversed loading conditions are performed, only one specimen end must be fixed.

Limitations:

1) Resonance loading condition

Resonance loading implies that all mechanical parts must have a relatively restricted shape. Actual components cannot be tested directly using ultrasonic fatigue. Single load cycles cannot be performed because the load is applied in pulses consisting of a minimum of 500 cycles.

2) Material temperature

Cyclic loading at ultrasonic frequency may lead to an increase in specimen temperature. Plastic deformation and friction can raise local temperature near the crack tip, especially if fatigue experiments with materials with low thermal conductivity are performed. Periodic pauses between pulses may be relatively long in these cases, which significantly increases the required testing times. Large internal friction or small thermal conductivity makes high frequency fatigue testing difficult in vacuum.

3) Load control

The displacement at the specimen ends or the strain in a vibration node may be used to control cyclic loading. Cyclic stress amplitudes in the specimen center cannot be measured directly, but must be calculated from the strain measurements based on Hooke's law. Therefore, the cyclic stress applied must be less than the yield strength so that the specimen deformation is nominally elastic.

4) Low cyclic loads

High frequency fatigue experiments are restricted to relatively low cyclic loads. A large cyclic plastic deformation may cause heating of the specimen and lead to unreliable fatigue data. Fatigue crack growth rates greater than approximately 10^{-7} m/cycle are difficult to control due to a rapidly advancing crack.

5) Influence of cycling frequency on fatigue process

When time dependent processes, e.g. corrosion, creep, or dynamic strain aging, are superimposed on the fatigue process, the fatigue data obtained at high and low cycling frequency may differ. For some materials, ultrasonic frequency may introduce a strain rate effect on the fatigue process.

2.2 Very high cycle fatigue of cast aluminum alloys

Performing fatigue tests into the very high cycle regime becomes practical with the use of ultrasonic testing techniques. With this approach, a specimen is tested at frequency of approximately 20 kHz, where applying 10^8 cycles requires two hours and applying 10^9 cycles can be completed typically within a day. Therefore, a significant amount of data can be established in a very short period of time and the fatigue strength at cycles greater than the expected service life can be empirically determined, rather than estimated from extrapolations.

For cast aluminum alloys, fatigue cracks readily initiate from large pores due to the higher stress concentration at the pores [20, 21] at high stress amplitude or in the lifetime regime $<10^7$ cycles. The initiation life is generally thought to be negligible, and the total fatigue life of the cast material is dominated by the crack propagation phase from the initiating pore to the final crack length.

In the very long lifetime regime (10^6 -10^{10} cycles), an asymptotic tendency is observed in the S-N curve [6, 8, 14, 22, 23]. In such situation, it is often assumed that the fatigue lifetime tested below a certain stress level is infinite and this stress amplitude is termed as the endurance limit (or fatigue limit). An example is shown in Figure 2.3 [14]. The data indicate that an endurance limit exists in W319-T7 when the cyclic loading was run to 10^9 cycles; the S-N plot exhibits a very distinct trend in the data where a horizontal slope is approached as the stress amplitude is decreased. The distinct endurance limits observed are thought to be a result of the defect-controlled fatigue performance of cast aluminum. Cycling at or below the endurance limit may cause crack initiation from pores;

however, these cracks do not propagate to failure because the driving force for crack advancement is below a critical threshold value [8, 14]. The existence of an endurance limit in the porous cast aluminum alloys therefore is caused by non-propagating fatigue cracks rather than by a non-initiation condition. The endurance limit was correlated with porosity through a critical stress intensity amplitude [8, 24, 25].

It is also seen in Figure 2.3 that the scatter in the data observed in the long lifetime regime is quite large. This was attributed to the sensitivity of fatigue resistance to the severity of crack initiation sites [14, 24, 25]. At low stress amplitudes, the largest pore in one specimen may be adequate to initiate and grow a crack to failure, while the largest pore in another specimen may not be large enough to produce a crack that can be driven to grow under the same conditions. In contrast, when higher stress amplitudes are applied, large and small pores alike possess stress intensities greater than the crack growth threshold and all specimens experience failure. The scatter under these conditions is significantly smaller.

2.3 Small crack growth behavior

When the driving force for crack advancement is above the threshold, the fatigue life of cast aluminum alloys is generally assumed to be dominated by the crack propagation phase from the initiating pore to the final crack length [4, 26]. In this case, prediction of the fatigue life based on crack growth behavior is appropriate.

The propagation of small fatigue cracks in metallic materials has received considerable attention over the past decades [26-32]. It was discovered that small, naturally-initiated cracks did not behave in accordance with conventionally acquired long crack data. When the crack growth rates were plotted as a function of the stress intensity factor range, ΔK, the small cracks displayed propagation at ΔK levels less than the long crack threshold, ΔK_{th}, and grew faster than long cracks for equivalent levels of ΔK [27, 29, 31]. Small crack behavior in cast aluminum alloys has been observed. Figure 2.4

gives an example of both small and long crack growth behavior in a cast W319 aluminum alloy [33]. It is apparent that a small crack effect occurs. The long-crack data (solid lines) indicated threshold stress intensity factors of approximately 2.7 MPa-$m^{1/2}$. Nevertheless, the cracks were seen to propagate at ΔK levels as low as 0.7 MPa-$m^{1/2}$ at 140MPa, and 1.1 MPa-$m^{1/2}$ at 100MPa, both significantly less than the measured long crack ΔK_{th} levels. It is also seen that the small crack growth rate is stress dependant.

Countless studies have been conducted on a wide array of materials in order to identify the mechanism controlling small crack growth and to develop reliable methods for characterizing this behavior. Three possible explanations have been proposed to account for the behavior of such small cracks: crack closure, breakdown in microstructural similitude and plasticity effects [34]. These mechanisms are briefly described below.

It has been recognized that crack closure reduces the driving force from (K_{max}-0) to (K_{max}-K_{op}) for long crack propagation [35]. Various sources of closure have been identified, such as plasticity, oxide or debris, roughness/microstructure, residual stress, viscous fluid penetration, phase transformation, etc [36]. However, small cracks typically do not experience the same levels of crack closure. Reduced levels of crack closure are therefore identified as one of the factors leading to the faster growth of small cracks [28].

Microstructural similitude refers to the condition where a crack front encounters a large numbers of microstructural units and the growth of the crack is averaged over a large number of microstructural units oriented favorably and unfavorably for continued propagation. For small fatigue cracks, microstructural similitude does not apply since the crack front encounters only a few microstructural units. As a result, small cracks exhibit an oscillating (acceleration/retardation) crack growth rate behavior, which can be rationalized through the reduction of the crack tip driving force when relevant microstructural obstacles are encountered. In wrought alloys, this retardation has been associated with grain boundaries, while in cast aluminum alloys it has been associated

with secondary microstructural phases such as eutectic Si particles [28].

Small scale yielding (SSY) ahead of the crack tip is generally assumed in using the linear elastic parameter ΔK. This assumption is violated for small cracks when the size of the plastic zone ahead of the crack tip is comparable to the size of the crack. It has been suggested that a reasonable limit for the applicability of ΔK is when the plastic zone size is less than approximately 1/5 the crack length [37]. The violation of SSY makes ΔK an inappropriate parameter for correlation small crack growth, and the increased plasticity experienced at higher stress levels can partially account for the influence of stress on small crack growth rates.

Small fatigue cracks can be categorized according to certain characteristics relative to the mechanisms just discussed [30]. Cracks are termed mechanically small when excessive plasticity precedes the crack tip and the plastic zone size is comparable to the crack size. Cracks are microstructurally small when the crack size is less than about five times the critical microstructural dimension, typically the grain size. Cracks are termed physically small when the crack size is less than about 1 mm. In addition, crack can be termed chemically small if the local crack tip environment promotes accelerated growth rates. Chemically small cracks can be as large as 10 mm. It is seen that the actual size of small fatigue cracks can vary considerably depending upon the material, applied stress, and the environment. The “universally defining characteristic” of all small cracks is that the growth rates are not adequately described by long crack data.

2.4 Effect of frequency and environment on fatigue of aluminum alloys

The ultrasonic test method is directly applicable when the test material ultimately will be applied in service at kilohertz frequencies, for example, high-frequency loading of turbines blades. For applications with lower frequency vibrations, for example, automotive engine components, the effect of frequency on test results must be interpreted and understood. The cycling frequency of ultrasonic instrumentation is about 2–10

decades higher compared with the conventional testing procedures. Intrinsic frequency effects may be attributed to high strain rates. The cycling frequency may also influence fatigue damage by time dependent interaction with the environment [2, 38-40].

2.4.1 Strain rate effect

The intrinsic effect of frequency in ultrasonic testing can be interpreted as the effect of increasing plastic strain rates on fracture and deformation behavior. For typical fatigue strain amplitudes in the range of 10^{-4} to 10^{-3}, the strain rate at 20 kHz ranges from 8 to 80 s^{-1}, while the strain rate at 30 Hz ranges from 0.01 to 0.1 s^{-1}.

Fatigue crack growth involves cyclic plastic deformation of the material near the crack tip. Therefore, the basic principles of frequency influences on crack propagation may be derived from the cyclic stress–strain behavior of materials. Laird and Charsley [41] gave an overview of frequency influences on cyclic plastic deformation, dislocation movement, damage localization, and fatigue crack growth in face-centered-cubic (FCC) and body-centered-cubic (BCC) metals. They concluded that FCC materials, e.g. aluminum and copper, exhibit a much lower strain-rate dependence than BCC materials, e.g. iron [41-43].

The cyclic stress–strain curve of FCC metals may be divided into three different regimes associated with certain dislocation structures [44, 45]. At low cyclic plastic strain amplitudes, an arrangement of trapped primary edge dislocation dipoles in a vein structure is formed. Cyclic plastic deformation is caused by screw dislocations which move back and forth in channels between the veins. For higher plastic strain amplitudes, dislocation arrangement consists of ill defined veins and persistent slip bands (PSBs), and plastic straining is mainly carried by PSBs. Under the influence of secondary slip a cell structure is formed at large plastic strain amplitudes. None of these dislocation structures is assumed to be particularly strain rate sensitive. The dislocation structures around fatigue cracks in polycrystalline copper cycled with conventional fatigue testing

equipment have been investigated by Lukas *et al.* [46] , Awatani *et al.*[47], and Tong and Bailon [48]. They found a dislocation arrangement of cells near the crack tip. Cell size increased with the distance from the fracture surface [47, 48]. PSBs and veins, loop patches, and triangles were found adjacent to the cells [48]. Lukas *et al.*[49] and Chen *et al.* [50] performed similar investigations after ultrasonic fatigue crack propagation. The dislocation structures for a cycling frequency of 20 kHz were reported to be similar to those found for low frequencies, i.e. a cell structure in the plastic zone near the crack tip and a PSB ladder-like structure in the adjacent material. Cell sizes at a certain distance from the fracture surface were found to coincide after cycling with the same stress intensity value for 100 Hz and 20 kHz [49]. Cell dislocation structures are relatively insensitive to changes in the stress amplitude and the cycling frequency. This is probably one reason for the moderate influence of the cycling frequency on the fatigue crack growth properties of FCC metals.

Because the cyclic deformation in FCC metals is weakly strain-rate dependent, it is unlikely that the mechanisms of crack initiation or propagation will be strain-rate sensitive if the environment is inert. Holper *et al*. [51, 52] investigated strain rate influences on fatigue crack growth of aluminum alloys (2024 and 7075) by performing near-threshold fatigue crack growth experiments at 20 kHz and 20 Hz in vacuum, as shown in Figure 2.5. Fatigue crack growth experiments in vacuum serves to determine strain rate influences on crack propagation excluding time dependent environmental effects. It can be seen from Figure 2.5 that no strain rate influences on near threshold fatigue crack growth in aluminum alloys are present, by changing the cycling frequency by three decades and testing at three different load ratios. This is consistent with the observations that plastic deformation of FCC metals is relatively insensitive to strain rates.

It should be noted, however, that the present findings for near-threshold cycling may not be equally valid at higher stress intensities. Frequency influences on crack growth on a FCC metal (304 stainless steel) have been reported at very high stress

intensities ($\Delta K > 25$ MPa-$m^{1/2}$) [53, 54]. Cyclic stressing near the fatigue limit or fatigue crack growth near the threshold stress intensity involves only a small cyclic plastic deformation, and intrinsic frequency influences are significantly moderated or absent. Therefore, ultrasonic lifetime and fatigue crack growth experiments should be restricted to small cyclic plastic deformations and low crack growth rates.

2.4.2 Environmental effect on fatigue

When the effect of strain rate is small, the effect of frequency on fatigue behavior is expected to be tied to one or more environmental effects. Since the duration of crack tip opening under high frequency loading is shorter than for conventional fatigue experiments, the environmentally assisted increase in fatigue crack growth rates is less pronounced, which may lead to lower crack growth rates.

2.4.2.1 Fatigue crack propagation in environments

A typical example [55] of fatigue crack growth behavior at room temperature is given in Figure 2.6 for single crystals of a high purity Al-Zn-Mg alloy tested in ambient air, nitrogen (containing traces of water vapor) and vacuum, at a frequency of 35 Hz. It can be seen that the fatigue crack growth threshold is decreased substantially by the presence of water vapor in the testing environment. In an inert gas (nitrogen) containing a small amount of water vapor (partial pressure of 15 Pa) the threshold range is the same as in air, which means a similar effect of water vapor even at such a low partial pressure. But at high growth rate, i.e., above 10^{-9} m/cycle, the behavior in nitrogen becomes similar to that in high vacuum. This indicates that, when the growth rate is fast, the influence of water vapor is observed only at much higher partial pressures such as that in ambient air. When the crack growth rate is even faster, i.e. above 10^{-6} m/cycle, the influence of water vapor becomes diminished even in ambient air. Similarly, Ruiz *et al*.[56] reported that, for 7017-T651 aluminum alloy, water vapor enhances crack growth rates for pressures in

the range from 5 to 200 Pa. As shown in Figure 2.7, the crack growth rate at 1 Pa is almost identical to high vacuum, and there is a sudden transition between 1 and 5 Pa. The crack growth rates from 5 to 100 Pa are very close and there appears to be a second transition between 100 and 200 Pa.

The influence of air humidity on fatigue crack growth in aluminum alloys was also observed at a frequency of 20 kHz and was very similar to that at low cyclic frequency. The crack growth curves of 2024-T3 obtained in vacuum, dry and ambient air are summarized in Figure 2.8 [57]. At 20 kHz, the fatigue crack growth threshold is decreased substantially by the presence of water vapor even at very low water vapor pressure. This implies that only a small amount of water vapor is sufficient to lower the threshold value compared with that in vacuum. Above the threshold regime (10^{-11} m/cycle $< da/dN < 10^{-10}$ m/cycle), crack growth rate is increased by increasing the water content in the testing environment. The crack propagation curve for dry air approaches that for vacuum when crack growth rate is greater than 10^{-10} m/cycle and the crack propagation curve for humid air approaches that for vacuum when crack growth rate is greater than 10^{-9} m/cycle. An environmental effect on crack growth of a cast aluminum alloy was reported by Papakyriacou *et al*. [58] (Figure 2.9). The difference between crack propagation rates in ambient air and in vacuum is most pronounced near the threshold stress intensity level and becomes smaller when growth rates are greater than 2×10^{-9} m/cycle. This is consistent with the work in [57].

The influence of frequency coupled with an environmental effect on fatigue crack growth of 7075-OA was studied by Stanzl-Tschegg [59] (Figure 2.10). In vacuum, similar growth rates were found at both frequencies. But in air, there is substantial influence of environment with the appearance of a plateau range; for low frequency (20 Hz), this occurs at growth rate of $\sim10^{-6}$ m/cycle, for ultrasonic frequency (20 kHz), this occurs at a growth rate of $\sim10^{-9}$ m/cycle. Near the threshold, no influence of the test frequency on the fatigue crack growth threshold was observed. Holper *et al*. [52] studied crack growth rate

of aluminum alloys 2024-T3 and 7075-OA in ambient air at 20 Hz and 20 kHz, as shown in Figure 2.11. It was found that fatigue cracks propagate at lower growth rates at ultrasonic frequency if cycled above threshold. In both alloys, the difference is most pronounced for fully reversed loading conditions, where fatigue cracks propagate by a factor of 5 to 50 faster at the lower frequency. With increasing load ratio, frequency influence becomes smaller.

2.4.2.2 Mechanisms and modeling

The deleterious effect of water vapor on fatigue crack growth behavior of aluminum alloys has been widely confirmed. In particular, a very demonstrative experiment was performed by Piasick and Gangloff [60] on a 2090 Al-Li alloy tested in a well-controlled environment (Figure 2.12). An important demonstration is that when a crack propagates in an ultra-purified gas such as oxygen or helium with traces of water vapor lower than one part per billion (ppb), its behavior is similar to that in ultra high vacuum. In moist air, a substantial acceleration of the crack propagation rate is demonstrated. These experiments clearly support that oxygen is not influencing the crack propagation at room temperature in aluminum alloy and water vapor is the detrimental active specie for Al alloy. In Figure 2.8, the increased fatigue crack growth rate in the plateau regime between dry air and humid air was argued to be determined mainly by water vapor and not by oxygen, as the oxygen content was not changed in the dry-air environment. Similar conclusions were draw by other researchers [40, 61, 62] and they showed that both crack initiation and crack propagation were affected by humid air.

There are three major mechanisms responsible for the crack growth rate enhancement in the presence of water vapor in the environment [40]: crack tip blunting, adsorption assisted cracking and hydrogen assisted cracking.

(1) Crack tip blunting

McEvily and Gozalez Vasquez [63] proposed that the higher growth rates in air

were associated with a lower degree of blunting as compared to that observed in vacuum. This can be explained in terms of concepts advanced by Pelloux [64] described in Figure 2.13, in which enhanced slip reversibility in high vacuum is related to the absence of absorbed gas molecules on the fresh fracture surface. In gaseous atmospheres, absorbed molecules or surface oxidation would restrict slip reversibility and favor the activation of new slip planes and thus localize the plastic strain. Furthermore, it has been shown [65] that as less energy is dissipated in plastic deformation in air, more energy becomes available for the growth process.

(2) Adsorption assisted cracking

Fatigue crack propagation might be influenced by adsorption of water vapor molecules onto fresh fatigue surfaces. Adsorption may induce enhanced plasticity of the cyclically strained material at the crack tip and result in a lower value of the critical displacement at the crack tip leading to rupture and enhanced crack growth rates [66]. Consistently, according to Lynch [67], adsorption or chemisorption of a few atomic layers would be sufficient to alter the cracking resistance of the material. This mechanism is generally predominant in the mid-rate range (10^{-8} to 10^{-6} m/cycle) [66].

(3) Hydrogen assisted cracking

Wei *et al.* [38, 68] proposed that the increase in the crack growth rate in presence of water can be attributed to hydrogen-assisted cracking. Hydrogen atoms are formed by the reaction of water with aluminum [69]. Subsequently, newly absorbed hydrogen atoms dissolve into the plastic zone in front of the crack tip by dislocation motion or diffusion and leads to increased crack growth rate. The release of hydrogen at the surface of fatigued Al specimens in moist air was observed by Bennett [62]. Ricker and Fuquette [70] showed that hydrogen dissolved in the plastic zone, and not surface-absorbed hydrogen, is responsible for the hydrogen-assisted cracking.

As for the mechanisms of hydrogen induced increase of crack growth rate in aluminum alloys, there are three major candidates advanced [39]: hydrogen-enhanced

decohesion (HEDE), adsorption induced dislocation emission (AIDE) and hydrogen enhanced localized plasticity (HELP), as described in the following:

1) Hydrogen enhanced decohesion (HEDE)

In this model [71], hydrogen atoms accumulate within the crack tip plastic zone and reduces the cohesive bonding strength between metal atoms. The HEDE provides the basic notion that hydrogen damage occurs in the plastic zone when the local crack tip opening tensile stress exceeds the maximum local atomic cohesion strength, which is lowered by the presence of hydrogen. In the HEDE scenario, hydrogen-damage sites are located at a distance ahead of the crack-tip, where tensile stresses are maximized.

2) Adsorption-induced dislocation emission (AIDE)

Lynch [67] argued that hydrogen-induced weakening of metal-atom bond strength results in enhanced emission of dislocations from crack-tip surfaces where hydrogen atoms is adsorbed. AIDE attributes hydrogen-induced increase of crack growth rate to this focused emission of dislocations, exactly from the crack front and along intersecting planes that geometrically favor sharp crack opening.

3) Hydrogen-enhanced localized plasticity (HELP)

Birnbaum and co-workers [72] proposed that dissolved hydrogen atoms enhance the mobility of dislocations, resulting in extreme localization of plastic deformation. The HELP mechanism differs from AIDE in that dislocation mobility is enhanced due to hydrogen accumulation about dislocation cores, resulting in reduced elastic energies of interaction between moving dislocations and a variety of obstacles. Since hydrogen reduces interaction energy, the stress required for dislocation motion is decreased and plasticity is enhanced.

Wei and co-workers [38, 68] investigated the influence of water vapor on surface reaction kinetics and crack growth rates at conventional cycling frequencies. The dependence of fatigue crack growth response on gas pressure (P), temperature (T) and fatigue loading frequency (f) was quantified in terms of gas phase transport, surface

reaction and hydrogen diffusion into the material ahead of the crack tip. Each of these processes operated in sequence, and the crack growth response is controlled by the slowest process in the sequence. For highly reactive gas-metal systems, such as water vapor and aluminum, crack growth is controlled by the rate of transport of the water vapor to the crack tip which is linearly proportional to p, and inversely proportional to f and $T^{1/2}$. As such, the fatigue crack growth response is given by the superposition model for fatigue crack growth at a certain stress intensity level:

$$(\frac{da}{dN})_{tot} = (\frac{da}{dN})_{mech} + [(\frac{da}{dN})_{sat} - (\frac{da}{dN})_{mech}][\frac{P/(fT^{1/2})}{(P/(fT^{1/2}))_s}], \quad \text{for } (\frac{P}{fT^{1/2}}) < (\frac{P}{fT^{1/2}})_s \qquad (2.9)$$

$$(\frac{da}{dN})_{tot} = (\frac{da}{dN})_{sat}, \qquad \text{for } (\frac{P}{fT^{1/2}}) \geq (\frac{P}{fT^{1/2}})_s \qquad (2.10)$$

where $(da/dN)_{mech}$ is the pure-mechanical fatigue crack growth rate, $(da/dN)_{sat}$ is the fatigue crack growth rate when saturation of environmental effect occurs and it denotes the maximum possible fatigue crack growth rate in environment, $[(\frac{da}{dN})_{sat} - (\frac{da}{dN})_{mech}][\frac{P/(fT^{1/2})}{(P/(fT^{1/2}))_s}]$ is the environemtnal contribution to the fatigue crack growth rate, $(da/dN)_{env}$. $(da/dN)_{tot}$ is the observed fatigue crack growth rate in the environment, which is assumed to be the sum of $(da/dN)_{mech}$ and $(da/dN)_{env}$.

Transport controlled crack growth behavior of a 7075-T651 aluminum alloy exposed to water vapor is presented in Figure 2.14 [68]. It is shown that fatigue crack growth response can be divided into two regions. In the low water vapor pressure, fatigue crack growth rates increased with water vapor pressure up to 4.7 Pa, and then became essentially independent of pressure up to about 67 Pa. In this region, crack growth rate is controlled by the rate of transport of water vapor to the crack tip by molecular flow and can be quantitatively described by the model for transport-controlled crack growth. A water vapor pressure of about 5 Pa, at a cycling frequency of 5 Hz, was sufficient to

obtain full environmental effect. Above 67 Pa, additional increases in growth rate occurred with further increases in pressure. This region is surface reaction controlled, which was attributed to the reactions of water with segregated magnesium in this alloy. In addition, it was observed that the fatigue crack growth response at 80^{o}C is similar to that at room temperature [68]. The crack growth rates increased with increasing water vapor pressure at low pressure then became independent of pressure after a saturation pressure of about 5.3 Pa had been reached. Unlike the response at room temperature, a second transition in crack growth with increasing water vapor pressure was not observed.

Similar dependence of crack growth rate on water exposure, defined as *P/f*, was observed for two planar slip prone Al-Cu-Mg/Li alloys [73], as shown in Figure 2.15. When stressed at a constant ΔK, four regimes of crack growth behavior were defined: below a threshold value of water exposure (0.01 to 0.06 Pa-s), crack growth rate is low and constant indicating absence of environmental effect; from 0.06 to 0.2 Pa-s, crack growth rate increases directly proportional to *P/f*; from 0.2 to 500 Pa-s, crack growth rate increases, but with a lower slope, above 500 Pa-s, crack growth rate is independent of water exposure, indicating a saturation of environmental effect. The authors attributed the decreased water exposure dependence at high *P/f* to crack growth limitation by hydrogen diffusion in the plastic zone and/or chemical reaction saturation.

2.4.2.3 Fractography of aluminum alloys in environments

In general, fatigue fracture surfaces of aluminum alloy specimens tested in vacuum or in inert environmental have a typical dull gray appearance compared to that obtained in humid air, which is more reflecting with morphologies more characteristic of crystallographic fracture surface.

Papakyriacou *et al*. [58] examined the fracture surfaces and the crack path of AlZnMgCu1.5-T6 wrought aluminum alloy after near threshold cycling (K_{max} = 3.5 MPa-$m^{1/2}$) in different environments (Figure 2.16). In vacuum, the fracture surface is rough

and facets approximately oriented in the direction of maximum shear stresses are visible. Rough and coarse fatigue fracture surfaces in vacuum were also reported for 7075-T6 [68] and 2024-T3 [57] aluminum alloys. In ambient air, the fracture surface is relatively smooth and the crack path is straight and approximately perpendicular to the orientation of maximum tensile stress. Crack growth in ambient air leads to a relatively straight crack path, whereas the crack path is tortuous in vacuum. The fracture surfaces obtained in distilled water are comparable to ambient air with exception of a greater tendency of secondary cracking.

Micro-Etch-Pit analysis [68] showed that the crack growth path of 7075-T651aluminum alloy specimens tested in water vapor is crystallographic, while the crack growth path in vacuum was not crystallographic in nature.

Detailed investigation on water exposure dependence of fatigue crack surface morphology and facet crystallographic orientation for two planar slip prone Al-Cu-Mg/Li alloys was conducted using an SEM-based EBSD/stereological method [73]. For these two examined alloys, crack surface morphology was found to depend on water exposure , *P/f*. Moderate to high levels of exposure eliminate {111} facets, characteristic of slip band cracking in high vacuum. This suggests that hydrogen assisted cracking does not promote slip-based damage process. A fraction of high index facets was observed at very low water exposure. A large fraction of low index fatigue facets; {100} for Al-Cu-Mg and {100}/{110} for Al-Cu-Li was observed as water exposure increased, which suggests damage mechanisms of hydrogen-enhanced decohesion.

In contrast to wrought aluminum alloys, the influence of environment on fracture surface appearance in cast aluminum alloy is less pronounced [58]. For cast aluminum alloys, fracture surfaces in ambient air and in vacuum are similar and show transcrystalline crack growth behavior. However, no further study was reported to explain this phenomenon.

2.5 Effect of temperature on fatigue of aluminum alloys

Although a number of studies have been performed on the fatigue properties of some aluminum alloys at room temperature, the description of the fatigue behavior of aluminum alloys at high temperature is not well established.

Based on a few available published studies, it is generally accepted that the fatigue resistance decreases at elevated temperatures. Engler-Pinto Jr. *et al*. [1] found a modest decrease in fatigue life between 20 and 150^{o}C for E319-T7 cast aluminum alloy using servo-hydraulic testing equipment at a cycling frequency of 40 Hz. The temperature effect was more pronounced for other cast aluminum alloys, such as W319-T7, A356-T6 and AS7GU-T64. Mayer *et al*. [74] found that for a high-pressure die-casting aluminum alloy AlSi9Cu3, increasing the test temperature to 150^{o}C shifts the S-N curves towards lower cyclic stresses and shifts fatigue crack growth curves towards lower cyclic stress intensities (Figure 2.17). Existence of a fatigue limit was observed at 150^{o}C and the fatigue limit and threshold stress intensity were about 80% of the respective values determined in ambient air using ultrasonic fatigue testing method. At elevated temperatures, fatigue cracks initiate exclusively at casting porosity and fracture surfaces appear similar at low and elevated temperatures. Shyam *et al*. [26] compared small fatigue crack growth rate in cast aluminum alloy W319 at 20, 150 and 250^{o}C and reported that the effect of temperature on small crack growth rate between 20 and 150^{o}C was negligible, but the crack growth rates increased by an order of magnitude at 250^{o}C at the same stress intensity range (Figure 2.18). The crack propagation rates at the three temperatures were shown to correlate well with the size of the plastic zone at the crack-tip.

The mechanisms of the effect on temperature on the fatigue properties can be summarized into three categories: temperature dependence of deformation, thermally induced changes in the microstructure and temperature dependence of the environmental effect on fatigue properties.

Temperature can influence fatigue properties of aluminum alloys through its influence on yield strength and modulus. Shyam *et al.* [32] showed that when temperature dependant changes of yield strength and Young's modulus were taken into account in the small crack growth model, crack growth rates at 20, 150 and 250°C of A356 cast aluminum alloys fell in the same data band. This indicates that the difference of crack growth rates between room temperature and high temperature primarily results from the difference in yield strength and Young's modulus. Baxter *et al.* [75] described the effect of temperature on fatigue behavior from another viewpoint. They proposed that the high temperature fatigue behavior is a stress-assisted thermally activated process based on the fact that increase of temperature leads to greater cyclic plasticity at the crack tip because lower stresses are required to move dislocations. Greater accumulated fatigue damage occurs and thus cyclic strength is decreased. In their model, the fatigue damage ($\dot{D}$) for a constant cyclic stress obeys the Arrhenius equation:

$$\dot{D} = N_f^{-1} = N_0^{-1} \exp(\frac{-Q}{RT}) \tag{2.11}$$

$$Q = Q_0 - \beta\sigma \tag{2.12}$$

where N_f is the number of cycles to failure, T is the absolute temperature, R is the gas constant, Q is the activation energy which decreases with increasing cyclic stress (σ), N_0 is the fatigue life when $Q<<RT$, Q_0 is the activation energy in the absence of an applied stress and β is the activation volume. When the testing temperature is high enough, creep/fatigue interaction could take place and this will also influence the fatigue properties. However, in the temperature range of 20°C to 250°C, effect of creep on fatigue behavior of aluminum alloys was not reported.

At elevated temperatures, water vapor in the atmospheric air can influence the crack growth behavior of aluminum alloys, similar to the scenario at room temperature [40, 68]. Water molecules migrate to the crack tip from the surrounding environment and react with aluminum on the freshly formed fatigue crack surface. Hydrogen atoms form

from the dissociation reaction and diffuse from the crack surface to the crack tip plastic zone, causing hydrogen-assisted cracking and accelerated fatigue crack growth. The crack growth response is governed by the rate of transport of water vapor to the crack tip, which is influenced by temperature. Therefore, the environmental effect on crack growth rate is influenced by temperature. Wei [38] proposed that the rate of transport of water vapor to the crack tip is inversely proportional to $T^{1/2}$. As such, the environmental contribution to crack growth rate decreases as temperature increases.

In addition, decreased fatigue resistance at elevated temperature was also related to increased cyclic softening [76, 77], which was attributed to the degradation or dissolution of matrix strengthening precipitates and the subsequent deterioration of strengthening contribution to the matrix. It was observed [77] that an under-aged aluminum alloy AA6110 showed cyclic hardening in fatigue tests at room and elevated temperatures up to 200^{o}C. The cyclic deformation behavior changed to cyclic softening at a test temperature of 250^{o}C due to structural alterations of the precipitates. Correspondingly, an increase in testing temperature shifts the S-N curves to lower fatigue lifetimes and the shift is most significant from 200 to 250^{o}C.

2.6 Effect of microstructure on fatigue of aluminum

2.6.1 Microstructure of 319-type cast aluminum

The microstructure of the 319 aluminum is typically composed of α-aluminum dendrites, eutectic silicon, intermetallics and pores. Figure 2.19 illustrates the typical microstructure observed in the cast 319 aluminum alloys [6].

The aluminum dendrites contain precipitate microstructure, which depends on heat treatment process. For T7 over-aged heat treatment, the precipitate microstructure is dominated by disk shaped θ′ (Al_2Cu) precipitates [78], as shown in Figure 2.20. The Al-Cu phase diagram [79] is shown in Figure 2.21 (a).

The eutectic silicon is not uniformly distributed, but tends to be concentrated at

the interdendritic boundaries. The Al-Si phase diagram [79] is shown in Figure 2.21 (b). Silicon particles can be present in the form of acicular needles, blocky plates, or a refined fibrous structure depending upon the level of chemical modification and the solidification rate. Eutectic silicon modification is typically accomplished by adding small amounts of Na or Sr to the melt. In unmodified 319 aluminum, the eutectic Si has a coarse, plate-like structure. Chemical modification of the eutectic silicon creates a three dimensional network.

Intermetallic phases typically form at grain boundaries and interdendritic regions. Most intermetallics are very brittle and tend to form platelets with sharp edges. The two major intermetallic phases in the 319 cast aluminum alloys are the Cu-based and Fe-based intermetallics. The Cu-based intermetallics are primarily Al_2Cu, which form as blocky plates or as an interdendritic eutectic network. This phase is especially present in 319-type aluminum alloys, which has a large amount of copper that is often not fully dissolved into the aluminum matrix. Iron-based intermetallics tend to form Al_5FeSi (β-phase) acicular platelets. Usually, manganese (Mn) is added to the melt to promote the formation of $Al_{15}(Fe, Mn)_3Si_2$, a less severe eutectic phase.

Aluminum oxide particles can arise in cast aluminum alloys when the surface of the molten metal is disturbed and the natural oxide “skin” is fragmented and mixed into the molten metal [80].

Porosity can result from three sources. The first source is from poor casting design that prevents the casting from properly filling and this porosity usually renders the casting unusable. The next source of porosity is gas that is entrapped or dissolved in the liquid metal during casting. This is often called “gas porosity” or “microporosity”. Generally, this gas is hydrogen (H_2), whose source is moisture which releases hydrogen when it contacts the surface of the molten aluminum [80]. When solidification begins, the decreasing solubility causes the H_2 to form bubbles in the interdendritic regions. The third source of porosity is due to the natural volume contraction that occurs when a liquid

solidifies. This is referred to as “microshrinkage porosity”. In general, aluminum can contract up to 8.5% upon solidification [81]. Microshrinkage porosity arises when the last portion to freeze is not well fed on a local scale, such as in thick sections. Thus the region does not have enough liquid metal present to compensate for the volume decrease caused by the contraction and a void arises. In general, “gas porosity” and “mixed (gas and microshrinkage) porosity” tend to be present in many commercial castings. Pure “microshrinkage porosity” appears to occur only when the level of dissolved hydrogen is low.

2.6.2 Effect of porosity

Porosity (mixed or microshrinkage) is the major microstructural feature controlling fatigue properties because it introduces very high stress concentrations within fatigue specimens, serving as primary sites for fatigue crack initiation. Numerous studies have been conducted to investigate the effect of porosity on fatigue properties of cast aluminum alloys. It has been widely concluded that fatigue cracks initiate predominantly from pores located at or close to the specimen surface (Figure 2.22). The number of cycles required to initiate a crack is small relative to the total fatigue life. Therefore, the fatigue life is dominated by the propagation of small cracks and the initiation life is generally considered to be negligible [7, 11, 27, 82, 83]. In hot isostatic pressed (HIP) aluminum, where porosity is greatly reduced, the initiation periods are finite; therefore the total fatigue life will be longer than that of non-HIP aluminum. A comparison of the HIP and non-HIP results in Figure 2.23 [5] shows that the presence of porosity significantly decreases the fatigue resistance. Similarly, a study on A356-T6 [84] found that for specimens with similar secondary dendrite arm spacing (SDAS) but different porosity levels, the fatigue lives tested at 138 MPa differ by approximately a factor of 10.

Porosity is the microstructural feature most detrimental to fatigue life. It overrides any influence from other factors such as oxide films, eutectic particles and slip bands [12].

An example is shown in Figure 2.24. In the absence of porosity, the negative effect of oxide films on fatigue life becomes pronounced. Compared with materials failed from porosity, the fatigue lives of specimens failed from oxide films are 4 to 5 times longer. However, even when the oxide films are crack initiators there is little improvement in fatigue data scatter. For detect-free specimens, fatigue cracks are usually initiated from slip bands and eutectic particles. The fatigue lives of these specimens are 25 times longer than those associated with specimens failed from porosity. In addition, the specimens failed from slip bands shows slightly less scatter in fatigue life.

Murakami *et al.* [10] showed that fatigue resistance mainly depends on pore size and its location, not its shape and volume fraction. Similar results were reported by Wang *et al.* [12]. Murakami *et al.* [10] recommend characterizing the size of pores as the square root of the projected two-dimensional area normal to the loading direction. In general, fatigue life increases with decreasing pore size because large pore sizes decrease the number of cycles that needs to fail the specimens. Decreasing the pore size is certainly beneficial; however, this holds true only up to the point when other fatigue crack initiators (e.g. oxide films, eutectic particles and PSBs) become dominant. The size of the critical pore for fatigue crack initiation is related to the material microstructure and loading conditions. A critical pore size of about 100 μm has been proposed for a 319 alloy [85] and 25 μm for a Sr-modified A356 alloys [12]. In addition, the distribution of initiating pore size does not show a distribution of all pore sizes in the material but a distribution of sizes of the largest pores. In the study of fatigue of cast 319 alloys, Boileau [5] found that the initiating pores were significantly larger than those observed on the metallographic surface. Major *et al.* [86] found that the fatigue life was sensitive to the maximum pore size.

Pore location is also an important factor that determines fatigue life of aluminum castings. For a given size pore, the stress intensity factor can be ~55% higher if the pore is located at the free surface rather than in the center of the specimen [12]. A large pore,

which is located in the center of the casting, may not affect fatigue performance. However, a small isolated pore near a surface may have a significant impact. This is consistent with the work of Murakami *et al.* [10].

The effect of porosity on fatigue crack growth has rarely been reported. In one study on fatigue behavior of A356-T6 aluminum cast alloys [12], it was found that the size and area fraction of porosity and oxide films on the fracture surface, particularly in the overloaded regions, was much higher than the area fraction determined by metallographic measurements. The authors attribute the higher fraction of porosity on the fracture surface to the fact that the fatigue crack always seeks the weakest path and porosity provides an easy path for crack propagation. In addition, the higher stress concentration field around porosity also enhances microcrack initiation and further linkage to a macro-crack in front of the main fatigue crack. Gall *et al*. [82] believed that porosity has an "indirect" influence on fatigue crack growth rates. The porosity generally enhances the nominal stress field experienced by the microstructurally small cracks and this enhancement leads to relatively higher small crack growth rate even in the absence of explicit interaction between the small cracks and pores.

2.6.3 Effect of eutectic Si

Silicon content has an influence on the long fatigue crack growth behavior of Al–Si–Mg alloys [28, 87]. As shown in Figure 2.25(a), the lower the Si content, the better the fatigue crack growth resistance due to higher roughness-induced closure in the low Si content alloys [28]. Si particles encountered along the crack path change the local slip orientation and crack path selection (Figure 2.26). In alloys with low eutectic Si, the crack advances on certain slip systems until an obstacle, such as a grain boundary, causes an orientation change. The low Si alloys, exhibit extended planar slip behavior that increases roughness. However, in higher Si alloys, the role of grain boundaries becomes less important. Instead, more frequent encounters with Si particles result in less variation

in the crack path, lower overall roughness. The relevance of closure is confirmed by the coincidence between closure corrected long crack growth data (Figure 2.25(b)) and physically small crack growth data (Figure 2.25(c)).

Roughness level is also influenced by Si morphology. Unmodified alloys have higher fatigue crack growth threshold (high thresholds being associated with enhanced high-cycle fatigue properties), while modified alloys present higher fracture toughness (high fracture toughness involving better low-cycle fatigue behavior) [28, 87]. At low ΔK, the cracks in unmodified alloys show more path deflection, resulting in higher roughness-induced closure and thus high fatigue resistance. At high ΔK, once debonding and fracture of Si particles largely occur, the coarse morphology provides convenient paths for the crack to slide along or cut through. Sr-modified alloys have small and round eutectic silicon particles that offer more fatigue resistance. Overall, Sr-modified alloys show longer fatigue lives compared to unmodified alloys [88, 89].

The effect of Si on crack growth behavior is different for small cracks. For a correct mechanistic understanding of the small fatigue crack growth behavior of aluminum alloys, a "microstructural characteristic distance (MCD)" [28] needs to be individually defined for each alloy and compared to the size of the actual crack. A growing crack is considered mechanically small if its length is of the order of the plastic zone size ($a \approx r_p$); microstructurally small if its length is of the order of the MCD ($a \approx 5 \times$ MCD to 10 ×MCD); and physically small when its length is significantly larger than the MCD ($a \gg$ MCD) [90, 91]. Small-crack behavior and the transition between different types of small cracks (mechanically to microstructurally to physically small) are strongly dependent on the alloy and its unique MCD. The oscillating (acceleration/retardation) crack growth behavior (Figure 2.25(a)) of microstructurally small cracks represents a result of the "barrier role" played by the controlling microstructural characteristics of the alloys. In wrought alloys, this retardation has been associated with grain boundaries [92, 93], while in cast aluminum alloys it has been associated with secondary microstructural

phases such as eutectic Si particles. When cracks are started at the microstructurally small stage, a ranking of the materials would be expected: the closer the characteristic microstructural obstacles the higher the threshold. This can lead to an opposite threshold behavior of microstructurally small cracks compared to long cracks [28, 87]. The physically small cracks have less microstructural influence and behave similarly to the long cracks except for the absence of closure since the amount of material buildup behind the crack tip is insufficient to create significant crack face interaction effects. The absence of closure explains the faster growth rates and the lower thresholds of physically small cracks.

2.6.4 Effect of intermetallics

When porosity is absent in the material, intermetallics were reported to act as the fatigue crack initiation site [33] (Figure 2.27).

Increasing Fe content decreases fatigue life [94], particularly for alloys with large secondary dendrite arm spacing (SDAS) values. The low fatigue life of high Fe content alloy was attributed to the increased amount and size of Fe-rich phases. Yi [95] found that increasing Fe-content reduces the fatigue life in the long lifetime regime ($>10^6$ cycles), however, Fe-content has no effect for medium fatigue life ($>10^5$ and $<10^6$ cycles) and it slightly increases the fatigue life in the short lifetime regime ($<10^5$ cycles). The existence of large plate-like Fe-rich intermetallic particles in high-Fe castings was found to promote fatigue crack initiation. However, these particles can cause retardation in the small crack growth stage when inclined to the crack growth path.

Increasing Mg content from 0.4% to 0.7% significantly decreases fatigue life of aluminum alloys [94]. The decrease of fatigue life with increasing Mg content can be attributed to the occurrence of microcracking. It is known that increasing the Mg content increases the eutectic particle size particularly in the Sr-modified alloy [96]. The increased eutectic particle size results in more particle fracture and thus shorter fatigue

lives.

2.6.5 Effect of precipitates

Precipitate microstructure in the aluminum dendrites influence fatigue properties by influencing the yield strength and slip mode of fatigue cracks.

The yield strength of aluminum alloys can be interpreted as the sum of an intrinsic strength, a precipitation-hardening strength and a solid-solution strength [97]. The precipitation and solid-solution strengths are determined by formation and growth of precipitates and by dislocation-precipitate interactions. The Al_2Cu precipitation sequence is generally described as: $\alpha_{ss} \rightarrow$ GP zones $\rightarrow \theta'' \rightarrow \theta' \rightarrow \theta$ [78]. The sequence begins with the decomposition of the supersaturated solid solution and clustering of Cu atoms, which leads to formation of subcritical crystal nuclei (Guinier-Preston Zones) and cause distortion of the lattice planes. The yield strength is increased primarily due to the increase in stress required to move a dislocation through the distorted regions. As the aging temperature is increased above 100^oC, the GP zones dissolve and are replaced by the θ'' precipitates, which are three-dimensional disk-shaped plates and are coherent with the matrix. Both the coherency strains and the particles impede dislocation movement through the matrix [98, 99]. The yield strength will continue to increase as the number and size of the precipitates increase up to a limit, giving peak yield strength to the material. However, as the precipitates increase in size and/or number, dimensional changes will occur [100]. For components with critical dimensions, this change must be accommodated. As aging proceeds, the θ'' starts to dissolve, and θ' begins to form by nucleating on dislocations and/or cell walls [98, 99]. θ' precipitates coarsen and become incoherent with the matrix. Both changes tend to decrease the yield strength by altering the mode of dislocation impedance. The yield strength will continue to decrease as the particle size and the interparticle spacing increase. However, in this condition, dimensional changes are minor [100]. Therefore, the over-aged heat treatment does have

the advantage of both thermally and dimensionally stabilizing the microstructure. Continued aging forms the equilibrium θ precipitate (Al_2Cu), which is completely incoherent with the matrix. This, combined with its relative large size and coarse distribution, reduces the strength properties significantly [98, 99]. An example of age-hardening response of the yield strength in a W319 aluminum alloy [78] is shown in Figure 2.28.

Figure 2.29 illustrates the influence of the aging condition on the fatigue crack propagation (after closure correction) for a 7075 alloy [101].The peak-aged aluminum matrix contains shearable GP zones and the precipitates which promote a localization of the plastic deformation within a single-slip system in each individual grain along the crack front, and favor a near-threshold crystallographic crack path. The over-aged aluminum matrix contains larger and less coherent precipitates which favor a wavy slip mechanism. The peak-aged condition leads to a very slow crystallographic propagation in vacuum, while an over-aged condition gives conventional stage II propagation. In ambient air, the single-slip mechanism, which is operative in the peak-aged alloy, is assumed to offer a preferential path for hydrogen assisted cracking, which leads to a strongly accelerated propagation. Conversely, ambient air has little influence on stage II regime in the over-aged alloy

2.6.6 Effect of SDAS

The secondary dendrite arm spacing (SDAS) is an important factor defining the metallurgical structure of aluminum castings. SDAS is governed by the solidification rate and thus provides a direct measurement of the solidification rate in a local area of the casting. Higher solidification rates yield finer SDAS [81]. In general, the mechanical properties in aluminum alloy correlates better with the SDAS than the grain size.

Aluminum alloys with large SDAS are characterized by large α-Al dendritic regions, and large spacing between consecutively sampled Si regions. As a result, the

crack roughness associated with these structures is higher than the roughness of small SDAS materials due to coarsely spaced fatigue crack-Si particle interactions, which results in higher closure, higher threshold, and better fatigue crack resistance in the near-threshold regime of long fatigue cracks.

However, at high ΔK levels, the size of eutectic regions and the Si particle morphology dictate the crack growth resistance. For coarse microstructures the eutectic regions as well as Si particle size are larger too, providing lower resistance to the crack advance. This behavior results is higher growth rates at high ΔK and lower pseudo-fracture toughness for the large SDAS materials. Similar behavior was experimentally observed for A356 [89, 102] and W319 [4] cast aluminum alloys.

2.7 Summary

Ultrasonic fatigue instrumentation, which operates at approximately 20 kHz, offers the possibility to investigate the high cycle fatigue behavior of cast aluminum alloys. The substantial increase of testing frequency might influence the fatigue performance of cast aluminum alloys, which are typically cycled at conventional frequencies (20 to 100 Hz) in applications. For aluminum alloys tested in ambient air, the effect of frequency is more relevant with time dependent environmental effect than strain rate effect. Since crack tip opening under high frequency loading occurs over a shorter time per cycle than for conventional fatigue experiments, an environmentally assisted increase in fatigue crack growth rates is less pronounced, which may lead to lower crack growth rates. For aluminum alloys, fatigue crack growth threshold is decreased and fatigue crack growth rate is increased by the presence of water vapor in the atmospheric air compared to the crack growth behavior in vacuum. Fatigue crack growth rate of aluminum alloys at 20 kHz in ambient air was observed to be lower than that at conventional frequency (20 Hz) and this is believed to be associated with the environmental effect. Based on the mechanisms of hydrogen assisted cracking, the

dependence of fatigue crack growth response on water vapor pressure, temperature and frequency was quantified in terms of water vapor migration, surface reaction and hydrogen diffusion into the material ahead of the crack tip. The fatigue crack growth rate at a given stress intensity factor range is characterized by a superposition model, in which crack growth rate in environment is interpreted as a sum of the pure-mechanical crack growth rate and the environmental contribution to the crack growth rate.

Although numerous studies have been performed on the room temperature fatigue properties of cast aluminum alloys, the understanding of frequency and environmental effects on cast aluminum alloys is not well established. The majority of the studies on frequency and environmental effect on crack propagation behavior focus on wrought aluminum alloys and the crack growth tests were conducted at relatively high stress intensity levels. There is no detailed information in the literature about the environmental effect on crack propagation behavior of cast aluminum alloys. Moreover, the superposition model deals with the crack growth behavior at a given stress intensity factor range for a specific alloy. A more general version that can model dependence of crack growth rate on stress intensity factor range as a function of water vapor pressure and/or frequency is needed to better understand and predict the effect of frequency and environment on fatigue performance of cast aluminum alloys.

Fatigue resistance decreases with increasing temperature for cast aluminum alloys. Based on review of the literature, studies of the fatigue behavior of cast aluminum alloys at elevated temperature using ultrasonic fatigue methods are few. Owing to the influence of temperature on reaction enthalpies, diffusion kinetics and complex interactions with fundamental deformation and damage mechanism, further studies relating to the effect of temperature on fatigue as a function of atmospheric pressure and test frequency are required in order to get a better knowledge of the respective contributions of temperature and environment in fatigue damage processes.

Fatigue performance of cast aluminum alloy is influenced by microstructure and

porosity is the major microstructural feature controlling fatigue properties. For cast aluminum alloys, fatigue cracks readily initiate from large pores due to the higher stress concentration at the pores at high stress amplitude. The initiation life is generally thought to be negligible, and the total fatigue life of the cast material is dominated by the crack propagation phase. In the very long lifetime regime (10^6 -10^{10} cycles), an endurance limit was observed in some cast aluminum alloys. The existence of an endurance limit in the cast aluminum alloys is believed to be caused by non-propagating fatigue cracks, for which the driving force for crack advance is below a threshold value. In some studies, the endurance limit was successfully correlated with the initiating pore size. The initiating pores measured on the fatigue fracture surface are significantly larger than the casting pores observed on the metallographic surface. Thus, a direct and deterministic relationship between the casting porosity population and the endurance limit becomes necessary in predicting fatigue performance of cast aluminum alloys. However, the correlation of casting porosity population with the fatigue endurance limit has not been well developed.

In this study, S-N behavior, crack initiation and propagation behavior are investigated for E319 cast aluminum alloy specimens tested at frequency of 20 kHz and 75Hz (or 30 Hz) and at temperature of 20, 150 and 250^{o}C. Based on analysis of the extensive experimental data acquired, the effect of frequency and the associated effect of environment on fatigue propagation and, therefore, the fatigue life are examined. According to the superposition model, fatigue crack propagation of E319 cast aluminum alloy is characterized as a function of environment. The effect of temperature on fatigue behavior and the effect of frequency and environment on fatigue properties of E319 cast aluminum alloy at elevated temperature are also discussed. By using ultrasonic fatigue, fatigue strengths at 10^8 cycles were estimated and correlated with the initiation pore size and pore location. A probabilistic model was developed to establish the relationship between the casting porosity population and the fatigue strength of the alloy.

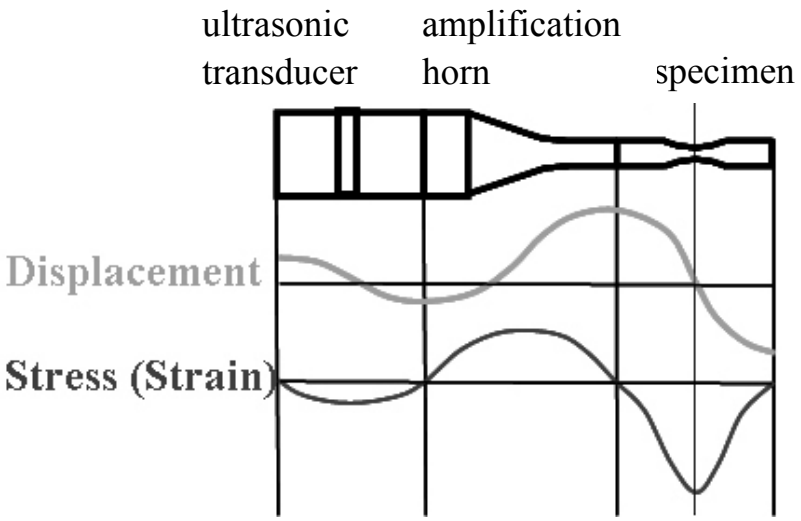

Figure 2.1 Schematic of principle of ultrasonic fatigue technique.

(a)

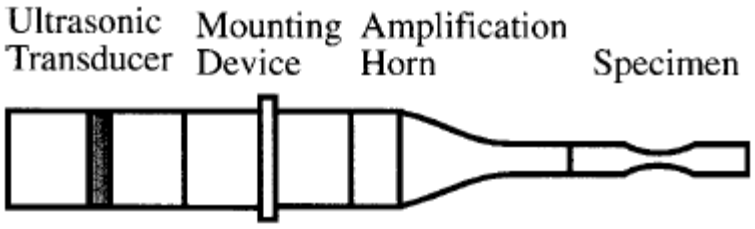

(b)

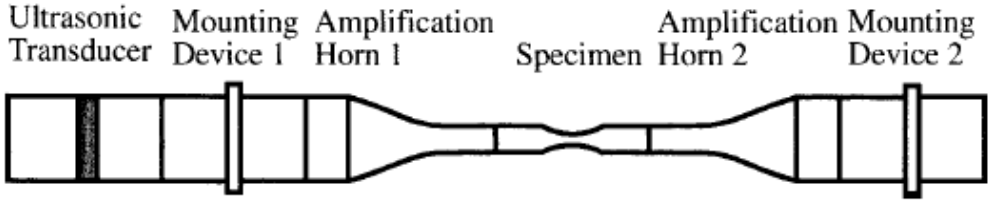

Figure 2.2 Schematic of mechanical equipment used to perform (a) ultrasonic fatigue experiments under fully reversed loading conditions and (b) ultrasonic fatigue experiments with superimposed external loads [2].

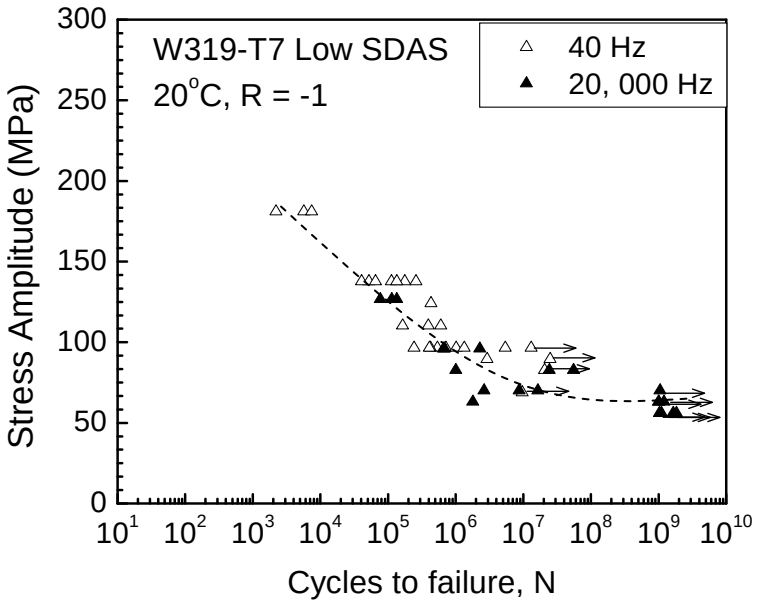

Figure 2.3 Results from fatigue lifetime testing conducted for the low SDAS conditions of W319-T7. The data obtained using the ultrasonic testing method (20 kHz) are compared to data obtained using servohydraulic frames at 40 Hz [14].

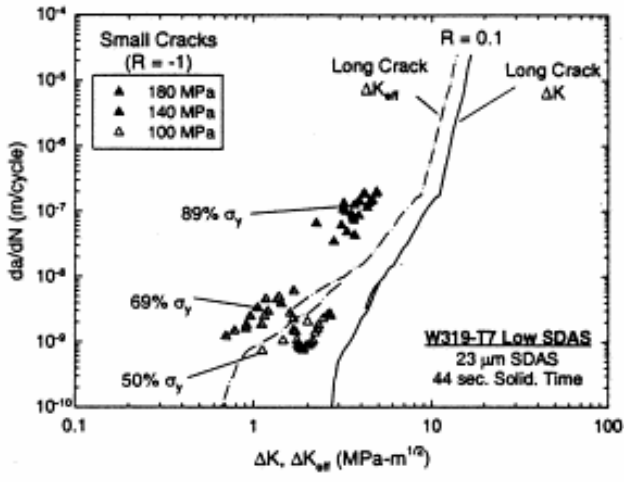

Figure 2.4 Long and small fatigue crack growth rates measured in W319-T7 for the low SDAS conditions [33].

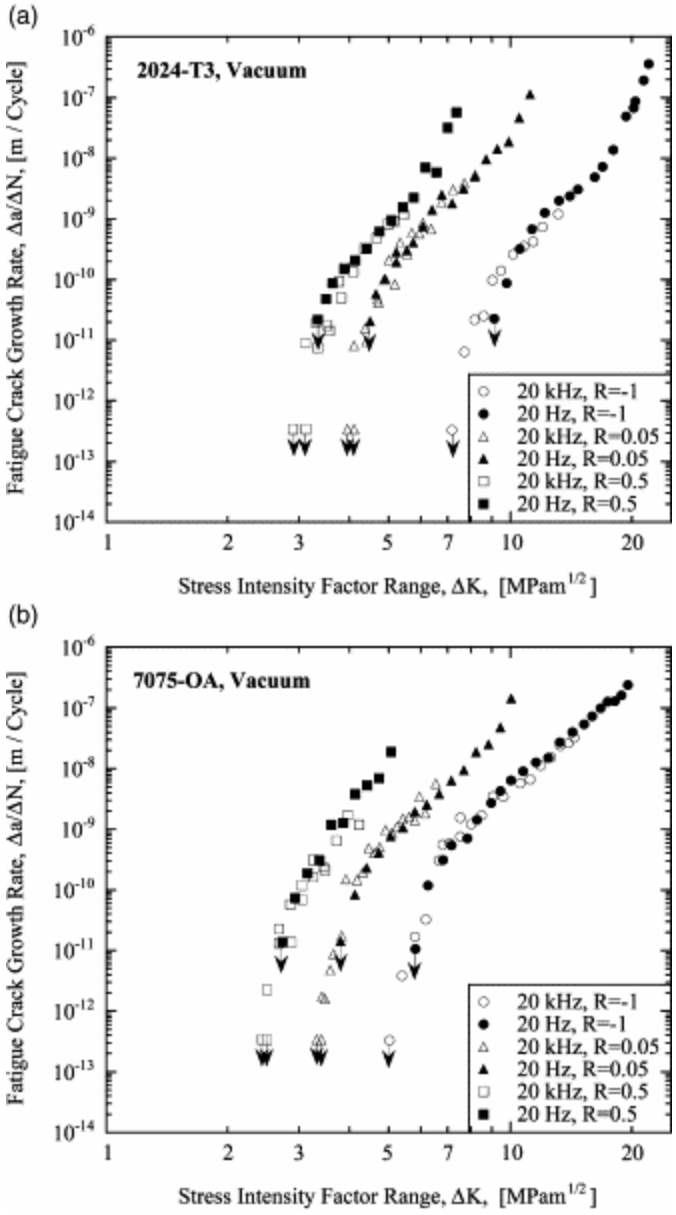

Figure 2.5 Fatigue crack growth in 2024-T3 (a) and 7075-OA (b) at load ratio $R = -1$, $R = 0.05$ and $R = 0.5$ in vacuum [52].

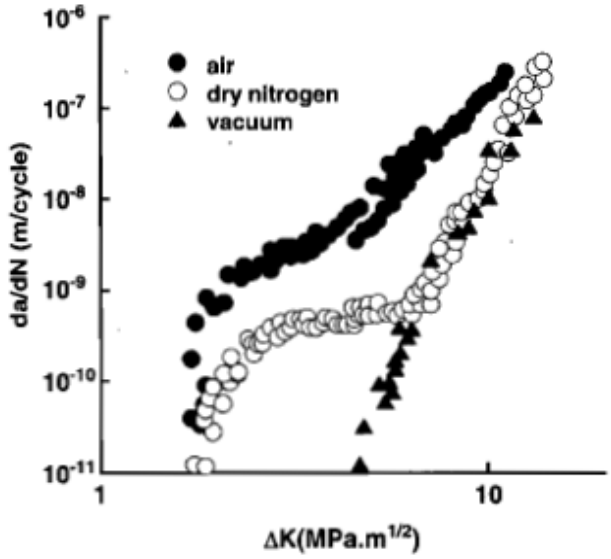

Figure 2.6 Fatigue crack propagation in a single crystal of Al - 4.5 wt. % Zn – 1.25 wt. % Mg in ambient air, high vacuum and dry nitrogen, R = 0.1 Hz and 35 Hz [55].

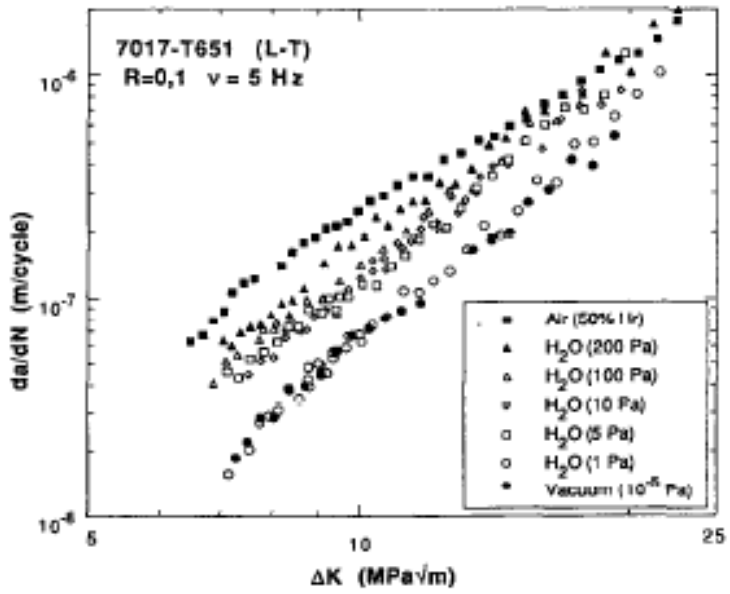

Figure 2.7 Crack growth rates in AA7071-T651 in environments with different water vapor pressures [56].

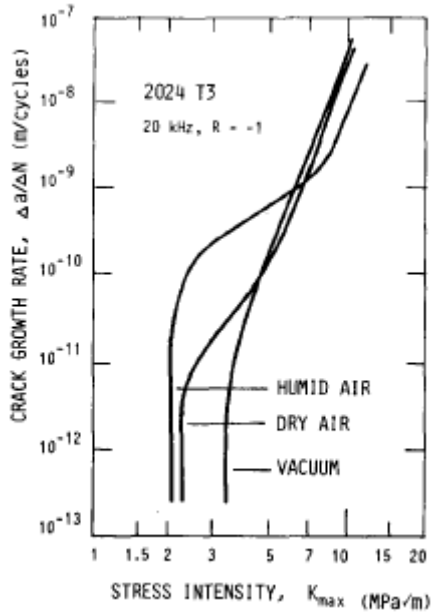

Figure 2.8 Comparison of fatigue crack growth of 2024-T3 in vacuum, dry air and humid air [57].

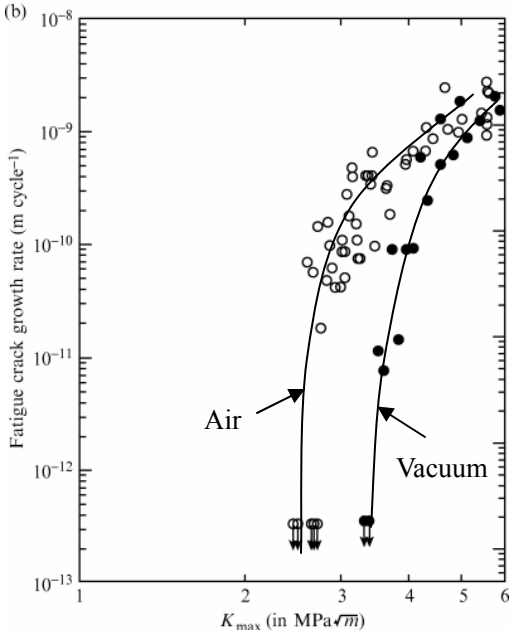

Figure 2.9 Fatigue crack growth rates of cast aluminum alloy AlSi9Cu3 in ambient air (o) and in vacuum (•), f = 20 kHz, R = −1 [58].

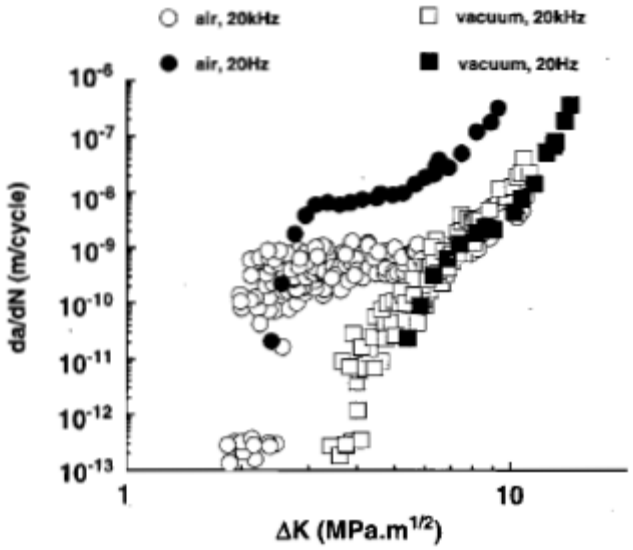

Figure 2.10 Comparison of rates of fatigue crack propagation at conventional frequency of 20 Hz and ultrasonic frequency of 20 kHz in a 7075-T351 alloy in room air and vacuum [59].

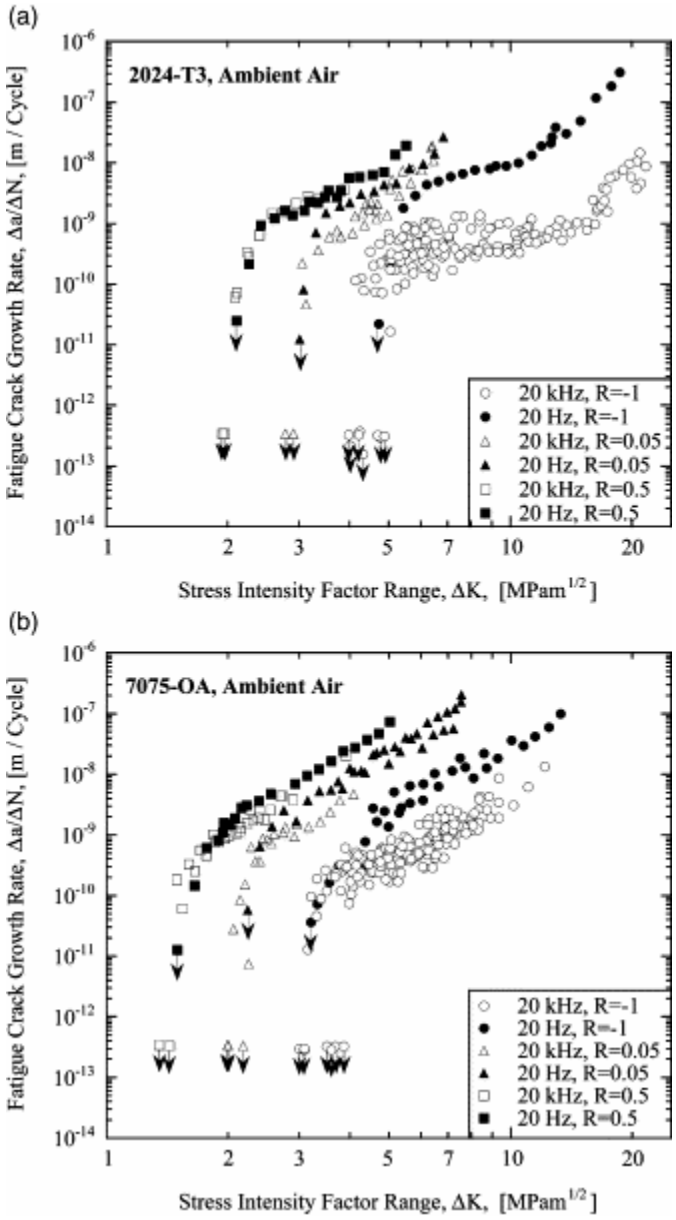

Figure 2.11 Fatigue crack growth in 2024-T3 (a) and 7075-OA (b) at load ratio R=−1, R=0.05 and R=0.5 in ambient air. Closed symbols refer to servo-hydraulic experiments at 20 Hz and open symbols refer to ultrasonic experiments at 20 kHz cycling frequency [52].

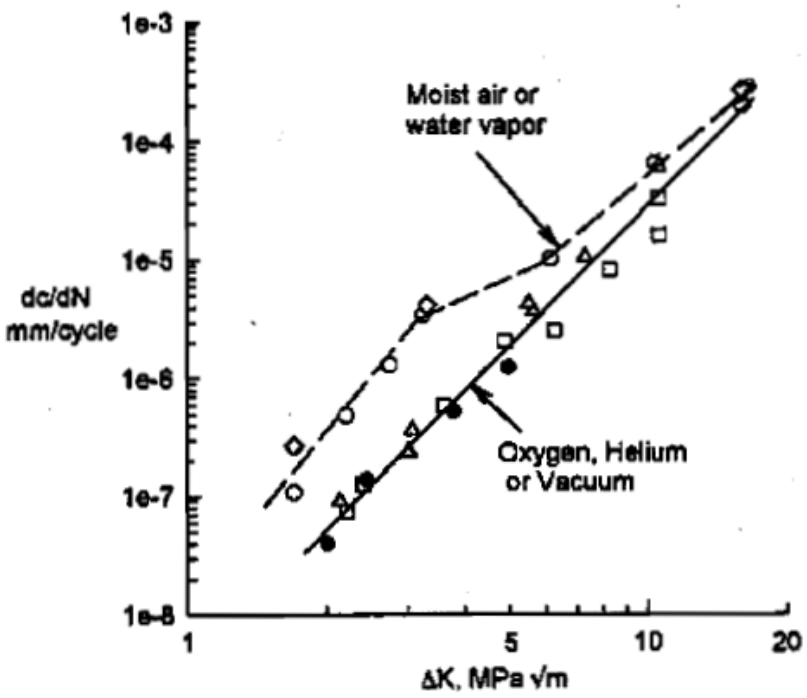

Figure 2.12 Experiments in ultra-purified oxygen and helium in comparison to high vacuum and moist air on a 2090 Al-Li alloy [60].

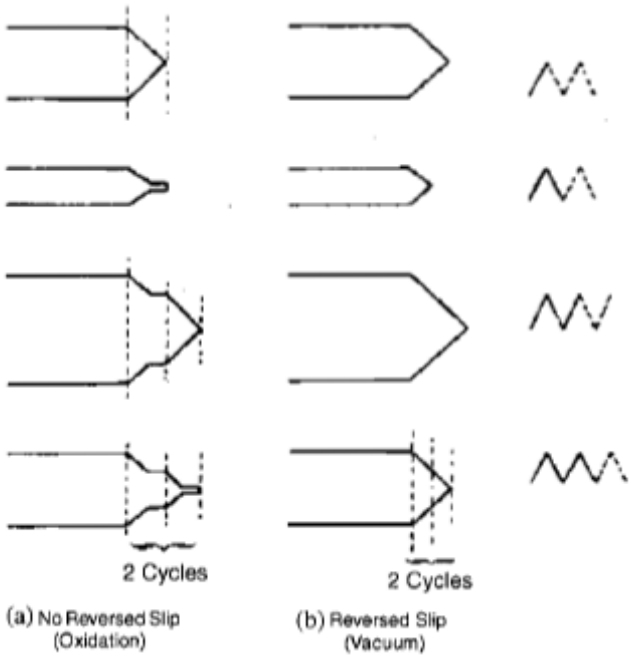

Figure 2.13 Schematic illustration of crack tip extension after two load cycles in air and in vacuum [64].

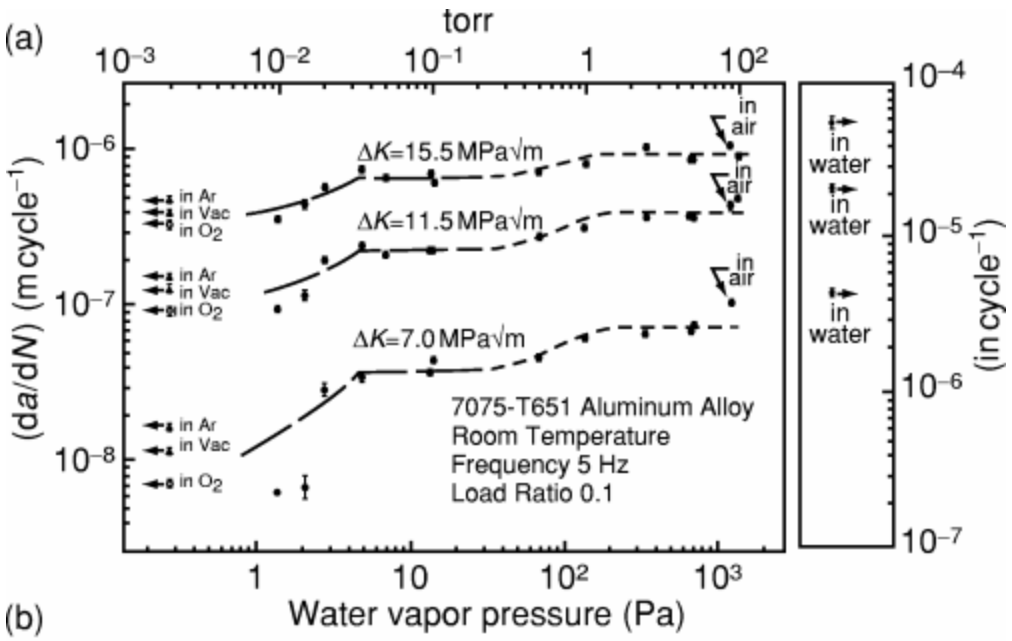

Figure 2.14 Influence of environment on fatigue crack growth at room temperature for a 7075-T6 aluminum alloy in water vapor and other environments, showing transport controlled (left) and surface reaction controlled (right) response [68].

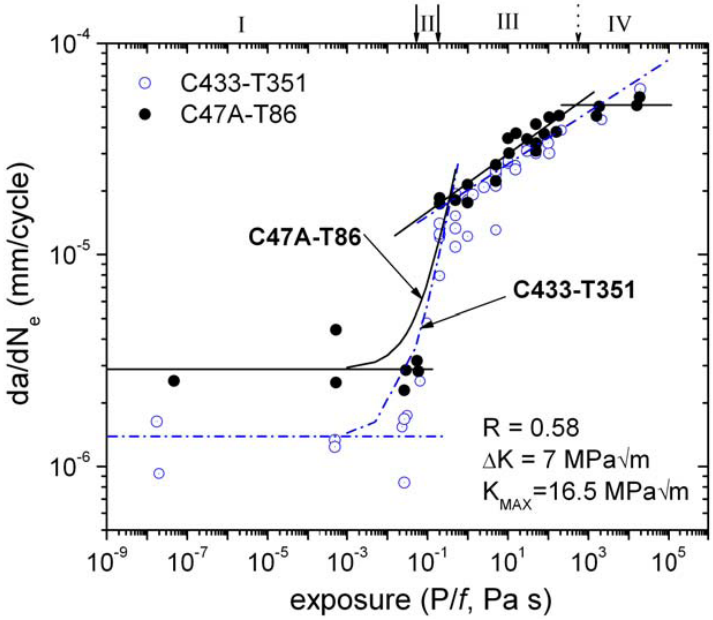

Figure 2.15 The effect of water vapor exposure (*P/f*) on crack growth rate for C433-T351 (o) and C47A-T86 (•) stressed at constant ΔK = 7 MPa-m$^{1/2}$, K_{max}= 16.5 MPa-m$^{1/2}$, and R = 0.58 [73].

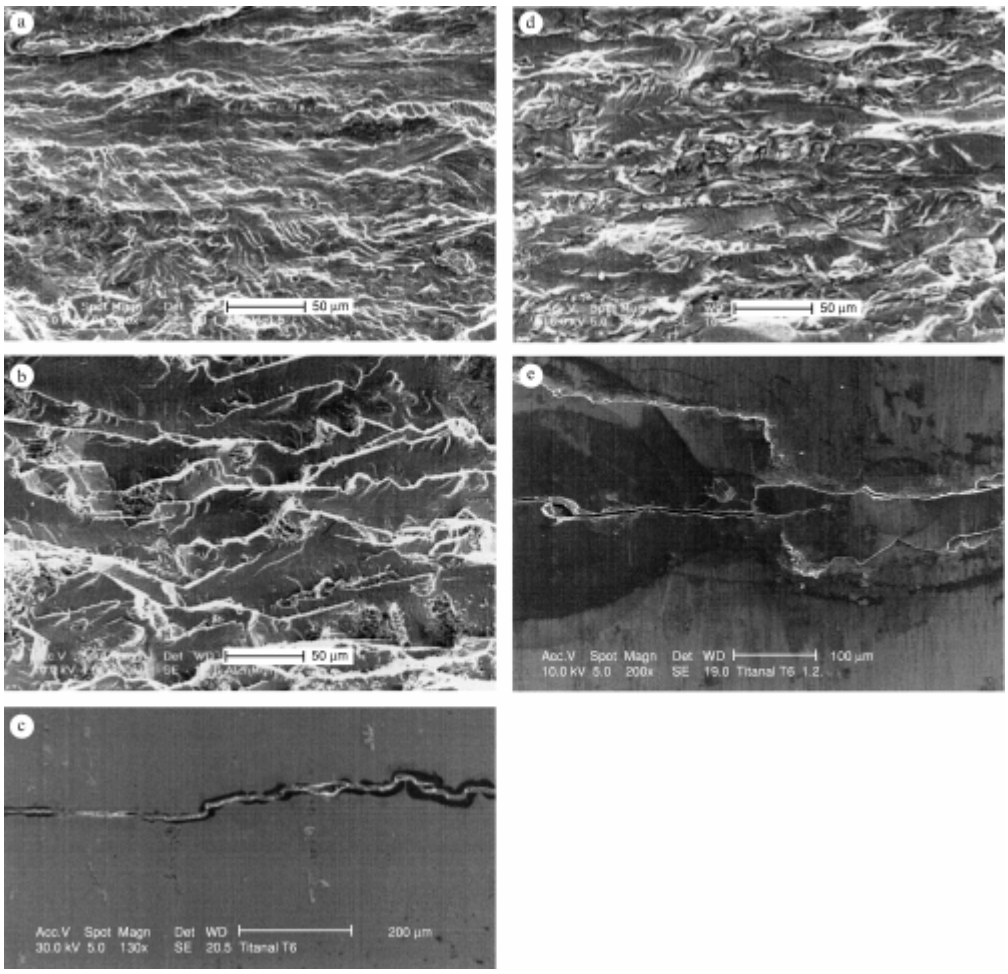

Figure 2.16 Fracture surface of AlZnMgCu1.5-T6 after near threshold ultrasonic cycling in (a) ambient air, (b) vacuum and (d) distilled water. In (c) the crack path at the surface of the specimen is shown after cycling in ambient air (left side of the picture) and in vacuum (right side of the picture), and (e) shows the surface of a specimen after cycling in distilled water [58].

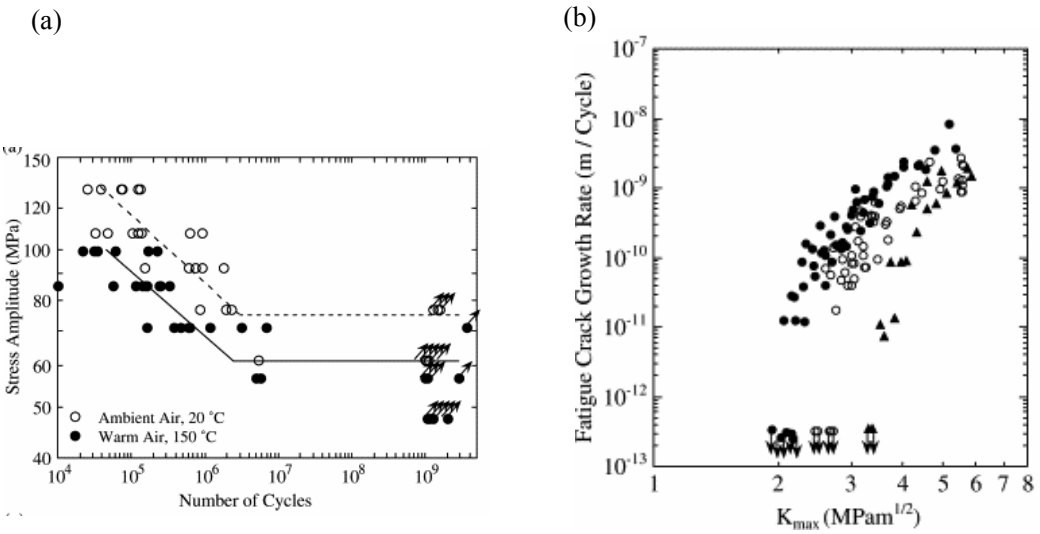

Figure 2.17 (a) S–N data and (b) crack growth of AlSi9Cu3 at ambient and elevated temperatures [74].

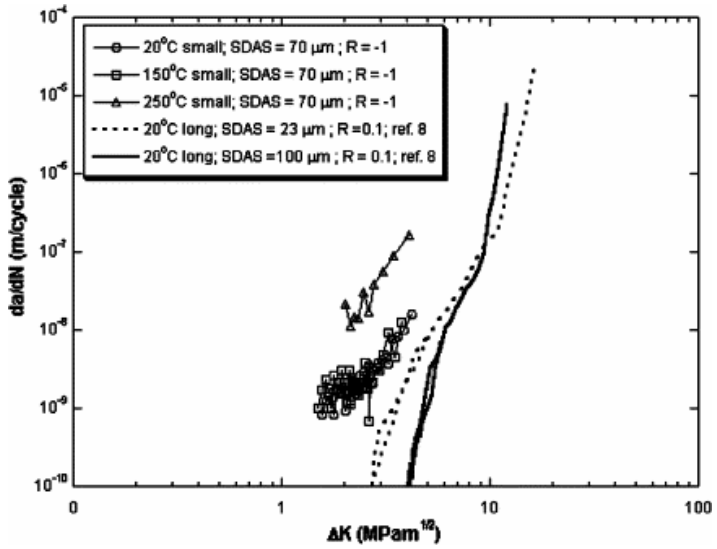

Figure 2.18 Small fatigue crack propagation (FCP) curves for 20, 150 and 250 °C. Also shown for comparison are long fatigue crack propagation curves at 20 °C for two different microstructures of W319 [26].

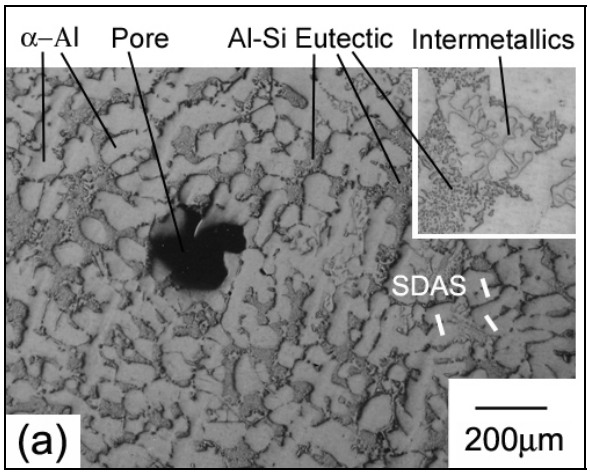

Figure 2.19 Optical microstructure of cast aluminum alloy E319 [6].

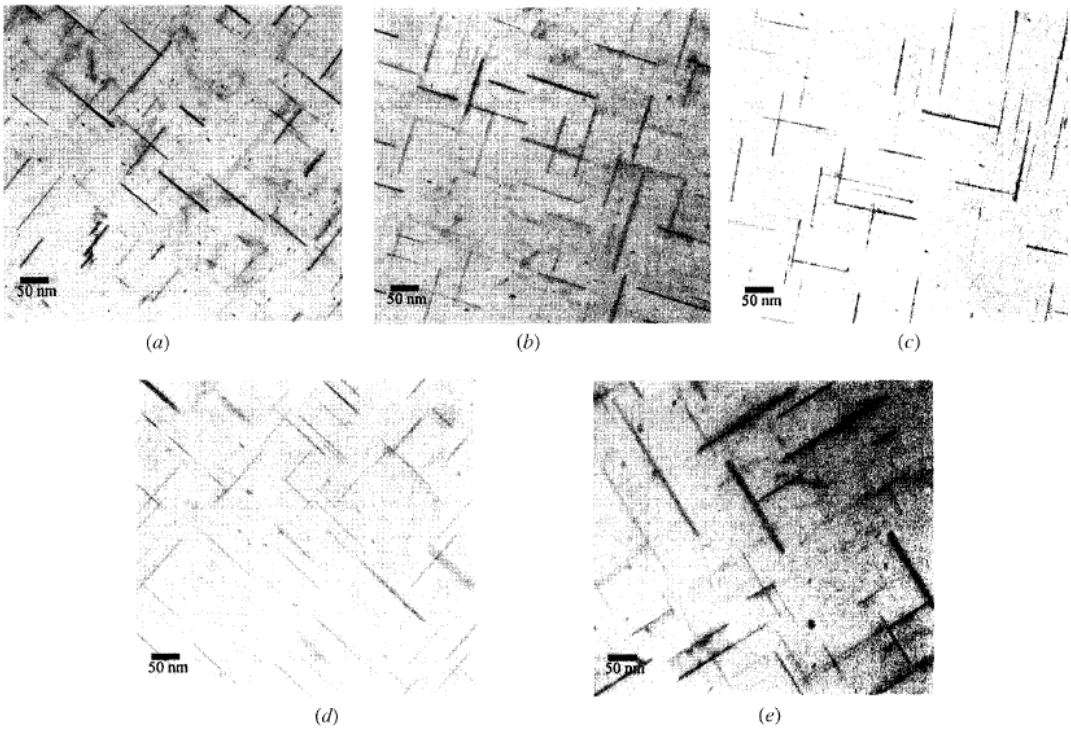

Figure 2.20 TEM micrographs taken of 3.5 pct Cu W319 alloy after aging at 260°C for (a) 10 min, (b) 20 min, (c) 30 min, (d) 1 h, and (e) 3 h [78].

(a)

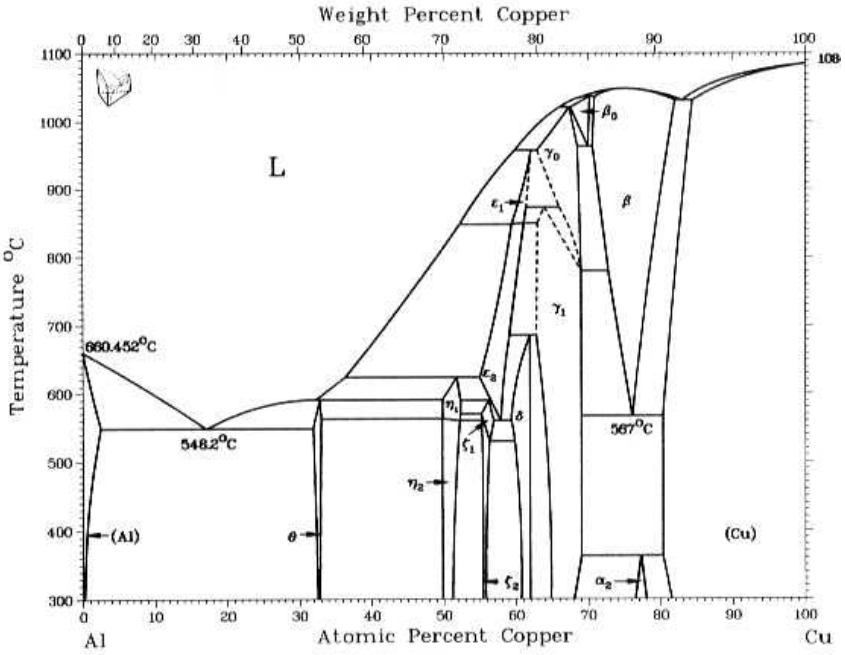

(b)

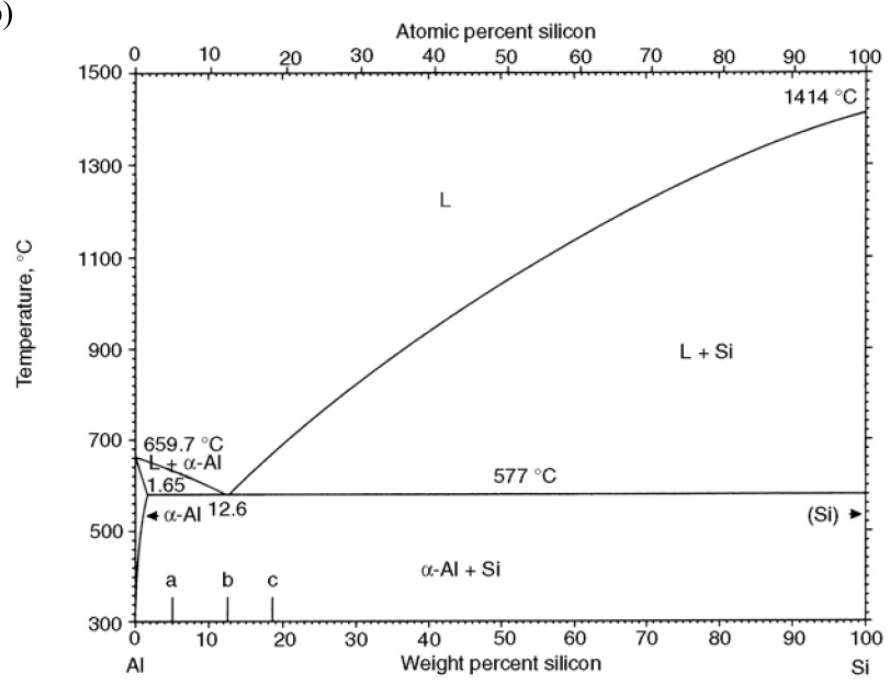

Figure 2.21 (a) Al-Cu phase diagram and (b) Al-Si phase diagram [79].

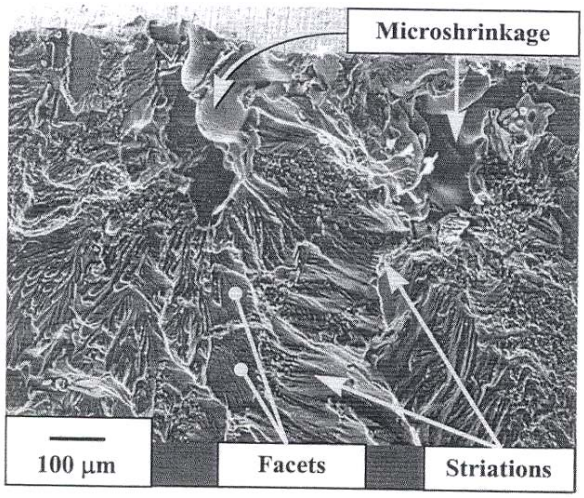

Figure 2.22 Typical fracture surface of the pore-containing W319 fatigue specimens [5].

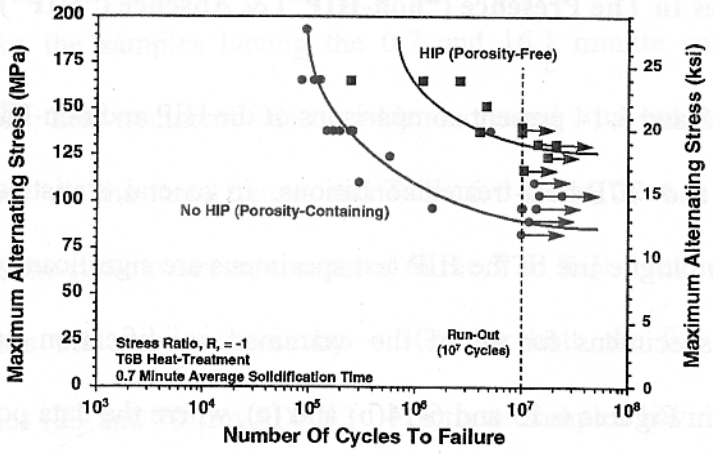

Figure 2.23 A comparison of the fatigue properties of W319-T6B aluminum in the HIP and Non-HIP conditions (23 μm SDAS) [5].

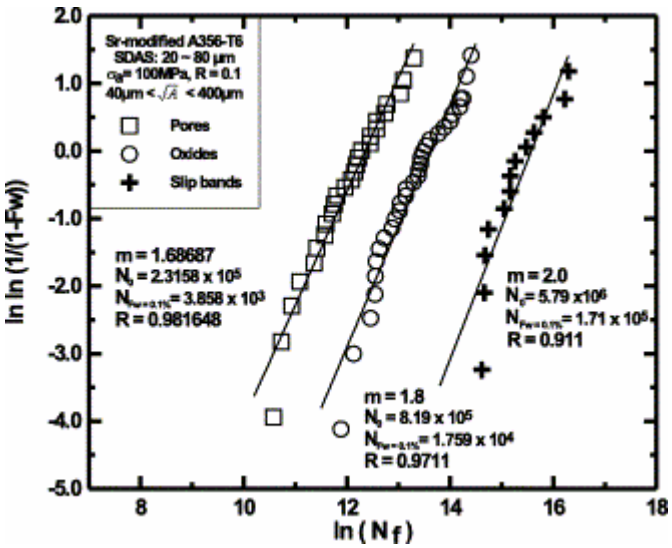

Figure 2.24 Two-parameter Weibull plot for fatigue life data of the Sr-modified A356 casting alloy containing a variety of defects [12].

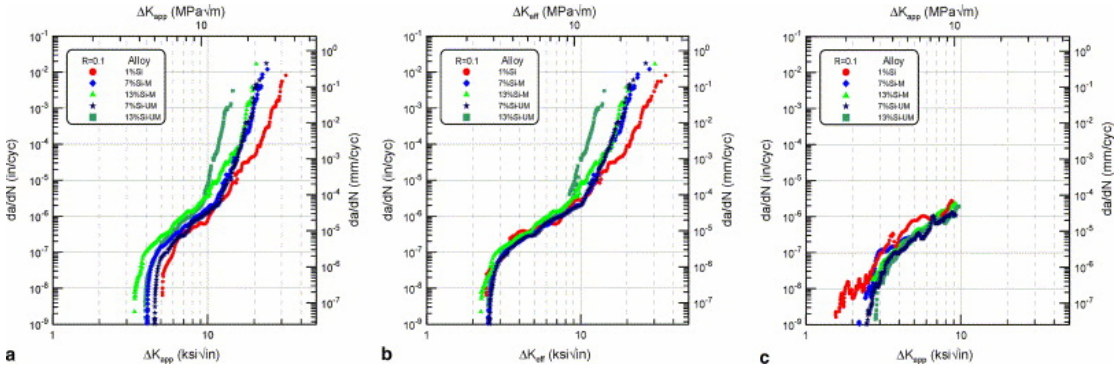

Figure 2.25 Fatigue crack growth data for 1%, 7% and 13% Si cast Al–Si–Mg alloys with no residual stress: (a) long-crack data – before closure correction (ΔK_{app}); (b) long-crack data – after closure correction (ΔK_{eff}) and (c) small-crack data [28].

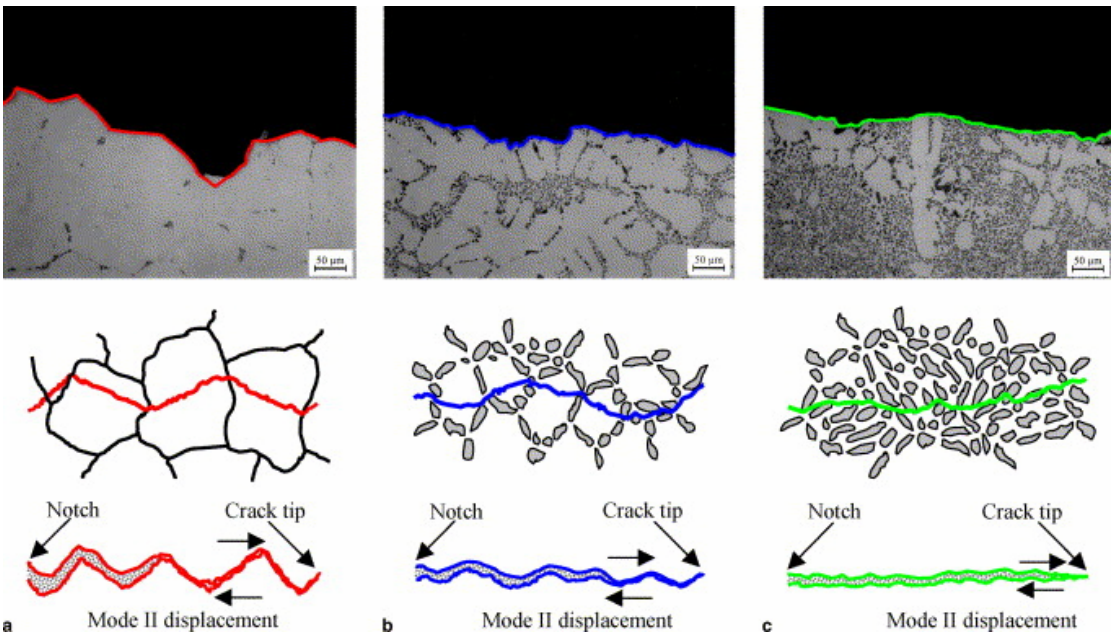

Figure 2.26 Crack path deflection patterns for three Al–Si–Mg alloys: (a) 1% Si; (b) 7% Si; (c) 13% Si (fractographic observations – top and crack path models – bottom); mode II displacement is also contributing to closure [28].

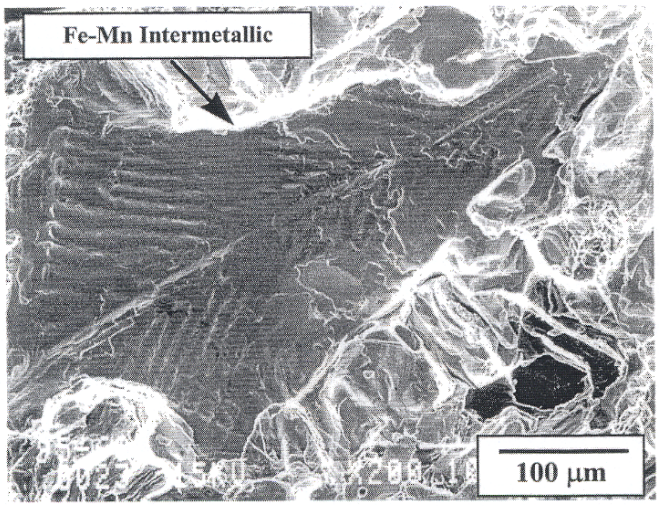

Figure 2.27 Iron based intermetallics that initiated failure in the HIP W319-T7 aluminum [33].

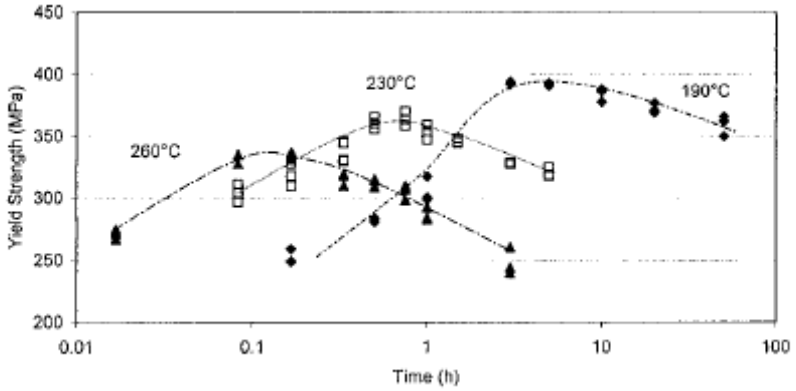

Figure 2.28 The effect of aging time and temperature on the yield strength in a W319 aluminum alloy [78].

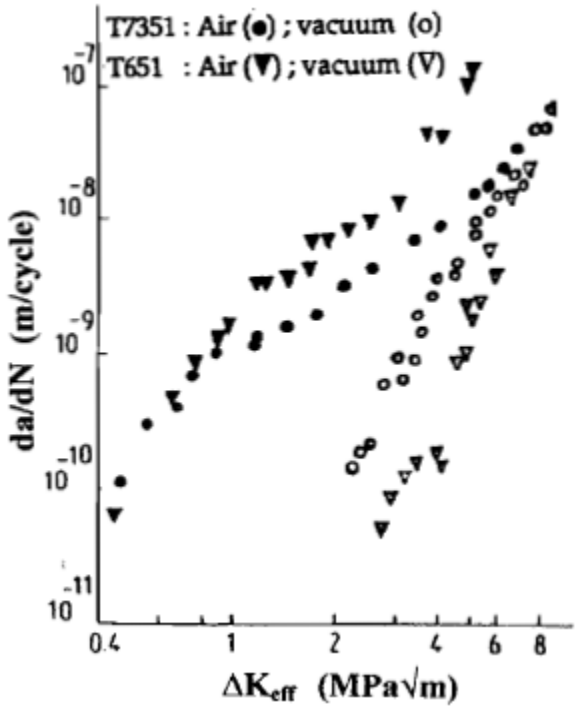

Figure 2.29 Influence of aging-condition on fatigue propagation behavior in 7075 alloys (T7351 and T651) tested in ambient air and high vacuum (R = 0.1, 35 Hz, including correction for crack closure) [101].

Chapter 3

Experimental details

3.1 Material

3.1.1 Composition

The alloy investigated in this study is a 319-type cast aluminum alloy, referred to as E319. It is a commercial alloy used in the production of automotive cylinder heads. Table 3.1 presents the average compositions of this alloy. The composition limits of the standard Aluminum Association 319 alloys (AA319) and W319, which were investigated by Caton *et al.* [103], are also included in the table for comparison. 319-type alloys are composed primarily of aluminum, silicon and copper. The 319 aluminum alloy in this research is higher in Si and Mg content than the AA319 and it possesses higher Fe content than W319. Thus, to avoid confusion, the 319 examined in this study will be referred to as E319 cast aluminum alloy.

Table 3.1 Compositions of E319, W319 and specification ranges for AA 319

Alloy	Si	Cu	Mg	Mn	Fe	Zn	Ti	Ni	Sr	Others	Al
E319	7.61	3.28	0.22	0.33	0.7	0.65	0.11	0.02	0.012	0.06	Balance
AA319	5.5-6.5	3.0-4.0	<0.1	<0.5	<1.0	<1.0	<0.25	<0.35	--	<0.5	Balance
W319*	7.69	3.58	0.3	0.22	0.32	0.22	0.15	-	0.01	--	Balance

*Note: The compositions of W319 are from [103].

3.1.2 Sample casting and microstructural analysis

The 319 alloy was melted in a gas-fired furnace at 750^{o}C. Alloying elements were added to the melts to make the alloy E319 aluminum based on the measured composition of melted 319 alloy and the E319 alloy composition specifications. Degassing was

performed using a mixture of 5% SF_6 in N_2 fed through a rotary degasser. After degassing 0.012% Sr was added to the melt in the form of Al-10% Sr master alloy. The Sr was then allowed to homogenize in the melt for at least 15 minutes prior to casting. TiB_2 was added to the melt before casting for grain refinement. An AlScan hydrogen analyzer was used to monitor the level of H_2 gas in the melts. In all castings, the final H_2 level was less than 0.15 ml/100g.

The molten aluminum alloy was then hand-ladled into rectangular resin-bonded silica sand molds with a copper chill embedded. After each pouring, the sand mold was rolled over so that the copper chill is below the casting plate to ensure good filling of material near the copper chill by gravity. As shown in Figure 3.1, each casting plate had a copper chill positioned along the edge, in order to control the solidification rate. The microstructure was essentially uniform along the isotherms of the casting and that the microstructure became increasingly coarse, in terms of pore size, secondary dendrite arm spacing (SDAS), eutectic silicon and the intermetallic particles, as the distance from the chill increased.

Figure 3.2 shows that SDAS increases with increasing distance from the chill. SDAS is measured as the average center-to-center distance of adjacent secondary dendrite arms. To determine the SDAS, the material was mounted and polished using standard metallographic techniques, no etchants were used. A KONTRON IBAS^{TM} image analyzer was used to measure a minimum of 150 SDAS at 100×. For the present study, all the rectangular bars were sectioned from the region 15 to 35 mm from the chilled edge, in a regime with an average SDAS of 30 μm.

The typical optical microstructure of E319 aluminum is shown in Figure 3.3 (a). The light gray features are primary α-aluminum dendrite arms; the dark gray region is Al-Si eutectic region. Pores as well as Cu-rich and Fe-rich intermetallic phases are also present. Figure 3.3 (b) shows an SEM micrograph at higher magnification revealing more details of the microstructure. Porosity represents a critical microstructure feature in cast

aluminum alloys. In Figure 3.3 (b), the microshrinkage pore has an irregular shape and outlines the surrounding dendrites; the bulbous features protruding into the cavities are dendrite arms of α-aluminum.

To determine the grain size, the polished samples were etched with Keller's reagent, which is composed of 2 ml HF (48%), 3 ml HCl (concentrated), 20 ml nitric acid (concentrated) and 190 ml distilled water. The samples were immersed in the etchant for 5-15 seconds, rinsed in soft running warm water, sprayed with ethanol, dried completely in flowing air and subsequently viewed by optical microscopy under polarized light. Figure 3.4 shows the optical microstructure using polarized light, where different grains show slightly different colors because their grain orientations are different. The grain boundaries are highlighted. A total of 138 grains were measured and the grain size was defined as the equivalent circular diameter. The nominal grain size is estimated to be 572±264 μm, which is much larger than the SDAS.

To quantitatively characterize the porosity population on a 2-dimensional metallographic section, a total area of at least 100 mm^2 was examined to ensure that a sufficient number of pores were counted for meaningful quantitative analysis. Because of the irregular nature of most pores it is impossible to describe their geometric feature accurately on the basis of a few parameters. Studies [10, 20, 104] have indicated that the size of the defects, rather than the shape, plays the key role in forming cracks from the defects. The equivalent circular diameter, D, is used here to characterize the pore size, which is defined as:

$$D = \sqrt{\frac{4}{\pi} A_{pore}} \tag{3.1}$$

where A_{pore} is the area of the two-dimensional projection of the microshrinkage pore.

Figure 3.5 shows the distribution of the pore sizes measured from 2-dimensional metallographic sections. Statistical analysis indicated that log-normal, Gumbel and 3-parameter Weibull distribution functions all give good fits to the pore size distributions

(correlation coefficient >0.98). For simplicity, the log-normal distribution function was used in the present study to describe the pore size distribution in the casting. Correspondingly, the mean value, standard deviation and number density of the porosity population were estimated, and the results are listed Table 3.2.

Table 3.2 2-D Characteristics of the porosity population determined using metallography of E319 cast aluminum alloy.

Mean (μm)	STDEV (μm)	Porosity number density (mm^{-2})	Area fraction
66	−20.8 / +30.4	0.50	0.40%

3.1.3 Heat treatment

The sectioned bars were all subjected to a T7 over-aged heat treatment which consists of an 8 hour solution heat treatment at 495^{o}C followed by boiling water quench at about 90^{o}C and 4 hours of aging at 260^{o}C.

For 319 type aluminum alloys, heat treatment influences the tensile properties primarily by influencing the size and volume fraction of the Al_2Cu precipitates as well as their coherency with the matrix, as detailed in section 2.6.5. The yield strength in the peak-aged condition (T6 heat treatment) is maximized due to the decreased size and spacing of the θ′ precipitates (Al_2Cu platelet) compared to that in over-aged condition (T7 heat treatment). Jahn et al. [105] revealed that the maximum diameter of θ′ precipitates in the T6 and T7 conditions of W319 are approximately 100 nm and 400 nm, respectively. However, thermal growth, defined as dimensional changes due to modifications in the precipitate type and morphology, occurs in the peak-aged condition [100]. This growth can produce unacceptable distortion and premature failure of the component. Therefore, this alloy is heat-treated to a T7 over-aged condition, which provides the necessary dimensional stability, but the tensile strength is reduced compared to a T6 heat treatment.

3.1.4 Mechanical properties

The tensile properties of E319 cast aluminum alloy at ambient and elevated temperatures are summarized in Table 3.3, where YS represents the 0.2% tensile yield strength, UTS is the ultimate tensile strength, Elong denotes the plastic strain at failure, E is the Young's modulus. The Young's modulus values were taken from Ref. [106], in which the specimens are cycled under load control between -30 and 30 MPa for twenty cycles at 1 Hz at room temperature. A linear equation is interpolated for all points at each cycle and the average slope of the twenty measurements gives the elastic modulus at the corresponding temperature. The same procedure was conducted at elevated temperatures and the modulus was found to vary with temperature following the empirical equation:

$$E(GPa) = 78.5 - 0.05 \times T(^{o}C) \tag{3.2}$$

where E is Young's modulus (GPa), T is temperature (^{o}C).

Table 3.3 Yield strength, ultimate tensile strength, elongation and Young's modulus at 20, 150 and 250^{o}C

Temperatrue (^{o}C)	YS (MPa)	UTS (MPa)	Elong (%)	E (GPa)
20	199	290	2	77.5
150	181	223	5	71
250	123	147	7	66

It is shown in Table 3.3 that yield strength, ultimate tensile strength and the Young's modulus decrease when temperature increases. The yield strength and the ultimate tensile strength decrease more from 150 to 250^{o}C compared to the decrease from 20^{o}C to 150^{o}C. In particular, yield strength decreases 18 MPa from 20^{o}C to 150^{o}C and decreases 58 MPa from 150^{o}C to 250^{o}C.

A small amount of the material was hot isostatically pressed (HIP) prior to the heat treatment. The HIP process reduces microshrinkage and gas porosity within the casting to a negligible level by applying high temperature and isostatic pressure for a

specified period of time (480°C and 105 MPa for 3 hours, in this case). The specimens used to monitor the growth of small fatigue cracks were taken from HIP material. It has been seen that scatter exists within tensile stress-strain data, and that within this scatter there appears to be no significant effect of HIP on the tensile properties of E319. Despite the similar tensile behavior, the application of HIP does significantly influence fatigue resistance.

3.2 Testing procedures

3.2.1 Specimen preparation

Figure 3.6 summarizes the procedure for specimen preparation. The first step in preparing all of the specimens was casting the plate shown in Figure 3.1. Then rectangular bars with dimensions of 20×20×160 mm were sectioned from each plate in the region of 15 to 35 mm from the chilled edge, as shown in the shaded area in Figure 3.1. Subsequently, a small number of the bars were hot isostatically pressed (HIP'ed) at 480°C and 105 MPa for 3 hours to reduce the shrinkage porosity to insignificant levels. All the HIP'ed and non-HIP'ed bars were then subjected to a T7 over-aged heat treatment, consisting of solution heat treatment at 495°C for 8 hours, followed by water quench at 90°C and aging at 260°C for 4 hours. After heat-treating, the non-HIP'ed bars were machined to specimens which are used to generate the S-N fatigue behavior with a cyclic frequency of either 20 kHz or 75 Hz at ambient and elevated temperatures. Fatigue specimens were machined from the HIP'ed bars to investigate crack growth behavior from micronotches with a cyclic frequency of either 20 kHz or 30 Hz at ambient and elevated temperatures. The geometry of the fatigue specimens is illustrated in Figure 3.7. All specimens have cylindrical gage sections. Diameters of the gage section of the specimens used in ultrasonic fatigue and conventional fatigue are the same. To ensure consistent surface finish with low residual stress, samples were machined using low stress turning at Westmoreland Material Testing. The specimens for crack growth tests

have two additional flats machined onto the gage sections. One of the flats on each specimen was hand polished to 1μm and a micronotch was then machined in the center of the polished flat using femtosecond laser, as shown schematically in Figure 3.7 (c) and (d).

3.2.2 S-N fatigue testing

3.2.2.1 Ultrasonic fatigue test

Ultrasonic fatigue tests were conducted in lab air at temperatures of 20, 150 and 250 ^{o}C, over a range of stresses using fully reversed loadings (R = -1). The specimen vibrates in resonance at approximately 20 kHz producing a displacement distribution with maximum amplitude at both ends and a vibration node in the center of the specimen. The strain amplitude along the length of the specimen has a maximum value in the center and the strain in the gage length was held constant to within 5%.The distributions of displacement and strain along the specimen are shown in Figure 3.8. Since the ultrasonic test is basically displacement or total-strain controlled, the stress amplitude can be calculated on the basis of Hooke's law as long as the specimen deformation is nominally elastic. The ultrasonic loading is applied in well controlled pulses (200 ms on / 800ms off) to reduce specimen heating [2].

For ultrasonic fatigue testing, an induction heating technique is used during the tests at elevated temperatures as shown in Figure 3.9. Careful design and placement of the copper coil allows the entire specimen to reach a uniform temperature and prevents elastic modulus gradients. A control thermocouple is located at the vibration node at the center of the specimen without damping the vibration. With this setup, the temperature can be maintained to within ±5^{o}C. Two strain gages at the center serve to monitor the strain at low displacement amplitudes, which is used to calibrate the strains at higher amplitudes. The strain during set-up at room temperature is linearly extrapolated to 250^{o}C.

A fiber-optic based measurement system (Fotonic^{TM} sensor) performs non-contact

displacement measurements at the end of the specimen. The Fotonic^{TM} probe contains two sets of optical fibers, light-transmitting fibers and light-receiving fibers, which are bundled together. Displacement measurement is based on the interaction between the field of illumination of the transmitting fibers and the field of view of the receiving fibers. At contact, or zero gap, most of the light exiting the transmitting fibers is reflected directly back into those fibers. No light is provided to the receiving fibers and the output signal is "zero". As the probe-to-target distance increases, increasing amount of light are captured by the receiving fibers and converted to a voltage signal. The voltage is then calibrated with the displacement. The Fotonic^{TM} sensor is capable of measuring vibration up to 150 kHz with resolution of 0.03 μm. The strain measured in the center of the gage and the displacement measured at the specimen free end are linearly related as shown in Figure 3.10.

3.2.2.2 Conventional fatigue test

The conventional S-N fatigue tests were conducted on the specimen configuration shown in Figure 3.7 (b) using a servo-hydraulic fatigue testing equipment under load control. Constant stress amplitudes at a frequency of 75 Hz and a stress ratio of -1 were used. Fatigue testing was conducted at temperatures of 20, 150^{o}C and 250^{o}C in laboratory air. Specimens were heated in an electric resistance furnace during fatigue testing at elevated temperatures, as shown in Figure 3.11.

Since the stress amplitudes applied to the specimens during fatigue testing are well below the yield strength, the deformation of the specimens is normially elastic. As such, there is no difference in the applied stress between load-control (for conventiosnal fatigue tests) and displacement control (for ultrasonic fatigue tests).

3.2.3 Crack growth testing

Fatigue crack growth studies have been performed on HIP'ed material with both

ultrasonic fatigue instrumentation and conventional servo-hydraulic fatigue testing equipment under fully reversed loading condition (R = -1). Specimens were cycled at frequencies of approximately 20 kHz and 30 Hz. The gage section of the specimens for crack growth tests had two additional flats machined onto them (Figure 3.7 (c) and (d)). This geometry not only provides a discrete plane of minimum cross section but also a plane of fixed focal value for laser machining and optical microscopy. The elastic stress concentration factor due to the flats is approximated from Peterson's handbook [107] to be $K_t \approx 1.04$. One flat on each specimen was hand polished using diamond paste to a finish of 1 μm. A micronotch was machined in the center of the polished flat by using a femtosecond laser beam, which introduces very small damage to the material around the notch, as shown in Figure 3.12.

A stress amplitude of 95 MPa and 80 MPa was applied for 20 and 250°C respectively. Cracks were observed with the aid of a Questar™ telescope mounted on the test frame. Crack length measurement was done by acquiring digital images using National Instruments IMAQ™ Vision Builder software and processing the images using Adobe® Photoshop® software. The resolution of the crack length measurement was close to 1 μm. The crack length projected in the pure-mode I plane was used for analysis.

Cyclic crack growth rate, *da/dN*, was determined from crack length versus number of cycles data using a 3-point sliding polynomial method described in ASTM E647 [106]. The stress intensity factor range, ΔK, corresponding to a given crack length was calculated using a solution presented by Newman and Raju [108] for a surface crack growing in a finite plate. In determining ΔK, the crack shape was assumed to be semicircular where the crack depth was estimated to be equal to half of the crack length and the stress intensity was assumed to be constant everywhere on the same semi-circle (Figure 3.13). Only the tensile portion of the applied stress range was used to calculate ΔK since it is thought that only this portion of the loading cycle contributes to crack growth.

3.3 Environmental control

To investigate the effect of water on fatigue properties of E319 cast aluminum alloy, ultrasonic fatigue specimens were tested at room temperature in various environments, i.e. ambient air with relative humidity (RH) of 20 ~90%, liquid distilled water, water vapor (RH ~ 100%) and dry air (RH 0.1~0.2%).

Relative humidity (RH) is defined as the ratio of the partial pressure of water vapor in a gas mixture to the saturated vapor pressure of water at a given temperature. RH is expressed as a percentage and is calculated in the following manner:

$$RH = \frac{P}{P_s} \times 100\% \tag{3.3}$$

where RH is the relative humidity of the gas mixture being considered, P is the partial pressure of water vapor in the gas mixture and P_s is the saturation vapor pressure of water at the temperature of the gas mixture.

Table 3.4 Saturated water vapor pressure at each temperature and the corresponding relative humidity at room temperature

Temperature (^{o}C)	Saturated vapor pressure (Pa)	Relative humidity (%)
-60	1.1	0.05
-50	3.9	0.2
-40	12.6	0.5
-30	37.4	1.6
-20	101.6	4.3
-10	256.0	10.9
0	602.7	25.8
10	1227.9	52.5
20	2338.5	100

The amount of water vapor in the ambient air is usually less than that required to

saturate the air, e.g. the relative humidity in the ambient air is approximately 20~90%. If the air is gradually cooled while maintaining a constant moisture content, the relative humidity will rise until it reaches 100%. This temperature, at which the moisture content in the air will saturate the air, is called the dew point. The dewpoint temperature is the temperature at which the liquid and gaseous phases of water are in equilibrium at a given gas pressure. In other words, the dewpoint temperature is the temperature at which the liquid water, or dew, evaporates at the same rate at which it condenses. If the air is cooled further, some of the moisture will condense and the saturated water vapor pressure will decrease. The saturated water vapor pressure at each temperature is listed in Table 3.4.

Based on this principle, dry air was generated, as schematically illustrated in Figure 3.14. Laboratory air (RH 20~90%, water partial pressure 450~2100 Pa) is pumped into the system and pre-dried by the desiccants. The pre-dried air is then cooled by the liquid nitrogen where the water vapor condenses and the air is dried to below 5 Pa. This dry air is subsequently pumped into the specimen chamber as the testing environment for fatigue crack growth test.

The specimen chamber is mounted on the vibration nodes on the load train without damping the vibration. To facilitate observation of crack growth optically, the specimen chamber is specially designed to have a flat window in the middle.

The partial water pressure in the dry air is measured by a hygrometer, Model OEM digital dewpoint transmitter, which can continuously monitor air dryer performance from dewpoint of -20^{o}C to as low as dewpoint of -80^{o}C (0.05~100 Pa equivalent) with accuracy of ±3^{o}C. The dewpoint sensor, which acts like a variable capacitor, consists of an aluminum core, a hygroscopic oxide dielectric film, and a thin covering of porous gold film. Since the pores of the gold film and oxide layers are extremely small, they are specific to the water vapor molecule. The dielectric oxide layer, only a few micrometers in thickness, rapidly achieves equilibrium of the water vapor pressure, which is proportional to the dewpoint temperature.

3.4 Statistical analysis of S-N behavior

S-N data of cast aluminum alloys typically show significant variation in fatigue life at certain stress amplitude, which is attributable to the variation of microstructure, e.g. porosity [6, 13, 24, 25]. A statistical analysis is therefore necessary to evaluate the fatigue response and account for the observed scatter in fatigue life.

3.4.1 Staircase test methodology

To determine the fatigue strength at a high number of cycles, e.g. 10^8 cycles for ultrasonic fatigue and 10^7 cycles for conventional fatigue, the staircase test methodology [109] was used at stress amplitudes ranging from 75 to 100 MPa. The specimens were tested sequentially. The first specimen is tested at a certain stress level. If the specimen fails at a number of cycles less than the pre-determined number (10^8 cycles for ultrasonic fatigue and 10^7 cycles for conventional fatigue), the next specimen is then tested at a stress level one-step lower than the failed specimen. If the specimen survives at the pre-determined cycles (termed as runouts), the next specimen is tested at a stress level one-step higher than the previous specimen. This methodology is repeated throughout the test program and the final outcome is that approximately half of the specimens fail and the other half does not, as the specimens are tested around the mean fatigue strength. The staircase data were then analyzed following the Dixon-Mood method [109], which consists of a convenient approximation for the maximum likelihood estimation applied to the staircase testing method and assumes that the fatigue strength is normally distributed. The fatigue strength was then expressed in terms of the mean value and standard deviation. It should be noted that Engler-Pinto *et al.* [110] applied the maximum likelihood estimation (MLE) method in evaluating the staircase testing results. They observed that the Dixon-Mood and MLE estimations are very similar when it is assumed that the fatigue strength follows a normal distribution.

3.4.2 Random fatigue limit (RFL) model

In the present study, while the majority of the S-N data were the staircase results within the range of fatigue strength, a number of complementary tests were conducted at higher stress amplitude to fill in critical regions of data to obtain a general trend of S-N behavior. Fitting an S-N curve to experimental results where only failures have been observed is a straightforward task. When runout data is mixed with failure data, however, the fitting is more complex. Here, a life-regression model, random fatigue limit (RFL) model proposed by Pascual and Meeker [111] is used to provide a method to fit S-N curve to a set of data containing both failures and runouts using the Maximum Likelihood Estimate (MLE) principles. The equation of RFL is:

$$ln(N) = \beta_0 + \beta_1 \ln(\sigma - \sigma_0) + \varepsilon\,,\ \sigma > \sigma_0 \tag{3.4}$$

where N is the fatigue life, σ is the stress amplitude, σ_0 is the fatigue limit of the specimen, β_0 and β_1 are empirical constants and ε represents the scatter in the fatigue life. In Equation 3.4, the logarithm of life is linearly related to the logarithm of the difference between applied stress and the fatigue limit. The RFL model assumes that there is a probabilistic fatigue limit for an infinite number of cycles as it varies from specimen to specimen and assumes that the random fatigue limit follows a Weibull distribution. Also, the fatigue life is assumed to have a lognormal distribution.

In the RFL model, five parameters must be determined and these five parameters are β_0, β_1, ε, mean and Weibull shape parameter of fatigue limit. To estimate these parameters from the experimental data, the maximum likelihood estimation (MLE) method is used [110-112] . The "best" parameter values are those that maximize the likelihood of experimental observations. The likelihood equation is a function of the experimental data and the unknown parameter. For a given stress amplitude, σ, the likelihood for RFL model can be defined as:

$$L = \prod_{i=1}^{n} f(N_F^i, \{p\}) \cdot \prod_{j=1}^{m} [1 - F(N_R^j, \{p\})] \tag{3.5}$$

where *n* corresponds to the number of failed specimens and *m* is the number of runouts, and *{p}* are the parameters that define the distribution. $f(N_F^i, \{p\})$ is the probability density function of fatigue life. $F(N_R^j, \{p\})$ is the cumulative density function of fatigue life. For failed specimens, the likelihood is the ordinate of the probability distribution at the observed fatigue life. For runout specimens, since the exact fatigue life is unknown but greater than the observed *N*, the likelihood is the fraction of the area under the distribution curve to the right of the suspension. In other words, the likelihood for a runout observation is equal to one minus the cumulative probability of failure at *N* cycles. The main advantages of the MLE method are the ability to correctly treat runout data and the fact that any distribution can be used as long as the likelihood equations are known [110-112].

An example of application of RFL in the S-N results of a cast aluminum alloy [6] is shown in Figure 3.15. *P*-percentile S-N curves, also called S-N-P curves were plotted to relate *p* percentile of fatigue life to the applied stress. Thus, each curve represents the S-N response corresponding to a constant probability of failure, *p*. For example, the bold curve in the middle represents the median curve, which corresponds to 50% failure probability. The curve at the bottom represents 1% failure probability and the curve at the top represents 99% failure probability. In the remainder of this thesis, all S-N curves, unless otherwise specified, refer to the 50% percentile curve fits based on the RFL model.

It can be seen from Figure 3.15 that the RFL model correctly captures the curvature beyond 10^7 cycles observed in the experimental S-N plot at lower stress levels. This curvature suggests an eventual true fatigue limit for a higher number of cycles, e.g. 10^8 cycles. Even if a true fatigue limit does not exist, the RFL model provides a useful empirical method to describe the curvature observed in the S-N fatigue curve for cast aluminum alloys [112]. It is also improves the statistical characteristics, as it uses the

failures and runouts data to fit the S-N curve, and allows the determination of the fatigue strength distribution for any number of cycles.

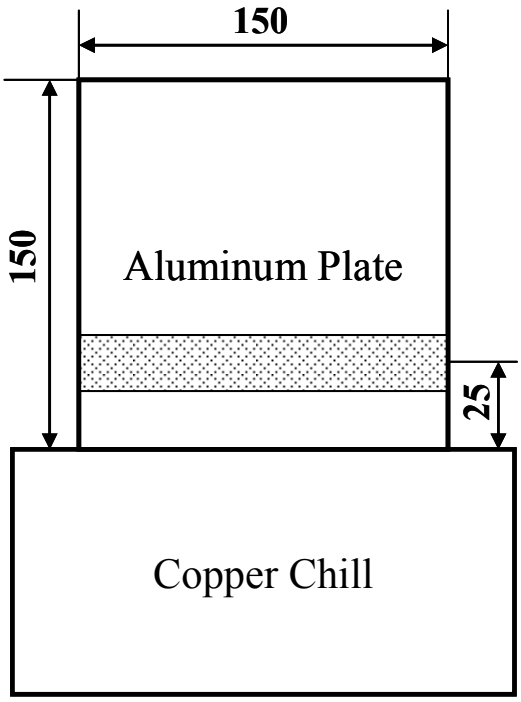

Figure 3.1 Schematic of sand cast aluminum plate with thickness of 20mm; the shaded area indicates the sectioned region with an average SDAS of 30μm.

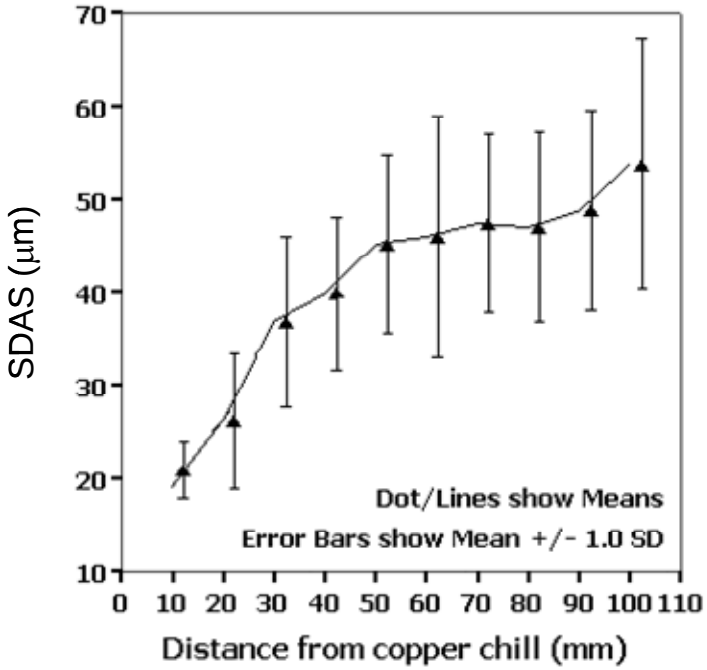

Figure 3.2 The SDAS increases with the increasing distance from the chill.

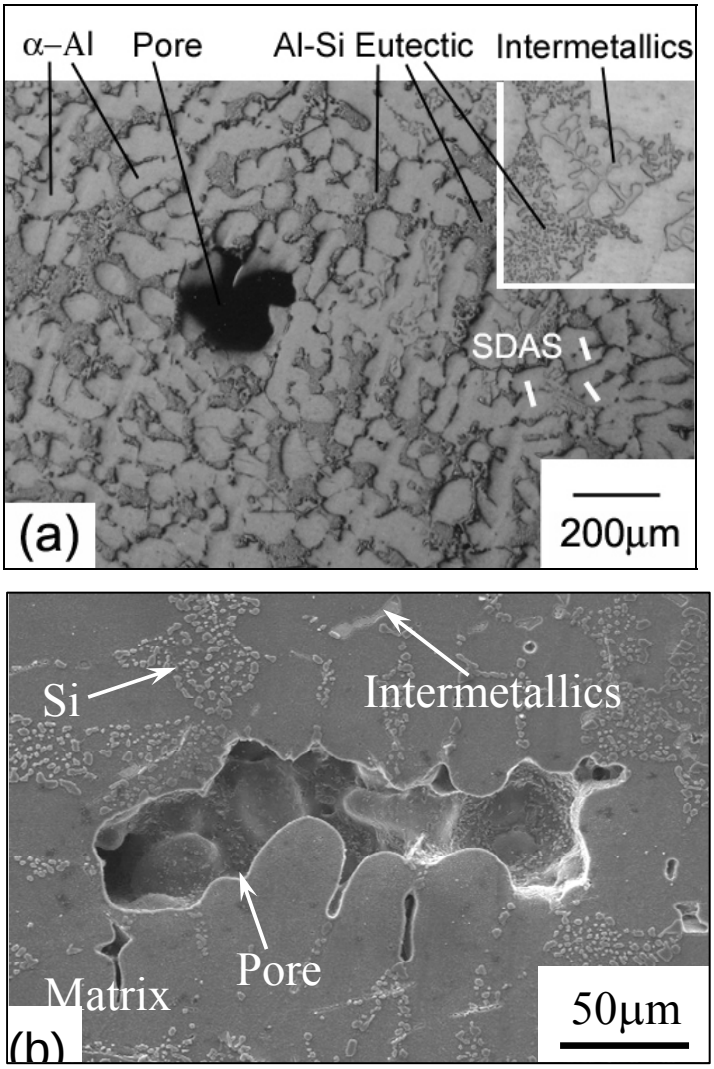

Figure 3.3 (a) The typical optical microstructure of E319 cast aluminum alloy from the sectioned region and (b) an SEM secondary electron image revealing more details of the microstructure. For the SEM image, the sample was polished and etched using 1.8% HF solution.

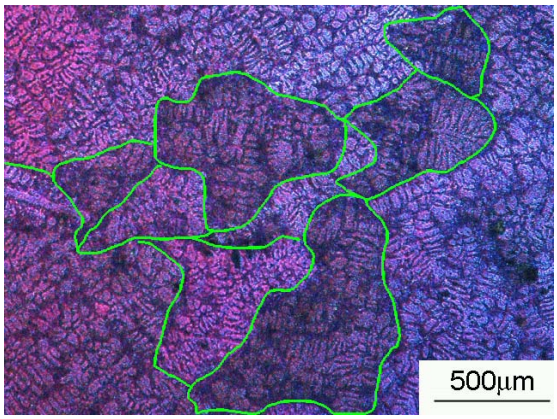

Figure 3.4 Grains in E319 cast aluminum alloy; the grain boundaries are high lighted.

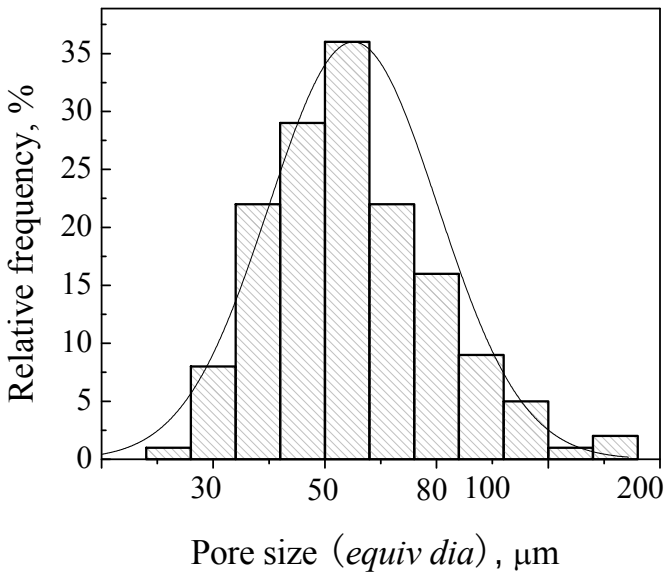

Figure 3.5 Log-normal distribution of measured 2-D pore sizes in E319 cast aluminum alloy from metallographic sections (note that the histogram bins were mapped from logarithmic values of the pore sizes).

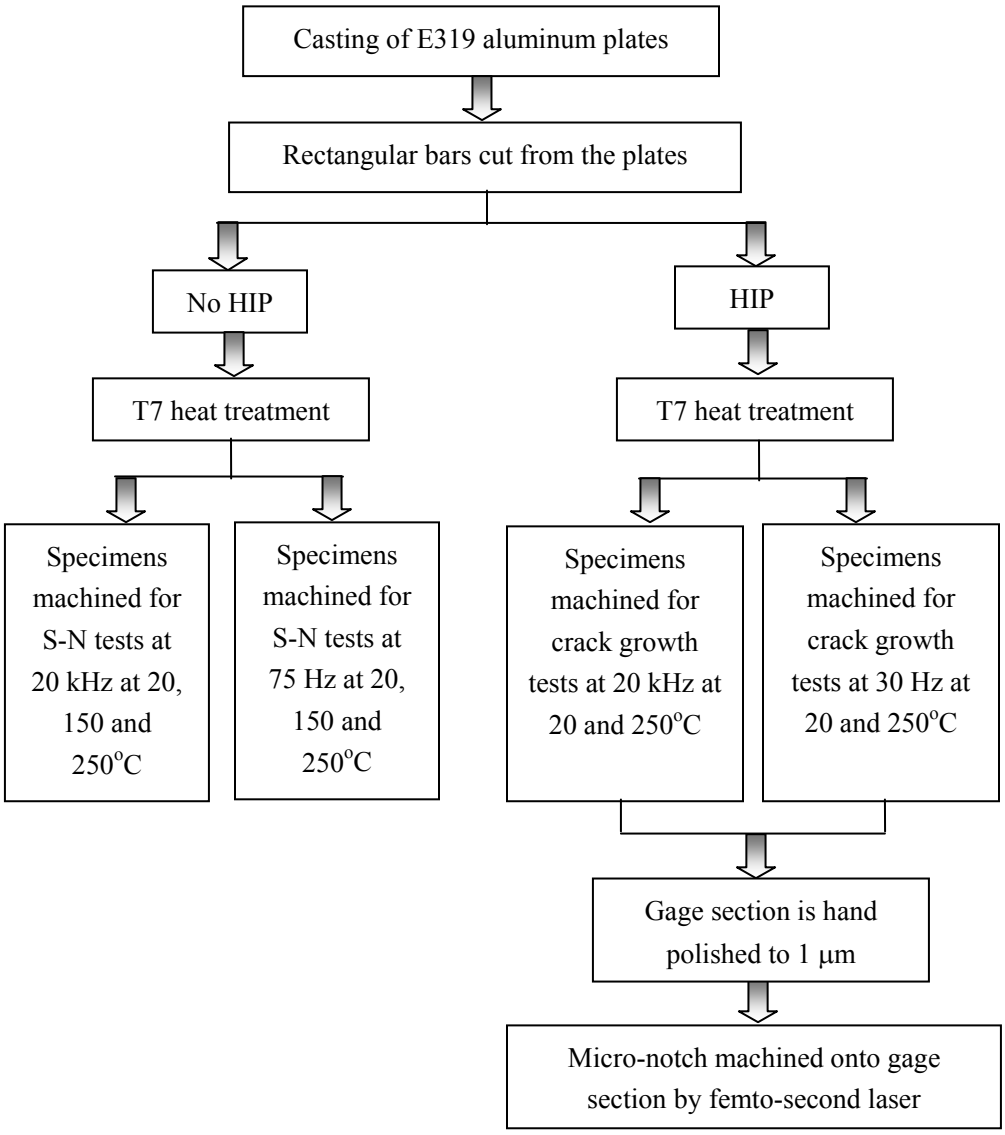

Figure 3.6 Procedure followed to prepare fatigue specimens of cast E319 aluminum.

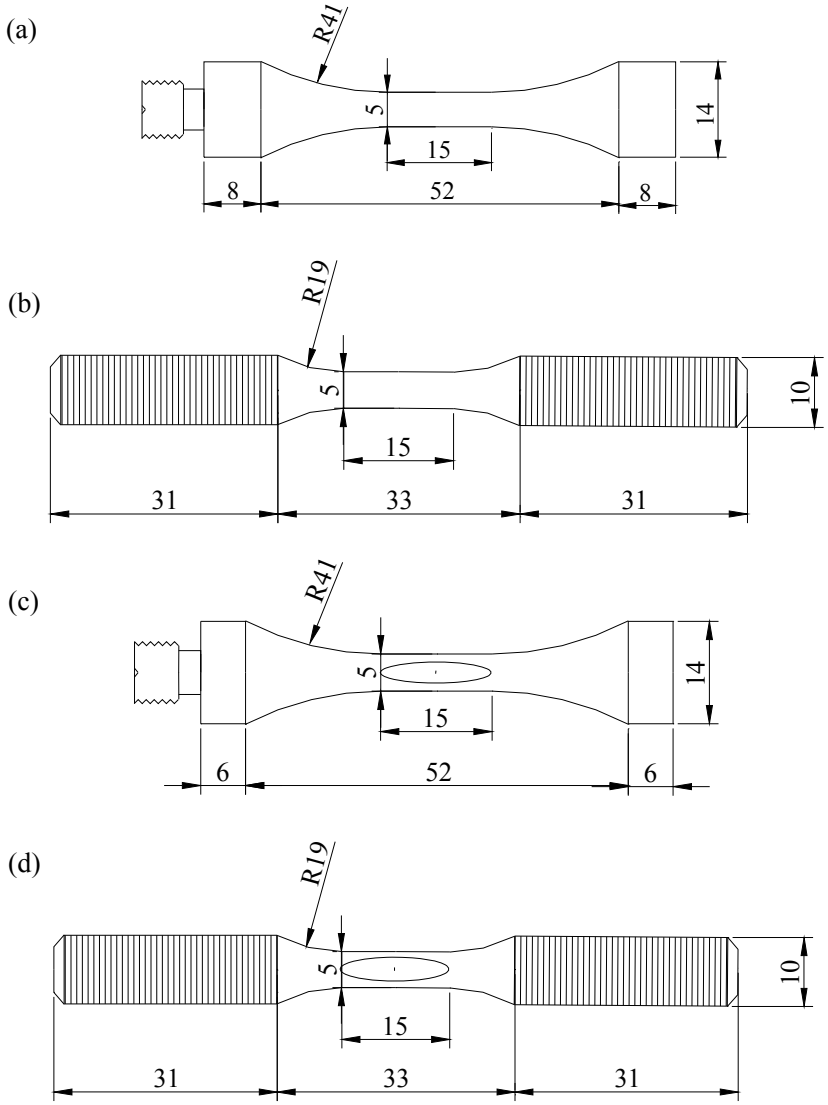

Figure 3.7 Specimen geometry used for (a) ultrasonic fatigue S-N test (20 kHz) for R = -1; (b) conventional fatigue S-N test (75 Hz); (c) ultrasonic fatigue crack growth test (20 kHz) for R = -1; (d) conventional fatigue crack growth test (30 Hz). Dimensions are in mm. Laser machined micronotches in the gage section of the crack growth specimens were schematically shown in (c) and (d).

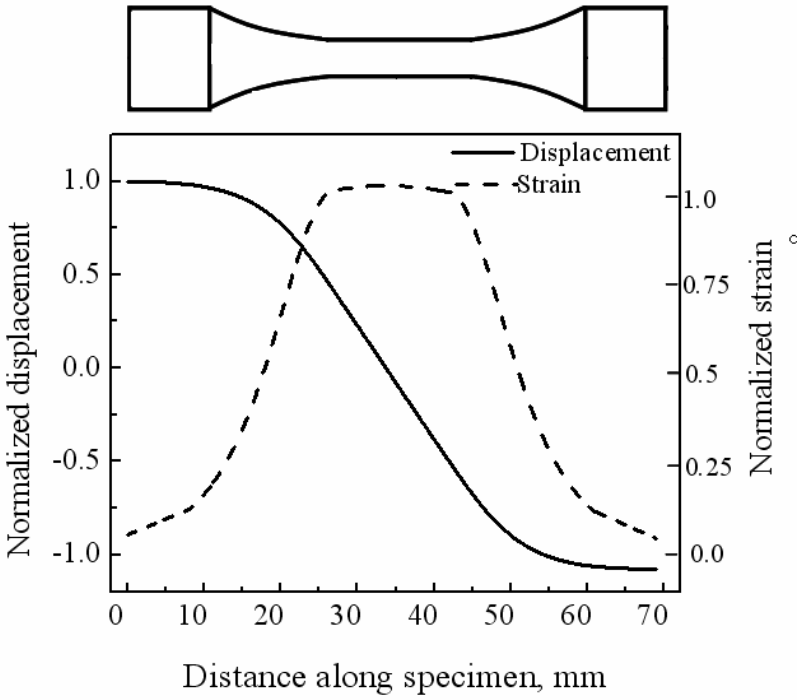

Figure 3.8 Distribution of displacement and strain along the ultrasonic fatigue specimen.

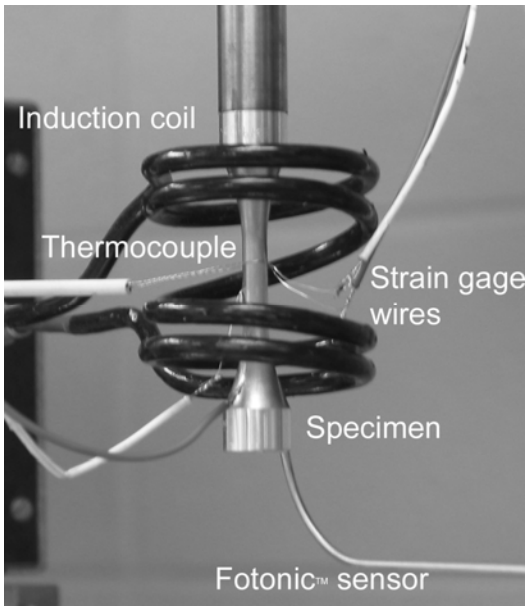

Figure 3.9 A specimen in ultrasonic fatigue testing with strain measurement, displacement measurement and induction heating arrangement.

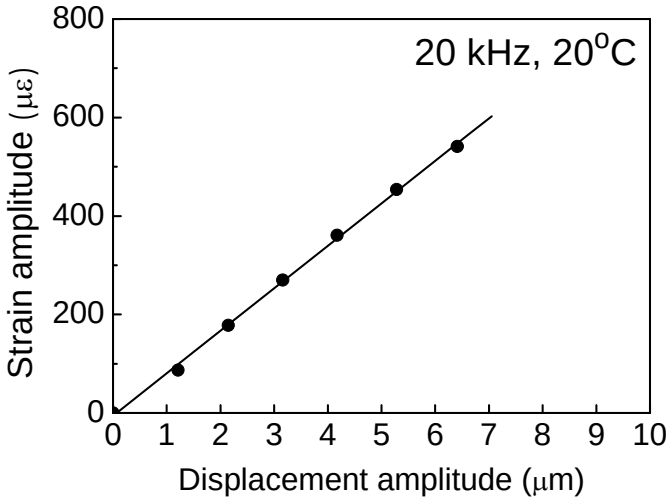

Figure 3.10 Correlation of strain amplitude in the center of the specimen and displacement amplitude at the end at 20°C.

Figure 3.11 Conventional fatigue testing system equipped with an electric furnace.

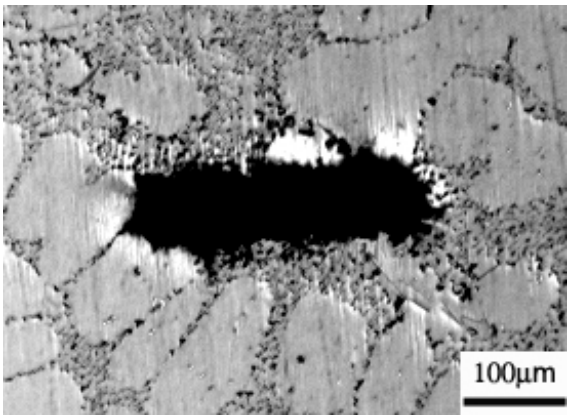

Figure 3.12 A micronotch machined onto the gage section of the specimen by femto-second laser beam which introduce very small damage to the material around the notch.

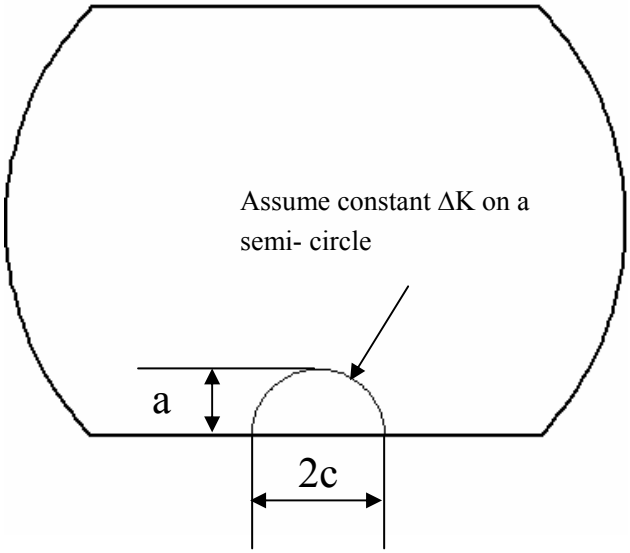

Figure 3.13 Schematic illustration of small surface crack as viewed from the interior cross-sectional plane for a crack growth specimen. A semicircular crack shape is assumed where a = c and ΔK is assumed constant on a semi-circle.

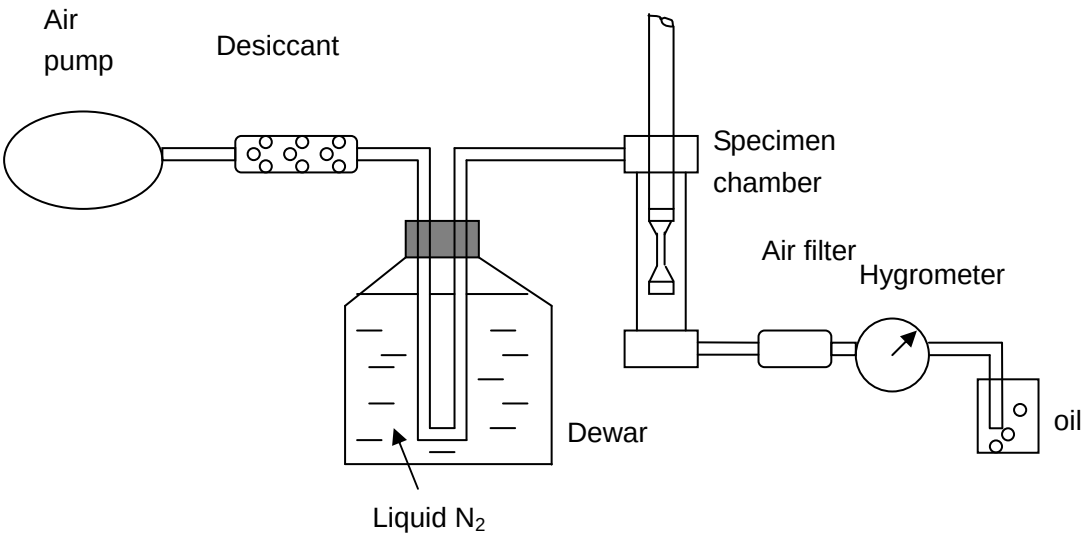

Figure 3.14 Schematic illustration of the system to obtain dry air.

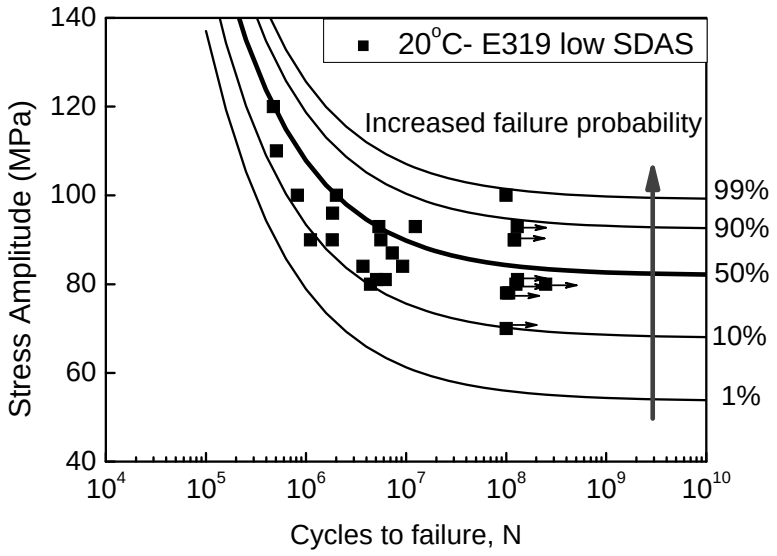

Figure 3.15 Random fatigue limit (RFL) model applied to the S-N results of E319 cast aluminum alloy [6].

Chapter 4

Effect of frequency, environment and temperature on fatigue performance of E319 cast aluminum alloy

Performing fatigue tests in the very high cycle regime becomes practical with the use of ultrasonic testing techniques. For example, applying 10^8 cycles requires approximately 2 hours when a specimen is tested at a frequency of 20 kHz. Therefore, a significant amount of data can be obtained in a short period of time and the fatigue strength at cycles greater than the expected service life can be empirically determined, rather than estimated from extrapolations. However, in actual components of cast aluminum alloys, the critical locations are subjected to a loading frequency of 20 - 100 Hz, which is 2 to 10 decades lower than the ultrasonic fatigue testing frequency. Some critical questions regarding the ultrasonic fatigue technique need to be answered before ultrasonic fatigue data can be used to predict the fatigue behavior of actual components. It is necessary to know if the fatigue process is significantly influenced by the substantial increase in the cycling frequency. One key factor to understand is whether fatigue data determined with the ultrasonic method are comparable to fatigue data generated with conventional fatigue testing equipment.

To examine these issues, the effect of frequency on fatigue response of materials may be subdivided into intrinsic effects, e.g. strain rate effect, and time-dependent, or extrinsic, effects, such as those attributable to environmental effects or fatigue/creep interaction. As discussed in section 2.4, it is unlikely that strain rate exerts a significant influence on the fatigue properties of aluminum alloys. Plastic deformation of face centered cubic (FCC) metals, including aluminum, has been reported to be relatively

insensitive to strain rates [41-43]. Also, cyclic loading near the fatigue limit or fatigue crack growth near the threshold stress intensity involves only minimal cyclic plastic deformation where the strain rate effect would be significantly moderated or absent [51, 52].

When the effect of strain rate is small, an effect of frequency is expected to be tied to an environmental effect. It has been observed that the fatigue behavior of aluminum alloys can be influenced by the presence of water vapor in atmospheric air [38, 40, 55-62, 68] . Since the duration of crack tip opening under ultrasonic frequency loading is shorter for each cycle than for conventional fatigue experiments, any environmentally assisted increase in fatigue crack growth rate is generally presumed to be less pronounced at ultrasonic frequency, which would lead to lower fatigue crack growth rates at ultrasonic frequencies than at conventional frequencies.

Temperature can also influence the fatigue behavior of cast aluminum alloys. The maximum operating temperature of cylinder heads can reach a peak temperature of over 200°C in automotive engines [3]. Since the crack growth rates can be influenced by environment, a question arises: is the effect of temperature on crack growth rates related to an intrinsic effect of temperature on the mechanical properties or to an effect of environment with increasing temperature? In addition, the effects of frequency on fatigue behavior at elevated temperature need to be explored in evaluating the ultrasonic fatigue data obtained by ultrasonic fatigue technique at elevated temperature.

In this chapter, the fatigue behavior of E319 cast aluminum at both room temperature and elevated temperature (150^{o}C and 250^{o}C) is studied at ultrasonic and conventional cyclic frequencies. The chapter begins by studying the effect of frequency and environment on fatigue performance of E319 cast aluminum alloy at room temperature. The S-N behavior, fatigue crack initiation and fatigue crack propagation at room temperature are investigated at ultrasonic and conventional frequencies and in various environments with different water pressures. The effect of frequency and

environment on fatigue propagation and therefore S-N behavior of E319 cast aluminum alloy is modeled and is comparable to the experimental results. Subsequently, the fatigue behavior at elevated temperature, 150 and 250^{o}C, at both ultrasonic and conventional frequencies is presented. The effect of temperature on fatigue properties of E319 cast aluminum alloy and the effect of frequency at elevated temperature are investigated and modeled. Based on this model, fatigue crack growth rates and, therefore, fatigue lives in environment can be predicted and the predictions generally agrees well with the experimental observations.

4.1 Effect of frequency on fatigue behavior at room temperature

4.1.1 Comparison of S-N results at 20 kHz and 75 Hz

The S-N results of the E319 cast aluminum alloy at frequency of 20 kHz are shown in Figure 4.1, which were generated at a load ratio of R = -1 in laboratory air at room temperature. The specimens that did not fail after 10^8 cycles are designated as runouts and indicated in the S-N plot with a small arrow pointing to the right. It can be seen from Figure 4.1 that the number of cycles to failure increases from 10^5 to 10^8 cycles as the stress amplitude decreases from 160 MPa to 70 MPa. Also, large scatter in the lifetime was observed, and the magnitude of scatter increases as the stress amplitude decreases. For example, at 80 MPa, one specimen failed at 4.4×10^6 cycles while another specimen survived even at 2.5×10^8 cycles. This constitutes approximately two orders of magnitude in scatter. The specimens that survived at 10^7 cycles typically survived at 10^8 cycles. The S-N curve represents the mean curve, which corresponds to 50% failure probability based on the random fatigue limit (RFL) model [111, 112] as described in section 3.4.2. The S-N curve exhibits a strong curvature and an asymptotic behavior in the lifetime regime beyond 10^7 cycles, indicating that a fatigue limit exists. The fatigue strengths are estimated to be 89.5 MPa at 10^7 cycles and 84.3 MPa at 10^8 cycles. These results are consistent with the reported S-N behavior of cast aluminum alloys [8, 14], where the existence of a fatigue limit was demonstrated at room temperature. It is

generally accepted that if the associated driving force of the fatigue crack is below the threshold value, the crack becomes non-propagating and failure will not ensue. This behavior leads to the flattening of the S-N curve and the occurrence of a fatigue limit. Gao *et al.* [20] suggested that the fatigue limit corresponds to a critical stress below which no micro-plasticity accumulation occurs in a cast aluminum alloy under cyclic loads, based on their finite element analysis. The fatigue strength at 10^8 cycles of E319 cast aluminum alloy is investigated in detail in Chapter 5.

For comparison, the S-N data were acquired using conventional fatigue test methods with a frequency of 75 Hz at a load ratio of -1 in laboratory air at room temperature. The diameter and length of the gage section of the specimens tested at 20 kHz and 75 Hz are equivalent (Figure 3.7). The S-N results at 75 Hz are shown in Figure 4.2 (a). The data at 10^7 cycles represent experimentally observed runouts. It can be seen from Figure 4.2 (a) that the fatigue life at 75 Hz gradually increases with decreasing stress amplitudes, without distinct flattening of the curve. The mean fatigue strengths at 10^7 cycles and 10^8 cycles are estimated to be 83.3 MPa and 76.2 MPa, respectively. However, the extrapolated S-N behavior beyond 10^7 cycles based on the experimentally acquired data at 75 Hz can be significantly conservative. As shown in Figure 4.1, at 20 kHz, the specimens that survived at 10^7 cycles also survived at 10^8 cycles and a plateau of the S-N curve occurs beyond 10^7 cycles. This behavior observed in earlier studies was found to be associated with non-propagating cracks for which the driving force for crack growth is below a threshold value [8, 14]. Moreover, it was reported that, for some aluminum alloys [51, 52, 59], cyclic frequency did not influence fatigue crack growth threshold. Therefore, it can be reasonably expected that, at room temperature, the runouts at 10^7 cycles at 75 Hz will very likely survive at 10^8 cycles. As such, a plateau of the S-N curve at 75 Hz occurs beyond 10^7 cycles based on the RFL model (Figure 4.2 (b)) and we believe that this RFL estimate is more representative of the S-N behavior of E319 cast aluminum alloy at 75 Hz than direct extrapolation from the experimental data (Figure 4.2

(a)). The fatigue strengths at 10^7 cycles and 10^8 cycles are estimated to be 87.5 MPa and 82.5 MPa, respectively.

The S-N results at 20 kHz and 75 Hz are compared in Figure 4.3 . Here, the 75 Hz RFL estimate (solid curve) is made assuming that the specimens that survived at 10^7 cycles actually survived at 10^8 cycles and this is consistent with observations from ultrasonic fatigue testing. At high stress amplitudes, fatigue life at a frequency of 20 kHz is longer than that at 75 Hz; however, the difference in fatigue life decreases as the stress amplitude decreases. For example, at a stress amplitude of 160 MPa, fatigue life at 20 kHz is 10^5 cycles, which is approximately 10 times of the fatigue life of 1.6×10^4 cycles at 75 Hz. At a stress amplitude of 120 MPa, fatigue life at 20 kHz is approximately 5 times of the fatigue life at 75 Hz. At lower stress levels of 80 to 90 MPa, the S-N curves at 20 kHz and 75 Hz become very close. The estimated fatigue strengths are similar at these two frequencies, as summarized in Table 4.1. At 10^8 cycles, the fatigue strength is 84.3 MPa at 20 kHz and 82.5 MPa at 75 Hz, which is only a 2% difference in fatigue strength. Considering the scatter in the fatigue data, 5% and 95% percentile S-N curves were plotted in Figure 4.3 (b) to illustrate the variability of fatigue life. It can be seen that at high stress levels, e.g. 160 MPa, the ranges of S-N data at 20 kHz and 75 Hz are separated; however, as the stress levels decrease, the scatter of the data increases and the ranges of S-N data at 20 kHz and 75 Hz become gradually overlapped. The fatigue strengths at 20 kHz and 75 Hz essentially fall in the same range, as illustrated in Table 4.1.

Table 4.1 Estimated fatigue strengths of E319 cast aluminum at ultrasonic frequency (20 kHz) and conventional frequency (75 Hz) based on RFL model

Frequency (Hz)	10^7 cycles		10^8 cycles	
	50% percentile fatigue strength (MPa)	5% to 95% percentile fatigue strength (MPa)	50% percentile fatigue strength (MPa)	5% to 95% percentile fatigue strength (MPa)
20,000	89.5	70.5 to 102.7	84.3	65.5 to 97.3
75*	87.5	68.8 to 100.7	82.5	63.5 to 95.5

*Estimation of fatigue strength at 75 Hz is based on the assumption that the specimens that survived at 10^7 cycles acturally survived at 10^8 cycles.

An important conclusion can be drawn that in the lifetime regime of less than 10^7 cycles, an effect of frequency on S-N behavior of E319 cast aluminum alloy was observed and the fatigue life at 20 kHz is 5 to 10 times longer than the fatigue life at 75 Hz; while beyond 10^7 cycles, the effect of frequency on the room temperature fatigue performance of E319 cast aluminum alloy is substantially reduced. In fact, recent publications have reported different correlations between ultrasonic and conventional fatigue for aluminum alloys. Caton *et al*. [4] observed no influence of frequency on high cycle fatigue for the cast aluminum alloy 319 at room temperature. Mayer *et. al* [113] also showed no frequency influence and similar lifetimes for a wrought aluminum alloy AlZnMgCu1.5 in the regime of 10^5~10^9 cycles. Engler-Pinto Jr. *et al.* [23, 114] reported that for some cast Al-Si alloys with low yield strength the fatigue lives at 20 kHz were similar to those at 75 Hz. However, Engler-Pinto Jr. *et al.* [23, 114] also reported that for some cast Al-Si alloys with high yield strength, the fatigue lives were several orders of magnitude longer than those at 75 Hz.

Examination of Figure 4.3 illustrates an important benefit of acquiring data in the very high cycle regime. As mentioned, conventional fatigue tests are stopped after 10^7 cycles if failure has not occurred and the fatigue behavior for higher applied cycles has to be inferred by extrapolating the data. With the acquisition of experimental data by ultrasonic fatigue testing, this approach can now be evaluated. It is seen that when considering only the conventional fatigue data, the fatigue life of the E319 cast aluminum alloy gradually increases with decreasing stress amplitude, without the occurrence of distinct flattening of the curve (dotted curve). As a result, the extrapolated fatigue strength at 10^8 cycles based on the conventional fatigue data is significantly lower than the estimated fatigue strength at 10^8 cycles based on the ultrasonic fatigue data. This may result in an under-prediction (conservative) of the fatigue life, which would lead to a non-optimized design. The very high frequencies of ultrasonic fatigue testing methods allow for the fatigue limit to be physically determined for cycles beyond an automotive service

life. By using ultrasonic fatigue, the fatigue strength at 10^8 cycles of E319 cast aluminum alloy has been investigated in detail and its correlation with microstructural features is discussed in Chapter 5.

Fatigue damage evolution can be divided into two stages [34]: fatigue crack initiation and fatigue crack propagation. To understand the observed effect of frequency on the S-N behavior shown in Figure 4.3, crack initiation and crack propagation of E319 cast aluminum alloy need to be examined and compared for tests conducted at ultrasonic frequency and at conventional frequency.

4.1.2 Crack initiation at room temperature

The fracture surfaces of the failed fatigue specimens tested at 20 kHz and 75 Hz were examined using SEM equipped with an energy-dispersive x-ray analysis system in order to identify the fatigue crack initiation sites. Crack initiation features on the fracture surfaces were quantified by analysis of the SEM images. The sizes of the porosity on the fracture surfaces were measured based on the 2-D projected area using an image analysis program.

In general, the fracture surface consists of three distinct regions: initiation, steady fatigue crack growth and fast fracture. Figure 4.4 (a) shows a typical fracture surface of an E319 fatigue specimen tested at room temperature. The fatigue crack initiated from the pore located at the specimen surface. In Figure 4.4 (b), the irregular shape and dendrite appearance of the pore are indicative of a microshrinkage pore; in the initiation and early fatigue crack growth region, the fracture surface is characterized by a large number of transgranular facets and chevron-like markings radiating from the initiation site. As fatigue crack growth continued, facets and striation-like features are observable; as Figure 4.4 (c) shows, the striation-like features appear as a series of very fine parallel lines. Very rarely was porosity observed in the fatigue crack growth regions. As Figure 4.4 (d) shows, the fast fracture region is characterized by microvoids.

Cyclic frequency does not appear to exert an influence on fatigue crack initiation.

The S-N specimens were pore-containing (no HIP condition) material that underwent the testing procedures described in Figure 3.6. Fractographic analysis shows that, for both testing frequencies of 20 kHz and 75 Hz, all of the cracks resulting in fatigue failure originated from microshrinkage pores; 27 and 24 failed specimens were examined for these two frequencies, respectively.

In ultrasonic fatigue specimens, 89% of the fatal fatigue cracks initiated from pores located at or very near to the specimen surface, as shown in Figure 4.5 (a). This percentage represents 25 of the 27 fatigue specimens examined. There are several cases where multiple pores were observed in close proximity to each other, as shown in Figure 4.5 (b). However, SEM examination of the pores indicated that they were microshrinkage pores and appeared to be interconnected to a certain degree. Since this implies that the observed multiple pores actually are very likely part of a single large pore, these specimens were not counted as having multiple initiation sites, and the pores were considered as a single pore for the purpose of measuring initiation pore size. In 2 of the 27 observed specimens, fatigue cracks initiated from pores located in the specimen interior, as shown in Figure 4.5 (c). These few observed cases were not found to have porosity adjacent to or intersecting the specimen surface. The S-N data corresponding to failure from interior pores are marked by circles in Figure 4.1. The interior pores do not appear to influence the fatigue life because of their large pore sizes (Figure 4.5 (c)). Similarly, in conventional fatigue specimens, all of the fatal fatigue cracks initiated from microshrinkage pores located at or near to the specimen surface, as shown in Figure 4.6. In contrast to results at 20 kHz, no crack initiation occurred from the specimen interior. It is believed that fatigue failure initiated from interior pores is a result of the statistical variation associated with the random pore distribution in the specimens, and is not indicative of an actual effect of frequency.

The distributions of initiation pore size, in terms of mean value and standard deviation, are essentially identical for specimens tested at 20 kHz and 75 Hz. The

initiation pore sizes, in terms of equivalent circular diameter, of the specimens tested at 20 kHz and 75 Hz were measured on the two-dimensional screen projections, as described in Equation 3.1. Figure 4.7 shows the distribution of the initiation pore size, which can be described with a log-normal distribution function. The corresponding mean value and standard deviation of the initiation porosity population were estimated, and the results are summarized in Table 4.2. The initiation pore size has a significant variation. For ultrasonic fatigue specimens, the mean value and standard deviation of the initiation pore size were estimated to be 313 μm and -147/+278 μm, respectively. For specimens fatigued at 75 Hz, the mean value and standard deviation of the initiation pore size were estimated to be 295 μm and -87/+124 μm, respectively. The mean pore size of the ultrasonic fatigue specimens is 6% larger than that of the conventional fatigue specimens. The initiation pore size of the ultrasonic fatigue specimens shows greater variation than that of the conventional fatigue specimens; this could result from the small number of measurements (27 measurements for ultrasonic fatigue specimens and 24 measurements for conventional fatigue specimens).

Table 4.2 Initiation pore size described as log-normal distribution at 20 kHz and 75 Hz

Frequency (Hz)	Initiation pore size	
	Mean (μm)	STDEV (μm)
20, 000	313	-147/+278
75	295	-87/+124

It is demonstrated that failure always occurs from micropores of similar size in E319 cast aluminum alloy, regardless of the testing frequency. Frequency did not influence the fatigue crack initiation of E319 cast aluminum alloy. This is consistent with previously published fatigue investigations on cast aluminum alloys [6, 7, 11, 27, 82, 83]. Numerous studies of the fatigue behavior of cast aluminum alloys have concluded that cracks initiate predominantly from pores which are most commonly located at or very near to the specimen surface. Cracks initiate from pores because of the associated high

stress concentration. Cracks initiate very early in the fatigue life and it is generally assumed that the entire fatigue life of a cast aluminum specimen is dominated by crack propagation phase. Caton [27] observed that fatigue cracks formed almost immediately from microshrinkage pores, even at stresses where failure did not result after 10^8 cycles and he concluded that, relative to the total fatigue life, the fatigue initiation life in pore-containing W319 specimens is negligible at all stress levels investigated.

It can be seen that there is considerable variation in initiation pore size and this is concluded to be the main reason for the scatter in fatigue life in cast aluminum alloys. Sizes and location are critical parameters in determining if a pore will initiate a crack. Not only do the larger pores increase the likelihood that a crack will initiate, but these pores also provide a larger initial crack size, which reduces the number of cycles required to fail the specimen. Also, the closer a pore is located to the specimen surface, the more likely it is to initiate a crack. Seniw *et al.* [115] reported that large pores located at a significant distance from the free surface were not detrimental to the fatigue life. Their findings are consistent with the work by Murakami and Endo [10].

Based on the fact that frequency did not influence size and location of the fatigue crack initiation pores, the observed difference in fatigue life of E319 cast aluminum alloy between 20 kHz and 75 Hz in the lifetime regime of $< 10^7$ cycles (Figure 4.3) is expected to result from different crack growth rates at different loading frequencies.

4.1.3 Crack propagation at room temperature

In order to investigate the fatigue crack propagation behavior of E319 cast aluminum alloy at ultrasonic and conventional frequencies, small crack growth tests were conducted on the specimens of pore-free (HIP condition) material that underwent the testing procedures described in Figure 3.6. The gage section of these specimens have two additional flats (Figure 3.7 (c) and (d)) and a micronotch was machined onto one of the flats by using a femtosecond laser beam to localize the crack initiation. Figure 4.8 (a) shows an example of fatigue cracks that nucleated from a laser-machined micronotch.

The crack growth direction is essentially normal to the loading direction. The micronotch on the fatigue fracture surface is shown in Figure 4.8 (b); the depth of the notch is approximately half of the length of the notch.

The fatigue crack propagation behavior is presented in Figure 4.9, where crack length is plotted as a function of cycles. Two specimens were tested at 20 kHz and one specimen was tested at 30 Hz, respectively, in ambient air. Fully reversed loading with stress amplitude of 95 MPa was used in this small crack growth study. It can be seen that the fatigue cracks nucleate immediately from the micronotches at both 20 kHz and 30 Hz. Cracks grow slowly at the beginning of crack growth and the majority of the fatigue life is spent in the early crack growth stage. It should be pointed out that the size of the micronotch in the specimen tested at 30 Hz is smaller than those in the specimens tested at 20 kHz and the crack grew very slowly at 30 Hz during the early crack growth stage; however, when the crack grew to the equivalent size of the micronotches in the ultrasonic fatigue specimens, the crack growth rate at 30 Hz increased substantially. Therefore, when compared at equivalent crack length, the crack growth rate at 30 Hz is greater than that at 20 kHz.

Crack growth rates at 20 kHz and 30 Hz in ambient air are compared in Figure 4.10, in which two tests at 20 kHz and one test at 30 Hz are shown. The two sets of crack growth data at 20 kHz are overlapped and the crack growth curve is obtained based on the combined data. Here, fatigue crack growth rates were plotted versus ΔK, with ΔK calculated utilizing the stress intensity solutions of Newman and Raju [108] for small semi-circular surface cracks in a finite plate. Only the tensile portion of the applied load range was used to calculate the stress intensity factor range, $\triangle K$. Crack growth rate, *da/dN*, was determined from crack length versus number of cycles data using a 3-point sliding polynomial method. As shown in Figure 4.10, the crack growth curves are generally parallel within the examined stress intensity range (1 to 4 MPa-$m^{1/2}$) for 20 kHz and 30 Hz. The crack growth rate at 30 Hz is approximately five times greater than that at

20 kHz at an equivalent level of stress intensity.

The observed lower crack growth rate at 20 kHz is consistent with the observed longer fatigue life at 20 kHz, as shown in Figure 4.3. The E319 specimens used in this study have a mean initiation pore size of approximately 300 μm, the stress intensities that these specimens experienced during S-N fatigue tests are roughly estimated to be 1.4 to 3.3 MPa-$m^{1/2}$, when the stress amplitudes examined are in the range of 70 to 160 MPa. It can be seen from Figure 4.10 that within this range of stress intensities, an influence of frequency on fatigue crack growth is demonstrated; fatigue cracks grow faster at frequency of 30 Hz than at 20 kHz.

By simply assuming Paris law behavior, the fatigue crack growth rate, *da/dN*, is related to the stress intensity factor range, ΔK, by the power law relationship

$$\frac{da}{dN} = C(\Delta K)^m \tag{4.1}$$

where *C* and *m* are constants, which are influenced by such variables as material microstructure, environment and temperature (both of which could promote an effect of cyclic load frequency and waveform), and load ratio. The estimated values of *C* and *m* for fatigue crack growth at 20 kHz and 30 Hz are listed in Table 4.3.

Table 4.3 Constants in Paris law for fatigue crack growth at 20 kHz and 30 Hz at 20°C

Frequency	C	*m*
20 kHz	10^{-11}	4.7
30 Hz	5×10^{-11}	4.9

For cast aluminum alloys, the crack initiation life can be assumed to be negligible and the total fatigue life is dominated by crack propagation. Therefore, integrating the crack growth relation provides the propagation life, which is equivalent to the number of cycles necessary to cause failure for pore-containing alloys. Here, the initial crack length is assigned the mean value of initiation pore size (300 μm) and the final crack length is assigned the value of 2 mm based on experimental observations. It can be seen from Table 4.3 that the value of *C* at 20 kHz is five times greater than the value at 30 Hz, while

the values of *m* are similar for 20 kHz and 30 Hz. This leads to the prediction that the fatigue life at 20 kHz is approximately five times longer than the fatigue life at 75 Hz at an equivalent level of stress amplitude. The predicted S-N behavior at 20 kHz and 75 Hz is presented and compared with the experiment results in Figure 4.11. The magnitude of the predicted differences in fatigue life at 20 kHz and 75 Hz agrees reasonably well with the experimental observations in the lifetime regime of $<10^7$ cycles. Beyond 10^7 cycles, an apparent fatigue limit occurs. Since the fatigue limit is caused by non-propagating cracks, it can not be predicted based on the crack growth relations, but can be correlated with fatigue crack growth threshold. This issue is addressed in Chapter 5.

For E319 cast aluminum alloys, fatigue cracks readily initiate from pores of similar size, regardless of loading frequency. When the cracks grow, the number of cycles required to cause failure is determined by the crack growth rate. The crack growth rate at ultrasonic frequency is lower than at conventional frequency and this in turn results in longer fatigue life at ultrasonic frequency in the lifetime regime of $<10^7$ cycles. The observed effect of frequency on the fatigue crack growth rate and therefore fatigue life of E319 cast aluminum alloy is more likely attributable to an environmental effect. For aluminum alloys, the presence of water vapor in the atmospheric air has been shown to have a deleterious effect on the fatigue behavior. It has been widely confirmed that water vapor can increase fatigue crack growth rate and decrease the threshold stress intensities, thereby, speeding the fatigue failure of structural components [38, 40, 55-62, 68]. Testing at lower frequency in air is presumed to be more damaging, as there is more time to accumulate environmental damage per cycle and the crack growth rate can be accelerated when the crack tip interacts with the environment. The effect of environment on fatigue performance of E319 cast aluminum alloy is discussed in Section 4.2.

Beyond 10^7 cycles, the existence of an apparent fatigue limit was demonstrated, and is believed to result from non-propagating cracks of which the driving force for crack growth is below a threshold [8, 14]. It can be seen from Figure 4.10 that the threshold of

fatigue crack growth at 20 kHz occurs at approximately 1.2 MPa-$m^{1/2}$. At this stress intensity factor range, crack growth rate at 30 Hz is decelerated to below 10^{-11} m/cycle. For E319 cast aluminum alloy, fatigue crack growth threshold in air is deduced to be approximately the same at 20 kHz and 30 Hz. This is consistent with the results reported for some wrought aluminum alloys [51, 52], where the fatigue crack growth threshold in air is not influenced by testing frequency, although it is decreased compared to that in vacuum. One possible reason for this phenomenon is that the fatigue crack growth threshold is sensitive to the environment, but not influenced by the cycle by cycle interaction between the alloy and the environment. Therefore, the fatigue crack growth threshold is not sensitive to the loading frequency. In addition, it is possible that the fatigue crack growth process in the threshold regime is an intermittent, rather than a cycle by cycle process [51]. This extends the time that water can interact with the crack tip from one to several load cycles and decrease the sensitivity of fatigue crack growth rate to the loading frequency. As such, the fatigue limit, which is closely associated with the threshold stress intensity for crack growth, can be expected to be independent of testing frequency. Therefore, for N $>10^7$ cycles, the effect of frequency on fatigue life is substantially reduced.

4.2 Effect of environment on fatigue behavior at room temperature

4.2.1 Experimental observations

To quantify the effect of water on the fatigue behavior of E319 cast aluminum alloy at room temperature, pore-containing specimens were tested at 20 kHz in various environments with different water content, e.g. distilled water, water vapor with 100% relative humidity (RH) and dry air with RH of 0.1~0.2% The S-N results are shown in Figure 4.12. It was found that the fatigue life is indeed influenced by the environment at ultrasonic frequency. Distilled water significantly decreased the fatigue lives at 20 kHz and the S-N data in distilled water at 20 kHz are close to the S-N curve at 75 Hz in air.

On the other hand, 100% RH water vapor appears to have only a moderate influence on the fatigue lives.

To determine if the decreased fatigue life in a moist environment is attributable to an increased fatigue crack growth rate, small crack growth experiments were conducted in different environments at 20 kHz and in ambient air at different frequencies.

As shown in Figure 4.13, at 20 kHz, crack growth rate was increased by increasing the water content in the environment. Here, two tests were conducted in water, two tests were conducted in ambient air and one test was conducted in dry air. The crack growth curves for water and ambient air were generated based on the combined data, respectively. In the examined stress intensity factor range from 1 to 4 MPa-$m^{1/2}$, the crack growth rates in dry air (water vapor partial pressure of less than 5 Pa) fall in the range from 10^{-12} to 10^{-9} m/cycle; the crack growth rates in ambient air (water vapor partial pressure of 935 Pa) fall in the range from 10^{-11} to 10^{-8} m/cycle; the crack growth rates in liquid water (water pressure assumed to be 10^{5} Pa) fall in the range from 10^{-10} to 10^{-8} m/cycle. The crack propagation curves for dry air and ambient air are essentially parallel and the crack growth rates in ambient air are approximately 10 times higher than the crack growth rates in dry air. The crack propagation curve for distilled water has a lower slope. The crack growth rates in water are more than 10 times higher than the crack growth rates in ambient air at low stress intensity levels and the difference in crack growth rates becomes smaller at high stress intensity levels.

In ambient air, the crack growth rate was also increased by decreasing the testing frequency, as shown in Figure 4.14. Here, two tests were conducted at 20 kHz, one test was conducted at 30 Hz and one test was conducted at 1 Hz. The crack growth curve for 20 kHz was generated based on the combined data. When stress intensity factor range increased from 1 to 4 MPa-$m^{1/2}$, the crack growth rates at 20 kHz increase from 10^{-11} to 10^{-8} m/cycle and the crack growth rates at 30 Hz and 1 Hz increase from 10^{-10} to 10^{-7} m/cycle. At 30 Hz, the initial deceleration of crack growth rates is believed to arise from

small crack growth behavior. The crack propagation curves at 20 kHz, 30 Hz and 1 Hz are essentially parallel. The crack growth rates for 30 Hz and 1 Hz are very similar and both of them are approximately five times higher than the crack growth rate at 20 kHz. The crack growth rate at 1 Hz is slightly lower than the crack growth rate at 30 Hz, which might be caused by the scatter of crack growth rate from specimen to specimen. From Figure 4.13 and Figure 4.14, it is expected that high water vapor pressure and low cyclic frequency have similar effects on crack growth rates.

4.2.2 Mechanisms of environmental effect

As reviewed in Section 2.4.2.2, the possible mechanisms involved in the environmental effect on fatigue crack growth in aluminum are: crack tip blunting arising from slip processes, adsorption assisted cracking and hydrogen assisted cracking [40]. In this section, the mechanisms of the influence of hydrogen and associated gas (H_2O) are investigated in detail for E319 cast aluminum alloy based on the model proposed by Wei and co-workers [38, 68].

In the model proposed by Wei and co-workers [38, 68], the processes for the increase of fatigue crack growth rates in the presence of water vapor are described in three steps: first, water molecules migrate to the crack tip by impeded molecular transport, i.e. Knudsen flow [116]; second, water reacts with aluminum on the freshly formed fatigue crack surface and hydrogen atoms form from the dissociation reaction; third, hydrogen atoms diffuse from the crack surface to the crack tip plastic zone, causing hydrogen-assisted cracking. These three steps operate in sequence, and the crack growth response is governed by the slowest process in the sequence. To determine which step is the rate-limiting process, the time needed for each step can be roughly estimated as follows:

Assume that the water vapor partial pressure in ambient air is 935 Pa (equivalent to 40% R. H.), and a stress amplitude of 95 MPa is applied to an E319 cast aluminum

specimen with a small surface crack (a = 300 μm). The time needed for 10^{-11} mol water vapor molecules to migrate to the crack tip by Knudsen flow [116], t_1, can be estimated by:

$$t_1 = \frac{N}{JA} = \frac{N}{\frac{P}{\sqrt{2\pi MRT}} 2a \frac{4\sigma a}{E}} = 5\times10^{-3} \text{ sec} \tag{4.2}$$

where N is the amount of water vapor molecules (10^{-11} mol), J is the flux of water molecules through a fatigue crack, A is the area of the crack opening, P is the water vapor partial pressure, M is the molecular weight of water, R is the gas constant, T is temperature, a is half crack length, σ is stress amplitude, E is the Young's modulus.

The time needed for 10^{-11} mol water vapor molecules to react with the fresh fracture surface, t_2, can be estimated by assuming first order reaction:

$$t_2 = -\frac{1}{4k_c}(\ln N_f - \ln N_0) = 6\times10^{-4} \text{ sec} \tag{4.3}$$

where k_c is the reaction rate constant for water-aluminum reaction (of the order 10^3 s^{-1} [117]), N_f is the amount of the remaining water vapor molecules (assuming $N_f = 10^{-12}$ mol), N_0 is the original amount of the water vapor molecules (10^{-11} mol).

The time needed for hydrogen atoms to diffuse to plastic zone, t_3, can be estimated by assuming that the hydrogen concentration profile ahead of the crack tip can be modeled by a steady-sate diffusion in a semi-infinite body with a fixed concentration source and that if the distance of diffusion exceeds the crack extension per cycle, hydrogen-assisted increase of crack growth rate will occur for the next cycle [118, 119].

$$t_3 = \frac{1}{D}\left(\frac{da/dN}{4}\right)^2 = 5\times10^{-6} \text{ sec} \tag{4.4}$$

where D is the diffusion coefficient (1.19×10^{-14} m^2/s [120]), da/dN is the crack growth rate (assuming $da/dN = 10^{-9}$ m/s).

By comparing t_1, t_2 and t_3, it can be seen that the time for migration of water molecules to crack tip is much longer than that for either surface reaction or hydrogen

diffusion. Therefore, migration of water molecules is the rate-limiting step. This is consistent with the results by Wei *et al.* [38, 68], i.e. for highly reactive gas-metal systems, such as water vapor and aluminum, hydrogen-assisted fatigue crack growth is controlled by the rate of transport of water molecules to the crack tip.

Based on the above analysis, we assume that:

1) Water vapor migrates from the bulk environment to the crack tip by Knudsen flow.

2) In each loading cycle, the fatigue crack length increases by a small amount (*da/dN*), and the newly created fatigue fracture surface near the crack tip is exposed to the environment. The newly created fracture surface prior to contact with the environment is termed fresh fracture surface.

3) Hydrogen atoms are produced by the reaction of water and aluminum on the fresh fracture surface during each loading cycle. The formation of hydrogen atoms and an oxide layer on a fresh aluminum surface can be described by

$$2Al + 4H_2O \rightarrow Al_2O_3 \bullet H_2O + 6H \tag{4.5}$$

4) Subsequently, hydrogen atoms diffuse to the plastic zone and increase the crack growth rate during the next loading cycle. The concentration of hydrogen atoms in the plastic zone is presumed to be equivalent to the concentration of hydrogen atoms produced on the fresh fracture surface. According to Equation 4.5, the concentration of hydrogen atoms is proportional to the concentration of water molecules.

5) The rate of fatigue crack growth in a deleterious environment, $(da/dN)_{tot}$, is the sum of two independent components, $(da/dN)_{mech}$ and $(da/dN)_{env}$.

$$(da/dN)_{tot} = (da/dN)_{mech} + (da/dN)_{env} \tag{4.6}$$

where $(da/dN)_{mech}$ is the fatigue crack growth rate in an inert environment (called pure-mechanical fatigue crack growth rate); $(da/dN)_{env}$ is the crack growth rate contribution from the environment. Therefore, for a given alloy at a given stress intensity factor range, $(da/dN)_{mech}$ is a constant and $(da/dN)_{env}$ varies, depending on the concentration of hydrogen atoms in the plastic zone.

6) When the entire fresh fracture surface has been reacted with water and a monolayer of hydrated oxide has formed, the maximum possible concentration of hydrogen is reached and the environmental effect becomes saturated, as shown schematically in Figure 4.15. Once saturation occurs, the concentration of hydrogen remains constant even though the concentration of water increases. Assuming that when saturation occurs a monolayer of atoms in the aluminum lattice has been reacted with water, the surface concentration of aluminum can be estimated to be 4×10^{-5} mol/m^2 based on Equation 4.7:

$$C_{Al} = \frac{d\rho_{Al}}{M_{Al}} \tag{4.7}$$

where d is the lattice constant of aluminum (4×10^{-10} m), ρ_{Al} is the density of aluminum (2.7×10^{6} g/m^3) and M_{Al} is the atomic weight of aluminum (27 g/mol). According to Equation 4.5, the concentrations of water and hydrogen at saturation are proportionally estimated to be 8×10^{-5} mol/m^2 and 1.2×10^{-4} mol/m^2, respectively.

8) When the environmental effect becomes saturated, the fatigue crack growth rate in environment, $(da/dN)_{tot}$, reaches the maximum value, which is denoted as saturated fatigue crack growth rates, $(da/dN)_{sat}$.

The concentration of hydrogen atoms produced in each loading cycle is an important parameter that determines the environmental contribution to the crack growth rate. The hydrogen concentration can be considered as a bridge that connects the influence of water on surface reaction kinetics and the resultant crack growth performance. However, the concentration of hydrogen is controlled not by hydrogen diffusion or the fracture surface reaction but by transport of water to the crack tip. To quantify the concentration of hydrogen, the concentration of water available on the fresh fracture surface has to be determined and this value is limited by the molecular flow (Knudsen flow [116]) of water vapor from the surrounding environment to the crack tip.

Knudsen flow [116] describes situations in which gas molecules collide more frequently with flow boundaries than with other gas molecules. It is encountered when the mean free path of gas molecules is of the order of the characteristic length scale of the flow field. The regime is of importance in situations involving very small length scales and/or very low gas density (large mean free path). The studies of Knudsen flow were conducted on the flow of gas molecules through a pinhole in the wall of a vessel [116]. As long as the hole is small enough that there is no bulk mass flow out the hole, the gas will leak out very slowly. Under these circumstances the number of molecules passing through the hole is determined by the product of the number of molecules entering the hole and the probability of a molecule which enters the hole passing through (i.e. not bouncing back out).

Consider a gas with a density of n (mol/m^3) at one side of a hole and a vacuum at the other side. The molecule flux J (mol/m^2) through the hole is given by:

$$J = wn\bar{C} \tag{4.8}$$

where, w is a dimensionless probability factor and is estimated to be 0.25 for an infinitesimally thin orifice [116]. $\bar{C}$ is the mean molecular speed (m/s) and is calculated using kinetic theory as:

$$\bar{C} = \sqrt{\frac{8RT}{\pi M}} \tag{4.9}$$

where R is the universal gas constant (8.314 J/mol/K), T is the temperature (K), and M is the molecular mass of water vapor (g/mol). The molecular density of gas can be estimated by:

$$n = \frac{P}{RT} \tag{4.10}$$

where P is the water vapor partial pressure (Pa).

Thus, the flux of water molecules through a fatigue crack can be estimated by:

$$J = \frac{1}{4}\sqrt{\frac{8RT}{\pi M}}\frac{P}{RT} = \frac{P}{\sqrt{2\pi MRT}} \tag{4.11}$$

For a semi-circular crack on the specimen surface shown in Figure 4.16, the number of molecules (mol) that transport through the crack to the crack tip during each loading cycle can be approximated as:

$$N = JAt = \frac{P}{\sqrt{2\pi MRT}}\delta(2a)\frac{1}{2f} \tag{4.12}$$

where A is the area of the crack opening ($A = \delta(2a)$), t is the time of crack opening during each loading cycle ($t = \frac{1}{2f}$), δ is the crack opening displacement (COD) (m), a is the half crack length (m), and f is the loading frequency (Hz).

The average concentration of water vapor (C_{H_2O}, in mol/m^2) on the fresh fracture surface can be estimated as:

$$C_{H_2O} = \frac{N}{2A'} = \frac{\delta}{a\sqrt{2\pi^3 MRT}}\frac{P}{f} \tag{4.13}$$

where A' is the area of the semi-circular fatigue crack ($A' = \frac{1}{2}\pi a^2$). Here, it is assumed that the water vapor molecules are uniformly distributed on the whole fracture surface; however, only the portion of water vapor molecules on the fresh fracture surface is involved in the reaction and the resultant environmental effect.

The crack opening displacement (COD), δ, can be estimated by [121]:

$$\delta = \frac{4\sigma_{\max} a}{E} \tag{4.14}$$

where σ_{max} is the maximum stress (MPa) and E is the Young's modulus (MPa).

By substituting Equation 4.14 for δ in Equation 4.13, the concentration of water vapor can be described as:

$$C_{H_2O} = \frac{4\sigma_{\max}}{E\sqrt{2\pi^3 MRT}}\frac{P}{f} \tag{4.15}$$

The concentration of hydrogen below saturation can be described as:

$$C_H = \frac{3}{2} C_{H_2O} = \frac{6\sigma_{\max}}{E\sqrt{2\pi^3 MRT}} \frac{P}{f} \tag{4.16}$$

Here, *(P/f)* is defined as water exposure, which describes the combined effect of water vapor partial pressure and cyclic frequency on the concentration of hydrogen.

Beyond saturation, the concentration of hydrogen remains 1.2×10^{-4} mol/m^2. Thus, the critical water exposure when saturation of hydrogen concentration occurs can be estimated by:

$$(\frac{P}{f})_s = 1.9\times10^{-3}\sqrt{T}\,\frac{E}{\sigma_{\max}} \tag{4.17}$$

At room temperature, when stress amplitude is 95 MPa, $(P/f)_s$ is estimated to be 26 Pa-s for water-aluminum system.

The estimated concentrations of water and hydrogen are plotted as a function of water exposure in Figure 4.17. It is shown that the concentration of water and hydrogen increases with water exposure until *P/f* = 26 Pa-s. Above *P/f* = 26 Pa-s, although the concentration of water still increases with water exposure, the concentration of hydrogen remains at the maximum value, which corresponds to a saturation of environmental effect when the entire fresh fracture surface has been reacted with water and a monolayer of hydrated oxide has been formed. Since the environmental contribution to the fatigue crack growth rate is determined by the hydrogen concentration, it can be assumed that the dependence of the fatigue crack growth rate in environment on water exposure will be similar to the dependence of hydrogen concentration on water exposure.

The experimentally observed dependence of crack growth rate of E319 at constant ΔK of 2 MPa-m$^{1/2}$ on water exposure is shown in Figure 4.18. It can be seen that crack growth rates increase with water exposure, and then become essentially independent of water exposure, indicating a saturated environmental effect. The water partial pressure (*P*) was calculated using 4.18.

$$P = P_s \times RH \tag{4.18}$$

where P_s is the saturation water partial pressure in ambient air (P_s=2338 Pa) and RH is the relative humidity.

Here, the relative humidity in laboratory air is measured to be approximately 40%. In this study, the pressure of liquid water was assumed to be 10^5 Pa. However, it should be pointed out that there is no agreement in the literature about this value during fatigue testing; the actual water pressure around the fatigue crack during cyclic loading could be less than 10^5 Pa. The water vapor pressure in dry air was controlled below 5 Pa. The calculated water exposure in each environmental condition is summarized in Table 4.4.

Table 4.4 Calculated water exposure in various environments

	f (Hz)	P (Pa)	P/f (Pa-s)
Dry air	20,000	5	2.5×10^{-4}
Lab air	20,000	935	0.05
Water	20,000	10^5	5
Lab air	30	935	31
Lab air	1	935	935

Interestingly, the dependence of fatigue crack growth rate on water exposure closely follows the assumed dependence of hydrogen concentration on water exposure. This is shown in Figure 4.18, where $C(H)$ is calculated based on Equation 4.16. The observed saturated environmental effect on crack growth rate and the estimated saturated concentration of hydrogen occur at approximately the same water exposure (P/f = 26 Pa-s). This correlation strongly supports the assumption that the increase in crack growth rate caused by environment is determined by the concentration of hydrogen produced by the crack tip surface reaction with water vapor. $(P/f)_s$ denotes the condition of saturated environmental effect under which there is sufficient time to fully react the new crack surfaces with the environment before the next increment of crack growth. $(P/f)_s$ is thus

termed as saturation water exposure and it represents saturated environmental effect on both hydrogen concentration and fatigue crack growth rate.

4.2.3 Fractography of E319 cast aluminum alloy in environment

Fractographic examination of the fatigue specimens of E319 cast aluminum alloy in environments with different water exposure at room temperature were examined using SEM. The fatigue fracture surfaces at ΔK of approximately 2.5 MPa-$m^{1/2}$ in these environments are shown in Figure 4.19. Figure 4.19 (a) and (b) represent the fracture surface at 20 kHz in dry air. Since the water exposure is very low in this condition, fatigue crack growth behavior can be considered as pure-mechanical. Figure 4.19 (c) and (d) represent the fracture surface at 20 kHz in ambient air, corresponding to hydrogen-assisted crack growth behavior with moderate environmental effect. Figure 4.19 (e) and (f) represent the fracture surface at 20 kHz in liquid water, corresponding to hydrogen-assisted crack growth behavior with significant environmental effect. Figure 4.19 (g) through (j) represent the fracture surface at low frequency (30 Hz and 1 Hz) in air, corresponding to the fatigue crack growth behavior at saturated environmental effect.

Surprisingly, although the crack growth rates were observed to be influenced by water exposure, the fatigue fracture surfaces do not exhibit obvious differences in morphology for various environments. In all cases, the fracture surfaces are generally normal to the loading axis. Crystallograhic features that were reported for some aluminum alloys that exhibit planar slip in [73] are not observed. This is consistent with the observations that fatigue crack growth in over-aged aluminum alloys favors a wavy slip mode and exhibites conventional stage II propagation [101].

At low magnification, the fracture surfaces are characterized by a large number of transgranular facets and “riverlines”. At high magnification, the striation-like features are observable. These striation-like features look finer for the cases of fatigue crack growth with small or moderate environmental effect (Figure 4.19 (b) and (d)) than those for the

cases of fatigue crack growth with significant environmental effect (Figure 4.19 (f), (h) and (j)). Three possible mechanisms for hydrogen assisted cracking have been proposed: [39]: hydrogen-enhanced decohesion (HEDE), adsorption induced dislocation emission (AIDE) and hydrogen enhanced localized plasticity (HELP). However, it is not possible to determine which mechanism is operative in the current study of the fracture surface morphologies. The subtle change of fracture surface morphology with water exposures indicates that although the fatigue propagation behavior is influenced by water exposure, the response of fatigue crack growth rate to the water exposure or hydrogen concentration for the investigated E319-T7 cast aluminum alloy is not as significant as those aluminum alloys which exhibited obvious morphology change of fracture surface in different environments.

4.2.4 Modeling of environmental effect

As discussed in Section 2.4.2.2, the fatigue crack growth response can be quantified by the superposition model proposed by Wei and co-workers [38, 68]. At a constant ΔK, the fatigue crack growth rate in environment, $(da/dN)_{tot}$, is the sum of the pure mechanical fatigue crack growth rate, $(da/dN)_{mech}$, and the environmetal contribution to the fatigue crack growth rate, $(da/dN)_{env}$. Here, $(da/dN)_{mech}$ is assumed to be independent of environment. When the saturation of environmental effect occurs, $(da/dN)_{tot}$ reaches its maximum value, which is termed the saturation fatigue crack growth rate, $(da/dN)_{sat}$. The dependence of fatigue crack growth rate in environment can be described by [38, 68]:

For $(\frac{P}{f}) < (\frac{P}{f})_s$:

$$(\frac{da}{dN})_{tot} = (\frac{da}{dN})_{mech} + (\frac{da}{dN})_{env} \tag{4.19}$$

$$(\frac{da}{dN})_{env} = [(\frac{da}{dN})_{sat} - (\frac{da}{dN})_{mech}]\frac{(P/f)}{(P/f)_s} \tag{4.20}$$

For $(\frac{P}{f}) \geq (\frac{P}{f})_s$:

$$(\frac{da}{dN})_{tot} = (\frac{da}{dN})_{sat} \tag{4.21}$$

Here, $(P/f)_s$ is estimated to be 26 Pa-s at stress amplitude of 95 MPa at room temperature from Equation 4.17. The environmental contribution to the fatigue crack growth rate is determined by $(da/dN)_{mech}$, $(da/dN)_{sat}$, P/f and $(P/f)_s$. The values of $(da/dN)_{mech}$ and $(da/dN)_{sat}$ can be estimated based on the experimental observations in Figure 4.18. At a constant ΔK of 2 MPa-$m^{1/2}$, $(da/dN)_{mech}$ was assumed to be 10^{-11} m/cycle, which is equivalent to the crack growth rate in dry air at 20 kHz where the environmental effect is very small and the crack growth can be reasonably considered as "pure-mechanical". $(da/dN)_{sat}$ was assumed to be 10^{-9} m/cycle, which is the average fatigue crack growth rate in ambient air at 30 Hz and 1 Hz where the environmental effect is saturated.

The predicted dependence of crack growth rate on water exposure based on the superposition model (Equation 4.19 through 4.21), with $(da/dN)_{mech}$=10^{-11} m/cycle and $(da/dN)_{sat}$=10^{-9} m/cycle, is shown in Figure 4.20. The predicted crack propagation curve exhibits a strong curvature at water exposure of 10^{-1} Pa-s; below this point, fatigue crack growth rates are not sensitive to water exposure and above this point, the fatigue crack growth rates increase abruptly with increasing water exposure until the environmental effect becomes saturated. However, the experimental results do not show such a sudden change of dependence of fatigue crack growth rate on water exposure. The prediction, therefore, does not agree well with the experimental observations. One possible reason is that in the superposition model, $(da/dN)_{env}$ is simply assumed to be linearly related to concentration of hydrogen, and therefore linearly related to water exposure. However, in the present study, $(da/dN)_{env}$ was found to be better described by the square root of the hydrogen concentration, as shown in Figure 4.21. Here, $(da/dN)_{env}$

was estimated according to Equation 4.19, based on the experimentally measured $(da/dN)_{tot}$ and the assumption that $(da/dN)_{mech}$ is equivalent to the crack growth rate in dry air at 20 kHz. The concentration of hydrogen for each environment was estimated based on Equation 4.16. It was also found that the square root correlation between $(da/dN)_{env}$ and hydrogen concentration fits the data better than other simple mathematic relations, e.g. logarithmic, exponential and polynomial.

The square root correlation suggests that the response of fatigue crack growth rate in E319-T7 cast aluminum alloy to water exposure is less significant than presumed in the superposition model, which has successfully modeled fatigue crack growth rate for some peak-aged (T6) aluminum alloys [38, 68]. In other words, the role of hydrogen concentration in increasing of fatigue crack growth rates might be different for T7 and T6 heat treated aluminum alloys. T6 heat treatment promotes localized plastic deformation within a single-slip system in each grain along the crack front, while T7 heat treatment favors a wavy slip mechanism [101]. In ambient air, the single-slip mechanism, which is operative in the peak-aged alloy, is assumed to offer a preferential path for hydrogen assisted cracking, which leads to a stronger environmental effect.

As such, for E319-T7, the superposition model was then modified as:

For $(\frac{P}{f}) < (\frac{P}{f})_s$:

$$(\frac{da}{dN})_{tot} = (\frac{da}{dN})_{mech} + [(\frac{da}{dN})_{sat} - (\frac{da}{dN})_{mech}]\sqrt{\frac{(P/f)}{(P/f)_s}} \tag{4.22}$$

For $(\frac{P}{f}) \geq (\frac{P}{f})_s$:

$$(\frac{da}{dN})_{tot} = (\frac{da}{dN})_{sat} \tag{4.23}$$

The predicted crack growth response at a constant ΔK of 2 MPa-$m^{1/2}$ as a function of water exposure based on the modified superposition model is shown in Figure 4.22. It can be seen that the predicted fatigue crack propagation curve gradually increases with

increasing water exposure, which agrees reasonably well with the experimental results. The predicted crack growth rate at 20 kHz in ambient air is still lower than the experimentally measured crack growth rate. The possible reason for this inconsistency is that the COD used in this model does not take into account of the effect of geometry and thus the calculated COD is possibly smaller than the actual value. When COD is small, $(P/f)_s$ is large and $(da/dN)_{env}$ is small (see Equation 4.13 and 4.22). Despite this limitation, for the purpose of studying the environmental effect on fatigue crack propagation of E319 cast aluminum alloy, we have assumed the applicability of this modified superposition model as the basis for modeling hydrogen assisted fatigue crack growth behavior.

At all levels of ΔK, $(da/dN)_{mech}$ and $(da/dN)_{sat}$ can be estimated by assuming Paris law:

$$(da/dN)_{mech} = C_1(\Delta K)^{m_1} \tag{4.24}$$

$$(da/dN)_{sat} = C_2(\Delta K)^{m_2} \tag{4.25}$$

where C_1, m_1 correspond to the fatigue crack growth rates in dry air at 20 kHz ($C_1 = 2\times 10^{-13}$, m_1=5.9) and C_2, m_2 correspond to the average fatigue crack growth rates in ambient air at 30 Hz and 1 Hz ($C_2 = 5\times 10^{-11}$, $m_2 = 4.5$). By incorporating Paris law (Equation 4.24 and 4.25) and $(P/f)_s$ (Equation 4.17) into the modified superposition model, the effect of environment on crack growth rates at all levels of stress intensity range, ΔK, can be estimated by:

For $(\frac{P}{f}) < (\frac{P}{f})_s$:

$$(\frac{da}{dN})_{tot} = C_1(\Delta K)^{m_1} + 23\times[C_2(\Delta K)^{m_2} - C_1(\Delta K)^{m_1}]\sqrt{\frac{\sigma_{\max}}{E\sqrt{T}}\frac{P}{f}} \tag{4.26}$$

For $(\frac{P}{f}) \geq (\frac{P}{f})_s$:

$$(\frac{da}{dN})_{tot} = C_2(\Delta K)^{m_2} \tag{4.27}$$

The predicted environmental effect on crack growth rates is shown in Figure 4.23. $(da/dN)_{mech}$ represents the fatigue crack growth rate without environmental effect and $(da/dN)_{sat}$ represents the fatigue crack growth rate with maximum environmental effect. Therefore, $(da/dN)_{mech}$ and $(da/dN)_{sat}$ can be considered as the lower bound and upper bound of crack growth rates in environment. In other words, crack growth rates under any water exposure would fall in the range from $(da/dN)_{mech}$ to $(da/dN)_{sat}$. The extent of the environmental effect on crack growth rate is determined by water exposure, *P/f,* at a given temperature and a given stress. At 20 kHz in ambient air (Figure 4.23 (a)), $(da/dN)_{tot}$ are approximately 5 to 10 times of $(da/dN)_{mech}$, suggesting that environment plays an important role in crack growth behavior. $(da/dN)_{tot}$ is more than 10 times lower than $(da/dN)_{sat}$, indicating that the environmental effect is far from saturated for fatigue testing in ambient air at 20 kHz. At 30 Hz in ambient air, (Figure 4.23 (b)), the environmental effect is saturated and $(da/dN)_{tot}$ reaches the upper bound. At 20 kHz in dry air (Figure 4.23 (c)), the environmental effect is so small that the crack growth rate in dry air is close to $(da/dN)_{mech}$.

The predicted crack growth response in environments based on the modified superposition model agrees well with the experiment results, as shown in Figure 4.24. In Figure 4.24 (a), the crack growth rates in ambient air at 20 kHz and 30 Hz are examined. The predicted crack propagation curve at 30 Hz in ambient air is actually the regression crack growth curve at 30 Hz and 1 Hz, which represent saturation fatigue crack growth rate. The predicted crack growth rates at 20 kHz in ambient air generally agrees with the experimental results, although the crack growth rates are modestly underpredicted. In Figure 4.24 (b), the crack growth rates at 20 kHz in various environments with different water content are examined. The predicted crack propagation curve at 20 kHz in dry air is essentially same as the regression crack growth curve at 20 kHz in dry air, which represents pure-mechanical fatigue crack growth. The predicted crack growth rates at 20 kHz in liquid water generally agrees with the experimentally measured crack growth rates,

which are close to the regime of saturated environmental effect. The experiment result of crack growth at 20 kHz in water vapor with 100% RH is not available, however, based on the prediction, the crack growth rates in this condition are expected to be close to but slightly greater than the crack growth rates in ambient air.

At a given stress level, integration of the crack growth relation in Equation 4.26 and 4.27 provides the fatigue propagation life, which is equivalent to the total fatigue life for pore-containing alloys. As such, S-N behavior in environments with different water exposure can be predicted (Figure 4.25). Here, the initial crack length is assigned the mean value of initiation pore size (300 μm) and the final crack length is assigned the value of 2 mm. The modified superposition model successfully predicted the effect of environment on S-N response. In Figure 4.25 (a), although the fatigue lives at 20 kHz in ambient air are modestly overestimated by the model, the magnitude of predicted differences in fatigue lives between 20 kHz and 75 Hz generally agrees with the experimental observations. In Figure 4.25 (b), the predicted fatigue lives at 20 kHz in ambient air are only slightly longer than predicted fatigue lives in 100% RH water vapor and both of them are significantly longer than the predicted fatigue lives in liquid water. The magnitude of predicted difference in fatigue lives in environments agrees well with the experimental observations. The S-N response in dry air has not been determined, however, fatigue lives in dry air are expected to be approximately 10 times longer than fatigue lives in ambient air based on the prediction.

Now it is clear that an effect of frequency on fatigue crack growth and thus the fatigue life can be expected when E319 cast aluminum alloy is tested in ambient air at ultrasonic frequency (20 kHz) and conventional frequency (10-100 Hz). Fatigue crack growth rates increase with increasing water exposure and then become independent of water exposure when environmental effect becomes saturated. In ambient air, fatigue testing at 20 kHz represents water exposure of 0.05 Pa-s. In this condition, hydrogen assisted increase of fatigue crack growth rate would occur, but the extent of

environmental effect on crack growth rate is moderate because the water exposure in this condition is well below the exposure for saturated environmental effect. On the other hand, fatigue testing at conventional frequency (10 ~100 Hz) represents water exposure of 9~94 Pa-s, which is within or very close to the regime of saturated environmental effect. Since ultrasonic fatigue in ambient air represent less water exposure than conventional fatigue, the concentration of hydrogen responsible for an increase in crack growth rate is less and, thus, the environmental contribution to the fatigue crack growth rate at ultrasonic frequency is lower than that at conventional frequency. The observed fatigue crack growth rate is assumed to be the sum of the pure-mechanical fatigue crack growth rate and the environmental contribution to the fatigue crack growth rate. Therefore, the observed crack growth rate at ultrasonic frequency is lower than that at conventional frequency. Because of the lower crack growth rate at ultrasonic frequency, fatigue life at ultrasonic frequency is longer than fatigue life at conventional frequency.

The correlation of fatigue crack growth rate with water exposure provides a method to account for the influence of frequency that is caused by an environmental effect. Crack growth behavior in vacuum (very low water exposure) and in air at low testing frequency (very high water exposure) can be treated, respectively, as the lower bound and the upper bound of crack growth rates in environment. With these two bounds as references, crack growth rates at any given frequency or water partial pressure can be estimated from Equation 4.26 and 4.27. When specimens are tested at 20 kHz in laboratory air, the relative humidity might fluctuate from 20% to 90%. In this case, the water exposure varies from 0.02 to 0.1 Pa-s and the corresponding crack growth rate changes within a factor of 2. When specimens are tested at 30 Hz in laboratory air, water exposure varies from 16 to 70 Pa-s and the fatigue crack growth rates are close to the saturation fatigue crack growth rate when the relative humidity fluctuates from 20% to 90%. Therefore, at both ultrasonic frequency and conventional frequency, fluctuation of humidity in laboratory air does not significantly influence the fatigue crack growth results.

When the lower bound and the upper bound of fatigue crack growth rates are known, the environmental contribution to the fatigue crack growth rate as a function of water exposure, temperature, maximum stress and Young's modulus can be estimated. When other parameters are constant, crack growth rate at higher maximum stress would be higher because the crack opening displacement would be larger and the environmental effect would be larger. Although the dependence of crack growth rate on maximum stress is subtle in the predicted S-N response shown in Figure 4.25, it can help understand the experimental observation that the difference in fatigue lives between 20 kHz and 75 Hz in ambient air decreases with decreasing stress amplitudes.

In the study by Engler-Pinto Jr. *et al.* [23, 114] it was reported that the higher the yield strength, the greater the influence of the water on crack propagation for some cast Al-Si alloys. This is possibly because that the higher yield strength is obtained from peak-aged (T6) heat treatment and the peak-aged aluminum alloy was found to be more sensitive to environmental effect than the over-aged alloy [101]. For these peak-aged alloys, the superposition model proposed by Wei and co-workers [38, 68] would give a better prediction about the effect of frequency on fatigue crack growth rate. As shown in Figure 4.20, by assuming a linear correlation between $(da/dN)_{env}$ and hydrogen concentration, the fatigue crack growth rates in ambient air at 20 kHz and 30 Hz differ by two orders of magnitude.

Since the crack growth rate in environment, $(da/dN)_{tot}$, is a function of temperature and Young's modulus when other parameters are constant, this model is also applicable for predicting environmental effect at elevated temperature. This issue is addressed in section 4.3.4.

4.3 Effect of temperature on fatigue behavior

4.3.1 S-N results at elevated temperature

The S-N behavior observed at 20, 150 and 250^{o}C using the ultrasonic fatigue

technique is shown in Figure 4.26. The S-N curves represent the mean fatigue lives, which correspond to 50% failure probability based on the random fatigue limit (RFL) model. At 20°C, the S-N curve shows a plateau beyond 10^7 cycles, indicating that an apparent fatigue limit exists. At elevated temperatures, however, the S-N curves continue to drop beyond 10^7 cycles and the slope of the curves increase with temperature.

Table 4.5 Estimated fatigue strength at 10^7 cycles and 10^8 cycles of E319 cast aluminum at 20, 150 and 250°C and at frequencies of 20 kHz and 75 Hz based on RFL model

Frequency (Hz)	Fatigue strength (MPa)			
		20°C	150°C	250°C
20,000	at 10^7 cycles	89	81	67
	at 10^8 cycles	84	77	58
75	at 10^7 cycles	87	68	58
	at 10^8 cycles	82	63	48

As shown in Figure 4.26, increasing temperature from 20 to 150°C resulted in a modest decrease in fatigue resistance, while a significant decrease in fatigue resistance was observed at 250°C, especially in the very high cycle regime (10^8 cycles). The estimated fatigue strength at 10^7 cycles and 10^8 cycles at each temperature was summarized in Table 4.5 based on the RFL model. Increasing temperature from 20 to 150°C results in a reduction of 7 MPa in fatigue strength at 10^8 cycles from 84 MPa to 77 MPa. At 250°C, the fatigue strength at 10^8 cycles further decreases to 58 MPa, an additional reduction of 19 MPa as compared with that at 150°C. The dependence of fatigue strength on temperature followed the same trend as the temperature dependence of yield and tensile strength (Figure 4.27). In the present study, fatigue strength remains approximately 0.4 to 0.5 of yield strength and 0.3 to 0.4 of ultimate tensile strength at each temperature investigated. These results are consistent with previous results on elevated temperature fatigue behavior of cast aluminum alloys. Engler-Pinto Jr. *et al.* [1] found a modest decrease in fatigue resistance from 20 to 150°C for E319-T7 aluminum alloy in the lifetime regime of 10^3~10^7 cycles using servo-hydraulic testing equipment at cycling frequency of 40 Hz. Mayer *et al*. [74] found that for a high-pressure die-casting

Al-Si-Cu aluminum alloy, fatigue strength at 10^9 cycles decreased from 75 MPa to 61 MPa by increasing the testing temperature from 20 to 150^{o}C.

4.3.2 Effect of frequency on fatigue behavior at elevated temperature

For comparison, the S-N data of E319 cast aluminum alloy at elevated temperatures were generated at 75 Hz. As shown in Figure 4.28, the fatigue resistance decreased with increasing temperature, which is similar to the trend observed at a testing frequency of 20 kHz. Increasing temperature from 20 to 150^{o}C, the fatigue resistance decreases modestly at high stress amplitude. At low stress amplitude, the decrease of fatigue resistance becomes significant as temperature increases from 20 to 150^{o}C. The estimated fatigue strength at 10^7 cycles and 10^8 cycles at 150 and 250^{o}C for 75 Hz were also listed in Table 4.5. At 75 Hz, decrease of fatigue strength at 10^8 cycles from 20 to 150^{o}C is more significant than the decrease of fatigue strength at 10^8 cycles from 150 to 250^{o}C.

The ultrasonic fatigue S-N results at 150 and 250^{o}C are compared to those at frequency of 75 Hz Figure 4.29 (a) and (b). At elevated temperature, fatigue life at 20 kHz is longer than that at 75 Hz, and the difference between these two frequencies persists over the entire stress range examined. As compared in Table 4.5, at 150^{o}C, the fatigue strength at 10^8 cycles at 75 Hz is 14 MPa lower than that at 20 kHz. At 250^{o}C, the fatigue strength at 10^8 cycles at 75 Hz is 10 MPa lower than the value determined at 20 kHz.

4.3.3 Crack initiation at elevated temperature

Fractographic analysis shows that at elevated temperature the initiation sites are predominantly shrinkage pores, which is similar to the observations at room temperature. This is consistent with previously published fatigue investigations on cast aluminum alloys [7, 11, 27, 82, 83]. The fatigue crack initiation sites are summarized in Table 4.6 for specimens tested at 20 kHz at both room temperature and elevated temperature.

Table 4.6 Characterization of fatigue crack initiation sites in specimens at 20 kHz at temperature of 20, 150 and 250°C

Temperature (°C)	Number of failed specimens				
	Surface pore	Interior pore	Planar facet	Oxide particle	Subtotal
20	25	2	0	0	27
150°C	20	0	3	0	23
250°C	21	2	2	1	26
Total	66 (87%)	4 (6%)	5(6%)	1(1%)	76

At 150°C, in 20 of the 23 specimens, the fatigue cracks have initiated from pores located at or near to the specimen surface (Figure 4.30 (a)). In the remaining three examined specimens, fatigue cracks initiated from large planar features, as shown in Figure 4.30 (b). The fracture surface reveals a smooth facet at an orientation of approximately 45 degrees to the loading direction. In these cases, the specimens did not likely possess pores that were of sufficient size and located close to the specimen surface. Therefore, other features were the "weakest links" and initiated the fatal cracks. Similar findings in cast aluminum alloy were reported by other researchers [5, 103] and they concluded that this kind of crack initiation feature represented a shear plane that is a twin boundary and the crack initiation occurred at the surface with the formation of slip bands.

At 250°C, in 21 of the 26 specimens, the fatigue cracks have initiated from pores located at or near to the specimen surface (Figure 4.31 (a)). In two of the 26 specimens, fatigue cracks initiated from pores located in the specimen interior (Figure 4.31 (b)); Planar facets were also occasionally observed to act as crack initiation sites (Figure 4.31 (c)). In one failed specimen, cracks were found to nucleate from an oxide particle located at the specimen surface (Figure 4.31 (d)). In this case, the crack initiation site contains high levels of Mg, which is a strong indication of the presence of an oxide particle likely introduced during the casting process.

In the E319 cast aluminum alloy, at room temperature and elevated temperatures, near-surface microshrinkage pores were observed to be the majority (~ 87%) feature

causing initiation of a crack that ultimately caused failure. A small number (~ 6%) of the fatigue failures in specimens were initiated from large planar facets. An interesting phenomenon is that facet-initiated failures only occurred at elevated temperature. However, because of its low occurrence frequency in the investigated samples, the issue of crack initiation from facets at elevated temperature is not covered here in further detail.

Table 4.7 Initiation pore size at 20, 150 and 250°C at 20 kHz

20°C		150°C		250°C	
Mean (μm)	STDEV (μm)	Mean (μm)	STDEV (μm)	Mean (μm)	STDEV (μm)
313	-147/+278	289	-113/+187	257	-134/+282

The distribution of initiation pore size, in terms of mean value and standard deviation, are similar for various temperatures. Figure 4.32 shows the distribution of the initiation pore size, which can be described with a log-normal distribution function. The corresponding mean value and standard deviation of the initiation porosity population are summarized in Table 4.7. These results, together with the results of crack initiation pore sizes at different frequencies at room temperature (Table 4.2 and Figure 4.7), demonstrate that fatigue failure always occurs from the "weakest link" in the E319 cast aluminum alloy specimens under fully reversed loading condition.

4.3.4 Crack propagation at elevated temperature

Figure 4.33 presents the fatigue crack propagation at 20 and 250°C, at a frequency of 20 kHz. Fully reversed loading at a stress amplitude of 95 MPa was used for 20°C and 80 MPa was used for 250°C. In the investigated stress intensity range (1 to 4 MPa-$m^{1/2}$), a substantial increase of crack growth rates results from the increase of temperature. At equivalent stress intensity levels, the crack growth rates increase by approximately an order of magnitude when the temperature increases from 20 and 250°C.

Since the crack growth rates have been observed to be influenced by the presence

of water vapor in laboratory air, a question arises: is this effect of temperature on crack growth rates related to an intrinsic effect of temperature on the mechanical properties or to an effect of environment with increasing temperature? The modified superposition model provides a basis to separately investigate the intrinsic effect of temperature on fatigue crack growth behavior and the environment induced effect of temperature on fatigue crack growth behavior. When temperature increases, the pure-mechanical fatigue crack growth rates are expected to increase because of greater cyclic plasticity, greater accumulated fatigue damage and, thus, lower cyclic strength of aluminum alloys. The environmental contribution to the fatigue crack growth rates are also expected to change with increasing temperature. Based on Equation 4.26, the environmental contribution to the fatigue crack growth rate is proportional to $(\sqrt{E\sqrt{T}})^{-1}$. Therefore, $(da/dN)_{env}$ decreases with increasing temperature, which can be explained by the lower concentration of hydrogen available for environmental effect. At higher temperature, the molecular density of water vapor at a constant pressure is decreased due to volume expansion and the number of water vapor molecules that transport through the crack by Knudsen flow is decreased. Thus the concentration of water vapor and the concentration of produced hydrogen are decreased. On the other hand, Young's modulus decreases with increasing temperature and this will increase COD and in turn increase the concentration of hydrogen. Therefore, $(da/dN)_{env}$ is expected to decrease with increasing temperature, but the decrease is offset by the simultaneously decreased Young's modulus.

When the stress intensity factor range is normalized by Young's modulus and yield strength, the fatigue crack growth rates at 250^{o}C become close to those at 20^{o}C, as shown in Figure 4.34. This suggests that the difference of crack growth rates between 20 and 250^{o}C in air primarily results from the change of their mechanical properties with temperature. For this cast aluminum alloy, it was also determined that normalization of stress intensity factor range by Young's modulus only is not sufficient to make the crack growth rates at 20 and 250^{o}C fall in the same data band, indicating that Young's modulus

is not the only factor influencing the temperature effect on crack growth rates. Therefore, both Young's modulus and yield strength were used to account for the intrinsic temperature effect on mechanical properties. After normalization of stress intensity factor range by both factors, the crack growth rates at 250^{o}C in air are slightly lower than those at 20^{o}C, indicating that effect of environment on fatigue crack growth rates operates slightly differently for 20 and 250^{o}C, but environment clearly is not a significant accelerating factor at least at 20 kHz.

To examine the effect of frequency on fatigue propagation at elevated temperature, the crack growth rates in air at 20 kHz and 30 Hz at 250^{o}C are compared, as shown in Figure 4.35. It can be seen that at 250^{o}C the fatigue crack growth rate at 30 Hz is approximately 2 to 5 times greater than that at 20 kHz at an equivalent level of stress intensity. This is compared well to an order of magnitude effect of frequency at room temperature (Figure 4.10). Similar to the scenario at room temperature, the observed effect of frequency is still attributable to an environmental effect albeit a reduced influence. At elevated temperature, another possible time-dependant deformation mechanism is creep. However, for E319 cast aluminum alloy, the fatigue crack growth rates at elevated temperature do not appear to be influenced by creep-fatigue interaction. At 250^{o}C, the creep strain rate is on the order of 10^{-8} per second at stress levels of 60 to 80 MPa [1]. As such, strain caused by creep during each cycle is approximately 10^{-10} at conventional frequency and 10^{-13} at ultrasonic frequency. These values are far below the fatigue strain amplitude which is on the order of 10^{-3}.

4.3.5 Modeling the combined influence of temperature and frequency

To investigate the combined influence of temperature and frequency on crack propagation of E319 cast aluminum alloy, Equation 4.26 and 4.27 were modified as follows to take into account the effect of temperature on fatigue crack growth behavior.

For $(\frac{P}{f}) < (\frac{P}{f})_s$:

$$(\frac{da}{dN})_{tot} = C_1^{'}(\frac{\Delta K}{E\sigma_{ys}})^{m_1^{'}} + 23\times[C_2^{'}(\frac{\Delta K}{E\sigma_{ys}})^{m_2^{'}} - C_1^{'}(\frac{\Delta K}{E\sigma_{ys}})^{m_1^{'}}]\sqrt{\frac{\sigma_{\max}}{E\sqrt{T}}\frac{P}{f}} \qquad (4.28)$$

For $(\frac{P}{f}) \geq (\frac{P}{f})_s$:

$$(\frac{da}{dN})_{tot} = C_2^{'}(\frac{\Delta K}{E\sigma_{ys}})^{m_2^{'}} \qquad (4.29)$$

Where $C_1^{'}$, $m_1^{'}$ correspond to *(da/dN)$_{mech}$* after normalization of stress intensity factor range ($C_1^{'} = 5\times10^{29}$, $m_1^{'}$ =5.9) and $C_2^{'}$, $m_2^{'}$ correspond to *(da/dN)$_{sat}$* after normalization of stress intensity factor range ($C_2^{'} = 8\times10^{20}$, $m_2^{'} = 4.5$). In Equation 4.28, the second term on the right represents *(da/dN)$_{env}$*, i.e.

$$(\frac{da}{dN})_{env} = 23\times[C_2^{'}(\frac{\Delta K}{E\sigma_{ys}})^{m_2^{'}} - C_1^{'}(\frac{\Delta K}{E\sigma_{ys}})^{m_1^{'}}]\sqrt{\frac{\sigma_{\max}}{E\sqrt{T}}\frac{P}{f}} \qquad (4.30)$$

It would be helpful if *(da/dN)$_{mech}$* and *(da/dN)$_{sat}$* at 250^{o}C were known. However, this information is not available. So we assume that *(da/dN)$_{mech}$* and *(da/dN)$_{sat}$* obtained at room temperature applies for all temperatures after normalization of stress intensity factor range by Young's modulus and yield strength. i.e. at equivalent levels of $\Delta K/(E\sigma_{ys})$, $(\frac{da}{dN})_{mech}^{250^{o}C} = (\frac{da}{dN})_{mech}^{20^{o}C}$ and $(\frac{da}{dN})_{sat}^{250^{o}C} = (\frac{da}{dN})_{sat}^{20^{o}C}$. *(da/dN)$_{tot}$* is then determined by the term $\sqrt{\frac{\sigma_{\max}}{E\sqrt{T}}\frac{P}{f}}$.

Based on Equation 4.28 and 4.29, the effect of temperature on fatigue crack growth rates can be predicted. Figure 4.36 presents the predicted crack growth rates at 20 and 250^{o}C in air at 20 kHz, as a function of normalized stress intensity factor range. Here, *(da/dN)$_{mech}$* and *(da/dN)$_{sat}$* are assumed to be independent of temperature and serve as the lower bound and upper bound of fatigue crack growth rates. The crack growth rates in

environment fall within the bounds. After normalization of stress intensity factor range, the fatigue crack growth rate at 250°C in air is slightly lower than that at 20°C, This is because, according to Equation 4.30, $(da/dN)_{env}$ decreases with increasing temperature, however the decrease in $(da/dN)_{env}$ is offset by the decrease of Young's modulus. Therefore, $(da/dN)_{env}$ is not sensitive to the temperature change, which is consistent with the experimental observations. It is now clear that the effect on temperature on crack growth arises mainly from the effect of temperature on Young's modulus and yield strength. Environmental effect on crack growth rate decreases modestly with increasing temperature.

The effect of frequency on fatigue crack growth rate at elevated temperature can be modeled based on Equation 4.28 and 4.29. The effect of frequency at elevated temperature is still attributable to an environmental effect. When other parameters are constant, increasing testing frequency will decrease water exposure and this will decrease $(da/dN)_{env}$ and therefore $(da/dN)_{tot}$. The predicted fatigue crack growth rates at 250°C at testing frequency of 20 kHz and 30 Hz are presented in Figure 4.37. It can be seen that, at 250°C, the predicted crack growth rates at 20 kHz are approximately an order of magnitude lower than the predicted crack growth rates at 30 Hz. Comparison of experimental results to the model indicates that the predicted difference in crack growth rates between 20 kHz and 30 Hz is greater than the experimental observations, but the trend of greater crack growth rates at lower frequency agrees well with the experimental results.

Integrating Equation 4.28 and 4.29 from initial crack length (300 μm) to final crack length (2 mm) provide a means to predict the S-N behavior at elevated temperature, as shown in Figure 4.38. This method predicts the S-N curve at elevated temperature based on the crack growth data at room temperature and the dependence of Young's modulus and yield strength on temperature. It does not require crack growth data at elevated temperature. It can be seen that at a given stress amplitude, the predicted fatigue

life decreases modestly from 20 to 150^{o}C and decreases significantly from 150 to 250^{o}C. Although the predicted S-N curve at 250^{o}C is somewhat conservative, especially at low stress amplitude, the predicted magnitude of decrease in fatigue resistance with increasing temperature is generally in good agreement with the experimental results.

The frequency effect on S-N behavior at elevated temperature can also be predicted by integrating Equation 4.28 and 4.29 as long as the Young's modulus and yield strength at a given temperature are known. Figure 4.39 presents the predicted S-N curves at 20 kHz and 75 Hz at 150^{o}C and 250^{o}C, respectively. It can be seen that at 150^{o}C the predictions agrees very well with the experimental data. At 250^{o}C, the predicted fatigue lives are shorter than the experimentally observed fatigue lives, however, the predicted magnitude of difference in fatigue lives agrees well with the experimental observations.

The effect of frequency was observed to persist over the examined stress range at elevated temperature, while at room temperature the effect of frequency was substantially reduced at 10^7 cycles. The persistence of the frequency effect on fatigue life at elevated temperature is believed to result from the fact that the stress range examined is above the fatigue limit, and therefore the fatigue lives are controlled by the fatigue crack growth rates. In this case, the effect of frequency caused by environmental effect on fatigue crack growth is present when the specimens are tested in laboratory air, and the effect of frequency on S-N fatigue performance is observed over the entire range of stress levels examined.

4.4 Summary

The fatigue behavior of E319 cast aluminum alloy was determined at both ultrasonic and conventional frequencies at room temperature and elevated temperature. The crack initiation and crack propagation behavior were examined at each testing frequency and at each temperature. The major conclusions are summarized as follows:

1) At room temperature, the S-N curve of E319 cast aluminum alloy shows a plateau

beyond 10^7 cycles at room temperature, indicating that an apparent fatigue limit exists. In the lifetime regime of less than 10^7 cycles, fatigue life at 20 kHz is 5 to 10 times longer than that at 75 Hz; while at 10^7 cycles, there is a substantially reduced effect of frequency on the room temperature fatigue performance. At elevated temperatures (150 and 250^{o}C), however, the S-N curves continue to drop beyond 10^7 cycles and the slopes of the curves increase with temperature. At 150 and 250^{o}C, a difference in fatigue life between 20 kHz and 75 Hz persists over the entire range of stress examined.

2) Fatigue crack initiation was not influenced by either frequency or temperature in the E319 cast aluminum alloy. The fatigue cracks initiated predominately from pores located at or very close to the specimen surface. Fatigue life is dominated by fatigue crack propagation and the number of cycles required to cause failure is determined by the crack growth rate. The crack growth rate at 20 kHz is lower than at 30 Hz at all temperature examined and this in turn results in the observed longer fatigue life at ultrasonic frequency.

3) The difference in fatigue crack growth rate between 20 kHz and 30 Hz in air at all temperature examined is attributable to an environmental effect. For aluminum alloys, water was found to increase fatigue crack growth rate and thereby speed the failure of the material. At a given stress intensity factor range, ΔK, fatigue crack growth rate increases with water exposure, *P/f*, until it reaches the maximum value when saturation of environmental effect occurs. Fatigue testing at 30 Hz in air represents higher water exposure than fatigue testing at 20 kHz, and therefore the crack growth rates at 30 Hz are higher than that at 20 kHz. The dependence of crack growth rate on water exposure closely follows the dependence of hydrogen concentration on water exposure, which supports the assumption that the enhancement of crack growth rate caused by environment is determined by the concentration of hydrogen in the plastic zone. This behavior is characterized by a modified superposition model of the influence of hydrogen on fatigue crack growth rate. In this model, hydrogen-induced increase of fatigue crack

growth rate is assumed to be proportional to the square root of hydrogen concentration, which is determined by the transport rate of water molecules from the surrounding environment to the crack tip. Based on the modified superposition model, fatigue crack growth rates over the entire range of ΔK in various environments with different water exposure can be predicted and the predictions generally agree well with the experimental observations.

4) Fatigue resistance decreases with increased temperature. At 20 kHz, increasing test temperature from 20 to 150^{o}C results in a modest decrease in fatigue resistance, while a significant decrease in fatigue resistance occurs at 250^{o}C. Temperature dependence of fatigue strength at 10^8 cycles follows the temperature dependence of yield and tensile strength closely. The fatigue crack growth rate at all temperatures can be successfully described by a universal version of the modified superposition model, in which crack growth rate is a function of normalized stress intensity factor range, $\Delta K/(E\sigma_{ys})$. This model provides a framework to separately characterize the intrinsic effect of temperature on mechanical properties and the effect of environment at elevated temperature. The effect of temperature on fatigue resistance primarily results from the intrinsic effect of temperature on Young's modulus and yield strength. The environmental contribution to fatigue crack growth rates modestly decreases with increasing temperature.

5) These results show that environmental effects need to be considered when ultrasonic fatigue is used to generate fatigue data for modeling the fatigue property of the aluminum alloys which are under conventional loading frequency in service. A modified superposition model was proposed to characterize the hydrogen induced increase of fatigue crack growth rates in E319 cast aluminum alloy. Although based on numerous assumptions, this model provides a basis for investigation of frequency effect on fatigue behavior due to environmental effect at both room temperature and elevated temperature.

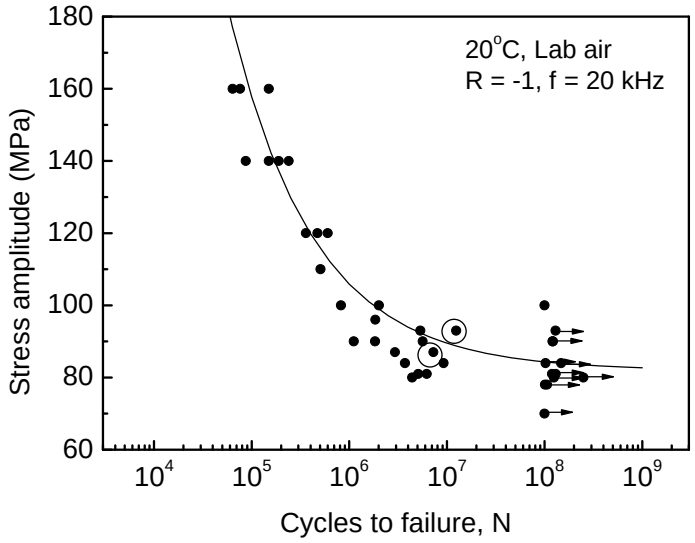

Figure 4.1 The S-N results of E319 cast aluminum alloy tested by using ultrasonic fatigue technique at 20°C in laboratory air (R = -1). The circled data represent failure from interior pores. Trend line represents the mean fatigue life based on the random fatigue limit (RFL) model.

(a)

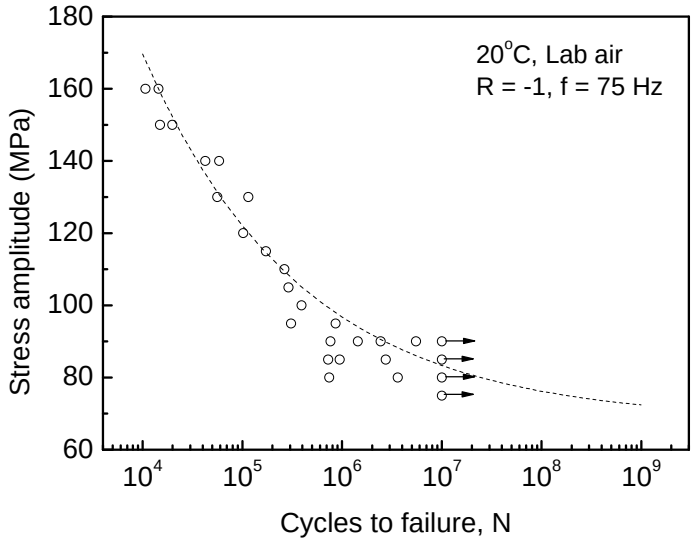

(b)

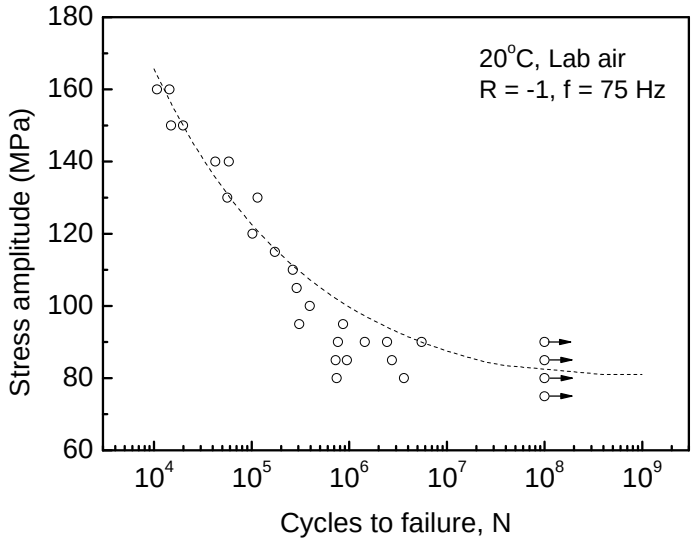

Figure 4.2 The S-N results of E319 cast aluminum alloy tested at 75 Hz at 20°C in laboratory air (R = -1). Trend lines represent the mean fatigue life based on the random fatigue limit (RFL) model. (a) The RFL estimate is based on the experimentally acquired S-N data up to 10^7 cycles and (b) the RFL estimate is based on the assumption that the specimens that survived at 10^7 cycles actually survived at 10^8 cycles.

(a)

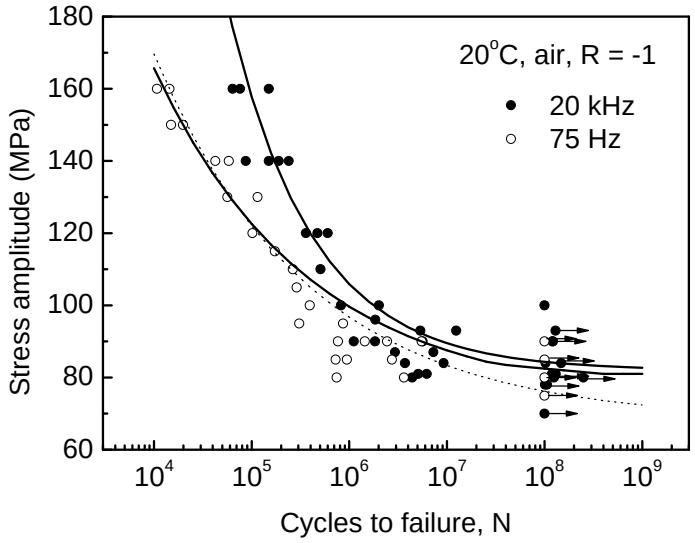

(b)

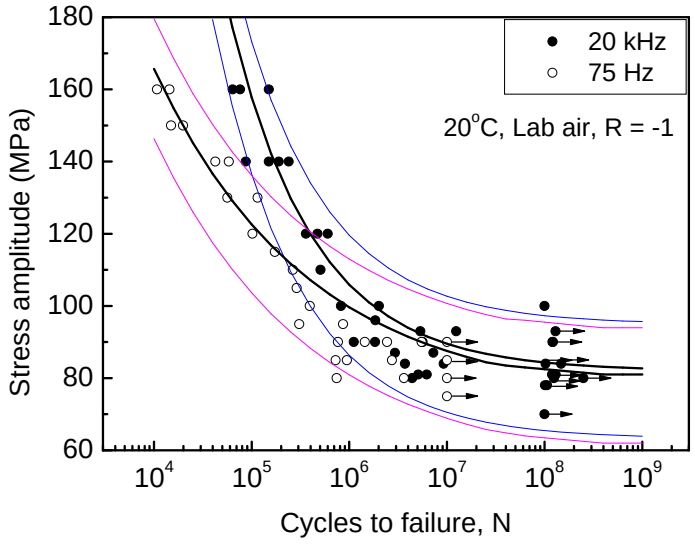

Figure 4.3 Comparison of S-N behavior of E319 cast aluminum alloy tested at 20 kHz and 75 Hz at 20°C in laboratory air (R = -1). (a) The S-N curves represent 50% failure probability based on the RFL model. The solid S-N curve for 75Hz is made by assuming the specimens that survived at 10^7 cycles acturally survied at 10^8 cycles and the dotted S-N curve for 75 Hz is made from the experimental observations that the specimens survived at 10^7 cycles. (b) the S-N curves represent 5%, 50% and 95% failure probabilities based on the RFL model. The 75 Hz RFL estimate is made assuming that the specimens that survived at 10^7 cycles actually survived at 10^8 cycles.

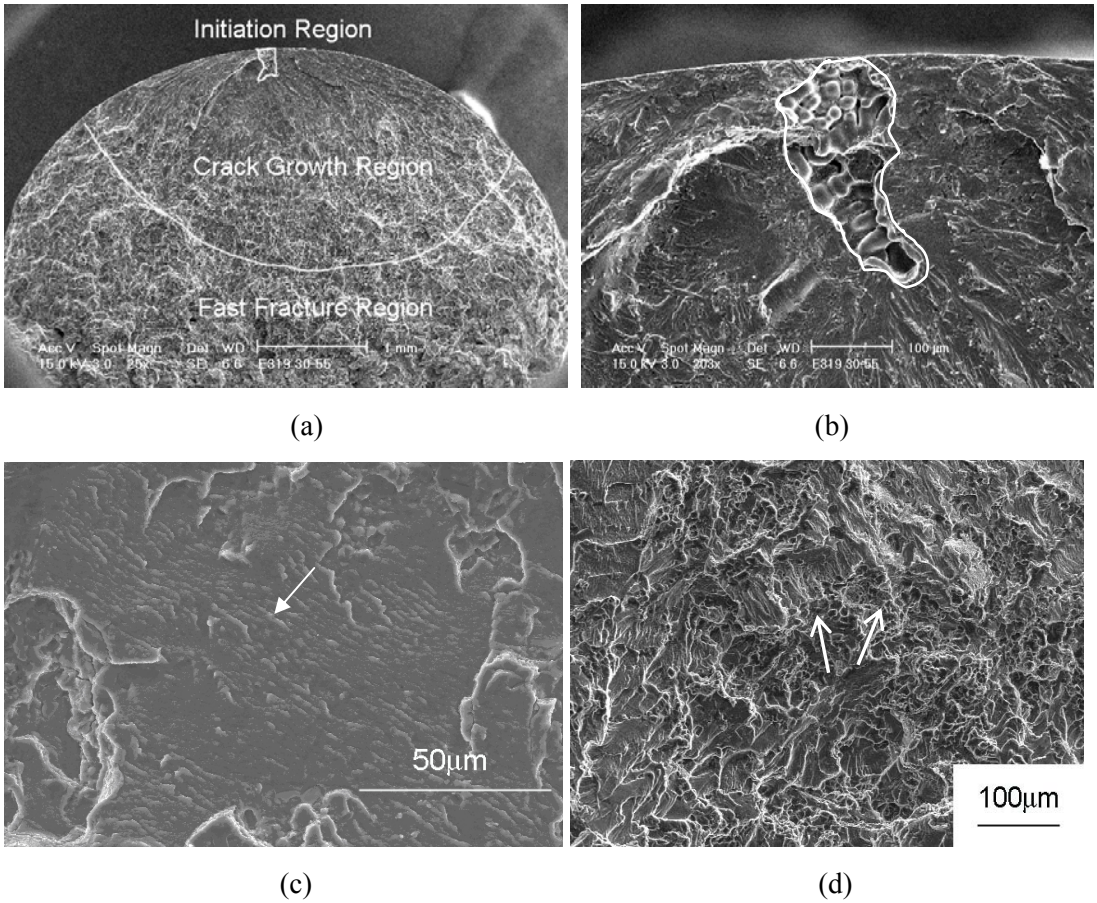

Figure 4.4 A typical fracture surface of E319 cast aluminum fatigue specimens: (a) the overall fracture surface showing crack initiation, steady crack growth and fast fracture regions; (b) crack initiation region showing a microshrinkage pore located at the specimen surface; (c) crack growth region showing striation-like features and (d) fast fracture region showing ductile microvoids.

.

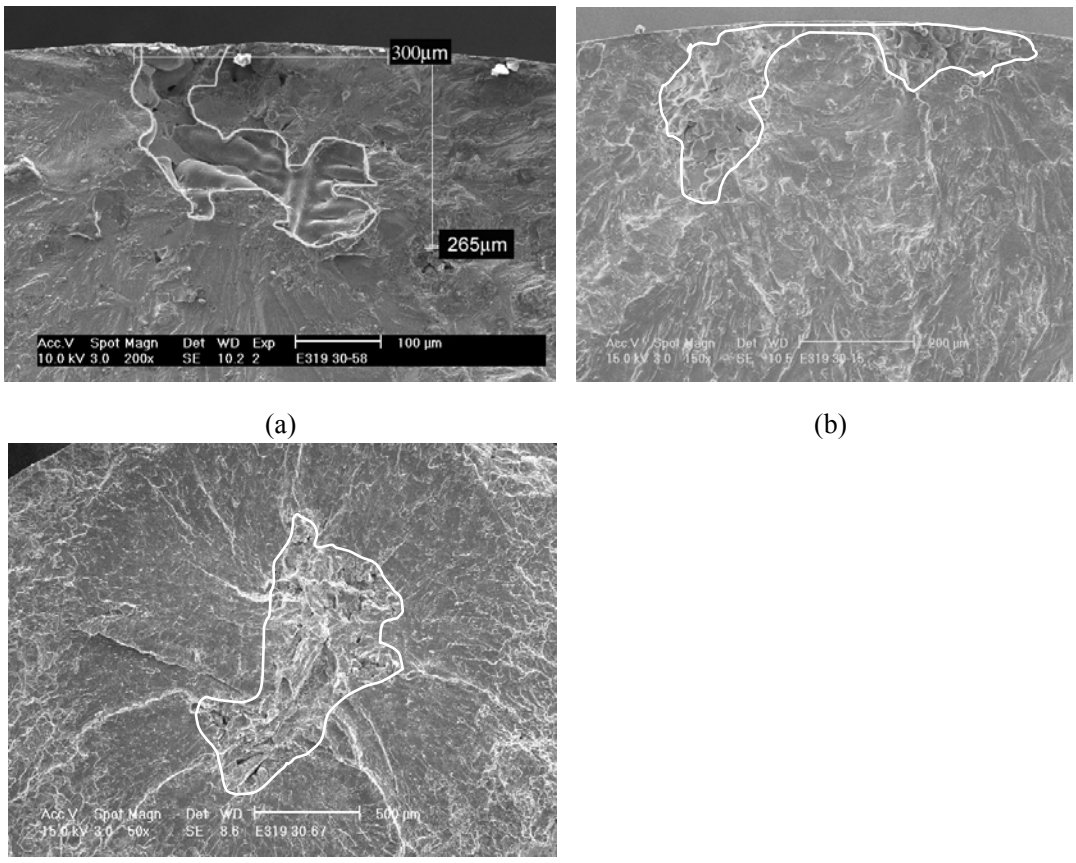

Figure 4.5 SEM photos of microshrinkage pores that initiated fatigue cracks in the E319 cast aluminum alloy specimens tested at frequency of 20 kHz. These specimens were tested in laboratory air at room temperature and load ratio of -1. (a) a single pore at the specimen surface; (b) observed multiple pores which are part of a single large pore at the specimen surface; (c) a pore in the specimen interior.

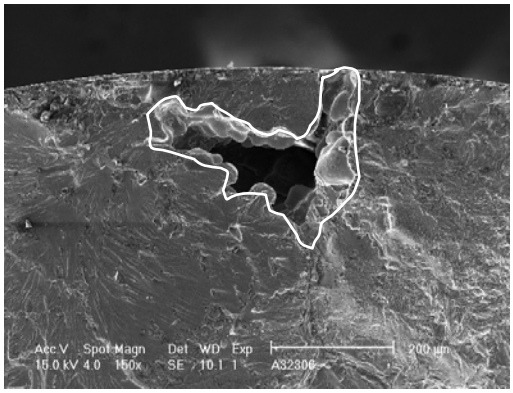

Figure 4.6 SEM photo of a single microshrinkage pore that initiated fatigue crack in an E319 cast aluminum alloy specimen tested at frequency of 75 Hz. The specimen was tested in laboratory air at room temperature and load ratio of -1.

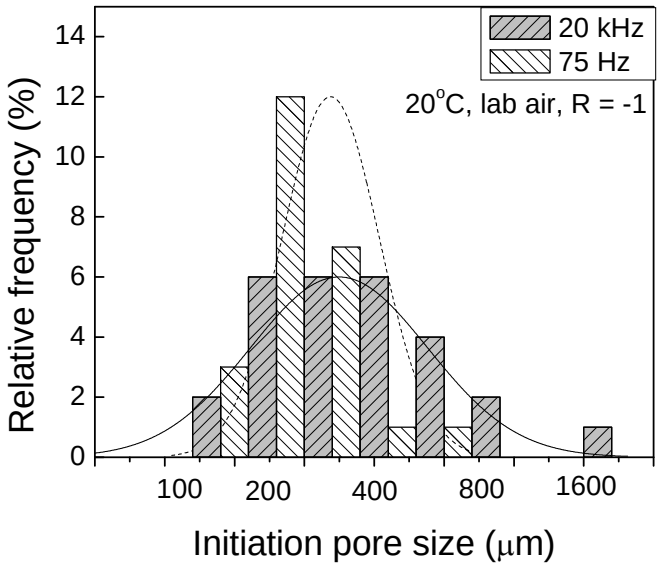

Figure 4.7 Log-normal distribution of measured initiation pore sizes in E319 cast aluminum alloy tested at 20 kHz (27 pores)and 75 Hz (24 pores)(note that the histogram bins were mapped from logarithmic values of the pore sizes).

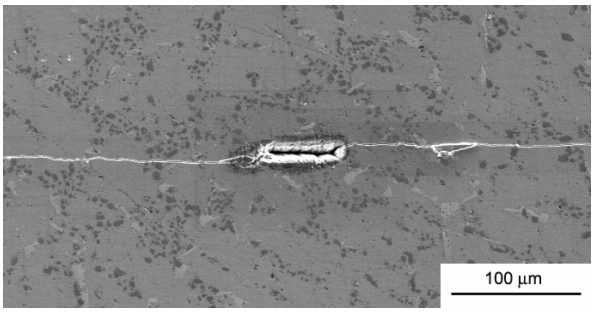

(a)

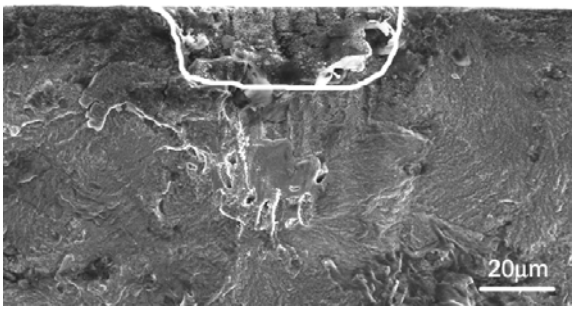

(b)

Figure 4.8 (a) A montage of SEM images showing a fatigue crack propagating from a laser-machined micronotch; (b) a normal view the fatigue fracture surface with the micronotch highlighted.

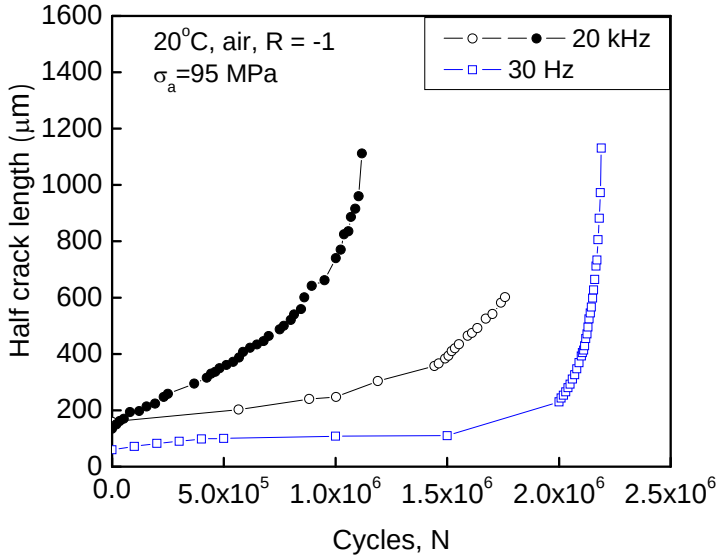

Figure 4.9 Fatigue crack length as a function of cycles during the crack growth tests; the specimens were tested at 20 kHz and 30 Hz in ambient air at fully reversed loading with stress amplitude of 95 MPa.

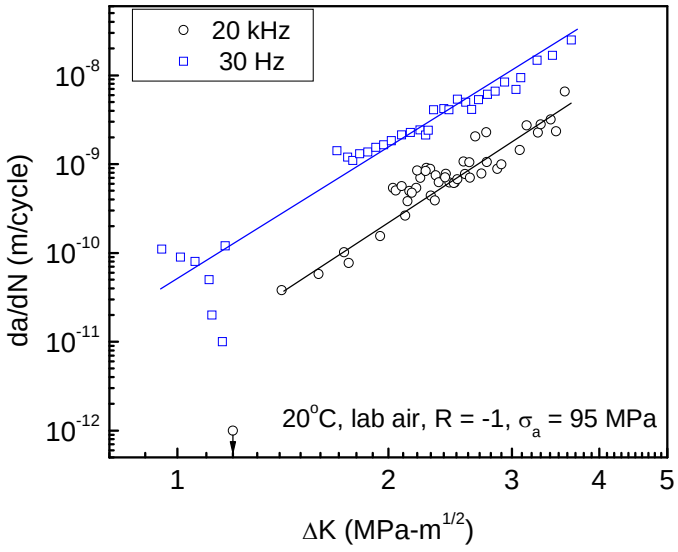

Figure 4.10 Fatigue crack propagation in E319 cast aluminum alloy tested at 20 kHz and 30 Hz at in laboratory air at room temperature at fully reversed loading with stress amplitude of 95 MPa. Here, two tests at 20 kHz and one test at 30 Hz were conducted. The two sets of crack growth data at 20 kHz are overlapped and the crack growth curve is generated based on the combined data.

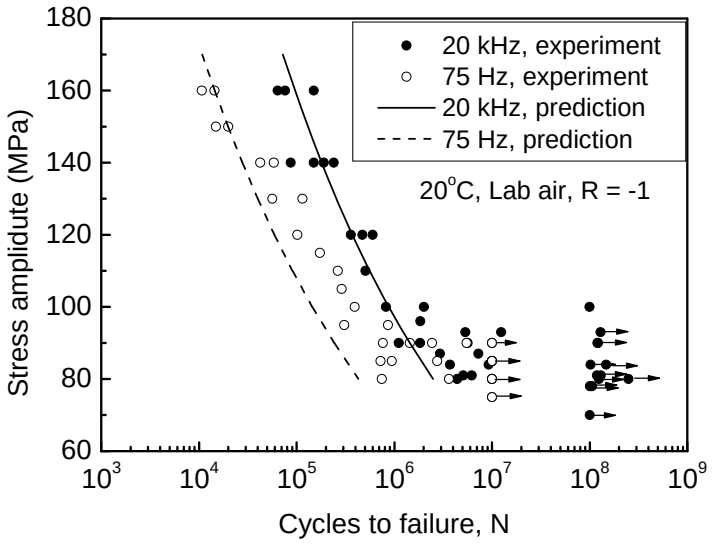

Figure 4.11 Predicted S-N behavior at 20 kHz and 75 Hz based on the crack growth data by assuming Paris law.

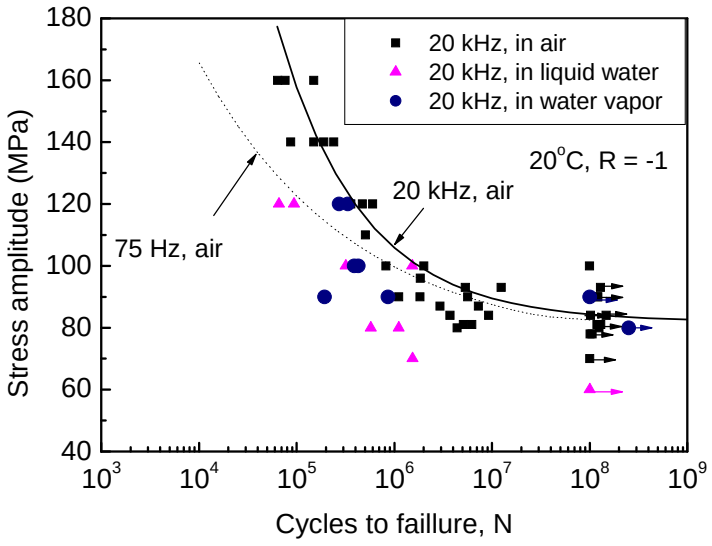

Figure 4.12 S-N results of E319 cast aluminum alloy tested at 20 kHz in ambient air (~ 40% RH), distilled water and 100% RH water vapor. The solid curve represents mean S-N curve based on RFL model for 20 kHz in air and the dotted curve represents mean S-N curve based on RFL model for 75 Hz in air.

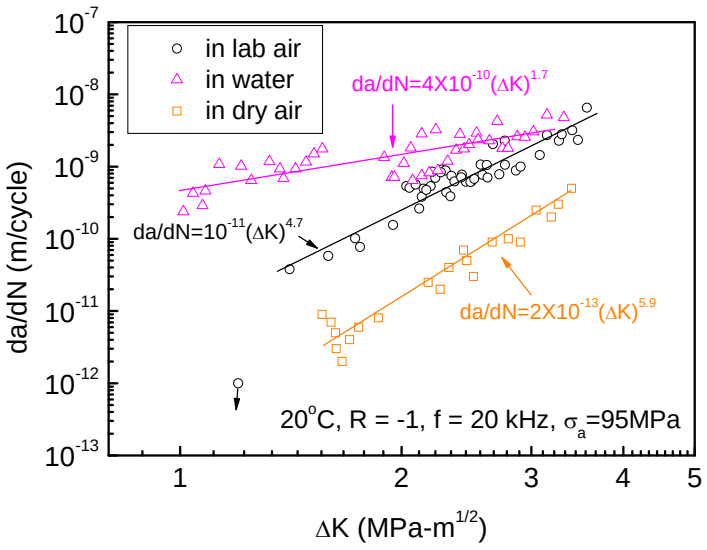

Figure 4.13 Fatigue crack propagation of E319 cast aluminum alloy in ambient air, distilled water and dry air at 20 kHz. Here, two tests were conducted in water, two tests were conducted in ambient air and one test was conducted in dry air. The crack growth curves for water and ambient air were generated based on the combined data, respectively.

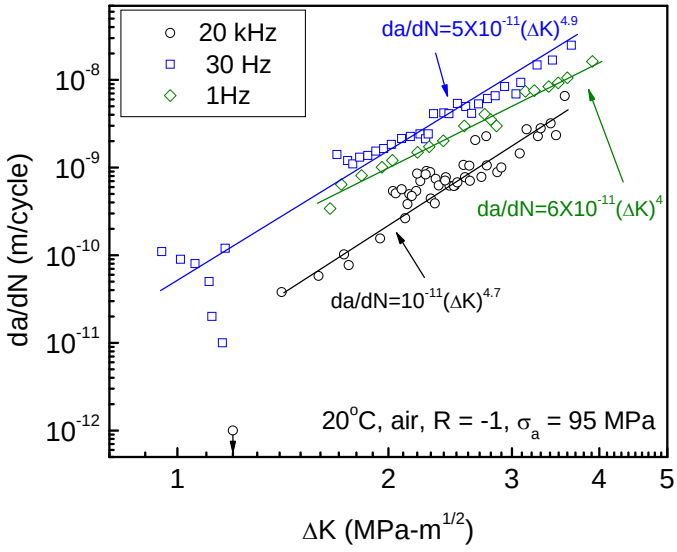

Figure 4.14 Fatigue crack propagation of E319 cast aluminum alloy at 20 kHz, 30 Hz and 1 Hz in ambient air. Here, two tests were conducted at 20 kHz, one test was conducted at 30 Hz and one test was conducted at 1 Hz. The crack growth curve for 20 kHz was generated based on the combined data.

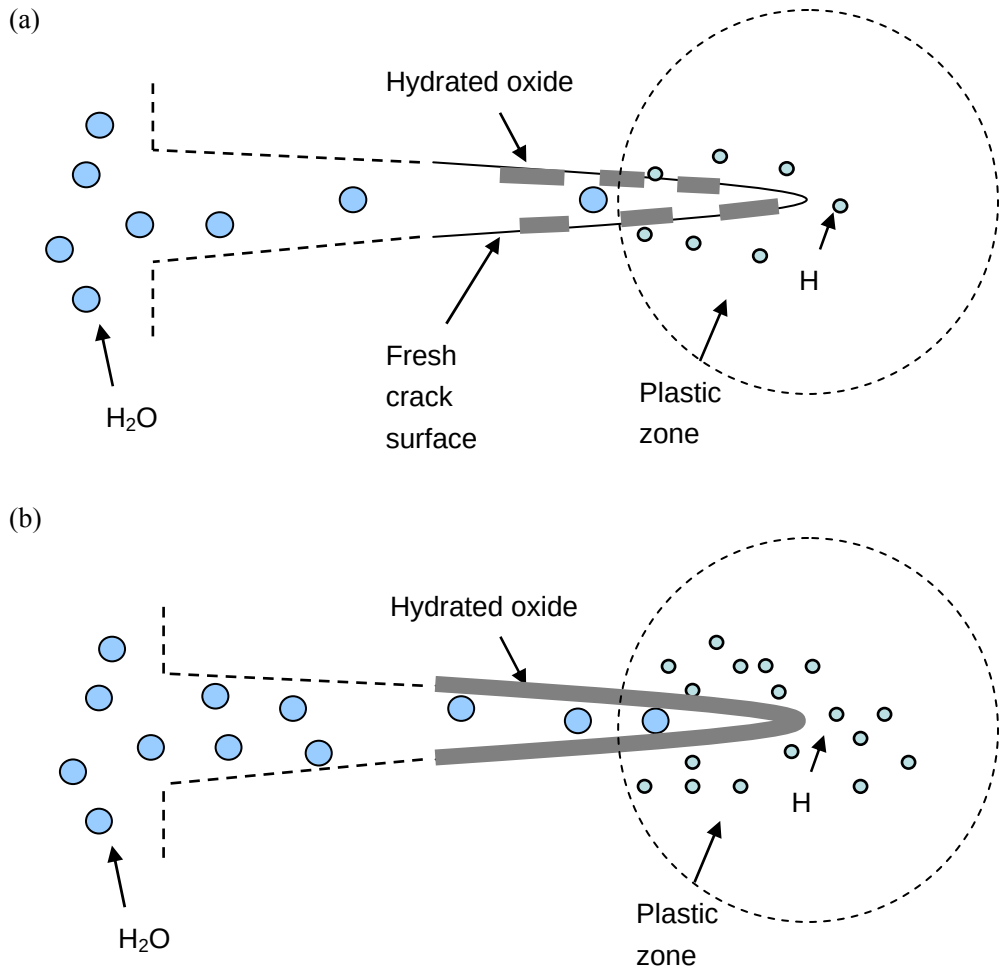

Figure 4.15 Schematic of the mechanisms of the crack tip surface reaction with water vapor forming a hydrated oxide and hydrogen atoms: (a) partially surface coverage and (b) saturated surface coverage.

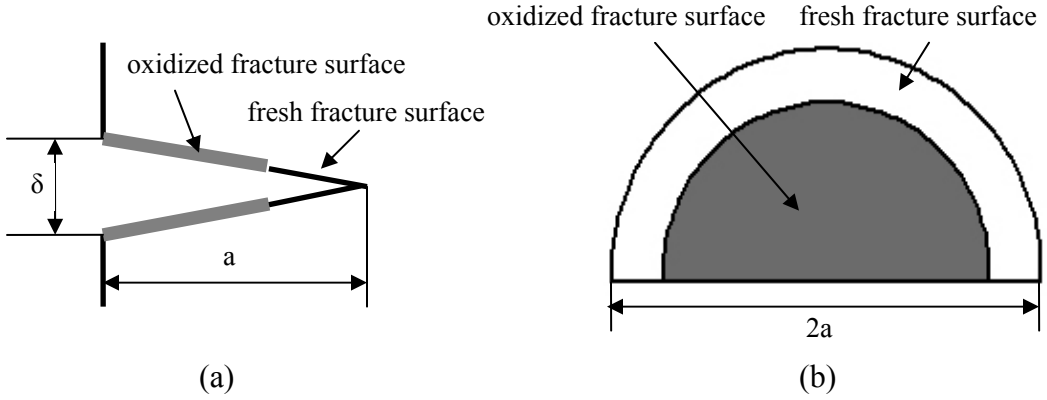

Figure 4.16 Schematic of the geometry of a semi-circular fatigue crack on the specimen surface. (a) a side view and (b) a normal view.

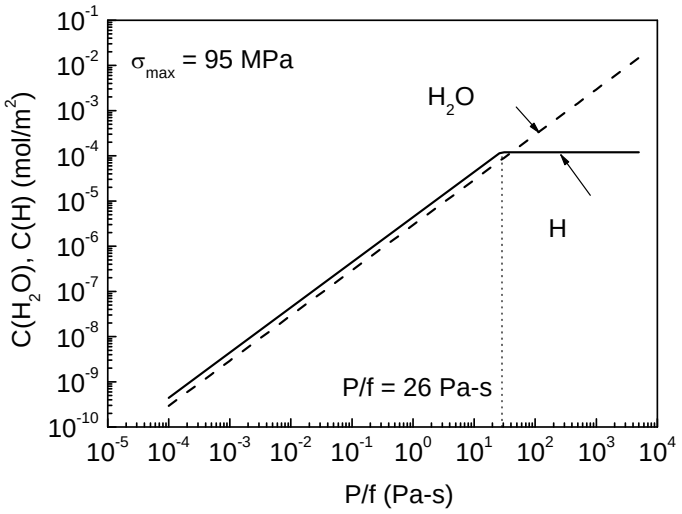

Figure 4.17 Estimated concentration of water vapor and hydrogen on the fresh fracture surface as a function of water exposure.

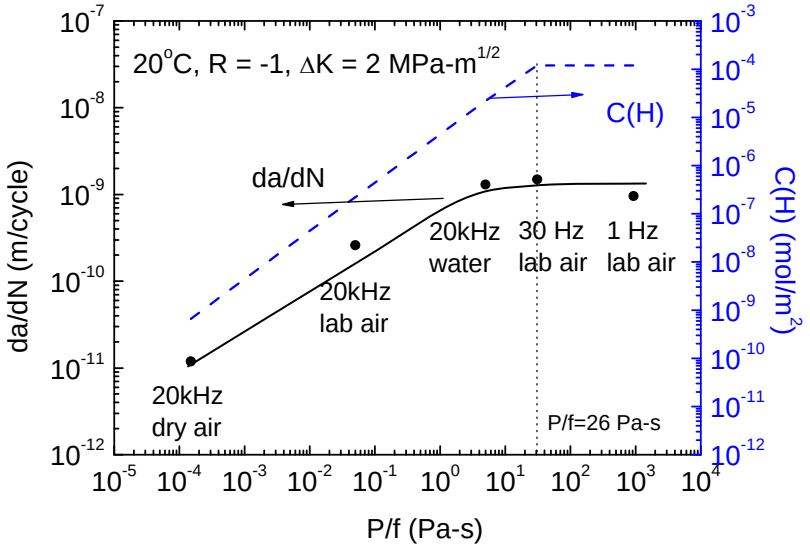

Figure 4.18 Dependence of crack growth and estimated hydrogen concentration on water exposure of E319 cast aluminum alloy at 20°C.

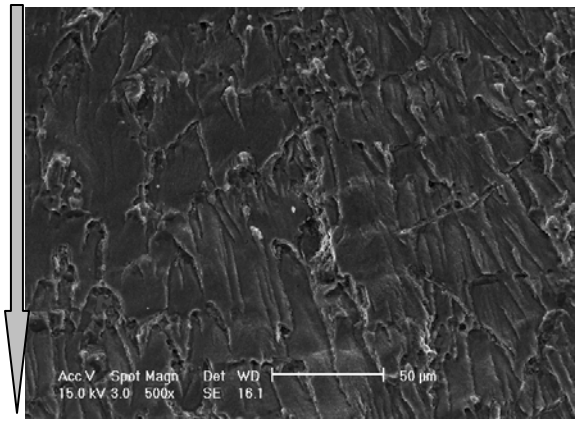
Acc.V Spot Magn Det WD
15.0 kV 3.0 500x SE 16.1
50 µm

(a)

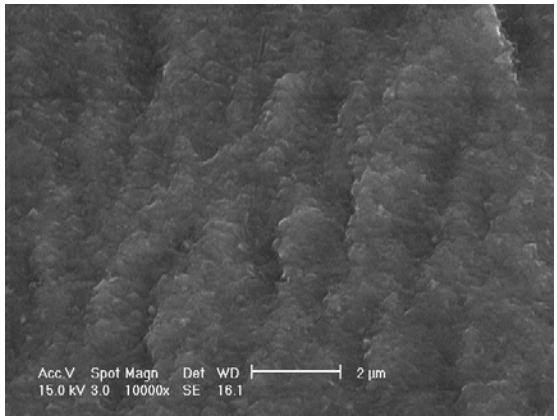
Acc.V Spot Magn Det WD
15.0 kV 3.0 10000x SE 16.1
2 µm

(b)

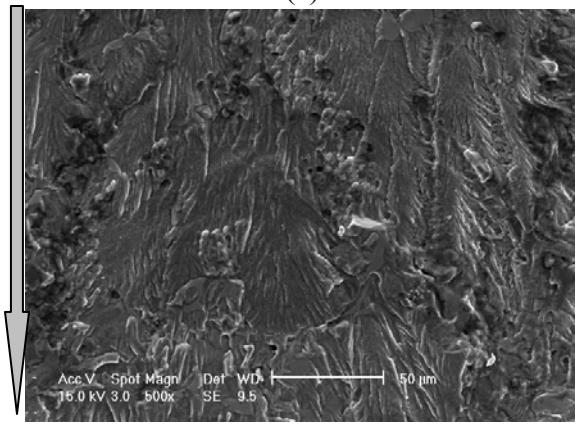
Acc.V Spot Magn Det WD
15.0 kV 3.0 500x SE 9.5
50 µm

(c)

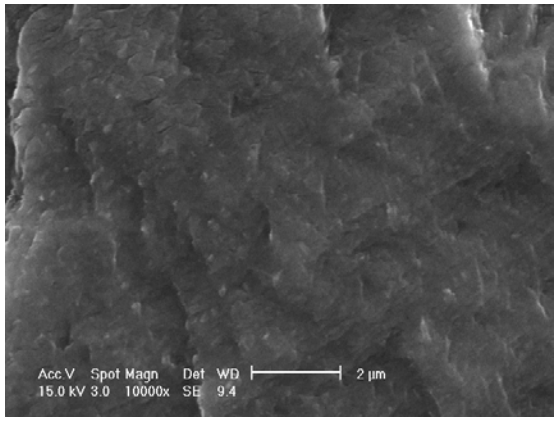
Acc.V Spot Magn Det WD
15.0 kV 3.0 10000x SE 9.4
2 µm

(d)

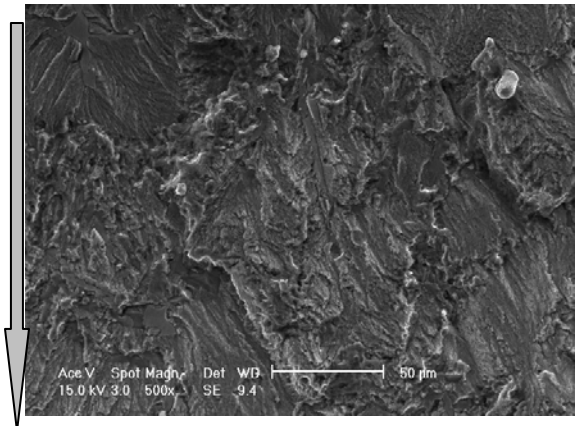
Acc.V Spot Magn Det WD
15.0 kV 3.0 500x SE 9.4
50 µm

(e)

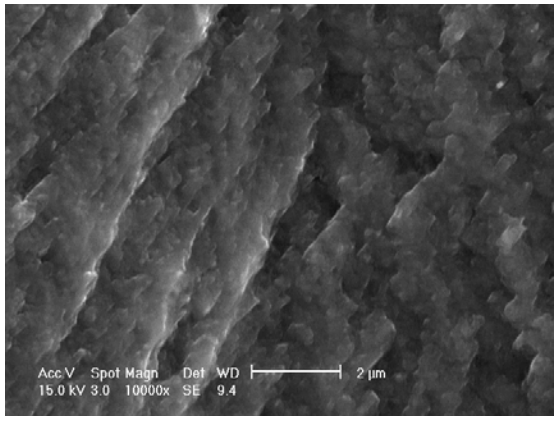
Acc.V Spot Magn Det WD
15.0 kV 3.0 10000x SE 9.4
2 µm

(f)

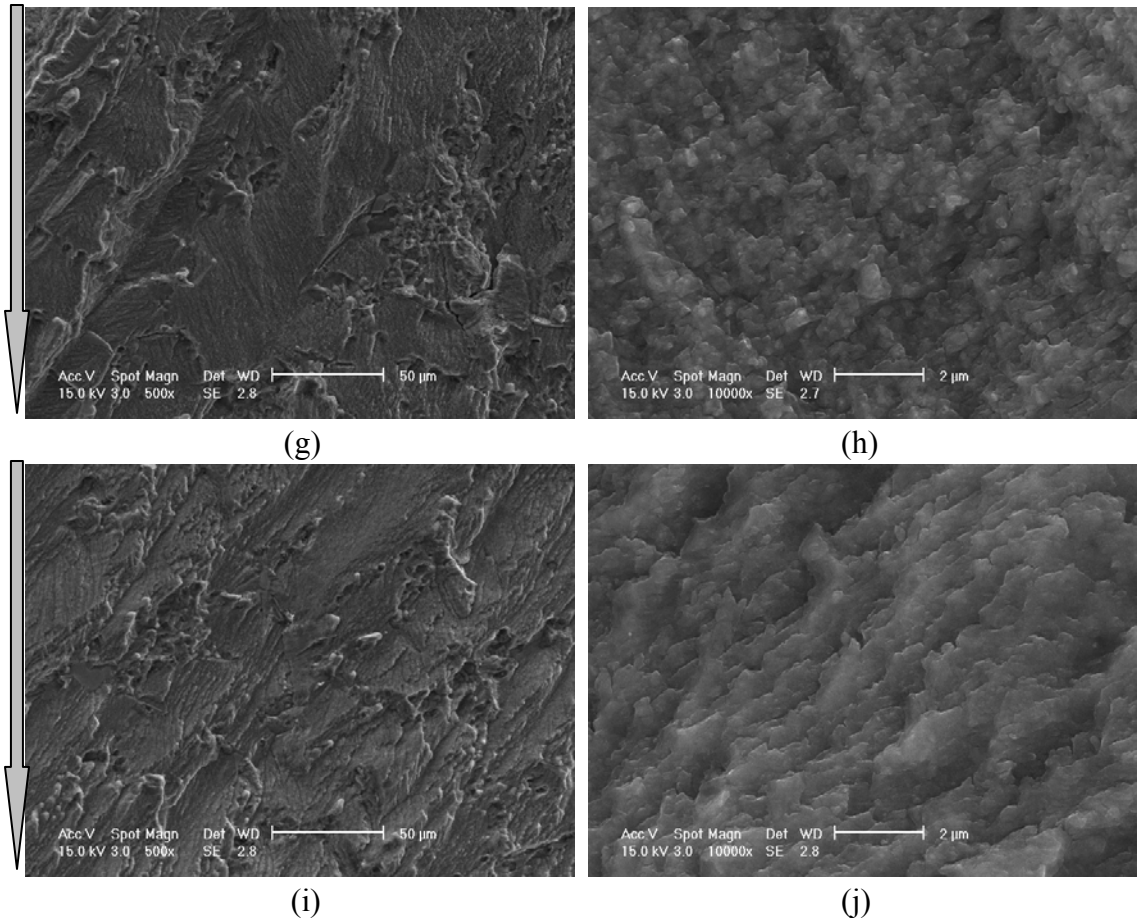

Figure 4.19 Fractographs of fatigue specimens of E319 cast aluminum alloy in environments with different water exposure at ΔK=2.5 MPa-$m^{1/2}$; crack growth direction is from top to bottom as indicated by the arrow. (a) 20 kHz, in dry air, low magnification, (b) 20 kHz, in dry air, high magnification, (c) 20 kHz, in ambient air, low magnification, (d) 20 kHz, in ambient air, high magnification, (e) 20 kHz, in liquid water, low magnification, (f) 20 kHz, in liquid water, high magnification, (g) 30 Hz, in ambient air, low magnification, (h) 30 Hz, in ambient air, high magnification, (i) 1 Hz, in ambient air, low magnification, (j) 1 Hz, in ambient air, high magnification.

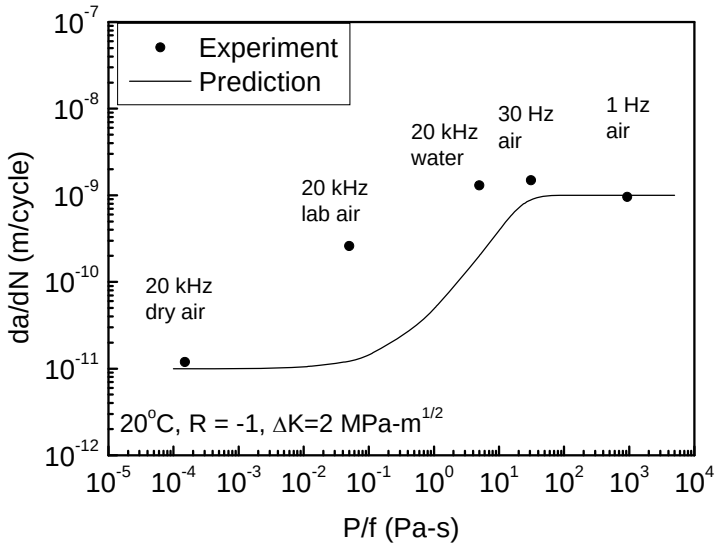

Figure 4.20 Predicted fatigue crack growth response as a function of water exposure based on the superposition model (Equation 4.19 through 4.21), compared with experimental data, at a constant ΔK of 2 MPa-$m^{1/2}$.

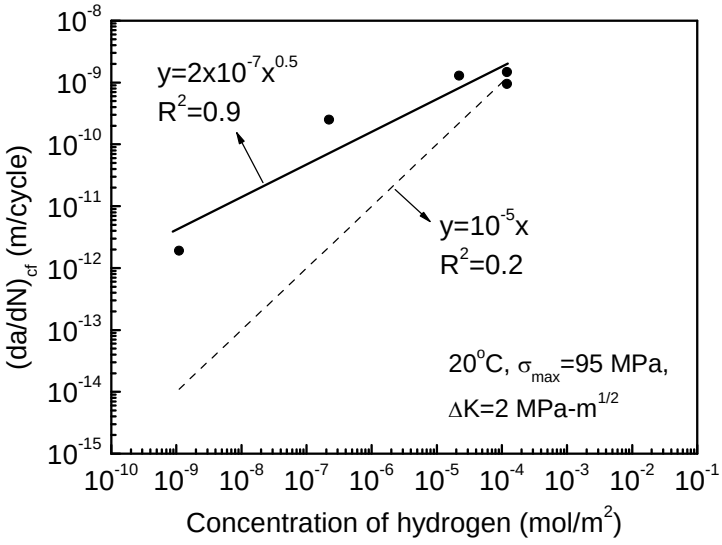

Figure 4.21 Correlation of environmental contribution to the fatigue crack growth rate and concentration of hydrogen.

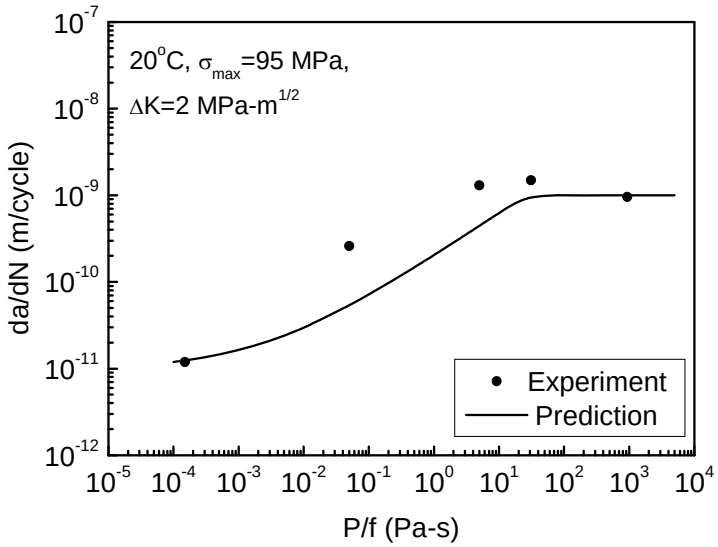

Figure 4.22 Predicted fatigue crack growth response as a function of water exposure based on the modified superposition model (Equation 4.22 and 4.23), compared with experimental data, at a constant ΔK of 2 MPa-$m^{1/2}$.

(a)

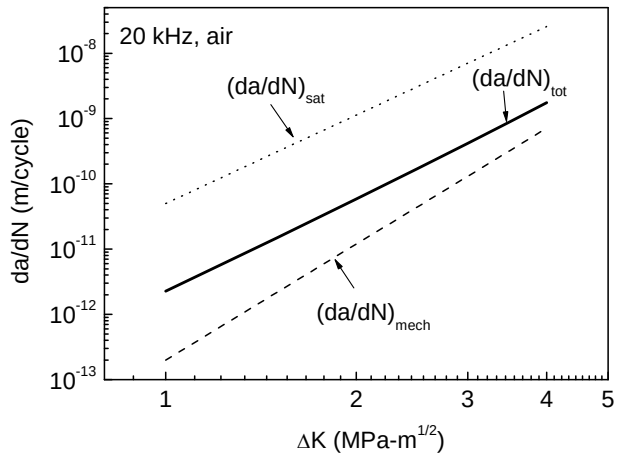

(b)

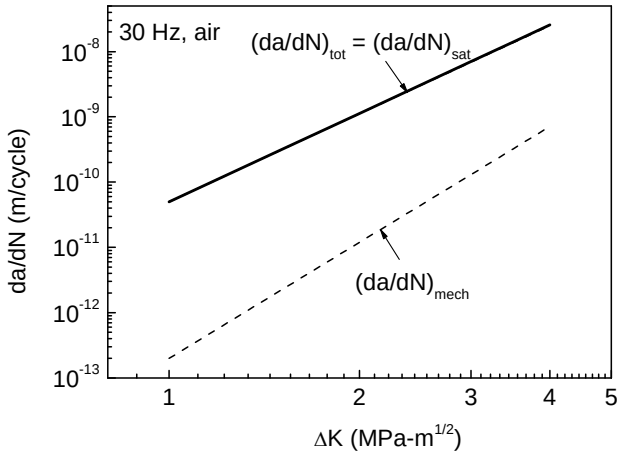

(c)

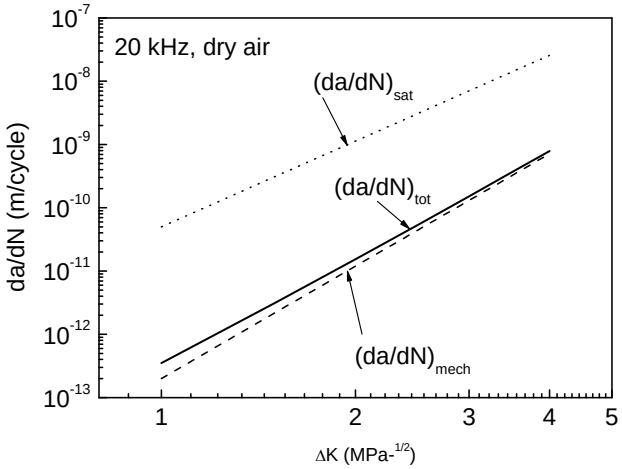

Figure 4.23 Predicted environmental effect on fatigue crack growth rate based on the modified superposition model (Equation 4.26 and 4.27). (a) 20 kHz in air, (b) 30 Hz in air and (c) 20 kHz in dry air. Here, $(da/dN)_{tot}$ is the crack growth rate in the environment, $(da/dN)_{mech}$ is the pure-mechanical fatigue crack growth rate, $(da/dN)_{sat}$ is the saturation fatigue crack growth rate.

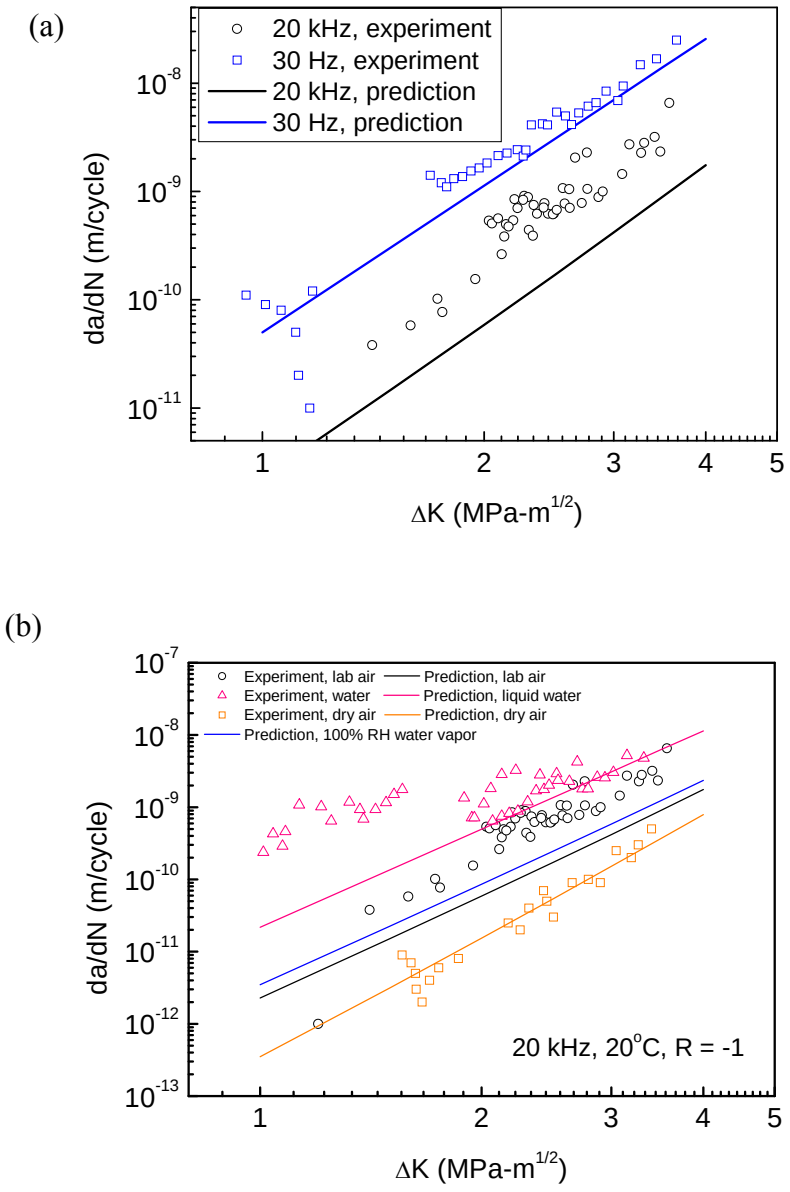

Figure 4.24 Predicted fatigue crack growth response based on the modified superposition model, compared with experimental data, in various environments with different water exposures. (a) in ambient air, at 20 kHz and 30 Hz and (b) at 20 kHz, in ambient air, liquid water, water vapor with 100% RH and dry air.

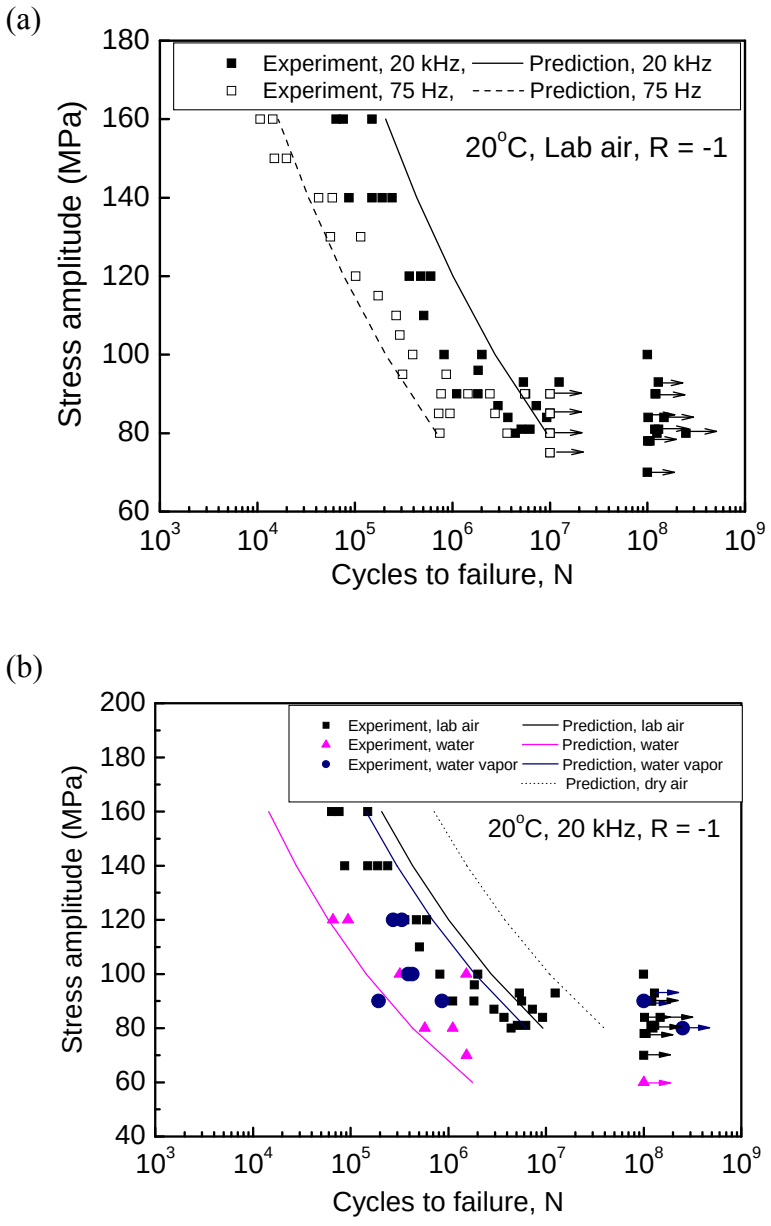

Figure 4.25 Predicted S-N behavior in various environments with different water exposures, compared with experiment results: (a) in lab air, at 20 kHz and 75 Hz and (b) at 20 kHz, in lab air, liquid water, water vapor with 100% RH and dry air. Note: S-N results in dry air are not available.

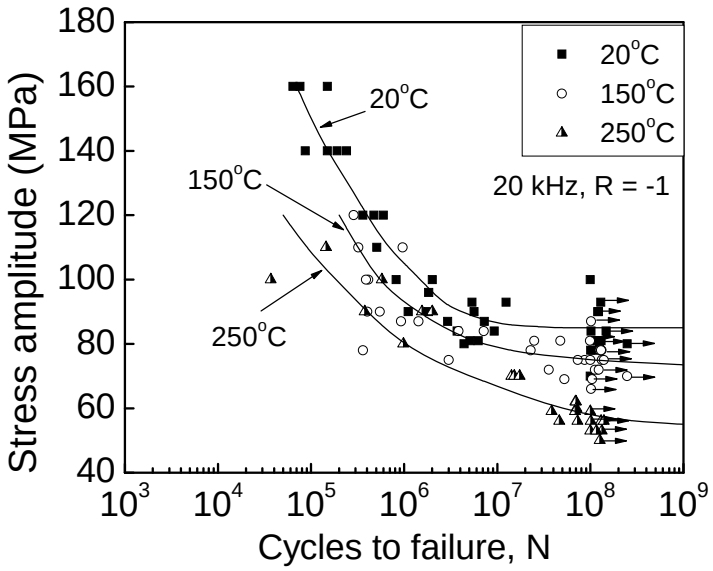

Figure 4.26 S-N results at 20, 150 and 250°C by using ultrasonic fatigue technique in laboratory air at R = -1. Trend lines represent mean S-N curves based on the RFL model.

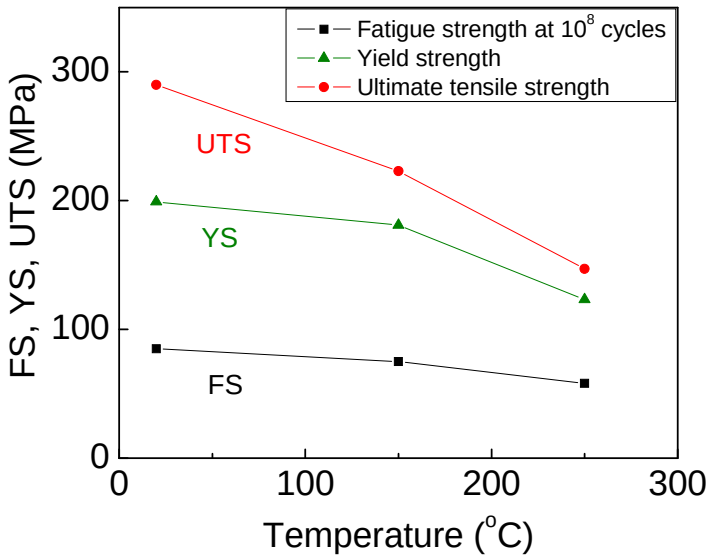

Figure 4.27 Temperature dependence of fatigue strength (FS) at 10^8 cycles, yield strength (YS) and ultimate tensile strength (UTS) of E319 cast aluminum alloy.

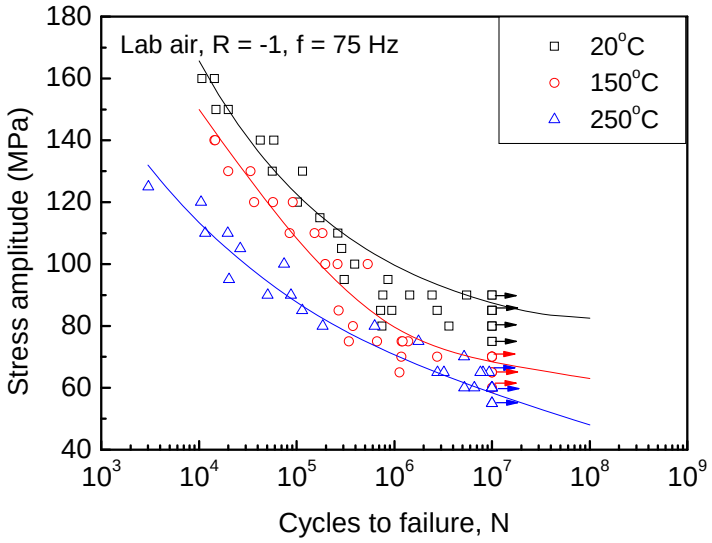

Figure 4.28 S-N results of E319 cast aluminum alloy at 20, 150 and 250°C at frequency of 75 Hz (R = -1). Trend lines represent mean S-N curves based on RFL model.

(a)

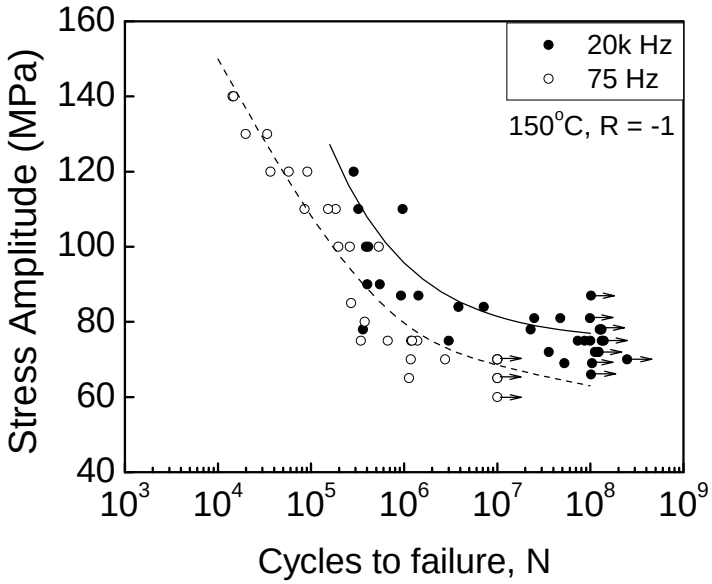

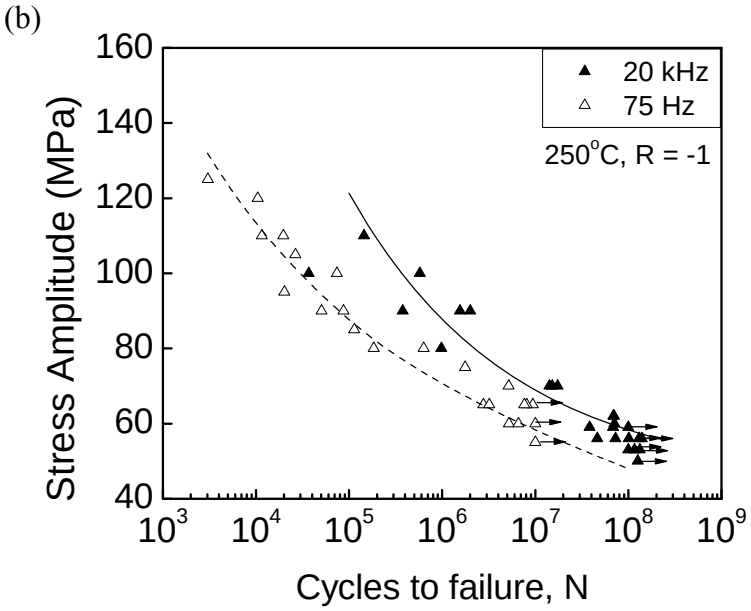

Figure 4.29 Comparison of S-N results at 20 kHz and 75 Hz at (a) 150°C and (b) 250°C.

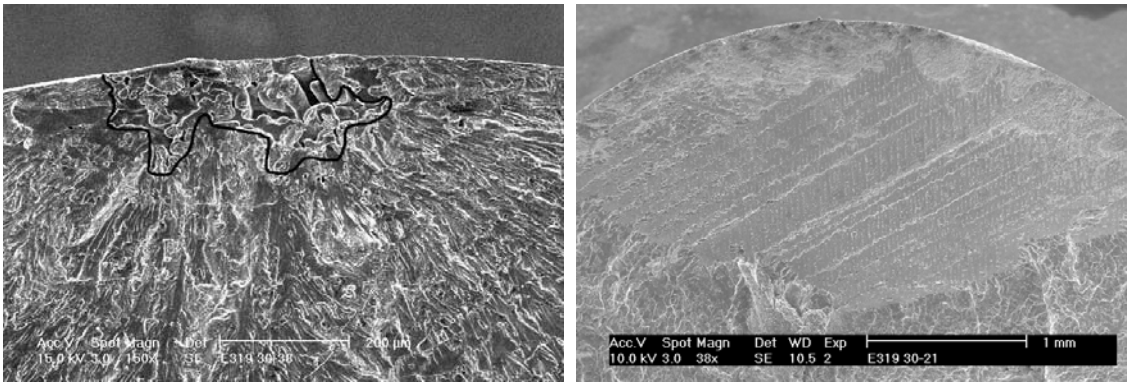

(a) (b)

Figure 4.30 Fatigue crack initiation at 150°C by using ultrasonic fatigue technique: (a) a microshrinkage pore located at the specimen surface; (b) a normal view of a planar facet which is actually oriented approximately 45 degrees to the loading direction.

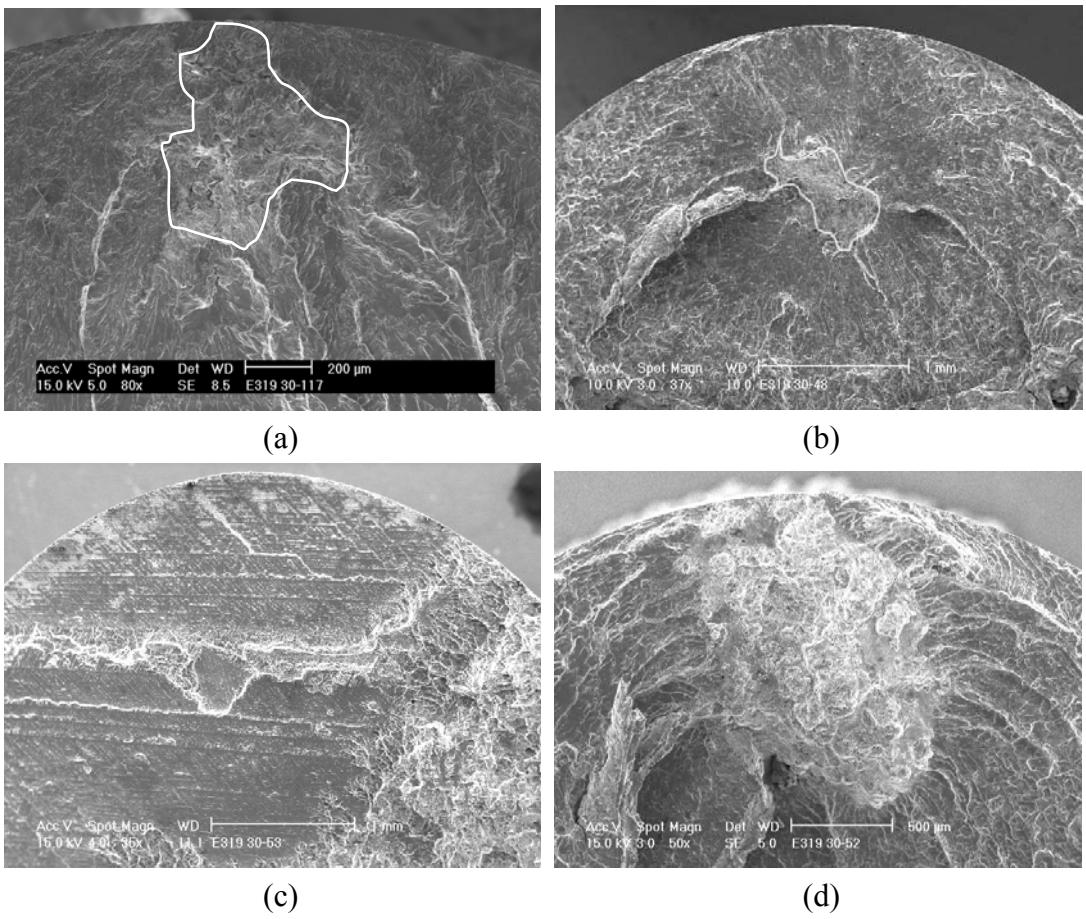

(a) (b)

(c) (d)

Figure 4.31 Fatigue crack initiation sites at 250^{o}C by using ultrasonic fatigue technique: (a) a microshrinkage pore located near the specimen surface; (b) a microshrinkage pore located in the specimen interior; (c) a planar facet; (d) an oxide particle which was likely introduced during casting process.

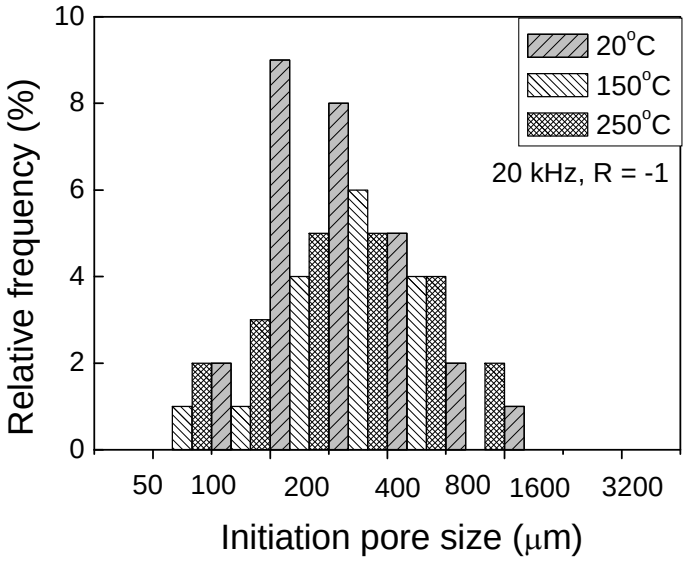

Figure 4.32 Log-normal distribution of measured initiation pore sizes in E319 cast aluminum alloy tested at 20, 150 and 250°C at 20 kHz (note that the histogram bins were mapped from logarithmic values of the pore sizes).

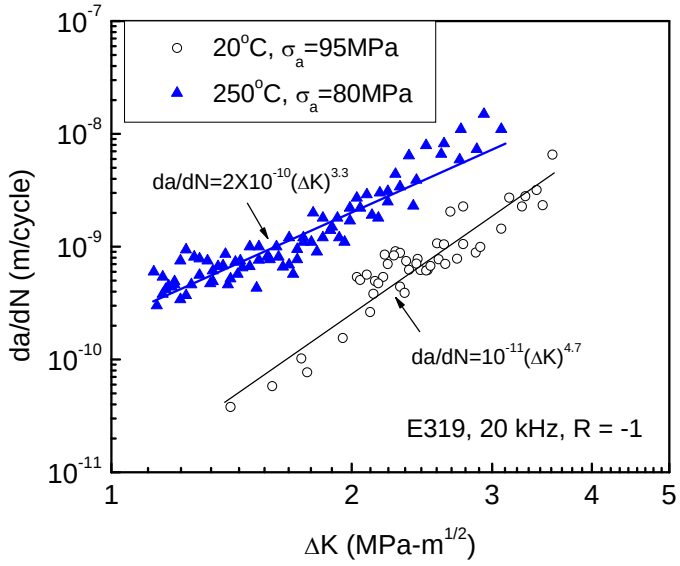

Figure 4.33 Small fatigue crack propagation in E319 cast aluminum alloy at 20 and 250°C, at testing frequency of 20 kHz and under fully reversed loading condition (R = -1).

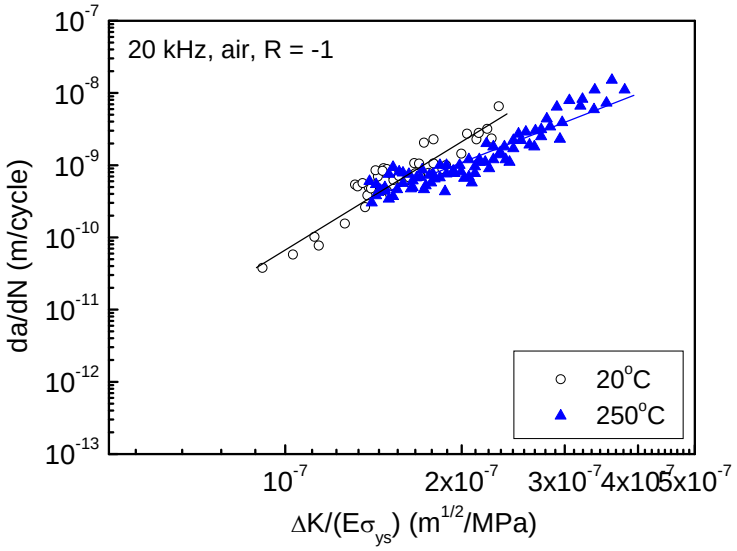

Figure 4.34 Fatigue crack propagation in E319 cast aluminum alloy at 20 and 250°C characterized by normalized stress intensity factor range ($\Delta K/(E\sigma_{ys})$).

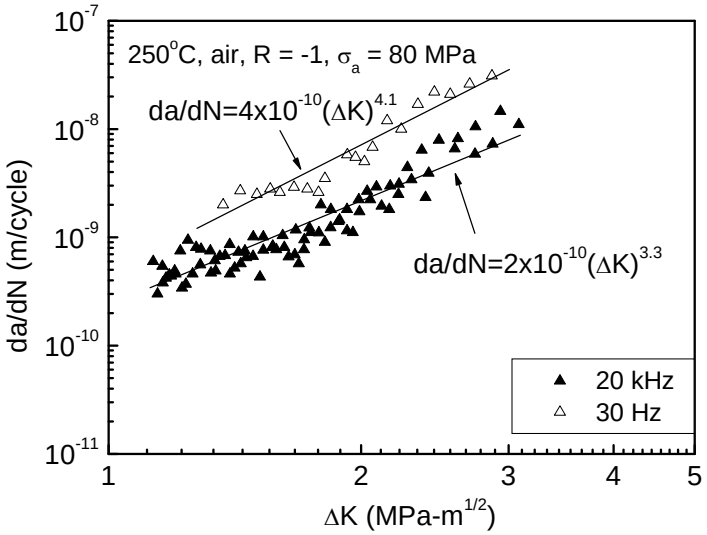

Figure 4.35 Fatigue crack propagation in E319 cast aluminum alloys tested at 20 kHz and 30 Hz at 250°C in laboratory air, R = -1,σ_a = 80 MPa.

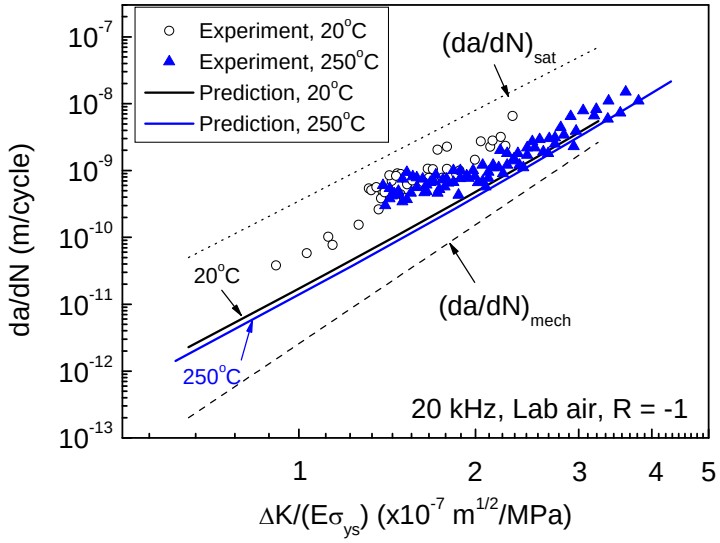

Figure 4.36 Predicted crack growth rates at 20 and 250°C in air at 20 kHz based on the modified superposition model (Equation 4.28 and 4.29), compared with experimental results. Stress intensity factor range is normalized by Young's modulus and yield strength.

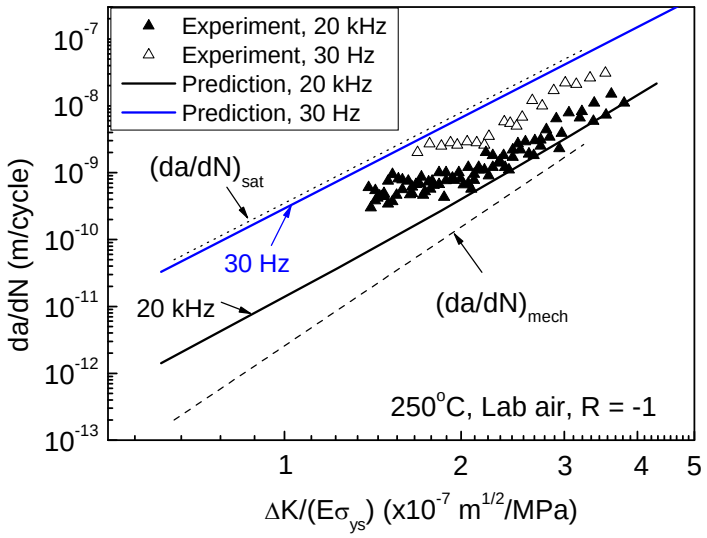

Figure 4.37 Predicted fatigue crack growth response at 250°C at 20 kHz and 30 Hz in laboratory air based on the modified superposition model (Equation 4.28 and 4.29), compared with the experimental results.

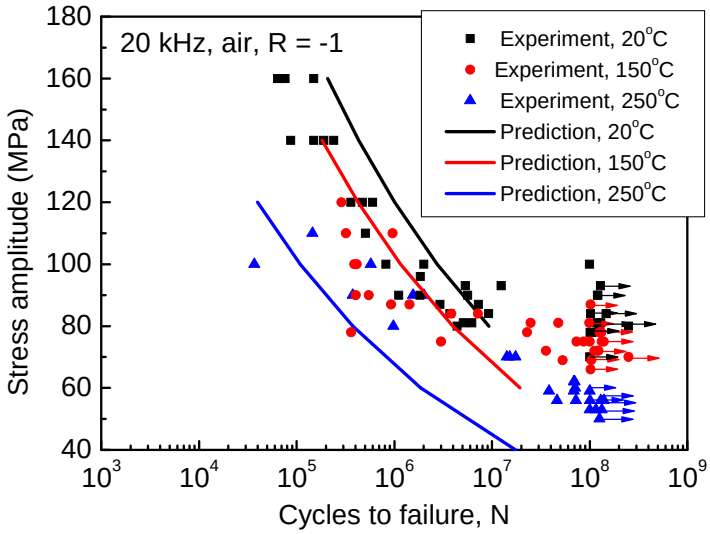

Figure 4.38 Predicted S-N behavior at 20, 150 and 250°C in air at 20 kHz based on the integration of the modified superposition model (Equation 4.28 and 4.29), compared with the experimental results.

(a)

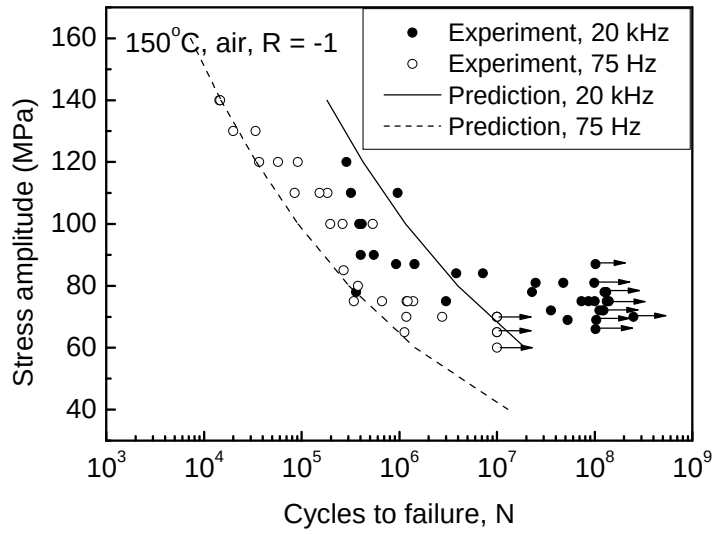

(b)

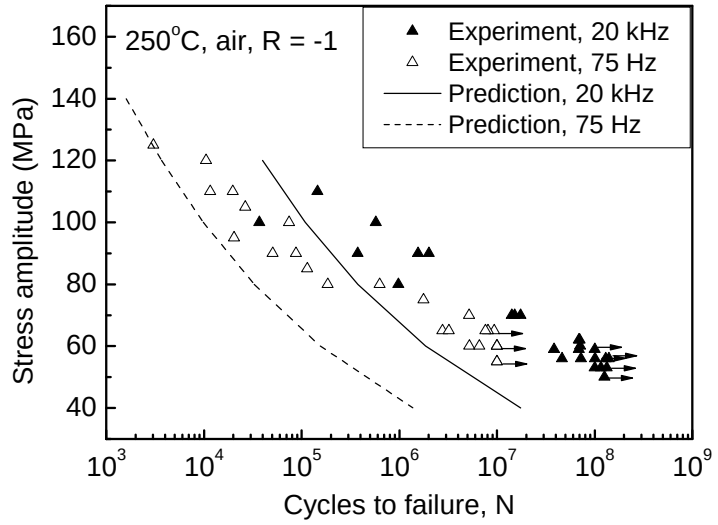

Figure 4.39 Predicted S-N response at testing frequency of 20 kHz and 75 Hz in air at (a) 150°C and (b) 250°C, based on the integration of the modified superposition model (Equation 4.28 and 4.29), compared with the experimental results.

Chapter 5

Probabilistic model of fatigue strength controlled by porosity population in E319 cast aluminum alloy at room temperature

Cast aluminum alloys inevitably have local variation in both microstructure and porosity which strongly influences mechanical properties and fatigue, in particular [5, 20, 33, 84]. Studies have indicated that porosity is the key microstructural feature controlling the fatigue properties in cast aluminum. At high stress amplitude or in the lifetime regime $<10^7$ cycles, fatigue cracks readily initiate from large pores due to the higher stress concentration at the pores [20, 21]. In such cases, the initiation life is generally thought to be negligible, and the total fatigue life of the cast material is dominated by the crack propagation phase from the initiating pore to the final crack length. At low stress amplitude, when the cyclic loading was run to 10^9 cycles by performing ultrasonic fatigue experiments, Caton *et al.* [14] reported the existence of an endurance limit in W319-T7. They observed that cycling at or below the endurance limit initially caused crack initiation; however, if the associated driving force was below a critical value, the crack became non-propagating and failure did not ensue. They concluded that this behavior led to the flattening of the S-N curve and the manifestation of an endurance limit. In this case, the effective long-crack threshold values were observed to provide good agreement with the experimentally determined endurance limit.

In Chapter 4, the fatigue behavior of E319 cast aluminum alloy at ultrasonic frequency and conventional frequency was investigated and compared. It was found that in the lifetime regime of less than 10^7 cycles, fatigue life at 20 kHz is 5 to 10 times longer than that at conventional frequency for E319 cast aluminum alloy. The observed

difference in fatigue life between ultrasonic and conventional frequency was attributed to an environmental effect on the fatigue crack growth rate. Testing at lower frequency in air is presumed to be more damaging, as there is more time to accumulate environmental damage and the crack growth rate can be accelerated when the crack tip interacts with the environment. On the other hand, at 10^7 cycles, there is a substantially reduced effect of frequency on the room temperature fatigue performance in E319. The S-N curve at 20 kHz shows a plateau beyond 10^7 cycles, indicating that an apparent fatigue limit exists. The experimental results for the E319 cast aluminum alloy suggested that ultrasonic fatigue is appropriate for studying fatigue properties in the very high cycle fatigue regime (10^7 ~10^9 cycles), where the effect of frequency on fatigue lifetime is small.

In this chapter, the fatigue strength at 10^8 cycles of E319 cast aluminum alloy was investigated using ultrasonic fatigue. The fatigue strength was correlated with the initiation pore size and pore location through a critical stress intensity factor for fatigue crack growth. Based on the experimental observations, a probabilistic model was then developed to establish the relationship between the porosity population and the fatigue strength of the alloy. Finally, the effects of porosity population and specimen geometry on fatigue strength were quantified by Monte-Carlo simulation that was incorporated in the model.

5.1 Fatigue strength at 10^8 cycles at room temperature

As shown in Figure 4.1, the S-N curve of E319 cast aluminum alloy was generated by ultrasonic fatigue in a lifetime regime of 10^5 to 10^8 cycles in ambient air. The fatigue life increases from approximately 10^5 cycles to slightly less than 10^7 cycles with decreasing stress from 160 to 100 MPa, then a plateau or endurance limit is exhibited when the stress amplitude is below 100 MPa. This observation is consistent with previous results for cast aluminum alloys [8, 14, 20].

Table 5.1 Staircase results and the characteristics of initiating pores

Sample	σ_a, MPa	Failure or Run-out	Initiator	Size, μm		Location (t), μm	Surface or Interior	ΔK, MPa-$m^{1/2}$	
				D	L			ΔK_{Deq}	ΔK_{Lmax}
1	90	Run-out	Pore	162	345	81	S	1.24	1.81
2	93	Failure	Pore	250	478	125	S	1.59	2.21
3	90	Run-out	Pore	313	479	379	I	1.33	1.64
4	93	Run-out	Pore	339	430	464	I	1.43	1.61
5	96	Failure	pore	371	867	185	S	2.01	3.07
6	93	Failure	pore	812	1315	1056	I	2.21	2.81
7	90	Failure	pore	223	474	111	S	1.46	2.13
8	87	Failure	pore	976	1408	1318	I	2.27	2.72
9	84	Failure	pore	573	759	286	S	2.18	2.51
10	81	Run-out	Pore	218	360	109	S	1.30	1.67
11	84	Failure	pore	588	892	414	I	1.70	2.09
12	81	Failure	pore	336	791	168	S	1.61	2.47
13	78	Run-out	pore	260	622	130	S	1.36	2.11
14	81	Failure	pore	287	431	143	S	1.49	1.82
15	78	Run-out	Pore	480	570	1415	I	1.43	1.55
16	81	Failure	Pore	250	259	125	S	1.39	1.41
17	84	Run-out	Pore	182	345	91	S	1.23	1.69
18	87	Failure	pore	291	621	145	S	1.61	2.35
19	84	Run-out	Pore	112	232	56	S	0.96	1.39

Notes:

1. D is the equivalent circular diameter of the initiating pore, defined as the initiating pore size; L is the maximum chord length of the initiating pore.
2. The initiating pore location (t) is defined as the distance from the center of the pore to the specimen surface. If $\frac{D}{t} \geq 1.6$, the pore is on the surface; if $\frac{D}{t} < 1.6$, the pore is in the material interior.
3. The stress intensity factors are calculated based on both the equivalent diameter, $\Delta \mathbf{K}_{Deq}$, and maximum chord length, $\Delta \mathbf{K}_{Lmax}$, of the initiating pores.

It is noted that near the endurance limit there is variability in the S-N response. In order to quantitatively characterize such a fatigue behavior, the fatigue strength at 10^8 cycles, determined by the staircase test method [109], was used to represent the endurance limit of the material. A total of 19 specimens were used in the staircase test

and the results are presented in Table 5.1 and Figure 5.1.

Assuming that the fatigue strength follows a normal distribution, the mean fatigue strength at 10^8 cycles and population standard deviation were estimated to be 85 MPa and 8.5 MPa, respectively, according to Dixon-Mood method [109]. The 95% confidence interval of the mean fatigue strength at 10^8 cycles is between 80 and 90 MPa.

5.2 Effect of porosity on fatigue strength

As shown in Table 5.1, for all test samples, porosity was observed to be the source of the initiation of the crack that ultimately caused failure. Only one crack initiation site was observed for each specimen (Figure 5.2). In approximately 70% of the samples the fatigue crack initiated at a pore located at or near the specimen surface (Figure 5.2 (a)). This is in agreement with the observations from other researchers [7, 11, 27, 82, 83]. In a small number of specimens, fatigue cracks initiated from large pores in the specimen interior (Figure 5.2 (b)). The initiating pores were outlined on the fracture surface, and their projected areas, distances from the specimen surface and maximum chord lengths were measured. The results for all staircase test specimens are presented in Table 5.1. Here, the initiating pore size refers to the equivalent diameter (D) as defined in Equation 3.1. The pore location is defined as the distance from the center of the pore to the specimen surface (t), which can be calculated by adding the equivalent radius ($\frac{D}{2}$) and the nearest distance from the edge of the pore to the specimen surface (Figure 5.2 (b)).

For the staircase test specimens, the initiating pores were observed to be generally large. The initiating pore diameters fall in the range of 100-1000 μm with an estimated mean value of 369 μm, as compared with the general casting porosity (Table 3.2) that had a mean 2-D pore diameter of 66 μm. These results are consistent with the results reported by Ting *et al.* [83], Yi *et al.* [13] and Boileau *et al*. [5]. The reason for this inconsistency between the metallographic and fractographic results is discussed later in this chapter.

In addition to pore size, location of the initiating pore relative to the free surface is

also an important factor. It is generally accepted [11, 83] that an interior pore is less detrimental to fatigue behavior than a surface pore. Here, the definition for differentiating surface pores from interior pores proposed by Murakami [122] is employed, i.e. if $\frac{D}{t} \geq 1.6$, the pore is at the surface; if $\frac{D}{t} < 1.6$, the pore is in the material interior.

Many studies have demonstrated that both pore size and stress level play an important role in determining the fatigue life of cast aluminum alloys [4, 6, 7, 11-13]. This holds true in the present study. As shown in Figure 5.3 (a), all specimens failed when the initiating pore size was greater than 500 μm within the range of stress amplitude examined in this study. To investigate the initiating porosity in the run-out specimens, those specimens that survived at 10^8 cycles in the staircase test were subsequently fatigued to failure at a stress amplitude of 110 MPa and the fracture surface was examined. According to the weakest link theory, we assume that the potential crack initiation site at both high and low stress level remains the same; thus the characteristics of the most critical pore can be measured for the run-out specimens. As shown in Figure 5.3 (a), the specimens survived 10^8 cycles when the critical pore size was less than 200 μm. When the critical pore sizes were between 200-500 μm, failure and run-out do not correlate with pore size and the equivalent circular pore diameter alone is insufficient to determine fatigue strength of the casting.

A clear distinction between the failures and run-outs is demonstrated when using ΔK as a correlating factor (Figure 5.3 (b)). The value of ΔK of the crack emanating from the initiating pores was estimated according to the equation proposed by Murakami *et al.* [122] and only the tensile portion of the applied stress range was used.

$$K_I = Y\sigma\sqrt{\pi\sqrt{A_{defect}}} \tag{5.1}$$

where K_I is the stress intensity factor; σ is the stress; A_{defect} is the area of the defect on the fracture surface; Y is a shape factor, which equals to 0.65 and 0.5 for a surface ($\frac{D}{t} \geq 1.6$) and internal pore ($\frac{D}{t} < 1.6$), respectively. Murakami *et al.* [122] showed that K_I mainly

depends on the area of the flaw and its location and is influenced by its shape by less than 10%. It can be seen from Figure 5.3 (b) that a threshold stress intensity factor range, ΔK_{th}, is apparent, below which specimen run-out occurs, and above which failure occurs in less than 10^8 cycles. This is consistent with the work of Mayer *et al.* [8], where the fatigue limit was correlated to the critical ΔK for die cast magnesium and aluminum alloys. For comparison, Figure 5.3 (c) gives the calculated results of ΔK based on the maximum chord length of the initiating pores. It is clear that, as compared with Figure 5.3 (b), the distinction between the failed and run-out specimens is less apparent, implying that the equivalent diameter is more suitable to correlate with fatigue strength of the present castings.

In fact, many experiments have demonstrated that fatigue cracks in cast aluminum alloy can readily initiate from pores even at a low stress level [4, 14]. This is because of the higher stress concentration developed at the sharp convex surfaces of the pores [20, 123]. Therefore, the endurance limit or fatigue strength at very high cycles should correspond to the stress level at which the crack emanating from the pore becomes non-propagating or arrested, rather than the stress at which no crack is initiated. Secondary cracks that emanated from pores were indeed observed in the fatigued specimens examined in this study (see an example shown in Figure 5.4). The metallographic sample was cut from the gage section of the specimen run-out at 81MPa, 10^8 cycles. The crack that emanated from the pore is assumed to be non-propagating as the specimen survived in the very long lifetime regime (10^8 cycles). The driving force for long crack growth is generally believed to be ΔK, or the effective stress intensity factor range, ΔK_{eff}, according to linear elastic fracture mechanics (LEFM) [7]. If ΔK of the long crack is below the crack growth threshold value, the crack should arrest; otherwise, the crack should continue to grow for the lifetime of the sample. Caton *et al.* [14] studied the endurance limit of W319 cast aluminum and suggested that ΔK_{eff} may offer a reasonable characterization of the non-propagation condition of small cracks.

However, a small crack effect has been observed for cast aluminum alloys [20, 26, 27, 104, 123] including the 319 aluminum examined here. An influence of stress level on small crack growth when using ΔK as a correlating parameter for cast aluminum alloy [4, 32] has also been observed. This indicates that ΔK is inappropriate for correlating the advance of small cracks when small scale yielding may be violated. Thus, there is a need to find a better correlation factor and its corresponding threshold, which is analogous to ΔK in LEFM, to characterize small crack behavior. Caton *et al.* [14, 103] proposed the parameter, $Q=[(\varepsilon_{max}\sigma_a/\sigma_{yield})^s a]$, to describe the small crack growth and the threshold value of this parameter worked well for prediction of the endurance limit. Subsequently, Shyam *et al.* [32] proposed another parameter which is the product of the monotonic and cyclic crack tip displacements to describe the growth rate of small fatigue cracks.

Despite these limitations on use of ΔK, for the purpose of developing an initial, simple statistical model describing the role of porosity on fatigue crack growth, we will presume the applicability of ΔK_{th} as the criterion for non-propagating cracks in cast aluminum. An apparent ΔK_{th} was determined from Figure 5.3 (b) to be 1.4 MPa $m^{1/2}$ for the present alloy. This result is similar to the results of Mayer *et al.* [8], in which the critical ΔK for small cracks emanating from porosity in a Al-Si-Cu high-pressure die-cast aluminum alloy is 1.85±0.10 MPa $m^{1/2}$ at a stress ratio of -1. This apparent ΔK_{th} can also be compared to threshold of long cracks measured for cast aluminum alloys, e.g., 2.7 MPa $m^{1/2}$ for a long crack of W319-T7 cast aluminum alloy with low SDAS at R = 0.1 was reported by Caton *et al.* [4]; 2.45-2.7 MPa $m^{1/2}$ was reported for an Al-Si-Cu die-cast aluminum at R = -1 [8]; 2.8-3.0 MPa $m^{1/2}$ was reported for an Al-Si cast alloy at R = -1 [22], and 1.1-1.4 MPa $m^{1/2}$ was reported for a Sr-modified A356 at R ≥0.8 [7]. The value of ΔK_{th} observed in the current study is somewhat below that of long cracks; this is consistent with observations of small cracks, which may grow at cyclic stress intensities below the long crack threshold.

5.3 A probabilistic model

Based on Equation 5.1, the initiating pore size and location was quantitatively correlated with the staircase test results. Nevertheless, it should be pointed out that all of these pores in this equation were pores from which the fatal crack initiated and the pore size was measured from the fractographs. Despite the success in correlating fatigue strength with the pores that initiated fatigue cracks [7, 8, 14], a direct and deterministic relationship between the casting porosity population and the fatigue strength should be more useful in predicting fatigue performance of cast aluminum alloys.

It is assumed that the fractographic measurements represent the pore size in a 3-dimensional space because the crack prefers to initiate from the largest cross section of the pore. However, the casting porosity population in Table 3.2 is based on 2-dimenstional measurements on metallographic sections. Therefore, in order to estimate the dependence of fatigue strength on the porosity population in the casting, it is necessary to reconstruct the 3-dimensional casting pore size distribution in the material based on the 2-dimensional measurements in order to correlate the size of metallographic and fractographic pores.

There is a significant difference in pore size characteristics determined using 3-dimensional and 2-dimensional analyses due to stereological effects and the irregular shapes of the pores. A statistical analysis of porosity in W319 cast aluminum [5, 124] showed that the pore size measured by 3-dimensional X-ray microtomographic method could be 3-4 times larger than the pore size measured by 2-dimensional metallographic techniques. A serial sectioning 3-D reconstruction method has also been developed recently by Lee *et al.* [125] to characterize the porosity in a cast magnesium alloy. As an engineering approximation, it can be assumed that the 3-dimensional pore sizes also obey a log-normal distribution. According to Fullman [126] and Underwood [127], the appropriate statistical parameters for the 3-dimensional pores can be estimated using the following expressions:

$$D_{3D} = \frac{\pi}{2m} \tag{5.2}$$

$$n_V = \frac{2mn_A}{\pi} \tag{5.3}$$

where D_{3D} is the average of the 3-D equivalent diameter; m is the average of the reciprocals of the equivalent pore diameter in a 2-D section, n_A and n_V are the number of pores per unit area and per unit volume, respectively. In accordance with Spowart *et al.* [128] each pore diameter in 2-D must be multiplied by a constant factor in order for Equation 5.3 to be valid. For the E319 investigated here, this factor was determined to be 1.36 using the method outlined in [128]. Similar to 2-D casting pore size, 3-D characteristics of casting pore size was assumed to have a log-normal distribution. Accordingly, the estimated average and standard deviation of the 3-D pore sizes along with the measured average and standard deviation of the 2-D pore sizes are presented in Table 5.2.

In order to estimate the dependence of fatigue strength on the porosity population in the casting, we assume that:

1) All pores are randomly distributed within the gage volume, with 3-D pore size following a log-normal distribution.

2) Since the porosity volume fraction is low (approximately 0.4%), the interaction among pores is assumed to be negligible.

3) The fatigue endurance limit can be represented by fatigue strength in the very long lifetime regime (10^8 cycles for this case), and its value is controlled by ΔK_{th}.

4) ΔK_{th} follows a normal distribution and is also assumed to be independent of stress level, crack length and SDAS of the material.

5) Whether or not a crack becomes dormant is determined by size and location of the pore that produces the maximum ΔK.

Table 5.2 Characteristics of the casting porosity population in E319 cast aluminum alloy in 2-D and 3-D

Dimension	Log-normal distribution		Porosity number density	Area or volume fraction
	Mean (μm)	STD (μm)		
Measured 2-D	66	−20.8 / +30.4	0.50 mm^{-2}	0.40%
Corrected 3-D	85	−26.8 / +39.1	5.48 mm^{-3}	0.40%

Accordingly, a probabilistic framework was developed to understand the effect of porosity population on fatigue strength in cast aluminum alloy. To predict the fatigue strength, a staircase test procedure is simulated using a modeling process schematically shown in Figure 5.5. Table 5.3 defines the terms and values used in the model.

Table 5.3 List of terms and values used in simulating the staircase test

Symbol	Meaning	Value
μ_p	Mean value of pore size in 3-D	85 μm
σ_p	Standard deviation of pore size in 3-D	−26.8 / +39.1 μm
n_V	Number of pores per volume	5.48 mm^{-3}
S	Surface area of the gage section	236 mm^2
V	Volume of the gage section	294 mm^3
σ_{a1}	Initial stress amplitude	81 MPa
σ_{ai}	Stress amplitude at sequence i	--
δ	Staircase stress increment	3 MPa
ΔK_{th}	Mean value of threshold stress intensity factor range	1.4 MPa-$m^{1/2}$
σ_K	Standard deviation of ΔK_{th}	0.1 MPa-$m^{1/2}$
$\Delta K(j)$	Stress intensity factor range of each pore	--
ΔK_{max}	Maximum value of $\Delta K(j)$	--
N_s	Number of specimens in a staircase test sequence	19
μ_s	Mean value of fatigue strength	--
μ_s	Standard deviation of fatigue strength	--

The procedure is illustrated as follows: a randomly distributed porosity population is initially generated within the gage volume (Figure 5.6), and each pore is assigned a size and location following the log-normal distribution. Regarding each pore size and location, the corresponding ΔK is calculated by Equation 5.1, in which Y = 0.65 for surface pores ($\frac{D}{t} \geq 1.6$) and Y = 0.5 for interior pores ($\frac{D}{t} < 1.6$). The maximum ΔK among these pores is thus identified and compared with ΔK_{th}. If the maximum ΔK is larger than ΔK_{th}, the specimen is predicted to fail, and the next simulation will generate a new gage volume with randomly distributed porosity and the individual ΔK for each pore will be calculated at a one-step lower cyclic stress level. If the maximum ΔK is less than ΔK_{th}, the specimen survives, and the next simulation will calculate individual ΔK for each pore at one-step higher stress level in a new gage volume. This process is repeated until the specified number of simulations is achieved. The generated results can then be statistically assessed according to the Dixon-Mood method [109].

Based on the porosity population listed in Table 5.2 and the specimen geometry shown in Figure 3.7 (a), the staircase test method for determining fatigue strength of E319 cast alloy was simulated using the probabilistic Monte-Carlo framework. A computer code was compiled using MatLab* to carry out the simulation. The staircase test with 19 samples in a group was simulated 100 times, and the results are presented in Figure 5.7. Figure 5.7 (a) shows the modeling results of mean and standard deviation of fatigue strength for each group of staircase test based on Dixon-Mood method. Figure 5.7 (b) compares the experimental results with the average of mean value and standard deviation of fatigue strength from simulation, which demonstrates that the modeling results (μ_s = 78 MPa and σ_s= 7.6 MPa) are in reasonable agreement with the staircase test results (μ_s = 85 MPa, and σ_s = 8.5 MPa), although the mean value (μ_s) and the standard deviation (σ_s) are slightly underestimated by the model. One reason for the difference is

* MatLab is a trademark of The MathWorks Inc.

possibly due to the method used for measuring porosity. Since the pore shape in 3-dimensions is quite irregular, a significant deviation may be generated when measuring the pore size (underestimated) and number density (overestimated) from 2-dimensional sections. A more detailed discussion is given in section 5.4 on the effect of porosity population on the fatigue strength.

In this model, the threshold stress intensity (ΔK_{th}) was regarded to be a random variable following a normal distribution with a mean value of 1.4 MPa-$m^{1/2}$ and a standard deviation of 0.1 MPa-$m^{1/2}$. Since the fatigue strength is proportional to the threshold stress intensity according to Equation 5.1, it can be expected that the fatigue strength is sensitive to the variation of the threshold stress intensity. Based on Monte-Carlo simulation, the sensitivity of fatigue strength to the variation of threshold stress intensity can be assessed. As shown in Figure 5.8 (a), when the standard deviation of ΔK_{th} is kept constant (0.1 MPa-$m^{1/2}$) and the mean value of ΔK_{th} increases from 1.0 to 2.0 MPa-$m^{1/2}$, the mean value of fatigue strength increases from 59 to 118 MPa while the standard deviation of fatigue strength is essentially unchanged. The subtle increase in standard deviation of fatigue strength with the mean value of ΔK_{th} is believed to result from sample to sample variations. Similarly, as shown in Figure 5.8 (b), when the mean value of ΔK_{th} is kept constant (1.4 MPa-$m^{1/2}$) and the standard deviation of ΔK_{th} increases from 0.1 to 0.5 MPa-$m^{1/2}$, the standard deviation of fatigue strength increases from 8 to 31 MPa-$m^{1/2}$ while the mean value of fatigue strength remains approximately 80 MPa-$m^{1/2}$.

The simulation results (Figure 5.9) show that the initiating pore size is approximately 250 μm on average, which is on the same order of magnitude with the experimentally measured mean value of initiating pore size of 369 μm, but three times the estimated mean pore size of the general pore population which is 85 μm (3-D). The major source of this difference between initiating pore size and general casting pore population lies in the fact that fractographic surface is a result of cracking through the

weakest links present in the test sample. Only the pore that carries the maximum ΔK in the gage section of the specimen is responsible for fatigue crack initiation; therefore the initiating pores tend to be those with large pore size and located near the specimen surface. As a result, the distribution of initiating pore size is not equivalent to the distribution of all porosity sizes in the material but is determined by the sizes of the large pores and their proximity to the surface.

This probabilistic model is capable of predicting the location at which a crack is initiated, either specimen surface or interior. As shown in Figure 5.10, $\frac{D}{t} \geq 1.6$ represents the surface pores and $\frac{D}{t} < 1.6$ represents the interior pores. The sharp peak of the distribution curve at $\frac{D}{t} = 2$ illustrates that most initiating pores are just touching the specimen surface. As $\frac{D}{t}$ increases from 2 to higher values, the pore begins to intersect the specimen surface. Thus the effective area of the pore inside the specimens becomes smaller, which results in a smaller ΔK, and therefore the probability of the pore as an initiator becomes lower. As $\frac{D}{t}$ decreases from 2 to lower values, the pore becomes an interior pore, and its ΔK is smaller than a surface pore of equivalent size. Therefore the probability of the interior pore will initiate a fatigue crack is lower. According to the simulation results, 60% of the initiating pores are defined as surface pores. This is in good agreement with the experimental results in which 70% of the initiation pores are surface pores.

This probabilistic model provides the opportunity of simulating fatigue strength, without conducting actual experimental tests which is expensive and time-consuming, as long as the casting porosity population within the specimens can be estimated. Based on this model, the effect of pore size distribution, effect of pore density, and effect of specimen volume and geometry on the fatigue strength can also be conducted. The results of these studies are described in the next section.

5.4 Parametric studies

Based on the probabilistic model described in Section 5.3, a procedure for Monte-Carlo simulation is developed. The major steps are:

1) Input the descriptors of the porosity population. These are: mean ($\ln(\mu_p)$) and standard deviation ($\ln(\sigma_p)$) of 3-D pore sizes, porosity number density (n_V), variables for materials and specimen geometry, including the threshold stress intensity factor of the alloy (ΔK_{th}), number of specimens to be tested (N_0), the specimen dimension (surface area (S) and volume (V)).

2) Calculate the total number of pores (N_t) to be generated for each specimen based on the specimen geometry and porosity number density ($N_t=n_V V$).

3) For each specimen, generate a porosity population sample (with total number of N_t pores) that is randomly distributed in the fatigue specimen, and the pore size follows a log-normal distribution with a mean value of $\ln(\mu_p)$ and a standard deviation of $\ln(\sigma_p)$.

4) From Equation 5.1, calculate the stress intensity factor range for each pore according to its diameter and distance to from the specimen surface at a certain level of stress amplitude (σ_a).

5) Identify the pore (initiating pore) which produces the highest value of stress intensity factor range, ΔK_{max}, in the specimen.

6) Based on the initiating pore size and location, calculate the fatigue strength, σ_0, of the specimen by

$$\sigma_0 = \frac{\Delta K_{th}}{Y\sqrt{\pi\sqrt{A}}} = \frac{\Delta K_{th}}{Q\sqrt{\pi x}} \tag{5.4}$$

7) Repeat steps 3) through 6) until the specified number of specimens (N_0) are modeled.

8) Statistically analyze the mean and standard deviation of the fatigue data by assuming the fatigue strength follows a normal distribution.

A total of 10^4 specimens were simulated for each case using the Monte-Carlo method. The preliminary simulated results have demonstrated that a sample size of 10^4

specimens is sufficient to produce consistent and accurate results. The parameters used for the simulation, together with three geometries of specimens with volume from 30-5000mm^3 are listed in Table 5.4. An example simulation is shown in Figure 5.11 for a given porosity population. It appears that the calculated fatigue strength can be described quite well by a normal distribution function.

Table 5.4 Parameters of porosity population and sample volume used for Monte-Carlo simulation

Porosity population			**Sample volume, mm^3**
Number density, n_v, mm^{-3}	**Mean value , μ_p, μm**	**Standard deviation σ_p, μm**	
Range: 0.1 to 20	80	-27/40	295
5.0	**Range: 30 to 300**	-10/15 to -167/250	295
5.0	80	**Range: 0.05 to 1.10**	295
5.0	80	-27/40	**Range: 30 to 5000**

[1] Note:

1. The pore sizes here are the equivalent diameters of the pores according to Equation 3.1.

2. The standard deviation of pore size is mapped from the lognormal distribution, which is dependent on the mean value of pore size (μ_p), and different in the positive and negative values.

5.4.1 Mean pore size

The influence of mean pore size (μ_p) on predicted fatigue strength is shown in Figure 5.12. Here, μ_p was varied from 30 μm to 300 μm. As expected, the predicted mean fatigue strengths (μ_s) decrease with increasing mean pore size (Figure 5.12 (a)). This is because a large mean pore size results in large initiating pores. Figure 5.13 shows the influence of assumed mean pore size distributions of casting porosity (30μm, 100μm and 300μm) on the predicted initiating pore size distributions generated using the Monte-Carlo simulation. It can be seen that, for a given casting porosity population and a specimen with a sufficient number of pores, the initiating pore sizes are usually those

large ones from the casting porosity. By Equation 5.4, a large initiating pore size results in low mean fatigue strength, as observed in Figure 5.12 (a).

On the other hand, the predicted standard deviation of the fatigue strength (σ_s) also decreases with increasing mean pore size. As shown in Figure 5.12 (b), the decrease in predicted σ_s follows a similar trend to the decrease in mean fatigue strength. This seems counterintuitive, but can be understood based on the fact that the distribution of fatigue strength is directly associated with the distribution of $\left(1/\sqrt{x_i}\right)$, rather than x_i, through Equation 5.4. This means that a smaller initiating pore (x_i) leads to a higher value of $\left(1/\sqrt{x_i}\right)$, thus a greater fatigue strength. Qualitatively, a variation in x_i for smaller pores will lead to a larger variation in $\left(1/\sqrt{x_i}\right)$, and thus a larger scatter in fatigue strength or σ_s compared to a porosity population with a larger mean pore size. An example is given in Figure 5.14, which shows that when other parameters are held constant and mean pore size is increased, the probability density function curves, $q(x)$, move toward large pore sizes, while the shape of the $q(x)$ curve does not change significantly (Figure 5.14 (a)). This implies that increasing mean pore size does not significantly change the scatter of initiating pore sizes. In contrast, it is noted from Figure 5.14 (b) that the scatter of $\left(1/\sqrt{x_i}\right)$ is decreased as the mean pore size (μ_p) increases from 50 to 150 μm, which in turn results in a lower σ_s, as observed in Figure 5.12 (b).

5.4.2 Standard deviation of pore size

Figure 5.15 shows the effect of a change in standard deviation (σ_p) of the assumed porosity population on the predicted fatigue strength. As σ_p is asymmetric, the data are presented in terms of $\ln(\sigma_p)$. It can be seen from Figure 5.15 (a) that the mean fatigue strength decreases with increasing σ_p when the mean pore size is kept constant. This is understandable based on the fact that high standard deviation of a porosity population generates more large pores, as illustrated in Figure 5.16 (a). Figure 5.16 (b) displays the

relative percentage of the predicted initiating pore sizes from porosity populations with the same mean pore size but with different standard deviation of pore size. It is clear that, even if the mean pore sizes are held constant, the casting pore size distribution with larger standard deviation produces much larger initiating pores. As shown in Figure 5.16 (b), when mean pore size is held constant at 80μm, but the log normal standard deviation is increased 50% (from -13/16 μm to -40/80μm), the expected crack initiation pore size range increases by a factor of 5 to 20 (from 80-200μm to 400-4000μm). Consequently, pore populations with high standard deviations should produce lower mean fatigue strengths, even if the mean pore size measured metallographically is unchanged.

The larger initiating pore sizes resulting from greater pore size variation will reduce the range of $\left(1/\sqrt{x_i}\right)$, resulting in a more uniform fatigue strength (lower σ_s). This has been demonstrated in Figure 5.15 (b), showing that σ_s decreases with increasing σ_p in particular, when $\ln(\sigma_p) < 0.69$ (or $\sigma_p < -40/80\mu m$).

5.4.3 Number density of pores

The effect of number density of pores in the specimen on fatigue strength is displayed in Figure 5.17. A large number density results in low μ_s and low σ_s in a specified specimen. As shown in Figure 5.17 (a), when the number density increases from 0.1 to 4.0mm^{-3}, μ_s decreases approximately 20-50%, depending on other parameters. When $n_V > 4.0\text{mm}^{-3}$, μ_s slightly decreases with increasing porosity number density. Similarly, a decrease in the σ_s was observed when $n_V < 4.0\text{mm}^{-3}$. When pore number density exceeds 4.0 mm^{-3}, fatigue strength variation remains low and nearly constant (see Figure 5.17 (b)).

When the overall number of pores in a given volume increases, the number of large pores that can initiate cracks also increases. An example showing the effect of increasing pore density on the initiating pore population is shown in Figure 5.18. When more large pores are available for crack initiation, one would expect both mean fatigue

strength and fatigue strength variation to be reduced.

5.4.4 Specimen volume and geometry

When applying the data obtained from laboratory specimens to cast components, the so-called size-effect must be taken into account. A large specimen volume means that more pores are present in the specimen ($N_t = n_V V$). In this sense, the influence of specimen volume on fatigue strength is similar to that of porosity number density.

For a given volume, the effect of specimen geometry on fatigue strength can also be simulated. To illustrate this, three types of specimen geometries were selected, i.e., cubic, cylindrical (with height equal to its radius), and spherical, respectively. A shape factor is used to discriminate their geometry differences, defined as:

$$S = \kappa V^{2/3} \tag{5.5}$$

where S and V are the surface area and volume of the specimen, respectively, and κ is the shape factor, which corresponds to 6.0, 5.86 and 4.84 for cubic, cylindrical and spherical specimens, respectively.

As shown in Figure 5.19, the mean fatigue strength and its standard deviation are predicted to decrease with increasing specimen volume. For the porosity population given in Figure 5.19 (a), the predicted fatigue strength generated from a typical fatigue testing specimen (100 - 300 mm^3) subjected to uniform stresses could be approximately 10% higher than those from cast components (usually >5000 mm^3). Moreover, the predicted fatigue strength is also dependent on specimen geometry. As shown in Figure 5.19 (a) and (b), for a fatigue specimen with volume of 30 - 5000 mm^3, the differences in predicted mean fatigue strength and its standard deviation are not evident between cubic and cylindrical specimens, suggesting that the geometry of the fatigue specimen gage volume, either cylindrical or cubic in general, has no significant influence on the testing results for cast aluminum alloys.

On the other hand, the predicted mean fatigue strengths for spherical specimens

are approximately 6%-10% higher than those of cubic and cylindrical specimens. This is because a high ratio of S/V enhances the probability for pores to locate in the surface volume of a specimen. As compared with interior pores with the same diameter, a surface pore gives a higher stress intensity factor (see Equation 5.1) due to the greater shape factor. Therefore, low fatigue strength is produced for specimens with high ratio of S/V. This is in agreement with the simulated results as indicated in Figure 5.19 (a) for the three types of specimens. The spherical specimen gives the highest mean fatigue strength owing to its lowest S/V ratio (4.84) as compared with cubic (S/V=6.0) and cylindrical (S/V=5.86) specimens. This suggests that the local geometry may have certain influence on the fatigue life of a practical casting with an irregular shape.

Additionally, it is noted that the S/V ratio does not significantly alter the distribution of initiating pore sizes, as demonstrated in Figure 5.20. All the initiating pore sizes fall in the same range of 100 to 350 μm for the three specimens. This accounts for the observation that no difference in standard deviation of fatigue strength is evident between the three specimen geometries.

5.5 Summary

The effect of porosity population on fatigue strength at 10^8 cycles was investigated for E319 cast aluminum alloy through both experiment and simulation, and the main findings are summarized as follows:

1) An endurance limit was observed for the E319 cast aluminum alloy in the long lifetime regime, and the fatigue strength at 10^8 cycles was statistically determined via the staircase test, which gives a mean value of 85 MPa and standard deviation of 8.5 MPa.

2) Large pores, either at specimen surfaces or in the specimen interior were found to be responsible for crack initiation in all tested specimens, and the fatigue strength was closely associated with an apparent ΔK_{th} for fatigue crack growth.

3) A probabilistic model was developed to establish the relationship between the general casting porosity population and the fatigue strength. Based on this model, the staircase test was simulated using the Monte-Carlo method, which gives mean value and standard deviation of fatigue strength of 78 MPa and of 7.6 MPa, respectively. This was in reasonable agreement with the experimental results.

4) Good agreement was obtained between simulation and experiment regarding the initiating pore size and location. The average initiating pore size is 369 μm in experiment, compared to the average initiating pore size of 250 μm in the simulation. The distribution of initiating pore size shows a distribution of sizes of large pores which is substantially higher than the distribution of all pore sizes in the material, as expected. The percentage of surface and subsurface pores among the initiating pores is 70% in experiment and 60% in simulation.

5) The simulated results showed that mean pore size, standard deviation and number density of the porosity population, together with specimen volume and shape, all are predicted to influence the fatigue strength of the alloys. In general, the fatigue strength is determined by the largest pores present in the castings. The mean and standard deviation of fatigue strength decrease with increasing mean pore size, standard deviation and number density of porosity by enhancing the probability that large pores will initiate fatal cracks in a given specimen. Specimen volume and geometry were also found to influence the fatigue strength by affecting the number of pores and their intersection with the specimen surface. Assuming an identical porosity population, increasing specimen volume and/or surface over volume ratio can lead to a decrease in fatigue strength by up to 10%.

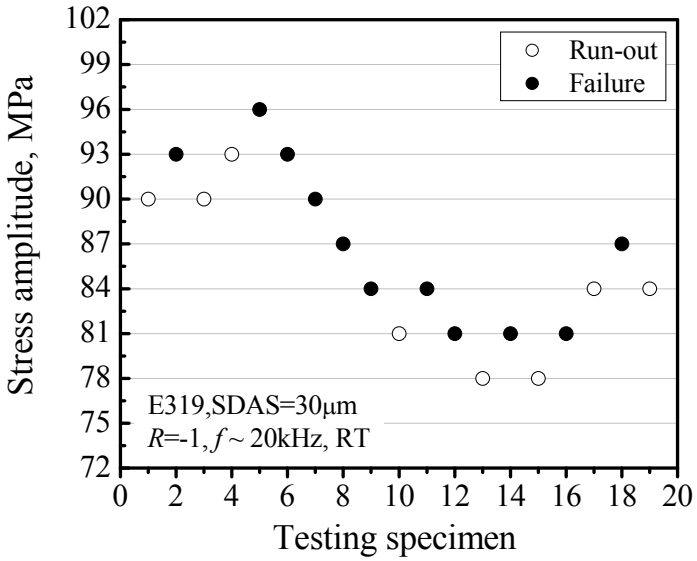

Figure 5.1 Experimental staircase test results for E319 cast aluminum alloy at 10^8 cycles, which gives a mean value of 85 MPa and a standard deviation of 8.5 MPa.

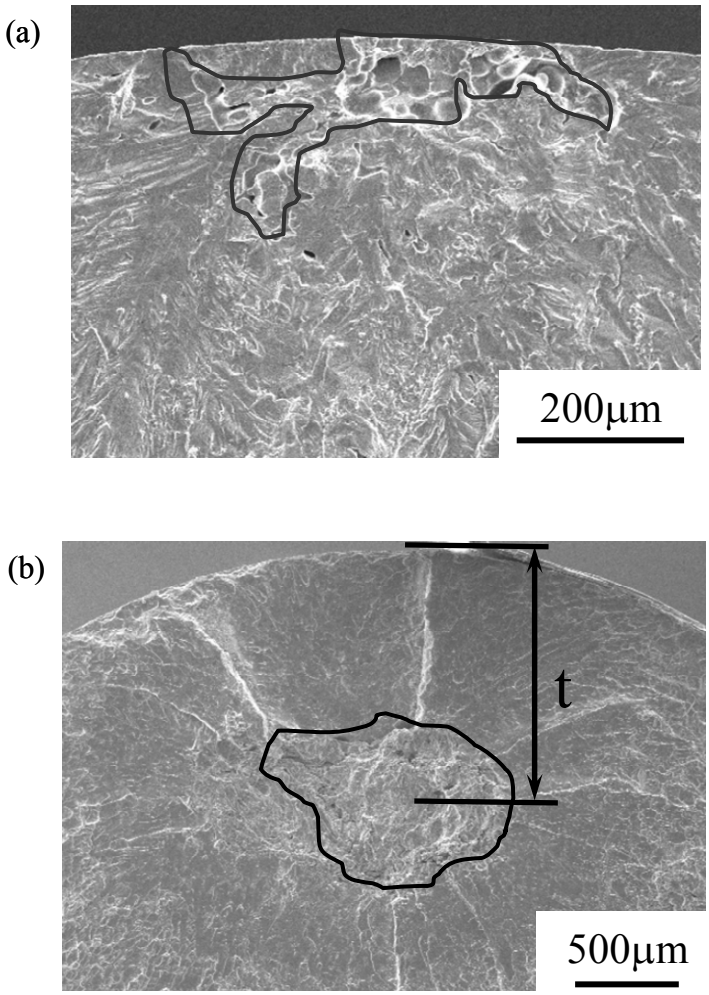

Figure 5.2 Fracture surfaces of specimens failed during staircase test (a) a pore at specimen surface acting as a crack initiator (σ_a = 90 MPa); and (b) a pore in the specimen interior acting as a crack initiator (σ_a = 87 MPa).

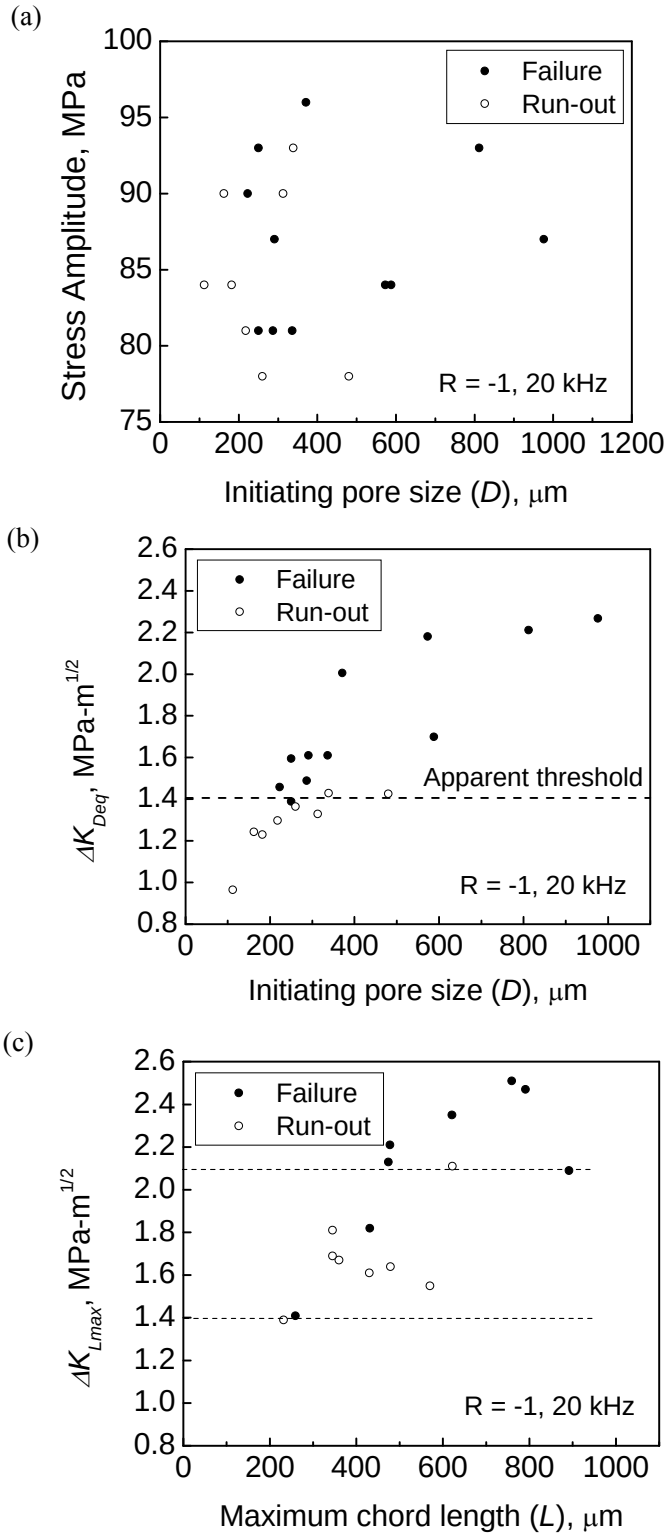

Figure 5.3 The correlation of staircase results with (a) the initiating pore size (D), (b) the calculated $\triangle K_{Deq}$ by using equivalent diameter of the initiating pore (D) as the crack size and (c) the calculated $\triangle K_{max}$ by using maximum chord length (L) of the initiating pore as the crack size.

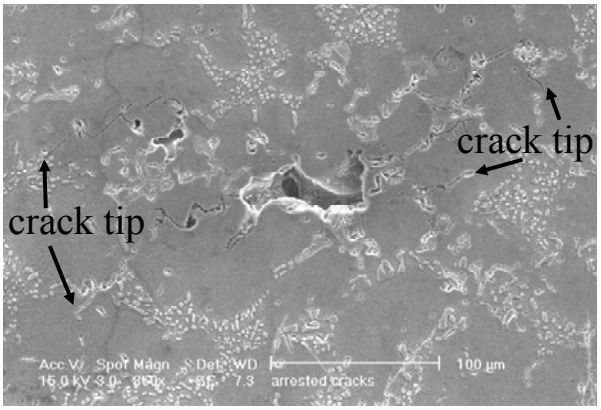

Figure 5.4 An SEM micrograph showing the secondary cracks emanated from a pore. The metallographic sample was cut from the gage section of the specimen run-out at 81MPa, 10^8 cycles.

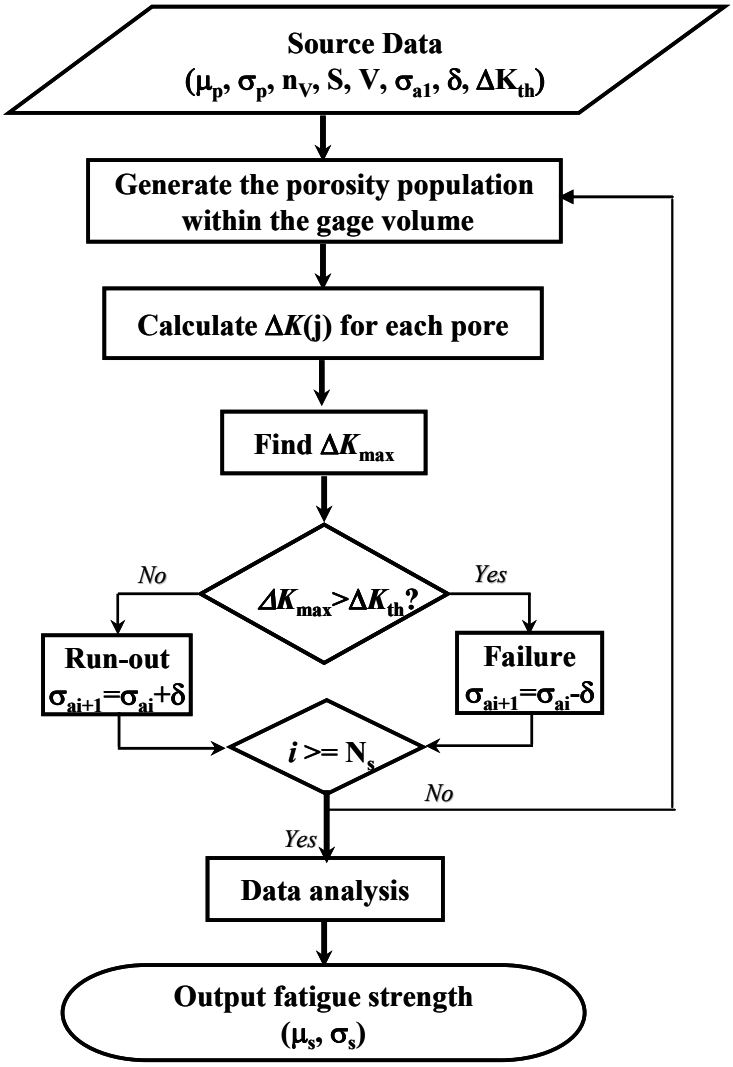

Figure 5.5 Flow chart for the Monte-Carlo simulation.

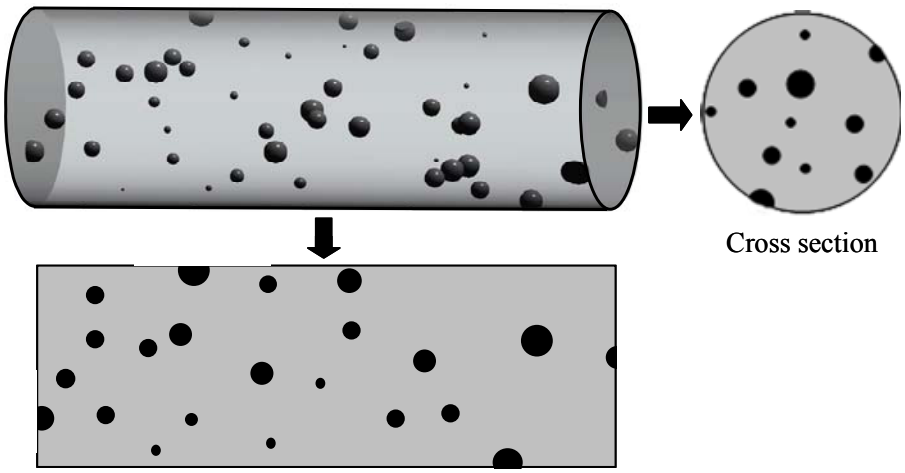

Figure 5.6 Schematic of porosity generated within the sample gage volume.

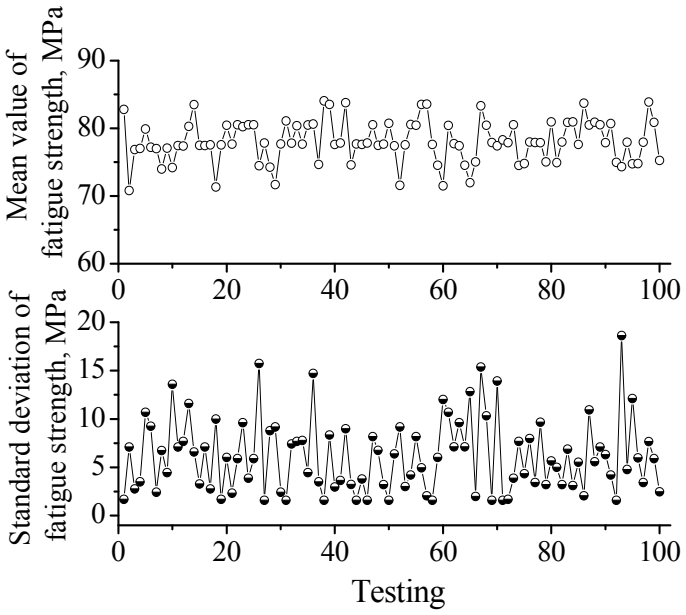

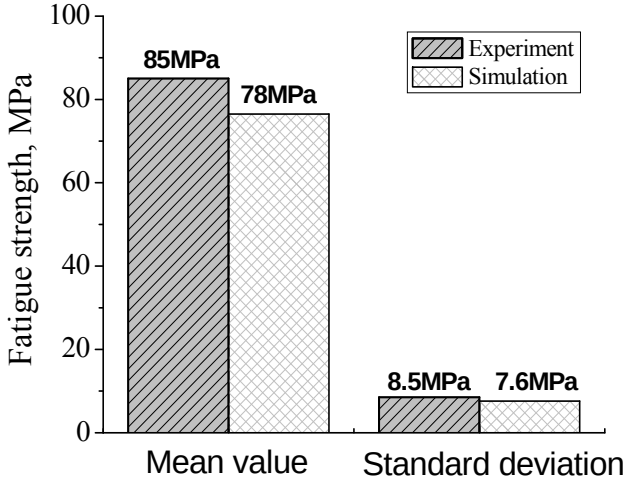

Figure 5.7 (a) The 100 simulated staircase results based on 19 specimens, and (b) the correspondent average of mean and standard deviation based on staircase simulations and comparison with experimental values.

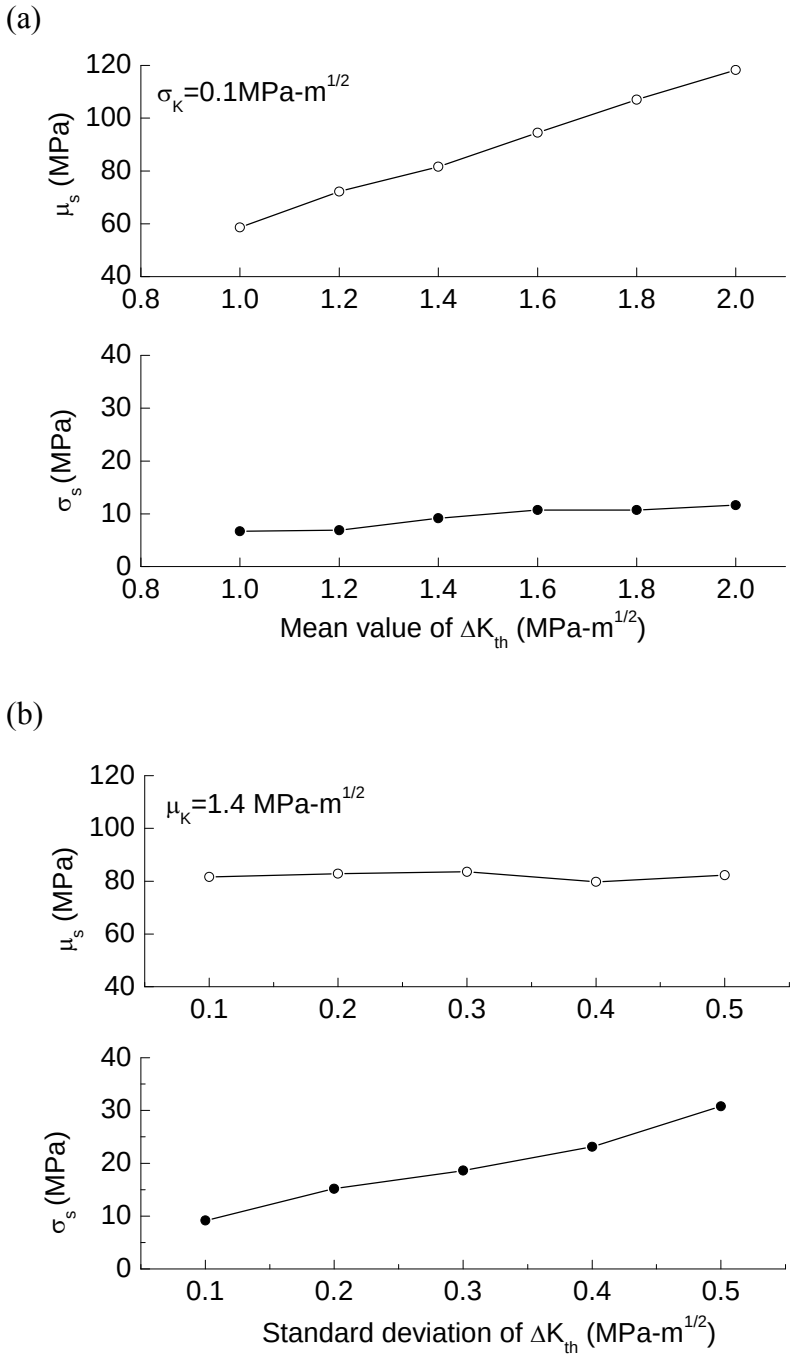

Figure 5.8 Sensitivity of fatigue strength to the variation of (a) the mean value of the threshold stress intensity ΔK_{th} and (b) the standard deviation of the threshold stress intensity ΔK_{th}.

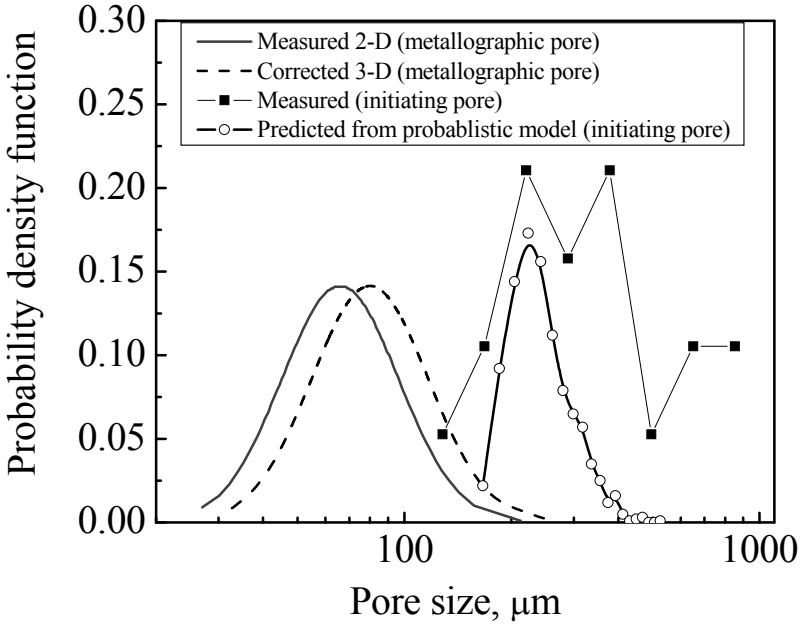

Figure 5.9 Comparison of initiating pore size distribution with the general casting (metallographic) pore size distribution.

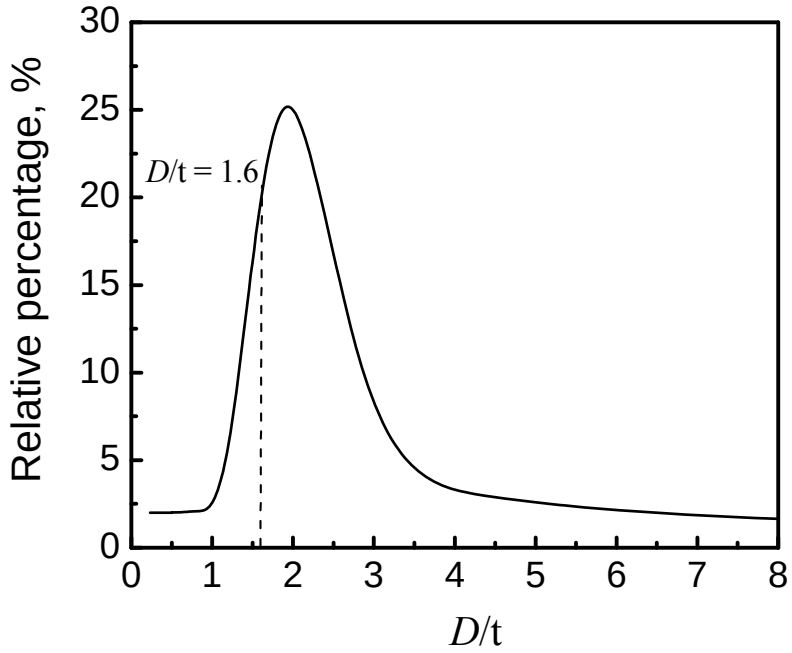

Figure 5.10 Distribution of initiating pore location relative to the specimen surface based on simulation; when D/t>1.6, the pore is on surface, when D/t<1.6, the pore is in the material interior, where D is the equivalent radius of a pore; t is the distance from the center of the pore to the specimen surface.

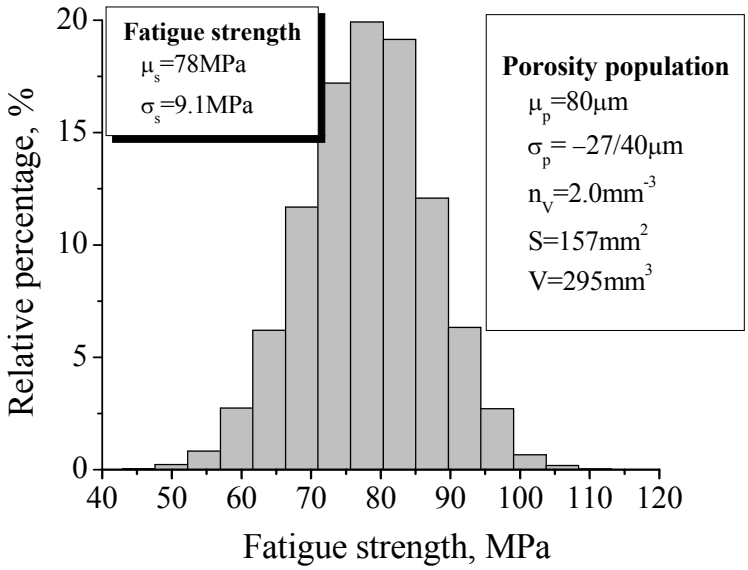

Figure 5.11 A simulated example of the predicted fatigue strength distribution based on the probabilistic model. The simulation was conducted on 10^4 specimens, showing that the fatigue strength can well be described by a normal distribution function with mean fatigue strength of 78 MPa, and standard deviation of 9.1 MPa.

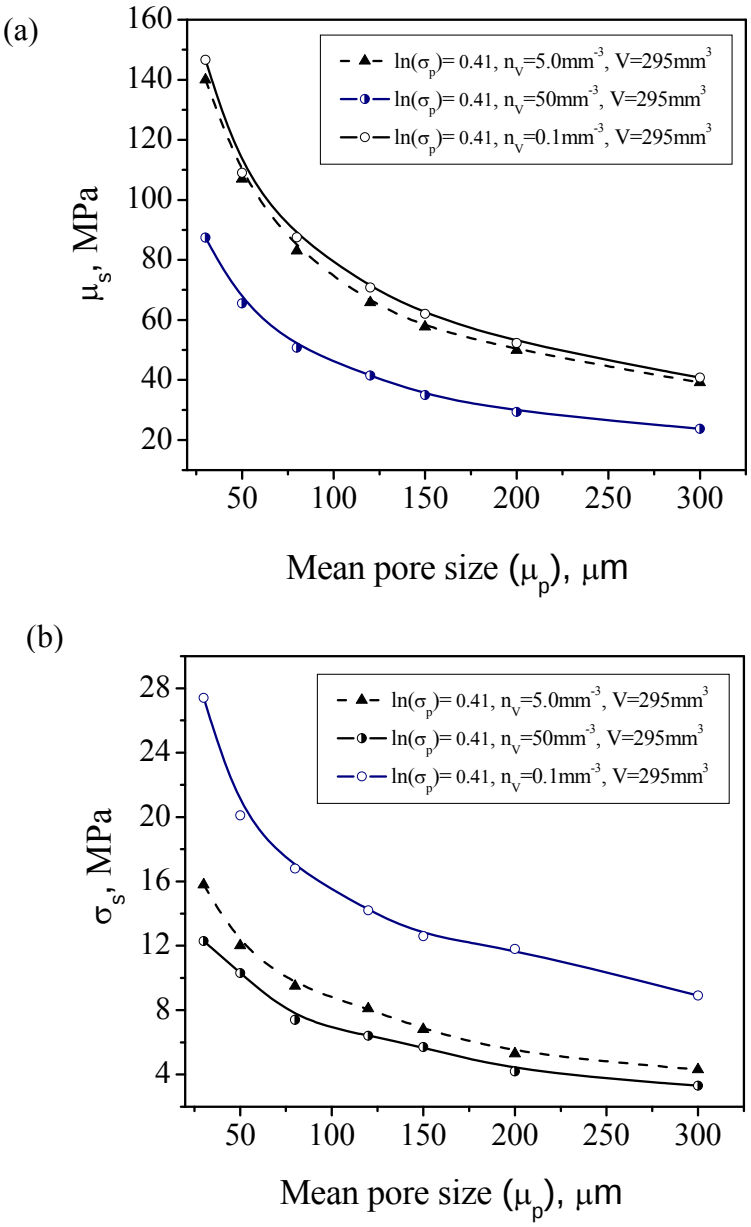

Figure 5.12 Influence of the assumed mean pore size on the predicted fatigue strength, indicating that both (a) mean value and (b) the predicted standard deviation, obtained using Monte-Carlo simulation for three different porosity populations.

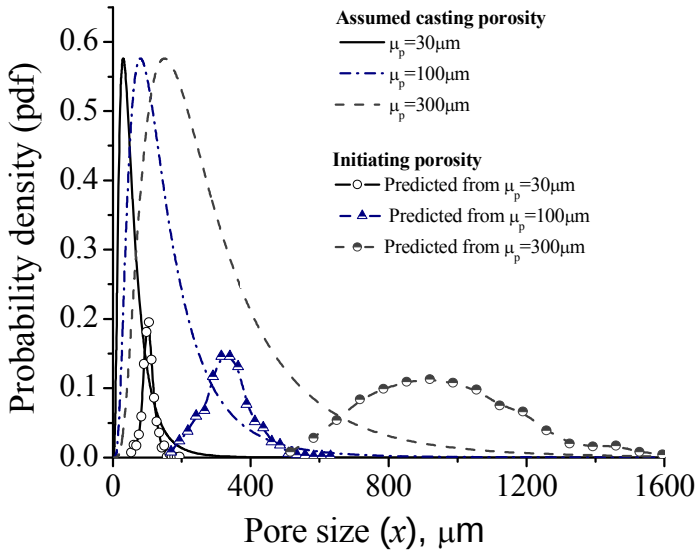

Figure 5.13 The distributions of casting pore size and the corresponding initiating pore size calculated based on the model. The mean pore sizes varies from 30μm, 100μm to 300μm, while other parameters kept constants ($\ln(\sigma_p)$= 0.41, n_v=2.0mm^{-3}, V=295mm^3).

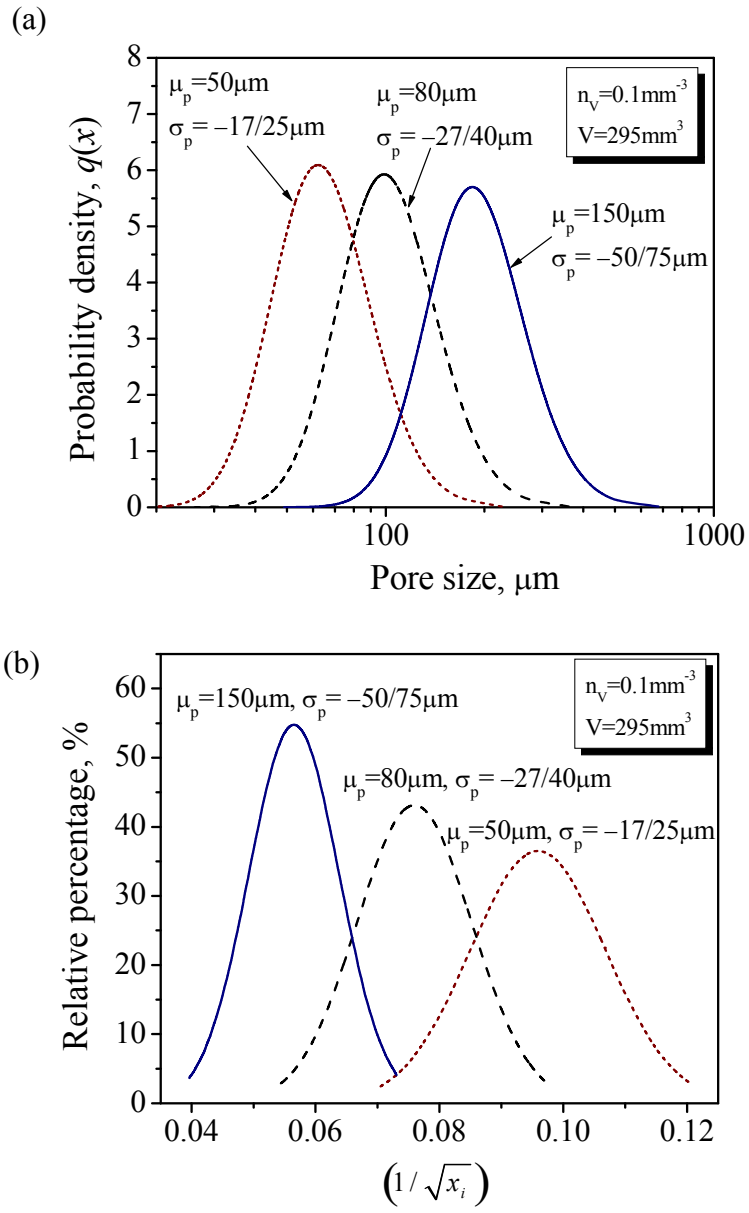

Figure 5.14 (a) Simulated probability density function of $q(x)$ for samples with three different mean pore size, and (b) the corresponding distributions of $\left(1/\sqrt{x_i}\right)$. Note that, although σ_p varies with μ_p, the value of $\ln(\sigma_p)$ was actually kept constant (0.41).

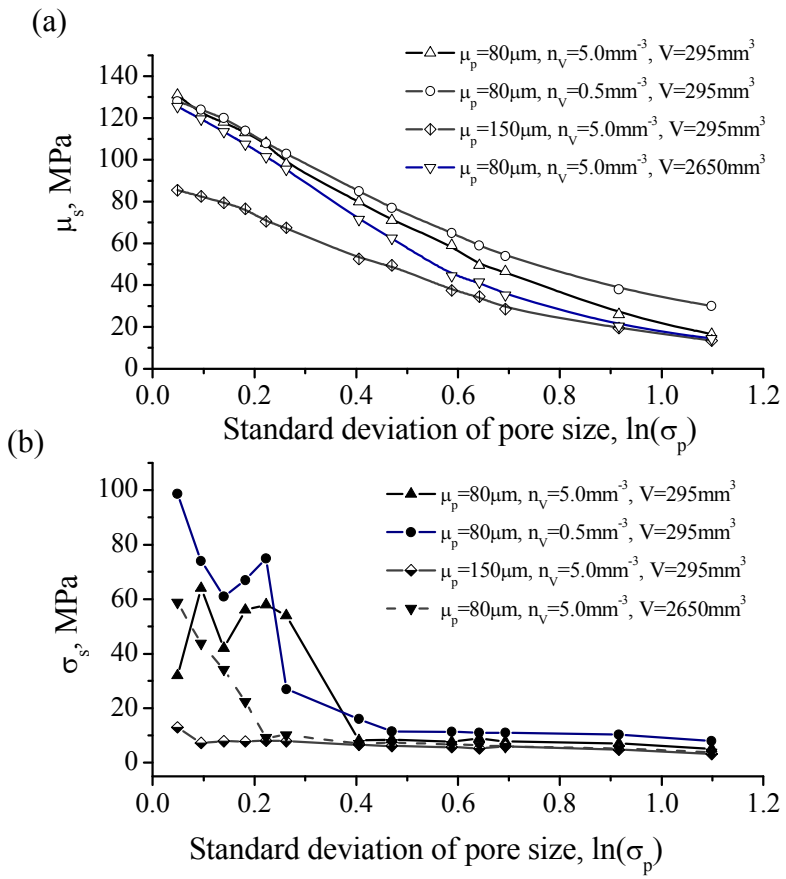

Figure 5.15 Influence of pore size standard deviation on (a) mean fatigue strength (μ_s), and (b) fatigue strength standard deviation (σ_s), obtained using Monte-Carlo simulation.

(a)

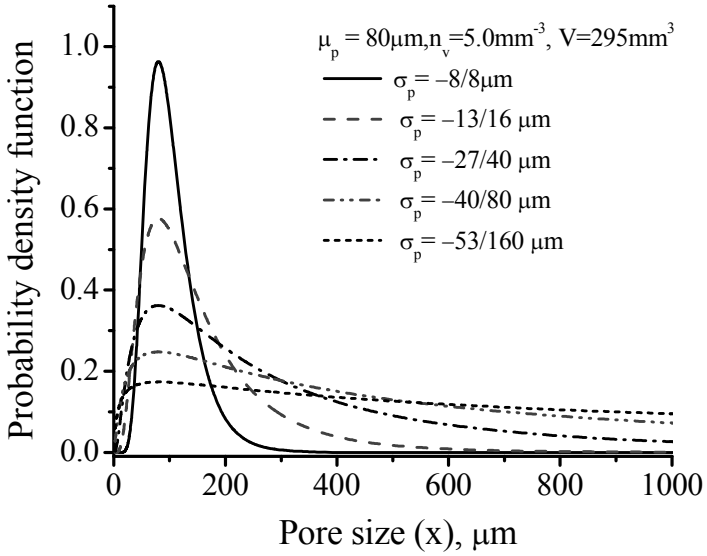

(b)

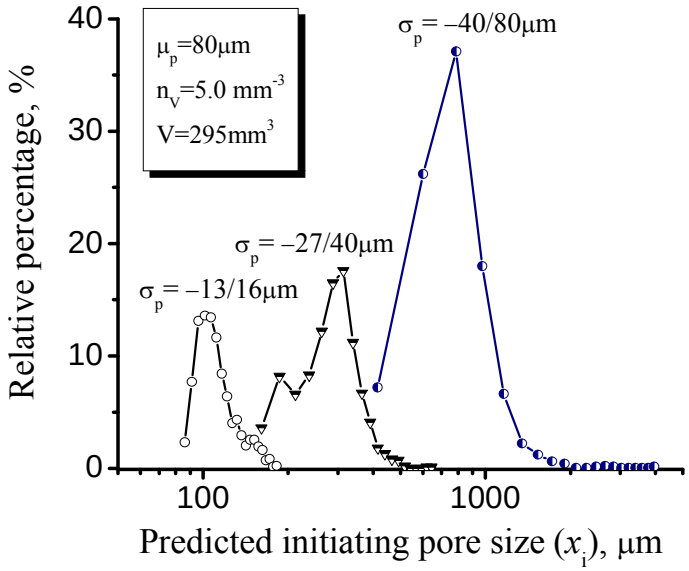

Figure 5.16 (a) The distributions of pore sizes from the general porosity population with various standard deviation, and (b) the resultant predicted initiating pore sizes distributions.

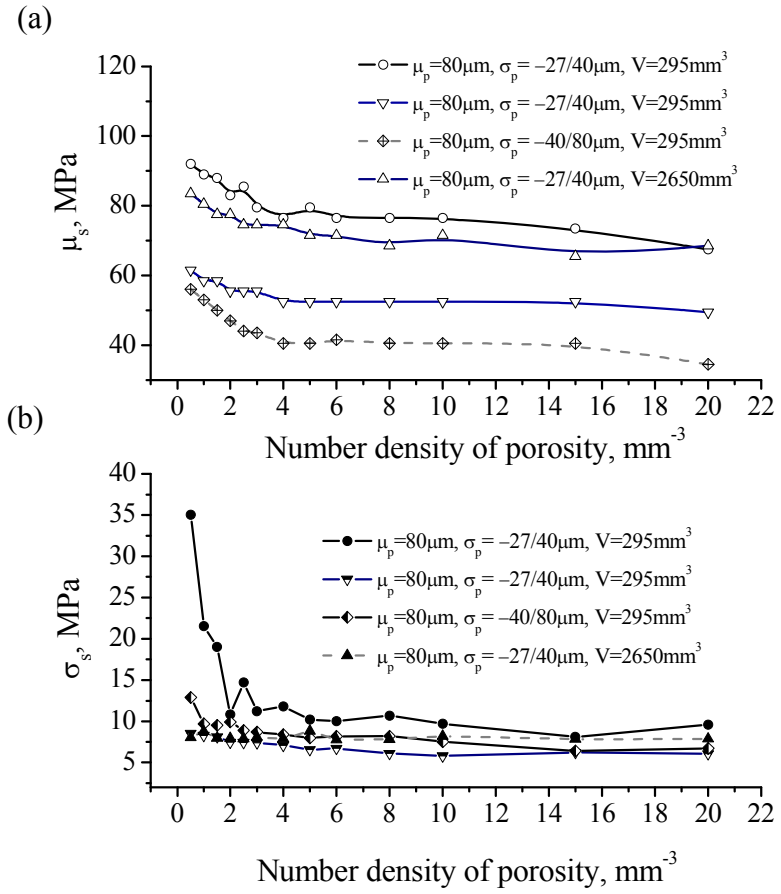

Figure 5.17 The effect of porosity number density on (a) mean fatigue strength (μs), and (b) fatigue strength standard deviation (σ_s).

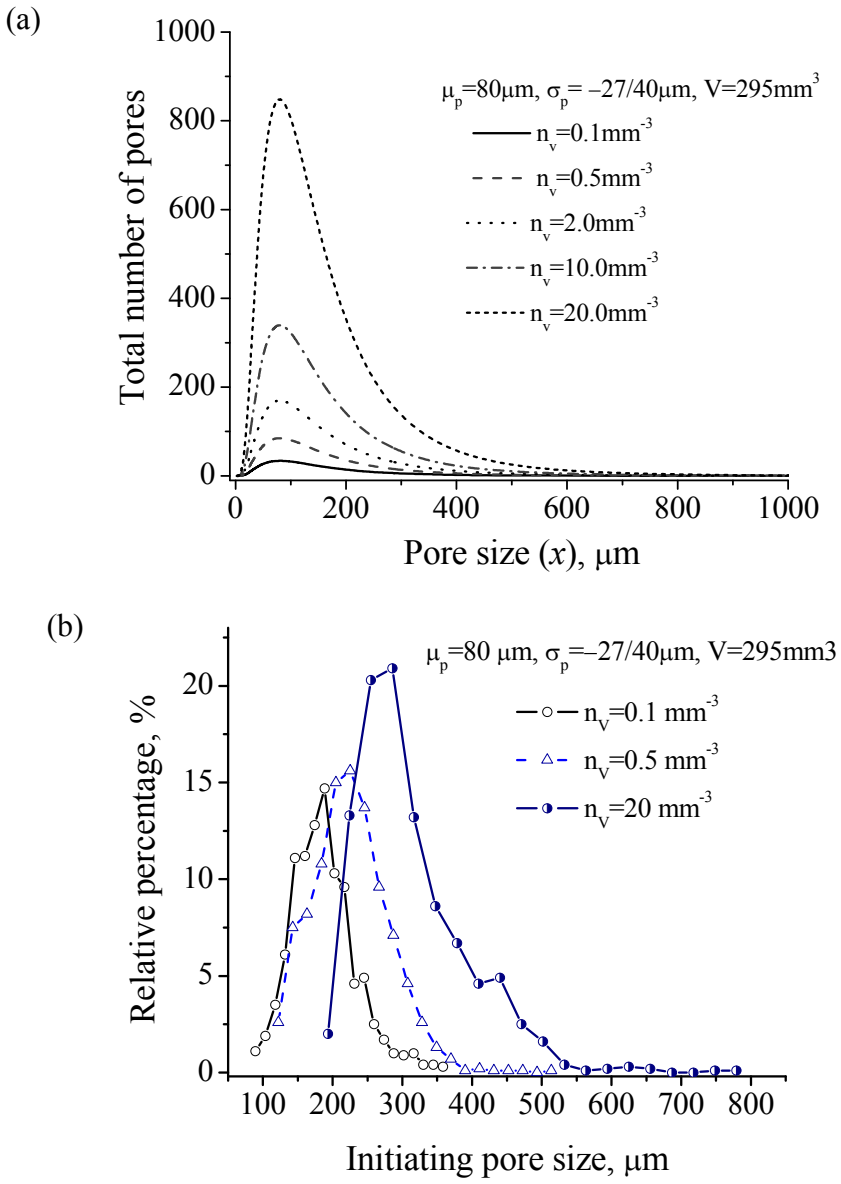

Figure 5.18 (a) The total pore size distribution of the general porosity populations with various number density in a specimen (V=295mm^3), and (b) the resultant initiating pore size distributions.

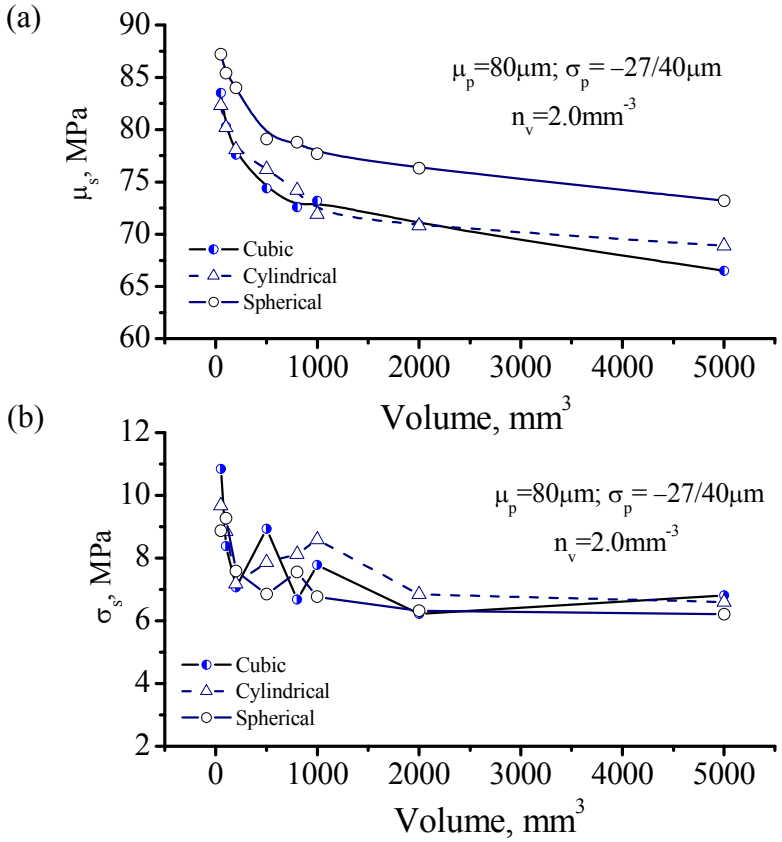

Figure 5.19 Effect of specimen volume, and specimen geometry on (a) mean fatigue strength (μ_s), and (b) fatigue strength standard deviation (σ_s).

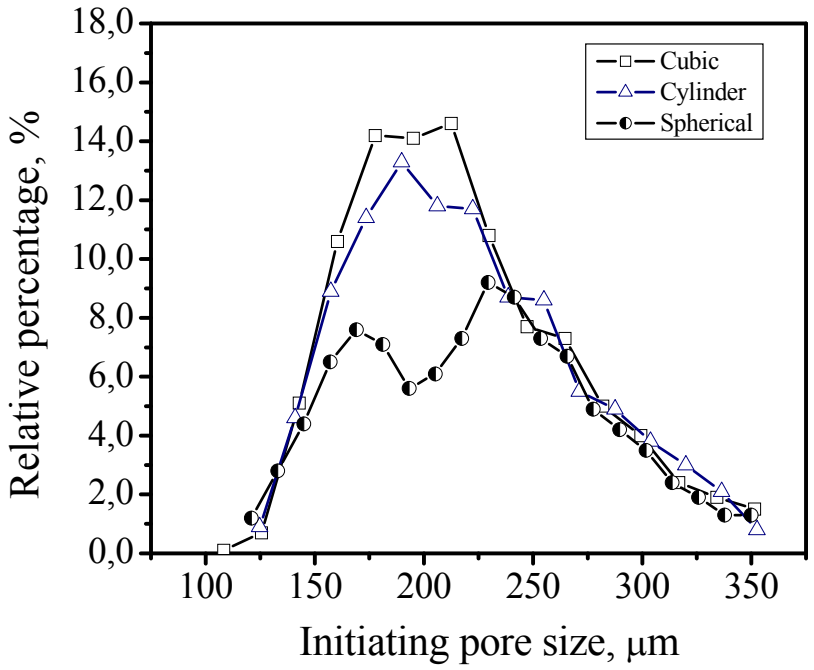

Figure 5.20 The simulated initiating pore size distributions for specimens with cubic, cylinder and spherical shapes at fixed volume ($V=50mm^3$). The general casting porosity is assumed to follow a lognormal distribution with $\mu_p=80\mu m$, σ_p = -27/40μm, $n_v=5.0mm^{-3}$.

Chapter 6

Conclusion and recommendations

6.1 Conclusions

A study of the fatigue behavior of an E319 cast aluminum alloy in the long lifetime regime was conducted at both ultrasonic and conventional frequencies at room temperature and elevated temperature. The S-N behavior, fatigue crack initiation and propagation at each frequency and at each temperature were examined and compared. Effect of frequency, environment and temperature on the fatigue crack growth behavior and, therefore, fatigue lives of the E319 cast aluminum alloy were investigated and modeled. Fatigue strength at 10^8 cycles was examined and a probabilistic model was developed to establish the relationship between fatigue strength and the porosity population in the E319 cast aluminum alloy. For this study, the following conclusions can be made.

(1) At room temperature, the S-N curve of E319 cast aluminum alloy shows a plateau beyond 10^7 cycles at room temperature, indicating that an apparent fatigue limit exists. In the lifetime regime of less than 10^7 cycles, fatigue life at 20 kHz is 5 to 10 times longer than that at 75 Hz; while at 10^7 cycles, the effect of frequency on the fatigue performance is substantially reduced. At elevated temperature (150 and 250^{o}C), however, the S-N curves continue to drop beyond 10^7 cycles and the slope of the curves increase with temperature. At 150 and 250^{o}C, the difference in fatigue life between 20 kHz and 75 Hz persists over the entire range of stress examined.

(2) Fatigue crack initiation was not influenced by either frequency or temperature in the E319 cast aluminum alloy. The fatigue cracks initiated predominately from pores located at or very close to the specimen surface. Fatigue life is dominated by fatigue

crack propagation and the number of cycles required to cause failure is determined by the crack growth rate. The crack growth rate at 20 kHz is lower than at 30 Hz at all temperature examined and this in turn results in the observed longer fatigue life at 20 kHz.

(3) The difference in fatigue crack growth rate between 20 kHz and 30 Hz in air at all temperatures examined is attributable to an environmental effect. For aluminum alloys, water was found to increase fatigue crack growth rate and thereby speed the failure of the material. At a given stress intensity factor range, ΔK, fatigue crack growth rate increases with water exposure, *P/f*, until it reaches the maximum value when saturation of the environmental effect occurs. Fatigue testing at 30 Hz in air represents higher water exposure than fatigue testing at 20 kHz, and therefore the crack growth rates at 30 Hz are higher than that at 20 kHz. The dependence of crack growth rate on water exposure closely follows the dependence of hydrogen concentration on water exposure, which supports the assumption that the enhancement of crack growth rate caused by environment is determined by the concentration of hydrogen in the plastic zone. This behavior is characterized by a modified superposition model of the influence of hydrogen on fatigue crack growth rate. In this model, hydrogen-induced increase of fatigue crack growth rate is assumed to be proportional to the square root of hydrogen concentration, which is determined by the transport rate of water molecules from the surrounding environment to the crack tip. Based on the modified superposition model, fatigue crack growth rates over the entire range of ΔK in various environments with different water exposure can be predicted and the predictions generally agree well with the experimental observations.

(4) Fatigue resistance decreases with increased temperature. At 20 kHz, increasing test temperature from 20 to 150^{o}C results in a modest decrease in fatigue resistance, while a significant decrease in fatigue resistance occurs at 250^{o}C. The temperature dependence of fatigue strength at 10^8 cycles follows the temperature dependence of yield and tensile strength closely. The fatigue crack growth rate at all temperatures can

successfully described by a universal version of the modified superposition model, in which crack growth rate is a function of normalized stress intensity factor range, $\Delta K/(E\sigma_{ys})$. This model provides a framework to separately characterize the intrinsic effect of temperature on mechanical properties and the effect of environment at elevated temperature. The effect of temperature on fatigue resistance primarily results from the intrinsic effect of temperature on Young's modulus and yield strength. The environmental contribution to fatigue crack growth rates modestly decreases with increasing temperature.

(5) The fatigue strength at 10^8 cycles in the E319 cast aluminum alloy was statistically determined at 20 kHz via the staircase test, which gives a mean value of 85 MPa and standard deviation of 8.5 MPa. Large pores, either at specimen surfaces or in the specimen interior were found to be responsible for crack initiation in all tested specimens, and the fatigue strength was correlated with both size and location of the initiating pores through a threshold stress intensity factor for fatigue crack growth, ΔK_{th}.

(6) A probabilistic model was developed to establish the relationship between the casting porosity population and the fatigue strength. Based on this model, staircase testing was simulated using the Monte-Carlo method, which gives mean value and standard deviation of fatigue strength of 78 MPa and of 7.6 MPa, respectively. This was in reasonable agreement with the experimental results. Good agreement was obtained between simulation and experiment regarding the initiating pore size and location. The average initiating pore size is 369 μm in experiment, compared to the average initiating pore size of 250 μm in the simulation. The distribution of initiating pore size shows, as expected, a distribution of sizes of large pores instead of a distribution of all porosity sizes in the material. The percentage of surface and subsurface pores among the initiating pores is 70% in experiment and 60% in simulation.

(7) The simulations show that mean pore size, standard deviation and number density of the porosity population, together with specimen volume and shape, all are predicted to influence the fatigue strength of the alloys. In general, the fatigue strength is determined

by the largest pores present in the castings. The mean and standard deviation of fatigue strength decrease with increasing mean pore size, standard deviation and number density of porosity by enhancing the probability of large pores to initiate dominant cracks in a specimen. Specimen volume and geometry were also found to influence the fatigue strength by affecting the number of pores and their intersection with the specimen surface. Assuming an identical porosity population, increasing specimen volume and/or surface over volume ratio can lead to a decrease in fatigue strength by up to 10%.

(8) Finally, environmental effects need to be considered when ultrasonic fatigue is used in the lifetime regime where fatigue lives are determined by the fatigue crack growth rates of aluminum alloys which are under conventional loading frequency in service. The modified superposition model in this thesis provides a basis to quantitatively characterize the environment-induced increase of fatigue crack growth rates in an E319 cast aluminum alloy. In the lifetime regime where a fatigue limit occurs, the effect of frequency is substantially reduced because the fatigue limit is correlated with the fatigue crack growth threshold, rather than the fatigue crack growth rate. In this case, the ultrasonic fatigue technique is a valuable method to rapidly quantify the fatigue limit and reveal the crack initiation pores. Even when environmental effect on fatigue performance is present, ultrasonic fatigue technique is still applicable in identifying the fatigue crack initiation sites because the fatigue cracks always initiate from the “weakest link” in the alloy.

6.2 Recommendations for future study

Based on the findings of the present study, the following recommendations are made for future work in this area.

(1) In the modified superposition model developed in this thesis, the hydrogen-induced increase of fatigue crack growth rate is proportional to the square root of water exposure for the E319-T7 cast aluminum. However, in the model in the published

literature, the fatigue crack growth rate is linearly proportional to the water exposure for some high strength aluminum alloys with peak-aged heat treatment. It is possible that the different correlations of fatigue crack growth rate and water exposure are caused by heat treatment which promotes different slip modes in crack propagation and, therefore, different dependence of fatigue crack growth rates on hydrogen concentration. However, this hypothesis needs to be proved. It was reported that the effect of frequency on A356-T6 cast aluminum alloy was more significant compared to E319-T7. So it would be helpful to investigate the environmental effect on fatigue crack propagation of A356-T6 to further explore the mechanisms of hydrogen assisted fatigue crack growth behavior.

(2) In the modified superposition model, the pure-mechanical fatigue crack growth rate is assumed to be equivalent to the experimentally measured fatigue crack growth rate at 20 kHz in dry air. Although the environmental effect can be reasonably expected to be small in this condition, it has been reported that a very small amount of water vapor would influence the fatigue crack growth rate. Therefore, it is recommended that small crack growth tests be conducted in high vacuum to obtain the pure-mechanical fatigue crack growth data. Similarly, at elevated temperature, the pure-mechanical and saturation fatigue crack growth rates are assumed to be equivalent to those at room temperature after normalization of stress intensity factor range by Young's modulus and yield strength. It would be more convincing to experimentally measure these values.

(3) Fatigue crack growth tests in water vapor with 100% and S-N tests in dry air are recommended to be conducted in order to confirm the prediction of the dependence of the fatuge crak growth rate and S-N behavior on water exposure based on the modified superspositon model.

(4) Although the dependence of fatigue crack growth rate on water exposure can be successfully explained by the mechanisms of hydrogen assisted cracking, there is no direct evidence from the detailed SEM observations of fatigue fracture surfaces that different mechanisms are operating. Detailed study of the dislocation structure ahead of

the crack tip might be able to provide some critical information about how hydrogen mechanisms are influencing fatigue crack growth behavior in this alloy.

(5) Significant scatter in the S-N fatigue data of E319 cast aluminum alloy was observed, which is believed to come from the variation of initiation pore size and the variation of crack growth rate. In this study, statistical analysis of initiation pore size has been performed. However, the variation of small crack growth rate, which can be affected by microstructure, heat treatment, load ratio, temperature and environment, is not well understood. A statistical analysis procedure needs to be developed to account for the variations in fatigue crack growth rates. Based on the knowledge of variation of initiation pore size and crack growth rate, probabilistic methods can be used to predict the variability of fatigue properties of cast aluminum through the crack growth model.

References

1. Engler-Pinto, C.C., Jr., et al., *A comparative investigation on the high temperature fatigue of three cast aluminum alloys*, in *SAE technical paper #2004-01-1029*.
2. Mayer, H., *Fatigue crack growth and threshold measurements at very high frequencies.* International Materials Reviews, 1999. **44**(1): p. 1-34.
3. Smith, T.J., et al., Metall. & Mater. Trans. A, 1999. **30**: p. 133-146.
4. Caton, M.J., et al., *The effect of solidification rate on the growth of small fatigue cracks in a cast 319-type aluminum alloy.* Metall. Trans. A, 1999. **30**(12): p. 3055-3068.
5. Boileau, J.M. and J.E. Allison, *The Effect of Solidification Time and Heat Treatment on the Fatigue Properties of a Cast 319 Aluminum Alloy.* Metallurgical and Materials Transactions A, 2003. **34A**(9): p. 1807-1820.
6. Zhu, X., et al., *Effects of microstructure and temperature on fatigue behavior of E319-T7 cast aluminum alloy in very long life cycles.* International Journal of Fatigue, 2006. **28**(11): p. 1566-1571.
7. Couper, M.J., A.E. Neeson, and J.R. Griffiths, *Casting Defects and the Fatigue Behaviour of an Aluminium Casting Alloy.* Fatigue Fract. Engng Mater. Struct., 1990. **13**(3): p. 213-227.
8. Mayer, H., et al., *Influence of porosity on the fatigue limit of die cast magnesium and aluminium alloys.* International Journal of Fatigue, 2003. **25**(3): p. 245-256.
9. McDowell, D.L., et al., *Microstructure-based fatigue modeling of cast A356-T6 alloy.* Engineering Fracture Mechanics, 2003. **70**(1): p. 49-80.
10. Murakami, Y. and M. Endo, *Effects of defects, inclusions and inhomogeneities on fatigue strength.* International Journal of Fatigue, 1994. **16**(3): p. 163-182.
11. Skallerud, B., T. Iveland, and G. Harkegard, *Fatigue life assessment of aluminum alloys with casting defects.* Engineering Fracture Mechanics, 1993. **44**(6): p. 857-874.
12. Wang, Q.G., D. Apelian, and D.A. Lados, *Fatigue behavior of A356-T6 aluminum cast alloys. Part I. Effect of casting defects.* Journal of Light Metals, 2001. **1**(1): p. 73-84.
13. Yi, J.Z., et al., *Scatter in fatigue life due to effects of porosity in cast A356-T6 aluminum-silicon alloys.* Metallurgical and Materials Transactions a-Physical Metallurgy and Materials Science, 2003. **34A**(9): p. 1879-1890.
14. Caton, M.J., et al., *Demonstration of an endurance limit in cast 319 aluminum.* Metall. Trans. A, 2003. **34A**(1): p. 33-41.
15. Roth, L.D., ed. *Ultrasonic fatigue testing*. 9 ed. Metals handbook: Mechanical testing, ed. J.R. Newby. Vol. 8. 1985, American Sociaty of Metals: Metals Park, OH.

16. Mason, W.P., *Piezoelectric crystals and their application in ultrasonics*. 1950, New York: Van Nostrand.
17. Tien, J.K., et al., Rev. Sci. Instrum., 1975. **46**: p. 840.
18. Kirchner, H.O.K., et al., *Plastic deformation under simultaneous cyclic and unidirectional loading at low and ultrasonic frequencies.* Materials Science and Engineering, 1984. **68**: p. 197-206.
19. Yeske, R.A. and L.D. Roth, in *Ultrasonic fatigue*, J.M. Wells, et al., Editors. 1982, TMS-AIME: Warrendale, PA. p. 365.
20. Gao, Y.X., et al., *A micro-cell model of the effect of microstructure and defects on fatigue resistance in cast aluminum alloys.* Acta Materialia, 2004. **52**(19): p. 5435-5449.
21. Yi, J.Z., et al., *Microstructure-based Fatigue Life Prediction for Cast A356-T6 Aluminum-Silicon Alloys.* Metall. Trans., 2006. **37B**: p. 301-311.
22. Stanzl-Tschegg, S.E., et al., *In-service loading of AlSill aluminium cast alloy in the very high cycle regime.* International Journal of Fatigue, 1993. **15**(4): p. 311-316.
23. Engler-Pinto, C.C., Jr., et al., *High cycle fatigue of cast aluminum alloys at ultrasonic frequency*, in *SAE technical paper #2006-01-0540*.
24. Zhu, X., et al., *A Probabilistic Model of Fatigue Strength Controlled by Porosity Population in A 319-type cast Aluminum Alloy Part I: Model Develop.* Metall. Trans. A, 2007. **38A**(5): p. 1111-1122.
25. Yi, J.Z., et al., *A Probabilistic Model of Fatigue Strength Controlled by Porosity Population in A 319-type cast Aluminum Alloy Part II: Monte-Carlo Simulation.* Metall. Trans. A, 2007. **38A**(5): p. 1123-1135.
26. Shyam, A., et al., *Small fatigue crack propagation from micronotches in the cast aluminum alloy W319.* Scripta Materialia, 2004. **50**(8): p. 1109-1114.
27. Caton, M.J., J.W. Jones, and J.E. Allison, *Use of small fatigue crack growth analysis in predicting the S-N response of cast aluminium alloys*, in *Fatigue Crack Growth Thresholds, Endurance Limits, and Design, ASTM STP 1732*, J.C.J. Newman and R.S. Piascik, Editors. 2000, ASTM: West Conshohocken, PA. p. 285-303.
28. Lados, D.A., D. Apelian, and J.K. Donald, *Fatigue crack growth mechanisms at the microstructure scale in Al-Si-Mg cast alloys: Mechanisms in the near-threshold regime.* Acta Materialia, 2006. **54**(6): p. 1475-1486.
29. Newman Jr, J.C., E.P. Phillips, and M.H. Swain, *Fatigue-life prediction methodology using small-crack theory.* Inter. J. Fatigue, 1999. **21**(2): p. 109-119.
30. Ritchie, R.O., in *Small fatigue cracks*, R.O. Ritchie and J. Lankford, Editors. 1986, The Metallurgical Society, Inc.: Warrendale, PA. p. 1-5.
31. Shiozawa, K.n.-b.s., Y. Tohda, and S.-M. Sun, *Crack initiation and small fatigue crack growth behaviour of squeeze-cast Al-Si aluminium alloys.* Fatigue & Fracture of Engineering Materials & Structures, 1997. **20**(2): p. 237-247.

32. Shyam, A., J.E. Allison, and J.W. Jones, *A small fatigue crack growth relationship and its application to cast aluminum.* Acta Materialia, 2005. **53**(5): p. 1499-1509.
33. Caton, M.J., J.W. Jones, and J.E. Allison, *The influence of heat treatment and solidification time on the behavior of small-fatigue-cracks in a cast aluminum alloy.* Materials Science and Engineering A, 2001. **314**(1-2): p. 81-85.
34. Suresh, S., *Fatigue of Materials*. Second edition ed. 1998: Cambridge University Press. 679.
35. Elber, W., *Damage tolerance in aircraft structures*, in *ASTM STP*. 1971, American Society for Testing and Materials: Philadelphia, PA. p. 230-242.
36. Taylor, D., Int J Fatigue, 1988. **10**: p. 67-79.
37. Smith, R.A., Int. J. Fract., 1977. **13**: p. 717-720.
38. Wei, R.P., *Environmental considerations for fatigue cracking.* Fatigue & Fracture of Engineering Materials & Structures, 2002. **25**(8-9): p. 845-854.
39. Gangloff, R.P., *Hydrogen-assisted cracking*. Comprehensive structural integrity :[fracture of materials from Nano to Marco], ed. I. Milne, R.O. Ritchie, and B. Karihaloo. Vol. 6. 2003: Amsterdam ; Boston : Elsevier.
40. Petit, J., G. Henaff, and C. Sarrazin-Baudoux, *Environmentally assisted fatigue in gaseous atmosphere*. Comprehensive structural integrity :[fracture of materials from Nano to Marco], ed. I. Milne, R.O. Ritchie, and B. Karihaloo. Vol. 6. 2003: Amsterdam ; Boston : Elsevier.
41. Laird, C. and P. Charlsey, *Ultrasonic fatigue*, in *Ultrasonic fatigue*, J.M. Wells, et al., Editors. 1982, TMS-AIME: Warrendale, PA. p. 183.
42. Coffin, L.E., *Ultrasonic fatigue*, in *Ultrasonic fatigue*, J.M. Wells, et al., Editors. 1982, TMS-AIME: Warrendale, PA. p. 423.
43. Tien, J.K., *Ultrasonic fatigue*, in *Ultrasonic fatigue*, J.M. Wells, et al., Editors. 1982, TMS-AIME: Warrendale, PA. p. 1.
44. F. Ackermann, et al., Acta Metall., 1984. **32**(5): p. 715-725.
45. Mughrabi, H., Mat. Sci. Eng., 1978. **33**: p. 207.
46. P. Lukas, M. Klesnil, and R. Fiedler, Philos. Mag., 1969. **20**: p. 799-805.
47. Awatani, J., K. katagiri, and K. Koyanagi, Philos. Mag. A, 1978. **38**(3): p. 349-352.
48. Tong, Z.X. and J.P. Bailon, Fatigue Fract. Eng. Mater. Struct., 1995. **18**(7/8): p. 847-859.
49. P. Lukas, et al., Mater. Sci. Eng., 1985. **70**: p. 91-100.
50. Chen, D.L., et al., *The electron channelling contrast technique applied to the characterisation of dislocation structures in the vicinity of fatigue crack.* Fatigue Fract. Eng. Mater. Struct., 1997. **20**(11): p. 1551-1561.
51. Holper, B., et al., *Near threshold fatigue crack growth in aluminium alloys at low and ultrasonic frequency: Influences of specimen thickness, strain rate, slip behaviour and air humidity.* International Journal of Fatigue, 2003. **25**(5): p. 397-411.

52. Holper, B., et al., *Near threshold fatigue crack growth at positive load ratio in aluminium alloys at low and ultrasonic frequency: influences of strain rate, slip behaviour and air humidity.* International Journal of Fatigue, 2004. **26**(1): p. 27-38.
53. Baik, Y.M. and K.S. Kim, *The combined effect of frequency and load level on fatigue crack growth in stainless steel 304.* Int J Fatigue, 2001. **23**: p. 417-425.
54. Shih, Y.-S. and J.-J. Chen, *The frequency effect on the fatigue crack growth rate of 304 stainless steel.* Nucl Engng Design, 1999. **191**: p. 225-230.
55. Gudladt, H.J. and J. Petit, *Stage II crack propagation of Al-Zn-Mg single crystals in dry & wet atmospheres.* Scr. Metall. Mater., 1991. **25**: p. 2507-2512.
56. Ruiz, J. and M. Elices, *Fatigue crack growth in high vacuum and gaseous atmospheres in an aluminium alloy.* Vacuum, 1994. **45**(10-11): p. 1069-1071.
57. Stanzl, S.E., H.R. Mayer, and E.K. Tschegg, *The influence of air humidity on near-threshold fatigue crack growth of 2024-T3 aluminum alloy.* Materials Science and Engineering A, 1991. **147**(1): p. 45-54.
58. Papakyriacou, M., et al., *Influence of atmospheric moisture on slow fatigue crack growth at ultrasonic frequency in aluminium and magnesium alloys.* Fatigue & Fracture of Engineering Materials & Structures, 2002. **25**(8-9): p. 795-804.
59. Stanzl-Tschegg, S., *Fatigue crack growth and thresholds at ultrasonic frequencies.* International Journal of Fatigue, 2006. **28**(11): p. 1456-1464.
60. Piasick, R.S. and R.P. Gangloff, *Environmental fatigue of an Al-Li-Cu alloy: Part I. Intrinsic crack propagation kinetics in hydrogenous environments.* Metall. Trans. A, 1991. **22A**(October): p. 2415-2428.
61. Broom, T. and A. Nicholson, *Atmospheric corrosion-fatigue of age-hardened aluminium alloys.* J. Inst. Metals, 1960. **89**: p. 183-190.
62. Bennett, J.A., *Changes in the influence of atmospheric humidity during fatigue of an aluminium alloy.* J. Res. National Bureau Standards-C. Eng. Instrum., 1964. **68C**(April - June): p. 91-100.
63. McEvily, A.J. and J.L. Gonzalez Velazquez, *Fatigeu crack tip deformation processes as influenced by the environment.* Metall. Trans. A, 1992. **23A**(August): p. 2211-2221.
64. Pelloux, R.M.N., *Crack extension by alternate shear.* Eng. Fract. Mech., 1970. **1**: p. 697-704.
65. Davidson, D.L. and J. Lankford, *The effect of water vapor on fatigue crack tip mechanics in 7075-T651 aluminum alloy.* Fatigue Eng. Mater. Struct., 1983. **6**(3): p. 241-256.
66. Henaff, G., K. Marchal, and J. Petit, *On fatigue crack propagation enhancement by a gaseous atmosphere: experimental and theoretical aspects.* Acta Metall. Mater., 1995. **43**(8): p. 2931-2942.
67. Lynch, S.P., *Environmetally-assisted cracking: overview of evidence for an adsorption-induced localised-slip process.* Acta Metall., 1988. **36**(10): p. 2639-

2661.
68. Gao, M., P.S. Pao, and R.P. Wei *Chemical and metallurgical aspects of environmentally assisted fatigue crack growth in 7075-51 aluminum alloy.* Metallurgical Transctions A, 1988. **19A**: p. 1739-1750.
69. E. E. Huber, J. and J. C. T. Kirk, *Work function changes due to the chemisorption of water and oxygen on aluminum.* Surf. Sci., 1966. **5**: p. 447-465.
70. Ricker, R.E. and D.J. Duquette, *The role of hydrogen in corrosion fatigue of high purity Al-Zn-Mg exposed to water vapor.* Metallurgical Transctions A, 1988. **19**: p. 1775.
71. Oriani, R.A., *Environment induced cracking of metals*, ed. R.P. Gangloff and M.B. Ives. 1990, Houston, TX: NACE.
72. Birnbaum, H.K. and P. Sofronis, *Hydrogen-enhanced plasticity - a mechanism for hydrogen related fracture.* Mater. Sci. Eng. A, 1993. **176**: p. 191-202.
73. Ro, Y.J., S.R. Agnew, and R.P. Gangloff. *Environmental exposure dependence of low growth rate fatigue crack damage in Al-Cu-Li/Mg*. in *VHCF-4*. 2007. Ann Arbor, MI: TMS.
74. Mayer, H., et al., *Endurance limit and threshold stress intensity of die cast magnesium and aluminium alloys at elevated temperatures.* International Journal of Fatigue, 2005. **27**(9): p. 1076-1088.
75. Baxter, W.J., D.R. Lesuer, and C.K. Syn, *Thermal activation of fatigue damage.* Metall. & Mater. Trans. A, 2000. **31A**: p. 63-69.
76. Srivatsan, T.S., *Mechanisms governing cyclic deformation and failure during elevated temperature fatigue of aluminum alloy 7055.* International Journal of Fatigue, 1999. **21**(6): p. 557-569.
77. Juijerm, P. and I. Altenberger, *Effect of temperature on cyclic deformation behavior and residual stress relaxation of deep rolled under-aged aluminium alloy AA6110.* Materials Science and Engineering: A, 2007. **452-453**: p. 475-482.
78. Cloutier, C.A., et al., eds. *A process model for the age hardening of a 319-type aluminum alloy*. Automotive alloys III, ed. S. Das. 1999, TMS: Warrendale, PA.
79. *ASM handbook - Volume 3 Alloy Phase Diagrams*. c1992, ASM International: Materials Park, Ohio
80. Campbell, J., *Castings.* Butterworth-Heinemann, Oxford, UK, 1991.
81. Gruzleski, J.E. and B.M. Closset, *The treatment of liquid aluminum-silicon alloys*. 1990, Des Plaines, IL: AFS Inc.
82. Gall, K., et al., *Environmentally influenced microstructurally small fatigue crack growth in cast magnesium.* Materials Science and Engineering A, 2005. **396**(1-2): p. 143-154.
83. Ting, J.C. and F.V.J. Lawrence, *Modeling the Long-Life Fatigue Behavior of a Cast Aluminum Alloy.* Fatigue and Fracture of Engineering Materials and Structures, 1993. **16**(6): p. 631-647.
84. Boileau, J.M., J.W. Zindel, and J.E. Allison, *The effect of solidification time on the*

mechanical properties in a cast A356-T6 aluminum alloy, in *SAE Technical Paper #970019*. 1997.
85. Ting, J.C., *The long-life regime fatigue analysis for lost foam cast Al- Si Alloy 319*. 1991, University of Illinois-Champaign, IL. p. 1?86.
86. Major, J.F., et al., *The Lincoln Mark VIII cast aluminum suspension control arm (parallel development)*, in *SAE Paper 940874*. 1994, SAE International: Warrendale, PA.
87. Lados, D.A. and D. Apelian, *Fatigue crack growth characteristics in cast Al-Si-Mg alloys: Part I. Effect of processing conditions and microstructure.* Materials Science and Engineering A, 2004. **385**(1-2): p. 200-211.
88. Kim, S.-W., et al., Mater. Lett., 2003. **58**: p. 257-261.
89. Kumai, S., et al., *Effects of dendrite cell size and eutectic Si particle morphology on fatigue crack growth in cast and HIPed AC4CH alloys.* Materials Transactions, JIM, 1999. **40**(7): p. 685-691.
90. Ritchie, R.O. and J. Lankford, Mater Sci Eng., 1996. **84**: p. 11-16.
91. Suresh, S. and R.O. Ritchie, *Propagation of short fatigue cracks.* International Metals Reviews, 1984. **29**(6): p. 445-476.
92. de los Rios, E.R. and A. Navarro, *Considerations of grain orientation and work hardening on short-fatigue-crack modelling.* Philosophical Magazine A (Physics of Condensed Matter, Defects and Mechanical Properties), 1990. **61**(3): p. 435-449.
93. Tanaka, K., ed. Small fatigue cracks, ed. R.O. Ritchie and J. Lankford. 1987, Metallurgical Society of the American Institute of Mining, Metallurgical and Petroleum Engineers: Warrendale, PA. 343?61.
94. Wang, Q.G., D. Apelian, and D.A. Lados, *Fatigue behavior of A356/357 aluminum cast alloys. Part II - Effect of microstructural constituents.* Journal of Light Metals, 2001. **1**(1): p. 85-97.
95. Yi, J.Z., *Effect of microstructure and defects on the fatigue behavior of cast A356-T6 aluminium-silicon alloy*, in *Department of Materials*. 2004, Imperial College: London, UK.
96. Caceres, C.H., et al., *The effect of Mg an the microstructure and mechanical behavior of Al-Si-Mg casting alloys.* Metallurgical and Materials Transactions A (Physical Metallurgy and Materials Science), 1999. **30A**(10): p. 2611-2618.
97. Weakley-Bollin, S.C., et al., *Modeling the age-hardening behavior of Al-Si-Cu alloys.* Metall. & Mater. Trans. A, 2003. **35A**(8): p. 2407.
98. Hatch, J.E., *Aluminum: properties and physical metallurgy*. 1984, Metals Park, OH: ASM International.
99. Porter, D.A. and E.K. E., *Phase transformations in metals and alloys*. 1981, Van Nostrand Reinhold, Berkshire, England.
100. Boileau, J.M., et al., *The dimensional stability of cast 319 aluminum*, in *SAE Technical paper #2003-01-0822*. 2003.

101. Petit, J. and C. Sarrazin-Baudoux, *An overview on the influence of the atmosphere environment on ultra-high-cycle fatigue and ultra-slow fatigue crack propagation.* International Journal of Fatigue, 2006. **28**(11): p. 1471-1478.
102. Kumai, S., et al., *Effects of solidification structure on fatigue crack growth in AC4CH cast aluminum alloys.* Journal of Japan Institute of Light Metals, 1995. **45**(4): p. 198-203.
103. Caton, M.J., *Predicting faigue properties of cast aluminum by characterizing small-crak propagation behavior*. 2000, University of Michigan, Ann Arbor, Michigan, USA.
104. Gall, K., et al., Inter. J. Fracture, 2001. **108**: p. 207-233.
105. Jahn, R., W.T. Donlon, and J.E. Allison, eds. *Age hardening behavior in a commercial cast 319-type aluminum alloy*. Automotive Alloys III, ed. S. Das. 1999, TMS: Warrendale, PA.
106. *Annual book of ASTM standards*. Vol. 03.01, E647. 1983, American Society for Testing and Materials: Philadelphia.
107. Peterson, R.E., *Stress concentration factors*. 1974: Wiley Co. 37.
108. Newman, J.C. and I.S. Raju, Eng Fract Mech, 1981. **15**: p. 185-192.
109. Collins, J.A., *Failure of Materials in Mechanical Design*. 1981, New York: John Wiley & Sons. 383-388.
110. Engler-Pinto Jr., C.C., et al., *Statistical approaches applied to fatigue test data analysis*, in *SAE technical paper #2005-01-0802*.
111. Pascual, F.G. and W.Q. Meeker, *Estimating fatigue curves with the random fatigue - limit model.* Technometerics, 1999. **41**(4): p. 277-290.
112. Annis, C. and J. Griffiths. *Staircase testing and random fatigue limit*. in *6th National Turbine Engine High Cycle Fatigue (HCF) Conference*. 2001. Jacksonville, FL.
113. Mayer, H., et al., *Influence of loading frequency on the high cycle fatigue properties of AlZnMgCu1.5 aluminium alloy.* Materials Science and Engineering A, 2001. **314**(1-2): p. 48-54.
114. Engler-Pinto Jr., C.C., et al. *Effect of frequency and environment on high cycle fatigue of cast aluminum alloys*. in *VHCF-4*. 2007. Ann Arbor, MI: TMS.
115. Seniw, M.E., et al. in *High cycle fatigue of structural materials: Paul Paris symposium materials week'97*. 1998. Indianapolis, IN: TMS, Warrendale, PA.
116. Mason, E.A. and A.P. Malinauskas, *Gas Transport in Porous Media: The Dusty-Gas Model*. 1983: Elsevier.
117. R. P. Wei, et al., *Fracture mechanics and surface chemistry studies of fatigue crack growth in an aluminum alloy.* Metall. & Mater. Trans. A, 1980. **11A**: p. 151-158.
118. Gingell, A.D.B. and J.E. King, *The effect of frequency and microstructure on corrosion fatigue crack propagation in high strength aluminium alloys.* Acta Materialia, 1997. **45**(9): p. 3855-3870.

119. Holroyd, N.J.H. and D. Hardie, *Factors controlling crack velocity in 7000 series aluminium alloys during fatigue in an aggressive environment.* Corrosion Science, 1983. **23**(6): p. 527-531.
120. Fisher, D.J., ed. *Hydrogen diffusion in metals - A 30- year retrospective*. 1999, Scitec Publications Ltd: Switzerland. 30-31.
121. Broek, D., *Elementary engineering fracture mechanics*. 4th Ed. ed. 1986, Dordrecht, The Netherlands: Martinus Nijhoff. 96-97.
122. Murakami, Y., *Metal fatigue: Effect of small defects and nonmetallic inclusions*. 2002, Boston: Elsevier Scicence Ltd. 369.
123. Buffiere, J.-Y., et al., *Experimental study of porosity and its relation to fatigue mechanisms of model Al-Si7-Mg0.3 cast Al alloys.* Mater. Sci. Eng., 2001. **A316**: p. 115-126.
124. Cheong, J., Master Thesis, Imperial College, UK, 2002.
125. Lee, S.G., A.M. Gokhale, and A. Sreeranganathan, Materials Science and Engineering A, 2006. **427**: p. 92-98.
126. Fullman, R.L., Trans. AIME, 1953. **197**: p. 447-52.
127. Underwood, E.E., Quantitative Stereology, Addison-Welsey, London, 1970: p. 109-45.
128. Spowart, J.E., B. Maruyama, and D.B. Miracle, *Multi-scale characterization of spatially heterogeneous systems: implications for discontinuously reinforced metal-matrix composite microstructures.* Materials Science and Engineering A, 2001. **307**(1-2): p. 51-66.